UNIVERSITAT ROVIRA i VIRGILI

Analysis of the Different Kinetic Processes in Perovskite Solar Cells

JESÚS JIMÉNEZ LÓPEZ

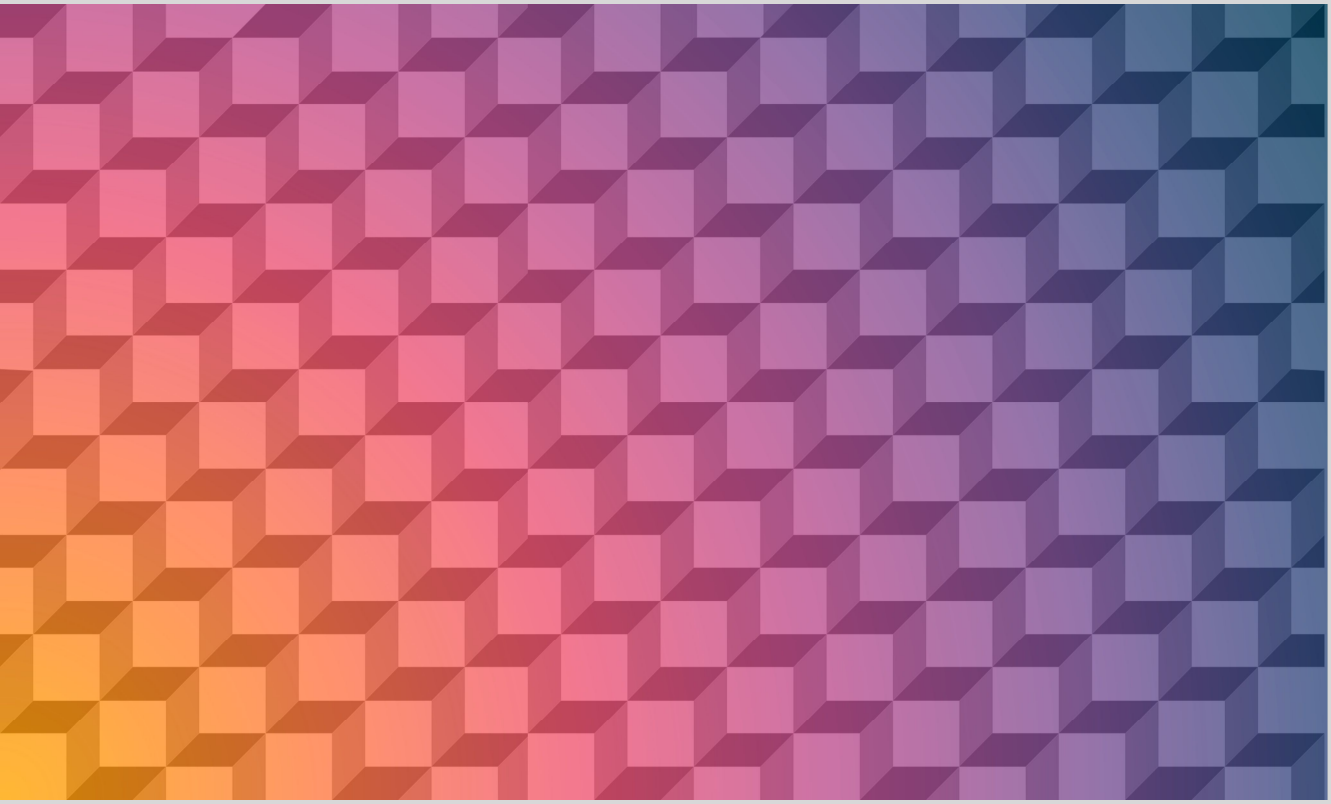

DOCTORAL THESIS
2019

Doctoral Thesis

Analysis of the Different Kinetic Processes in Perovskite Solar Cells

Jesús Jiménez López

Supervised by Prof. Emilio José Palomares Gil

Universitat Rovira i Virgili

Institut Català d'Investigació Química

Tarragona

November 2019

Prof. Dr. Emilio J. Palomares Gil, group leader at the Institute of Chemical Research of Catalonia (ICIQ) in Tarragona and Research Professor at the Catalan Institution for Advanced Studies (ICREA) in Barcelona

I STATE that the present study, entitled "**Analysis of the Different Kinetic Processes in Perovskite Solar Cells**", presented by Jesús Jiménez López for the award of the degree of doctor, has been carried out under my supervision at the Institute of Chemical Research of Catalonia (ICIQ) and that he fulfills the requirements to obtain the distinction of international doctor.

Tarragona, November 22nd 2019

Prof. Dr. Emilio J. Palomares Gil

Doctoral thesis supervisor

UNIVERSITAT ROVIRA i VIRGILI

ICIQ Institute of Chemical Research of Catalonia

Acknowledgements

After four years, it is the moment to close this stage of my life. In this period, I have lived in two different cities, Tarragona and Erlangen, and, most importantly, I have met many amazing people from all over the world. It is time now to show my gratitude to all of them, which have made this time so special.

First, to my supervisor, Prof. Emilio Palomares, thanks for your supervision and guidance, for showing me your point of view on science, and for always believing in us as scientists.

Thanks to all my colleagues in the ICIQ, it's been a pleasure to share with you all this time. Thanks to Maria, Santi, Ilario, Sofia, Cristina, Núria, Lydia, Werther, Georgiana, Ece, Dora, Jonas, Sarika, Lijun, Tsung Yu, Rajesh, Iker, Toni, David, Paola, Alba, Andrea, and Javi. Special thanks to Eva, Aurora, and Bea, for always helping us. Also, many special thanks to Maria, Ilario, and Cristina for helping me with the corrections on the thesis.

Thanks to the Pavipollos group, Nuria, Miguel, Kike, Jesús, Ester, Cris, Andreu, Alicia Monleón, Alicia Martínez, Alba, and Raúl. Hanging out with you is the best way to disconnect from work in Tarragona, always laughing and sharing so many good moments. I really will miss you.

Now, it's time for the people of Erlangen, thanks to Prof. Dirk M. Guldi and all the people in the Guldi group, for making me feel like at home during my time there. Special thanks to Dr. Bianka Puscher, it's been a real pleasure to meet you and collaborate with you.

Also, thanks to all the people I met in Erlangen, for making that time so great, Ciccio, Janina, Ale, Ricardo, Luis, Yamina, Frania, Emilio, Rubén, Waldemar, Pablo, Dani, and Adri.

To all my people in Ávila, for all the time we shared in these years. Really looking forward to meeting you guys.

I don't want to forget all my people in Mogambos, always looking forward to meeting you again. Specially Adri and Pedro, for so many concerts, visits, and infinite laughs, thanks.

A mi familia, padres y hermanas, gracias infinitas por vuestro apoyo y por mandarme fuerzas y energía a diario. Gracias por haberme inculcado todos los valores que han hecho que sea de esta manera. Gracias

Por último, a Ana, no creo que de verdad te pueda agradecer todo lo que te mereces. Gracias por sacarme todos los días una sonrisa, por toda tu energía, por ser siempre tan positiva, por aguantarme en cada momento, por todos tus consejos... En definitiva, gracias por hacerme feliz.

To all of you, thank you!

A mis padres y mis hermanas

Para Ana

Table of Contents

Chapter 1: Introduction 1

Chapter 2: Motivation and Aims 45

Chapter 3: Experimental Procedures and Characterization Techniques 51

Chapter 4: Charge carrier interfacial processes at the perovskite/hole transporting material interface 97

Chapter 5: Charge carrier interfacial processes at the perovskite/electron transporting material interface 143

Chapter 6: Charge carrier processes at the perovskite layer ... 175

Chapter 7: General Conclusions 201

Summary of the thesis

Photovoltaics have become one of the most popular renewable source of energy. Photovoltaic technologies transform sunlight into electricity, they are available worldwide, and they do not depend on the conversion of motive power, making this technology quite easy to implement. Nowadays, silicon is still the most used material for photovoltaics. Anyway, new photovoltaic technologies have emerged as alternatives to silicon, as they are cheaper, easier to process, and, they are possible to use on flexible substrates. Among them, lead halide perovskites have become one of the most popular choice in the scientific community, due to the great properties that this material presents. While efficiencies have risen above 25%, which is close to their maximum theoretical limit, there is still debate about the processes happening in the device. In this thesis, we try to gain insight into charge carrier processes from their generation to their recombination at both perovskite interfaces, and also in the bulk of the material. Using advanced characterization techniques, such as transient photovoltage (TPV), transient photocurrent (TPC), charge extraction (CE), and femtosecond transient absorption spectroscopy (fsTA) we obtained important findings about charge carrier losses, and artifacts affecting charge carrier recombination in functional devices that lead to lower power conversion efficiencies.

Resumen de la tesis

La energía fotovoltaica se ha convertido en una de las alternativas más populares como fuente de energía renovable. Se basa en la transformación directa de radiación solar en electricidad. Se encuentra disponible a escala global y además no precisa de ningún transformador para convertir la energía mecánica en energía eléctrica, lo que hace que sea fácil de implementar. Hoy en día, el material más utilizado para aplicaciones fotovoltaicas sigue siendo el silicio. En cambio, el desarrollo de nuevas tecnologías, más baratas, fáciles de procesar y que además pueden utilizarse en sustratos flexibles, ha surgido como alternativa al silicio. De todas ellas, las perovskitas basadas en haluros de plomo se han convertido en una de las mejores opciones para la comunidad científica debido a las excelentes propiedades fotovoltaicas que presenta. Aunque las eficiencias de los dispositivos preparados con perovskitas han alcanzado el 25%, un valor que se encuentra muy cercano a su máximo teórico, los procesos que tienen lugar en estos dispositivos aún no son del todo conocidos. En esta tesis se trata de obtener información acerca de los procesos de los transportadores de carga, desde cómo se generan hasta la recombinación, tanto en las interfaces como en el interior del propio material. Para ello, se han utilizado distintas técnicas de caracterización avanzadas como el fotovoltaje transitorio (TPV), fotocorriente transitoria (TPC), la extracción de carga (CE) y la espectrocopía de absorción transitoria en la escala del femtosegundo (fsTA), obteniendo importantes conclusiones sobre pérdidas y procesos que afectan a la recombinación de transportadores de carga que llevan a peores eficiencias en celdas solares.

Resum de la tesi

L'energia fotovoltaica s'ha convertit en una de les alternatives més populars com a font d'energia renovable. Es basa en la transformació directa de radiació solar en electricitat. Es troba disponible a escala global i a més no necessita de cap transformador per convertir l'energia mecànica en energia elèctrica, el que fa que sigui fàcil d'implementar. Avui en dia, el material més utilitzat per a aplicacions fotovoltaiques segueix sent el silici. En canvi, el desenvolupament de noves tecnologies, més barates, fàcils de processar i que a més poden utilitzar-se en substrats flexibles, ha sorgit com a alternativa al silici. De totes elles, les perovskita basades en halurs de plom s'han convertit en una de les millors opcions per a la comunitat científica a causa de les excel·lents propietats fotovoltaiques que presenta. Tot i que les eficiències dels dispositius preparats amb perovskita han arribat al 25%, un valor que es troba molt proper al seu màxim teòric, els processos que tenen lloc en aquests dispositius encara no són del tot coneguts. En aquesta tesi es tracta d'obtenir informació sobre els processos dels transportadors de càrrega, des de com es generen fins a la recombinació, tant en les interfícies com a l'interior del propi material. Per això, s'han utilitzat diferents tècniques de caracterització avançades com el fotovoltatge transitori (TPV), la fotocorrent transitòria (TPC), l'extracció de càrrega (CE) i l'espectroscòpia d'absorció transitòria en l'escala del femtosegon (FSTA), obtenint importants conclusions sobre pèrdues i processos que afecten la recombinació de transportadors de càrrega que porten a pitjors eficiències en cel·les solars.

Contributions to Scientific Literature

The following publications are based on the work described in this thesis:

1. **J. Jiménez-López**, W. Cambarau, L. Cabau, and E. Palomares; *"Charge Injection, Carriers Recombination and HOMO Energy Level Relationship in Perovskite Solar Cells"* Scientific Reports, **2017**, 7 (1), 6101, DOI: 10.1038/s41598-017-06245-5

2. **J. Jiménez-López**, B.M.D. Puscher, W. Cambarau, R.H. Fink, E. Palomares, and D.M. Guldi, *"Hot Electron Injection in Polymer Based-Perovskite Solar Cells; the Role of Semiconducting Polymers"*, Nanoscale, **2019**, **Accepted Article**

3. **J. Jiménez-López**, and E. Palomares, *"Interfacial Recombination Kinetics in Aged Perovskite Solar Cells Measured Using Transient Photovoltage Techniques"* Nanoscale, **2019**, **Accepted article**, DOI: 10.1039/C9NR06278E

4. **J. Jiménez-López**, B.M.D. Puscher, D.M. Guldi, and E. Palomares, *"Improved Carrier Collection and Hot Electron Extraction Across Perovskite, C_{60}, and TiO_2 interfaces"* J. Am. Chem. Soc., **2019**, **Submitted article**

The following publications are not included in this thesis

5. N.F. Montcada, J.M. Marín-Beloqui, W. Cambarau, **J. Jiménez-López**, L. Cabau, K.T. Cho, M.K. Nazeeruddin, and E. Palomares; *"Analysis of Photoinduced Carrier Recombination Kinetics in Flat and Mesoporous Lead Perovskite Solar Cells"* ACS Energy Lett., **2017**, 2 (1), 182, DOI: 10.1021/acsenergylett.6b00600

6. E. Aktas, **J. Jiménez-López**, C. Rodríguez-Seco, R. Pudi, M.A. Ortuño, N. López, and E. Palomares, *"Supramolecular Coordination of Pb^{2+} Defects in Hybrid Lead Halide Perovskite Films Using Truxene*

Derivatives as Lewis Base Interlayers", ChemPhysChem, **2019**, 20, 1-11 DOI: 10.1002/cphc.201900068

7. **J. Jiménez-López**, and E. Palomares, *"Flat Is Boring in Perovskite Light Detectors"* Chem, **2019**, 5 (4), 748, DOI: 10.1016/j.chempr.2019.03.014

Oral and Poster Presentations at Conferences

- **Workshop on Flexible Electronics**, Tarragona (Spain), June 2016. Oral presentation: *"Photo-induced charge kinetics of $MAPbI_3$ vs $FAPbI_3$ perovskite solar cells"*
- **European Optical Society Annual Meeting 2016 (EOSAM 2016)**, Berlin (Germany), September 2016. Oral presentation: *"Photo-induced charge kinetics of $MAPbI_3$ vs $FAPbI_3$ perovskite solar cells"*
- **Perovskite Solar Cells and Optoelectronics 2017 (PSCO 2017)**, Oxford (United Kingdom), September 2017, Poster presentation: *"Charge Injection, Carriers Recombination and HOMO Energy Level Relationship in Perovskite Solar Cells"*
- **Stability of Emerging Photovoltaics 2018 (SEPV 2018)**, Barcelona (Spain), February 2018, Oral and poster presentation *"Charge Injection, Carriers Recombination and HOMO Energy Level Relationship in Perovskite Solar Cells"*
- **2nd ICIQ PhD Day 2018**, Tarragona (Spain), June 2018, Oral presentation: *"Hot electron injection into semiconducting polymers limits the efficiency in perovskite solar cells"*
- **International Conference on Nanotechnology and Bionanoscience (NanoBio 2018)**, Heraklion, Crete (Greece), September 2018, Oral presentation: *"Hot electron injection limits the efficiency in perovskite solar cells"*
- **NanoGe Fall Meeting 2019**, Berlin (Germany), November 2019, Poster presentation: *"Interfacial Recombination Kinetics in Aged Perovskite Solar Cells Measured Using Transient Photovoltage Techniques"*

List of abbreviations

α power law exponent in current versus illumination intensity relationship

A area

AFM atomic force microscopy

AM 1.5 air mass 1.5

CE charge extraction

CBD chemical bath deposition

CBM conduction band minimum

$CH(NH_2)_2^+$ formamidinium cation

$CH_3NH_3^+$ methylammonium cation

FK209 Co(III) TFSI tris(2-(1H-pyrazol-1-yl)-4-tert-butylpyridine)cobalt(III) tri[bis(trifluoromethane)sulfonimide]

CB conduction band

CCD charge coupled device

C_{geo} geometric capacitance

CsFAMAPbIBr triple cation perovskite; cesium formamidinium methylammonium lead ioidide bromide perovskite

$cTiO_2$ compact titania

$C(V_{OC})$ capacitance at every voltage

C_{60} fullerene C_{60}

δ recombination order

ΔA difference absorption

ΔQ extra carriers generated by the small perturbation induced with the laser pulse

ΔV laser induced small perturbation in voltage

d distance between the two plates of a capacitor

DiffCap differential capacitance

DFT density functional theory

DMF N,N-dimethylformamide

DMSO dimethyl sulfoxide

DSSC dye sensitized solar cells

ε electrical permittivity

ε_r relative permittivity

ε_0 electric constant

E_A activation energy

E_B exciton binding energy

ESEM environmental scanning electron microscopy

ETM electron transport material

Φ light intensity

FA^+ formamidinium cation

FAI formamidinium iodide

FF fill factor

fsTA femtosecond transient absorption spectroscopy

FTO fluorine tin oxide

FWHM full width at half maximum

GSB ground-state bleaching

HOMO highest occupied molecular orbital

HTM hole transporting material

IE ionization energies

IR infrared

ITO indium tin oxide

J net currrent

$\mathbf{J_{MPP}}$ maximum power point current

$\mathbf{J_{SC}}$ short-circuit current

$\mathbf{J_0}$ dark diode saturation current

JV current density-voltage

$\mathbf{K_B}$ Boltzmann constant

λ factor that describes the slope in the relationship of the small perturbation lifetime as a function of the carrier density

λ_{exc} excitation wavelength; pump pulse

λ_{probe} detection wavelength; probe pulse

L device thickness

LED light emitting diode

LiTFSI lithium bis(trifluoromethanesulfonyl)imide

LO longitudinal optical phonons

LUMO lowest unoccupied molecular orbital

μ_h hole mobility

m factor related with the deviation from the thermal voltage of carrier density

MA^+ methylammonium cation

MABr methylammonium bromide

MAI methylammonium iodide

$MAPbI_3$ methylammonium lead iodide perovskite

MPP maximum power point

$mTiO_2$ mesoporous titania

n carrier density

n_{eq} equilibrium carrier concentration

n_{id} ideality factor

NIR near infrared

NOPA non-collinear optical parametric amplifier

OPA optical parametric amplifier

OSC organic solar cells

PCE power conversion efficiency

PCPDTBT poly[2,6-(4,4-bis-(2-ethylhexyl)-4H-cyclopenta[2,1-b;3,4-b′]dithiophene)-alt-4,7(2,1,3-benzothiadiazole)]

$PC_{61}BM$ [6,6]-phenyl C_{61} butyric acid methyl ester

$PC_{71}BM$ [6,6]-phenyl C_{71} butyric acid methyl ester

PEDOT:PSS poly(3,4-ethylenedioxythiophene) polystyrene sulfonate

PIA photo-induced absorption

P_{in} incident light power density

P_m maximum power output

PL photoluminescence

PMT photomultiplier

PTAA poly(triaryl amine)

PSC perovskite solar cells

P3HT poly(3-hexylthiophene-2,5-diyl)

PTB7 poly[[4,8-bis[(2-ethylhexyl)oxy]benzo[1,2-b:4,5-b']dithiophene-2,6-diyl][3-fluoro-2-[(2-ethylhexyl)carbonyl]thieno[3,4-b]thiophenediyl]]

θ factor related with the deviation from the thermal voltage of the small perturbation lifetime

Q charge density

q elementary charge

QFLS quasi Fermi level splitting

R resistance

SCLC space charge limited current

spiro-OMeTAD $N^2,N^2,N^{2\prime},N^{2\prime},N^7,N^7,N^{7\prime},N^{7\prime}$-octakis(4-methoxyphenyl)-9,9′-spirobi[9H-fluorene]-2,2′,7,7′-tetramine

SRH Shockley-Read-Hall recombination

ssDSSC solid state dye sensitized solar cells

SEM scanning electron microscopy

τ total carrier lifetime

τ_{cap} capacitive component in small perturbation lifetime obtained from transient photovoltage decays

$\tau_{\Delta n}$ small perturbation lifetime

$\tau_{\Delta n0}$ equilibrium small perturbation lifetime

T temperature

TBP **4**-tert-butylpyridine

TCO transparent conductive oxide

TCSPC time correlated single photon counting

TPC transient photocurrent

TPV transient photovoltage

TRPL time resolved photoluminescence

TROTTR transient of transient photovoltage

UV-Vis ultraviolet and visible radiation

V voltage

VB valence band

VBM valence band maximum

V_{bi} built-in voltage

V_{MPP} maximum power point voltage

V_{OC} open-circuit voltage

XRD x-ray diffraction

List of Figures

Figure 1.1. Perovskite crystalline structure following the ABX_3 chemical formula.

Figure 1.2. Scheme showing the different perovskite architectures employed in literature.

Figure 1.3. Timeline showing the different processes happening in a perovskite solar cell and the different techniques employed in this thesis to analyze them.

Figure 1.4. Isosurface plot of the electron density associated with the VBM and the CBM of $MAPbI_3$. Reproduced from Brivio, F.; Walker, A. B.; Walsh, A. APL Mater. 2013, 1 (4), 042111 with the permission of AIP Publishing.

Figure 1.5. (A) Reciprocal space 3D view showing the first Brillouin Zone of the Pm3m space group. Points of high symmetry are denoted with the letters Γ (center of the Brillouin zone), X (center of a face), M (center of an edge), and R (Corner point). **(B)** Electronic band structure of $MAPbI_3$, adopted from the DFT calculations. Adapted with permission from Even, J.; Pedesseau, L.; Katan, C., J. Phys. Chem. C 2014, 118 (22). Copyright © 2014 © 2014 American Chemical Society.

Figure 1.6. (A) Normalized bleaching kinetics at 480 nm and 760 nm which show the slow formation of the GSB at 760 nm after excitation at 400 nm (top) and 600 nm (bottom). Reprinted with permission from Xing, G.; Mathews, N.; Sun, S.; Lim, S. S.; Lam, Y. M.; Gratzel, M.; Mhaisalkar, S.; Sum, T. C. Science 2013, 342 (6156), 344–347 Copyright © 2013, American Association for the Advancement of Science. **(B)** Spectral broadening of the GSB to higher energies after the excitation at 2.25 eV. Reprinted with permission from Price, M. B.; Butkus, J.; Jellicoe, T. C.; Sadhanala, A.; Briane, A.; Halpert, J. E.; Broch, K.; Hodgkiss, J. M.; Friend, R. H.; Deschler, F. Nat. Commun. 2015, 6 (May), 8420 Copyright © 2015, Springer Nature.

Figure 1.7. Scheme showing the different stages on the carrier relaxation process. Adapted with permission from Richter, J. M.; Branchi, F.; Valduga de Almeida Camargo, F.; Zhao, B.; Friend, R. H.; Cerullo, G.; Deschler, F. Nat. Commun. 2017, 8 (1), 376. Copyright © 2017, Springer Nature

Figure 1.8. Recombination mechanisms in perovskite. **(A)** Trap-assisted recombination, **(B)** band-to-band bimolecular radiative recombination, and **(C)** Auger recombination, which involves a third component, the energy of recombination is transfer to another carrier and it is also possible to be assisted by phonons.

Figure 3.1. (Left) Scheme with the different layers of a n-i-p type perovskite solar cell. **(Right)** Picture of a complete solar cell view from the Au electrode side.

Figure 3.2. Typical JV curve of a perovskite solar cell (black line) and its power conversion output (blue line). It is also shown the MPP (red), V_{OC}, and J_{SC} (green). The ratio between the red and grey rectangles areas is the fill factor.

Figure 3.3. (A) JV curve measured on forward (dashed) and reverse (line) conditions. This cell presents high degree of hysteresis, which is corroborated by the difference between the areas of the FF on forward (red area) and reverse (green area) conditions. **(B)** Influence of the scan speed on the JV performance for a same solar cell which presents negligible hysteresis at 40 mV/s, while some degree of hysteresis is observed at 200 mV/s. The shadowed areas indicate the difference of the forward and reverse JV curves.

Figure 3.4. JV curves measured under different light intensitites from 1 Sun to dark (100, 81.3, 51.5, 25.2, 12.6, and 5.1 mW/cm^2) on forward (dashed) and reverse (line) conditions.

Figure 3.5. (A) J_{SC} dependence with the light intensity obtained from the reverse JV curves on Figure 3.4. obtaining a linear increment of J_{SC} with Φ. **(B)** V_{OC} dependence with Φ obtained from Figure 3.4. The n_{id} found suggests a recombination regime ranging from interfacial to bulk recombination.

Figure 3.6. UV-Vis absorption spectra of the $MAPbI_3$ perovskite. It is clearly observed the two different absorbance features at 760 and 480 nm.

Figure 3.7. Scheme of the transient absorption principle.

Figure 3.8. Picture of a fsTA spectrometer with the main components highlighted.

Figure 3.9. Schematic description of the fsTA spectrometer setup.

Figure 3.10. Scheme summarizing the CE measurement process.

Figure 3.11. (A) CE decay from a perovskite device. In blue, it is shown the experimental data, in orange the exponential fit, and in pink the obtained integrated charge density. **(B)** Carrier density obtained from the integration at different light intensities plot as a function of the voltage. In pink it is shown the experimental data obtained from every CE decay, and the blue line shows the corresponding fitting.

Figure 3.12. Scheme summarizing the TPV measurement process.

Figure 3.13. (A) Example of a TPV decay (blue) and the monoexponential fit (orange). We obtain from this decay $\tau_{\Delta n}$ and the intensity of the small

perturbation, ΔV. **(B)** $\tau_{\Delta n}$ as a function of the different photovoltage obtained (blue) and the exponential fit (orange).

Figure 3.14. Scheme summarizing the TROTTR measurement process.

Figure 3.15. Scheme summarizing the TPC measurement process.

Figure 3.16. **(A)** Differential Capacitance plot obtained from a combination of TPV and TPC decays at different light intensities as a function of the light bias. The orange line shows the exponential fit. **(B)** Carrier density as a function of the light bias obtained from the integration of the differential capacitance. The orange line shows the fit using equation 3.10 **(C)** Differential Capacitance plot intensities as a function of the light bias after the subtraction of the C_{geo}. The orange line shows the exponential fit. **(D)** Carrier density as a function of the light bias obtained from the integration of the differential capacitance after the subtraction of C_{geo}. The orange line shows the fit using equation 3.16

Figure 3.17. **(A)** Comparison for carrier density obtained from the CE and DC methods for $MAPbI_3$ perovskite. **(B)** Comparison for the carrier density obtained from the CE and DC methods for CsFAMAPbIBr perovskite.

Figure 3.18. **(A)** Small perturbation lifetime as a function of the carrier density obtained from the DiffCap method. **(B)** Small perturbation lifetime as a function of the carrier density obtained from the DiffCap method after the subtraction of C_{geo}. In orange it is shown the experimental data for the CsFAMAPbIBr perovskite with the power law fitting as a blue line, and purple shows the experimental data from the $MAPbI_3$ perovskite and the purple line the power law fitting.

Figure 3.19. Total carrier lifetime obtained from the correction of the small perturbation lifetime with the recombination order as a function of the carrier density obtained from the DiffCap method.

Figure 3.20. Small perturbation as a function of the light bias in the region around 1 Sun (orange) and calculated τ_{cap} using equation 3.15 that confirms that we are measuring lifetimes corresponding to bulk dynamics.

Scheme 4.1. Molecular structure of the different HTM employed in this chapter.

Figure 4.1. **(A)** XRD pattern of $MAPbI_3$ perovskite. AFM images of $MAPbI_3$ **(B)** and $MAPbI_3$ covered with the different HTM under study, spiro-OMeTAD **(C)**, PTB7 **(D)**, P3HT **(E)**, and PCPDTBT **(F)**.

Figure 4.2. **(A)** JV curves of the best performing devices on reverse scan (V_{OC} to J_{SC}) under 1 Sun conditions. **(B)** Scheme containing the energetic levels of the different HTM compared to $MAPbI_3$.

Figure 4.3. Statistical distribution of the photovoltaic parameters obtained from the JV curves measured under 1 Sun Conditions.

Figure 4.4. (**A**) Light intensity dependence with Jsc and (**B**) V_{OC} for the different HTM under study.

Figure 4.5. (**A**) Normalized PL spectra of the MAPI and MAPI/HTM films. (**B**) PL decay dynamics of the perovskite/HTM films under. Both measurements were obtained after a excitation at 470 nm.

Figure 4.6. TPV decays measured under 1 Sun conditions for all the devices studied, (**A**) spiro-OMeTAD, (**B**) PTB7, (**C**) P3HT, and (**D**) PCPDTBT. It is also shown the monoexponential fit to obtain the perturbation lifetime.

Figure 4.7. Perturbation lifetime obtained from the TPV decays as a function of the voltage generated at different light intensities.

Figure 4.8. (A) Differential Capacitance plot as a function of the V_{OC} for the different HTM used including the geometric capacitance. **(B)** Differential Capacitance after subtracting the geometric capacitance.

Figure 4.9. (A) Carrier density obtained from the integration of the differential capacitance at the same voltages. **(B)** Carrier density obtained after the subtraction of the geometrical capacitance, reflecting the carriers stored in the perovskite bulk. **(C)** Carrier density obtained from the CE method.

Figure 4.10. (A) Carrier lifetime as a function of the carrier density in the device considering the geometric capacitance and **(B)** after the subtraction of the geometric capacitance.

Figure 4.11. JV measurements of the hole only devices for each HTM under study. The lines correspond to the fitting of the SCLC method.

Figure 4.12. UV-Vis absorption spectra of the $MAPbI_3$ film.

Figure 4.13. FsTA spectra in the visible and NIR of $MAPbI_3$ films using λ_{exc} = 460 nm and a laser fluence of 130 $\mu J/cm^2$.

Figure 4.14. (A, **C)** Differential absorption spectra of $MAPbI_3$ with time delays of 0.5 ps (blue), 3 ps (purple), and 20 ps (orange) **(A)**. Time absorption profiles of $MAPbI_3$ at 480 nm (blue) and 760 nm (orange) **(C)** using λ_{exc} = 460 nm and a laser fluence of 130 $\mu J/cm^2$. **(B**, **D)** Differential absorption spectra of $MAPbI_3$ with time delays of 0.5 ps (blue), 3 ps (cyan), and 20 ps (green) **(B)**. Time absorption profiles of $MAPbI_3$ at 480 nm (blue) and 760 nm (green) **(D)** using λ_{exc} = 695 nm and a laser fluence of 130 $\mu J/cm^2$.

Figure 4.15. FsTA spectra of TiO_2/MAPI films with λ_{exc} = 460 nm. Differential absorption spectra **(A)** with time delays of 0.5 ps (blue), 3 ps (purple), and 20

ps (orange). Time absorption profiles **(B)** at 480 nm (blue), 760 nm (purple), and 970 nm (orange) showing the electron injection into the TiO_2 layer.

Figure 4.16. UV-Vis absorption spectra of the different $MAPbI_3$/HTM and HTM films. **(A)** $MAPbI_3$/spiro-OMeTAD and spiro-OMeTAD films; **(B)** $MAPbI_3$/PTB7 and PTB7; **(C)** $MAPbI_3$/P3HT and P3HT; and **(D)** $MAPbI_3$/PCPDTBT and PCPDTBT. The dashed blue line indicates the excitation wavelength in the fsTA experiments.

Figure 4.17. Differential absorption spectra obtained by spectroelectrochemical oxidation at different voltages for spiro-OMeTAD ($V_{spiro\text{-}OMeTAD}$ = +0.27 V) **(A)**, PTB7 (V_{PTB7} = +1.52 V) **(B)**, P3HT (V_{P3HT} = +1.07 V) **(C)**, and PCPDTBT ($V_{PCPDTBT}$ = +0.07 V) **(D).** All potentials vs Fc/Fc^+.

Figure 4.18. Comparison of the differential absorption spectra in the visible and NIR region of the different films, $MAPbI_3$, TiO_2 / $MAPbI_3$, $MAPbI_3$ / spiro-OMeTAd, $MAPbI_3$ / PTB7, $MAPbI_3$ / P3HT, and $MAPbI_3$ / PCPDTBT at 1.2 ps with λ_{exc} = 460 nm and a laser fluence of 130 $\mu J/cm^2$.

Figure 4.19. Time absorption profiles obtained at the maximum of the polaron features for every HTM: **(A)** spiro-OMeTAD, **(B)** PTB7, **(C)** P3HT, and **(D)** PCPDTBT. The fast component of the decay is associated with hole injection.

Figure 4.20. (A-C) FsTA spectra in the visible and NIR (600-1100 nm) of $MAPbI_3$ **(A)**, $MAPbI_3$/spiro-OMeTAD **(B)**, and $MAPbI_3$/PCPDTBT **(C)** using λ_{exc} = 460 nm and a laser fluence of 64 $\mu J/cm^2$. **(D)** Differential absorption spectra with a time delay of 0.5 ps for $MAPbI_3$ (grey), $MAPbI_3$/spiro-OMeTAD (green), and $MAPbI_3$/PCPDTBT (pink). Solid lines are added to highlight the PIA signals of hot carriers (780 nm). Vertical dashed lines highlight the polaron of spiro-OMeTAD at 965 nm and PCPDTBT at 905 nm. Horizontal dashed lines indicate the time delay of 0.5 ps.

Figure 4.21. Comparison of differential absorption spectra at 0.5 ps with λ_{exc} = 460 nm and laser fluences of 26 $\mu J/cm^2$ **(A)**, 64 $\mu J/cm^2$ **(B)**, 130 $\mu J/cm^2$ **(C)**, and 191 $\mu J/cm^2$ **(D)** of $MAPbI_3$ (grey). $MAPbI_3$/spiro-OMeTAD (green), and $MAPbI_3$/PCPDTBT (pink).

Figure 4.22. Time absorption profiles of spiro-OMeTAD **(A)** and PCPDTBT **(B)** polaron signals at 965 nm and 905 nm, respectively with increasing laser fluences from 26 to 191 $\mu J/cm^2$.

Figure 4.23. Kinetic traces obtained for $MAPbI_3$ (grey), TiO_2/$MAPbI_3$ (blue), $MAPbI_3$/spiro-OMeTAD (green), and $MAPbI_3$/PCPDTBT (pink) using λ_{exc} = 460 probing at 780 and a laser fluence of 130 $\mu J/cm^2$ **(A)**. Kinetic traces probing at 760 nm and a laser fluence of 130 $\mu J/cm^2$ **(B)** and a laser fluence of 26 $\mu J/cm^2$ **(C)**. **(D)** Scheme showing the proposed mechanism. Hot electrons are either injected into TiO_2 (1) and/or PCPDTBT (2). The electrons injected into

PCPDTBT are transferred back to $MAPbI_3$ (3). Additionally, there is the hole injection into the HTM (4).

Figure 5.1. ESEM images of the four different architectures employed in this study **(A)** $cTiO_2$, **(B)** $cTiO_2/C_{60}$, **(C)** $mTiO_2$, and **(D)** $mTiO_2/C_{60}$.

Figure 5.2. JV curves of the champion devices of the four different types of devices under study. Both forward (dashed lines) and reverse (solid lines) were measured under 1 Sun conditions (100 mW/cm^2, AM 1.5G) with a scan rate of 40 mV/s. The shadowed area shows the degree of hysteresis in every device.

Figure 5.3. Photovoltaic parameters derived from the JV measurement in both forward and reverse conditions of 15 PSC. All JV curves were measured under 1 Sun conditions (100 mW/cm^2, AM 1.5G) with a scan rate of 40 mV/s.

Figure 5.4. (A) DiffCap plots as a function of the applied light bias. **(B)** DiffCap after subtracting C_{geo} (carriers stored at the contacts). **(C)** Total charge carrier density at different V_{OC} values, including carriers in the bulk and the contacts. **(D)** Charge carrier density in the perovskite bulk.

Figure 5.5. Small perturbation lifetime from TPV experiments as a function of the light bias. The lines relates to the exponential fit from **Equation 5.4.**

Figure 5.6. Small perturbation lifetime from TPV measurements as a function of the carrier density in the devices after subtracting C_{geo} **(A)** and including C_{geo} **(B)**.

Figure 5.7. Carrier lifetime obtained from the TPV measurements as a function of the carrier density based on the DiffCap method. The lines show the power law fitting used to estimate the recombination order.

Figure 5.8. V_{OC} stabilization times for $mTiO_2/MAPbI_3$ and $mTiO_2/C_{60}/MAPbI_3$ devices. The dotted vertical lines indicate the times at which TPV transients were acquired in **Figure 5.9**.

Figure 5.9. TPV transients measured after 3, 5, 10, and 30 s of illumination at 1 Sun conditions for $mTiO_2/MAPbI_3$ **(A)** and $mTiO_2/C_{60}/MAPbI_3$ **(B)** using a laser excitation wavelength of 590 nm.

Figure 5.10. Differential absorption spectra at 0.7 ps of the different $ETM/MAPbI_3$ films with **(A)** $cTiO_2$ and $cTiO_2/C_{60}$; **(B)** $mTiO_2$ and $mTiO_2/C_{60}$ compared with the reference $MAPbI_3$ using λ_{exc} = 695 nm and a laser fluence of 64 $\mu J/cm^2$.

Figure 5.11. Kinetic traces probing at 950 nm of the different $ETM/MAPbI_3$ films with **(A)** $cTiO_2$ and $cTiO_2/C_{60}$ as well as **(B)** $mTiO_2$ and $mTiO_2/C_{60}$ compared with the reference $MAPbI_3$ using λ_{exc} = 695 nm and 64 $\mu J/cm^2$ as laser fluence

Figure 5.12. Normalized kinetic traces probing at 780 nm **(A**, **B)** and as-measured kinetic traces probing at 780 nm **(C-F)** of the different ETM/$MAPbI_3$ films with **(A**, **C**, **E)** $cTiO_2/C_{60}$, as well as **(B**, **D**, **F)** $mTiO_2$, and $mTiO_2/C_{60}$ compared with the reference $MAPbI_3$ using λ_{exc} = 695 **(A-D)** and 460 nm **(E**,**F)** using a laser fluence of 64 $\mu J/cm^2$.

Figure 5.13. PIA intensity dependence with the laser fluence ranging from 26 to 191 $\mu J/cm^2$ which results in an exponential dependency for $MAPbI_3$ and $cTiO_2/MAPbI_3$ and linear dependency for $cTiO_2/C_{60}/MAPbI_3$ **(A)**. The dependency is linear for $mTiO_2/MAPbI_3$ and $mTiO_2/C_{60}/MAPbI_3$ in **(B)**.

Scheme 5.1. Energy levels characteristics in the early stages of illumination. The presence of ions at the interface drives ions into the opposite direction of extraction **(A)**. The use of C_{60} layer mitigates this effect blocking ionic movement and improving carrier collection **(B)**.

Figure 6.1. (A) Photovoltaic parameters obtained from the JV curves of the devices measured on day 3 and 45. **(B)** JV curves of the same device measured on day 3 and day 45. All the measurements were done at 1 Sun conditions (AM 1.5 G, 100 mW/cm^2) and a scan rate of 40 mv/s.

Figure 6.2. JV curves of the same solar cell measured on different days, while it was stored under air or N_2 conditions. The shadowed area shows the degree of hysteresis on the device.

Figure 6.3. V_{oc} stabilization over time of the devices measured on days 3 and 45. Dashed lines show the times at which TPV pulses for transient of the transient were acquired.

Figure 6.4. Scheme showing the possible band diagrams in different stages. Dashed lines show the Fermi levels, complete lines show the valence and conduction band of the perovskite, and the squared positive and negative symbols shoe the ions in the perovskite.

Figure 6.5. (**A)** TPV signals of the device measured on day 3 with different illumination times. (B) TPV signals of the device measured on day 45 with different illumination times.

Figure 6.6. Amplitude of the negative transient deflection at different illumination times obtained from the TPV measurements.

Figure 6.7. (**A**) Small perturbation lifetime as a function of the photovoltage generated in the devices with the exponential fitting (**A**) and the calculation of the capacitive discharge (dashed lines, **B**).

Figure 6.8. JV curves under different light intensities for the devices measured on day 3 (**A**) and day 45 (**B**). J_{sc} values at different light intensities and the fitting to a power law dependence in reverse conditions (**C**). V_{oc} dependence

with the light intensity in reverse conditions (**D**) used to estimate the ideality factor.

Figure 6.9. (**A**) Differential capacitance at different voltages (light bias). (**B**) Carrier density obtained upon integration of the capacitance at the same voltages. (**C**) Differential capacitance plot after the subtraction of the geometric capacitance (carriers at the contacts), and (**D**) carrier density obtained upon the integration of the capacitance in (**C**) showing the carriers stored in the bulk of the perovskite.

Figure 6.10. Small perturbation lifetime as a function of the carrier density obtained from the integration of differential capacitance.

Figure 6.11. Small perturbation lifetime obtained from the TPV as a function of the carrier density obtained from the integration of the differential capacitance after the subtraction of the geometric capacitance.

Figure 6.12. (**A**) Carrier density obtained at different voltages using the CE technique. (**B**) Small perturbation lifetime as a function of the carrier density obtained from CE.

List of tables

Table 4.1. Photovoltaic parameters obtained from the JV curves in Figure 4.2. In parentheses, the average and the standard deviation is shown for the efficiency of all the devices.

Table 4.2. TRPL lifetimes obtained from the fitting of PL decays in Figure 4.5.B to a biexponential fitting.

Table 4.3. HOMO and LUMO values of the different HTM, hole injection rates derived from the fastest component in the kinetic traces of the oxidized species of the HTM, and power conversion efficiencies obtained from **Table 4.1** on the reverse sweep conditions.

Table 5.1. Summary of the photovoltaic parameters obtained from the JV measurement under 1 Sun conditions

Table 6.1. Summary of the photovoltaic parameters of the cells tested in the study. The results were obtained under 1 Sun conditions (AM 1.5G, 100 mW/cm^2) and a scan rate of 40 mV/s.

Table 6.2. Summary of the fitting parameters to calculate the Voc obtained from the TPV and TPC techniques.

Chapter 1

Introduction

CHAPTER 1: INTRODUCTION 1

1.1. Energy consumption 5

1.2. Historic overview of photovoltaics 5

1.3. Lead Halide Perovskites 7
1.3.1. Crystalline structure 7
1.3.2. Evolution of Perovskite Solar Cells 8
1.3.3. State of the art perovskite solar cells 11
1.3.4. Working mechanism of perovskite solar cells 12
1.3.5. Charge carrier generation 13
1.3.6. Hot carriers 16
1.3.7. Charge carrier relaxation 17
1.3.8. Charge carrier injection 19
1.3.9. Charge carrier recombination 21
1.3.10. Ion migration 26

1.4. References 29

1.1. Energy consumption

Global electricity demands are constantly increasing. To cover all these demands, the major source to generate electricity is still burning coal, which is associated with the large CO_2 emissions. The good news is that the use of renewable energies already covers one-quarter of the total global electricity needs, and, just in 2018, the use of photovoltaics, wind, and hydropower increased 30% compared to the previous year. Yet, this does not cover all the new electricity demands, and therefore, the use of fossil fuels also increased to meet all the needs[1].

A larger fossil fuel consumption supposes larger CO_2 emissions, which are directly related to global warming. The consequences of it are already perceived, and it is urgent to take action. We need to reduce the use of fossil fuels to minimize CO_2 emissions, and the use of renewable sources appears to be the best choice to generate electricity. Between these, the best alternative is the use of photovoltaics that directly transform sunlight into electricity. Nowadays, the fabrication costs of silicon panels are reduced to the minimum, and, additionally, huge research efforts are driven to new photovoltaic technologies which are paving the way towards an efficient, clean, and cheap source of electricity.

1.2. Historic overview of photovoltaics

The photovoltaic effect was first reported in 1839 by Edmond Becquerel, when he created the first photovoltaic cell. The device consisted in two silver plates, working as electrodes, immersed in an electrolytic media. When the electrodes were exposed to light, he observed a current flowing between them[2]. Then, in the 1870s, Adams and Day reported that light cause a flow of electricity in solid materials when light irradiates selenium bars[3]. Later on, in 1883 Fritts fabricated the first solar cell. He employed selenium bars coated with a thin layer of gold obtaining a continuous and constant current[4].

Another breakthrough was the description of the photoelectric effect, in 1905, by Einstein, who described the emission of electrons when light hits a material. He discovered that light contains packets of energy, now called photons, whose energy is dependent on the wavelength. For this discovery, Einstein received the Nobel Prize in 1921.

However, it was not until the 1950s when Bell laboratories in the USA announced the invention of the first practical solar cell[5]. It was based on a silicon p-n junction with an efficiency of 6%. This opened the way to the development of photovoltaic technologies based on silicon, which has reached nowadays 26.7% with silicon single crystals.

In the last 30 years, intense research efforts are driven to the developments of new photovoltaic technologies, to obtain low-cost and high-efficiency devices that can compete with silicon solar cells in the solar market. In 1991, Grätzel and O'Regan developed the Dye-Sensitized Solar Cells (DSSC)[6], which use a film coated with TiO_2 nanoparticles, and sensitized with an organic dye. This resulted in low cost, and highly efficient solar cells.

Another emerging technology is Organic Solar Cells (OSC), which has attracted the interest of many research groups. OSC show great characteristics, they are fabricated via solution-process methods, they are low-cost, lightweight, and environmentally friendly.

In the last ten years, the development of hybrid organic-inorganic lead halide perovskite has supposed a revolution in the field of photovoltaics. Many research groups turn their eye into this technology. These efforts have resulted in a big race for the highest efficiency that surpassed this year 25 %[7], which is already really close to the values obtained for silicon.

1.3. Lead Halide Perovskites

1.3.1. Crystalline structure

The term perovskite refers to a class of materials that present the same crystal structure as the mineral perovskite, calcium titanate ($CaTiO_3$). This mineral was discovered in 1839 by Gustav Rose, who named it after the Russian mineralogist Lev Alekseevich Perovski[8]. Perovskite materials follow the ABX_3 chemical formula where A and B are the cations and X are the anions. The B cations are located in the corners of a cubic structure, and they are bonded by the X anions, which are located at the center of the edges. Then, A, which is bigger than B, is located in the center of the cube (**Figure 1.1**).

In the case of lead halide perovskites, the A cation is the organic fraction, which usually is methylammonium ($CH_3NH_3^+$), formamidinium ($NH_2CHNH_2^+$), or alkaline cations like Cs^+, although it has been reported Rb^+, K^+, or even Na^+. In the B position, metals from the group 14 of the periodic table, normally Pb^{2+}, is found. In order to avoid the Pb compounds, there is increasing interest in Sn^{2+} perovskites (known as lead-free). The X anions correspond to the halides, which most commonly is occupied by I^- or Br^-, although Cl^- has also been used.

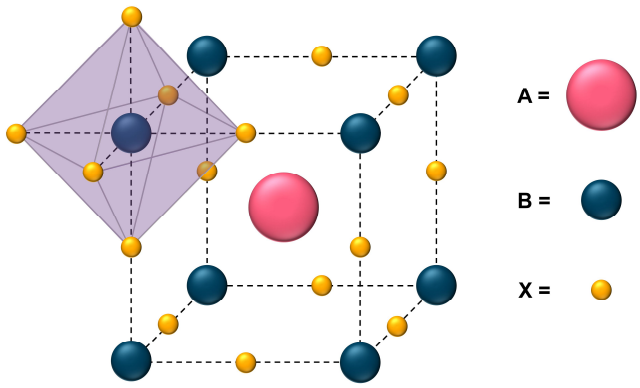

Figure 1.1. Perovskite crystalline structure following the ABX_3 chemical formula.

1.3.2. Evolution of Perovskite Solar Cells

The first report on lead halide perovskite was given by Wells in 1892[9]. However, it was not until 1959 when the crystalline structure was deduced by Moller. Also, he observed photoconductivity in $CsPbX_3$[10]. Later on, in 1978, Weber described for the first time the hybrid organic-inorganic perovskites[11]. In the following decades, there were several reports studying the diverse optical, magnetic, and electronic properties on these perovskites[12–15], while in the 1990s there was an increasing interest in perovskites for fabrication of field-effect transistors[16], or light emitting diodes[17]. Although they show excellent optoelectronic properties, they were not applied on photovoltaic devices.

Then, in 2009, Miyasaka[18] and co-workers reported for the first time the use of lead halide perovskites in solar cells using methylammonium lead iodide ($CH_3NH_3PbI_3$). The first use was as a dye in DSSCs, obtaining an efficiency of 3.8%. Another approach for perovskites used as DSSCs was given by Park and co-workers in 2011[19]. In this case, they used perovskite quantum dots as dye sensitizers reaching efficiencies of 6.5 %. However, both approaches suffered great stability issues due to the use of the liquid electrolyte, which dissolved the perovskite material. For this reason, at the beginning, perovskite did not receive much attention.

A major breakthrough occur in 2012 when two different papers were published almost at the same time. The first one, by Park's group, which implemented perovskite in solid state DSSC (ssDSSC), using spiro-OMeTAD as hole transporting material (HTM)[20]. Spiro-OMeTAD was already well-known as HTM in ssDSSCs, since the first reported use was in 1998 by Grätzel's group[21]. The use of spiro-OMeTAD in perovskite solar cell increased both, device efficiency up to 9.7 %, and stability (up to 500 hours). The second paper was published by Snaith and co-workers and their work was based on the substitution of the mesoporous TiO_2 scaffold with Al_2O_3[22] . They observed that

although Al_2O_3 is an insulator, device efficiency increased. This led to the conclusion that perovskite was not acting only as an absorber, but it was capable of charge transportation, which suggested that perovskites can work in a planar configuration, without the use of a mesoporous layer.

The reported low trap density and long carrier diffusion length in lead halide perovskites[23,24] direct the device fabrication towards thicker perovskite layers, thus, the absorption is improved, avoiding the possible shunts between the contacts. These findings open the way to the development of both mesoporous perovskite devices, in which the mesoporous layer is reduced, as well as the introduction of planar perovskite devices, either in n-i-p configuration or p-i-n configuration.

The next challenge for perovskites in order to obtain high efficiencies was to obtain high-quality perovskite films, with big crystal size, and without pinholes. This was achieved introducing sequential deposition methods, most commonly known as two-step deposition, introduced by Burschka *et al.*[25] In this approach, a solution of PbI_2 is spin-coated followed by a deposition of a methylammonium iodide (MAI) solution by spin coating or dipping. Other alternatives to obtain high-quality films are vapor deposition[26], in which the MAI powder are heated up, and their vapors react with the PbI_2 film to form the perovskite layer. Another alternative is the deposition of the material precursors using thermal evaporation in ultra-high vacuum conditions[27].

Afterwards, advanced engineering techniques were developed, leading to >20 % device efficiencies. These techniques were based in solvent engineering, deposition process, as well as band-gap engineering. Solvent engineering is referred to the mixture of solvents in the perovskite solution preparation that allows us to use single step deposition processes resulting in uniform perovskite films. The most common approach is the mixture of DMSO with DMF introduced by Jeon *et al.*[28] DMSO forms an intermediate phase with

PbI_2 and MAI that delays the crystallization process. This results in bigger and more uniform perovskite crystals. Also introduced by Jeon *et al.*[28] is the anti-solvent treatment, which consists in dripping a solvent while the substrate is still spinning. The most common solvents used for this approach are chlorobenzene, toluene, or diethyl ether, among others. The anti-solvent procedure accelerates the nucleation and crystal growth of the perovskite films.

Furthermore, we like to comment on the band-gap engineering for perovskite solar cells. This is achieved by mixing different precursors that introduces in the perovskite structure different cations for the A and B position, and halides for the X position. The most typical have been the introduction of mixtures of methylammonium (MA^+) and formamidinium (FA^+) in the A position, and the mixture of I^- and Br^- in the X position[29]. However, there have also been examples using Sn^{2+} in order to replace Pb^{2+}. From all these approaches, the use of the commonly known triple cation perovskite[30], which combines MA^+, FA^+, and Cs^+ in the A position together with Pb^{2+} as cations with mixtures of I^- and Br^- has become the most employed and the reference composition in perovskite solar cells. With this mixture, it is possible to obtain a perovskite that absorbs towards lower energies, increasing the current density. The introduction of Cs^+ stabilizes the solar cell, and also reduces the trap density and carrier recombination[31].

Nowadays, in order to continue increasing the device efficiencies towards the theoretical maximum, the trend is to passivate the interfaces in order to reduce the interfacial recombination. For example, very recently, it was reported that the use of phenylethylamine effectively passivates defects at the surface of the perovskite, increasing the efficiency to 23.3 %[32]. All of these advances in perovskite solar cell research have made that in just ten years efficiencies have increased from the initial 3.8 % to 25.2 % recently reported[7].

1.3.3. State-of-the-art of perovskite solar cells

Perovskite solar cells are based on a stacked structure in which the perovskite layer is sandwiched between the selective contacts. Depending on which selective contact is deposited on top of the conductive glass, we differentiate between two types of perovskite architecture. First, the n-i-p architecture, which has also been referred as "regular" structure and presents the n-type selective contact on top of the glass. The second, the p-i-n or "inverted", where the p-type selective contact is deposited on top of the conductive glass. From this two, we can also split into two different kinds for the n-i-p structure, depending on the use of a mesoporous layer or not[33]. **Figure 1.2** summarizes the three main architectures explained in this section.

- Mesoporous n-i-p perovskite solar cells. In this device, which is still the most used, normally fluorine tin oxide (FTO) is employed as the transparent conductive oxide (TCO). Then, a thin layer of compact TiO_2 is deposited followed by a mesoporous TiO_2 layer. The thickness of the mesoporous layer has been reduced over time, and nowadays, a thin layer of about 100-150 nm is deposited. Then, the perovskite layer, with a thickness between 400-600 nm. The next layer is the HTM. Despite of being the most used spiro-OMeTAD, it presents some stability problems, reason why there is huge research efforts to synthesize new HTM[34]. As an alternative to it and with competitive results, several commercially available polymers such as PTAA[35] or P3HT[36] have been used. The last step of the device fabrication, is the deposition of a metal electrode, usually gold or silver.

- Planar n-i-p perovskite solar cells. Normally, FTO is used as TCO, although indium tin oxide (ITO) can also be used. Then, some examples using compact TiO_2 are reported, but in many cases they suffer from a strong hysteresis behavior and low stabilized efficiencies,

which is linked to the energetic barrier due to the amorphous nature of the compact TiO_2[37]. Recently, the highest efficiencies have been reported using SnO_2 as ETM[32]. Then, the perovskite layer is deposited, and finally, the HTM, which is the same as in the previous architecture, spiro-OMeTAD, PTAA, or P3HT are deposited. The device is completed with the metal contact, usually gold or silver are used.

- Planar p-i-n perovskite solar cells. Finally, this is the third most used perovskite architecture. Now, ITO is usually used, then as HTM PEDOT:PSS or PTAA are used, followed by the perovskite layer and as ETM fullerene derivatives are usually employed, being evaporated C_{60}, or solution processed $PC_{61}BM$, or $PC_{71}BM$[38]. In most examples, a thin layer of BCP is deposited afterwards, and finally, silver as the metal electrode.

It has been challenging for the scientific community to get efficient devices with all three different architectures. Last year, Saliba *et al.* published an article with a very detailed procedure to prepare solar cells in these three different architectures[35].

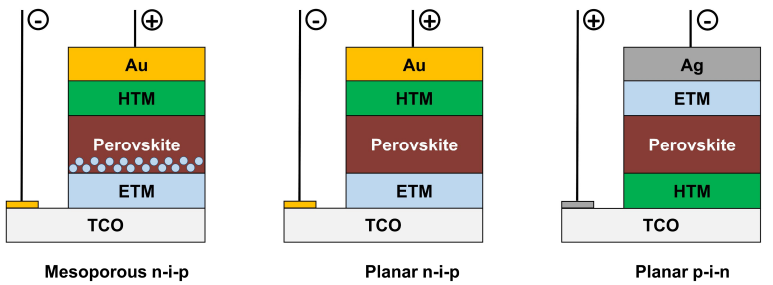

Figure 1.2. Scheme showing the different perovskite architectures employed in literature.

1.3.4. Working mechanism of perovskite solar cells

In a perovskite solar cell, the absorption of light generates excitons or free carriers that are excited to the conduction band of perovskite. If the energy of the photons is larger than the band-gap of the perovskite, hot carriers are

created. Then, these carriers relax to the conduction band minimum and they diffuse through the perovskite absorber. Once they reach the interface, charge carriers (holes and electrons) are injected into the selective contacts, and, finally, after some time, they are collected in the electrodes. However, in this time frame, different mechanisms of recombination take place, radiative, non-radiative, and interfacial recombination. Once charge carriers are in the electrodes, they are transported through an external electric circuit and load to produce electrical work. The timeline of these processes is summarized in **Figure 1.3** and they will be extensively studied in the following sections of this Chapter.

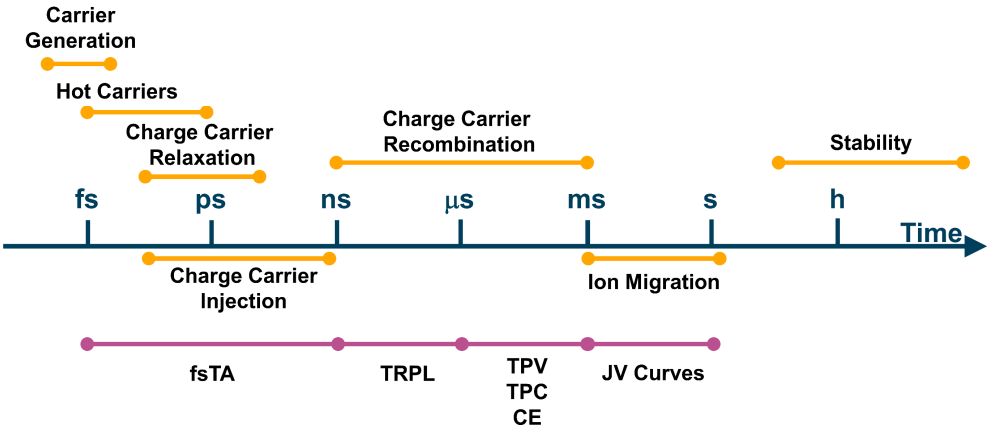

Figure 1.3. Timeline showing the different processes happening in a perovskite solar cell and the different techniques employed in this thesis to analyze them.

1.3.5. Charge carrier generation

In order to analyze the dynamics of excited states in perovskite, it is necessary to know the origin of these photoexcited states[39]. Therefore, the determination of the band structure and the possible optical transitions in perovskites have been the focus of several research groups[40–44]. A reliable model for the band structure has been obtained using density-functional theory (DFT) simulations. For methylammonium lead iodide ($MAPbI_3$) perovskite at room temperature the valence band maximum (VBM) is formed

by a combination of anti-bonding 5p I orbitals and 6s Pb orbitals, while the conduction band minimum (CBM) is mainly formed by empty 6p Pb orbitals[39,42] (**Figure 1.4**).

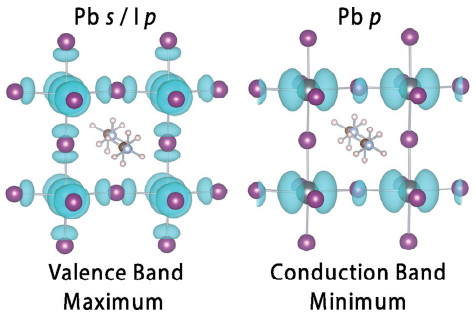

Figure 1.4. Isosurface plot of the electron density associated with the VBM and the CBM of $MAPbI_3$. Reproduced from Brivio, F.; Walker, A. B.; Walsh, A. APL Mater. 2013, 1 (4), 042111 with the permission of AIP Publishing.

From the DFT calculations, it is deduced that the optically allowed transitions from the VBM to the CBM at the R high symmetry point correspond to the band-gap energy[40,43]. The R high symmetry point corresponds to the corner point of the first Brillouin Zone while the M point is located at the center of the edge in a cubic structure[45]. It is also important to note that there is a clear connection between the M and R points in the reciprocal space that allow the photogeneration of charge carriers in a wide range of wavelengths that will relax into the R point associated with the CBM[43] (**Figure 1.5**). These observations explain the observed optical transitions with energies bigger than the band-gap energy, and also the shape of the UV-Vis absorption spectrum with the presence of the two bands at 480 and 760 nm that correspond to the optical transitions at the M and R points respectively.

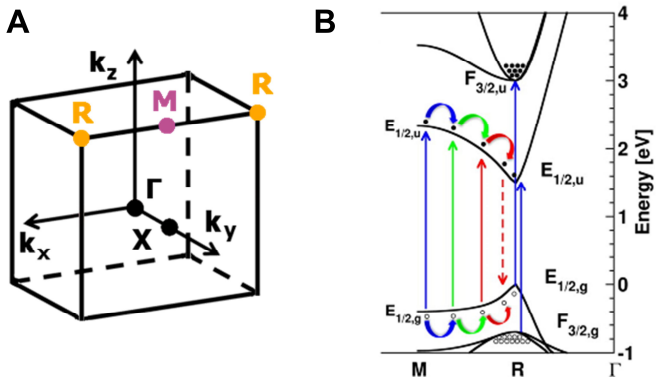

Figure 1.5. **(A)** Reciprocal space 3D view showing the first Brillouin Zone of the Pm3m space group. Points of high symmetry are denoted with the letters Γ (center of the Brillouin zone), X (center of a face), M (center of an edge), and R (corner point). **(B)** Electronic band structure of $MAPbI_3$, adapted from the DFT calculations. Adapted with permission from Even, J.; Pedesseau, L.; Katan, C., J. Phys. Chem. C 2014, 118 (22). Copyright © 2014 © 2014 American Chemical Society.

After photoexcitation, three types of carriers can be found: free charge carriers which are electrons and holes; and coulombically bound electron-hole states, namely excitons[46]. The excitons present an associated binding energy (E_B) that should be overcome to generate free carriers, electrons and holes[39]. Thus, a small E_B is desirable for photovoltaic applications. In the case of lead halide perovskite, with their hybrid organic-inorganic nature, there has been debate about the nature of the carriers, if they are excitonic or free carriers. Although it exists a wide deviation in the estimation of the E_B of perovskites, there is a consensus about the direct generation of free charges from photoexcitation at room temperature[47]. However, the E_B values increase with the band-gap energy, obtained after the modification of the halide and cation composition[46]. Also, E_B is affected by the perovskite's microstructure, as it was found the exciton features increased in larger crystals, while films with smaller crystals suppress their formation[48]. Additionally, E_B has been found to be dependent with the temperature, observing a more excitonic behavior when decreasing temperatures[46]. In summary, at room temperature, most of the photogenerated carriers are free charges, with a small portion of excitons[46].

1.3.6. Hot carriers

Photons with an energy greater than the perovskite band-gap can create carriers with an excess energy. The temperature of such carriers is higher than the lattice temperature, thus they are termed as hot carriers[49,50]. If these hot carriers are extracted before they relax to the band edge the efficiencies can extend surpassing the Shockley-Queisser limit for solar cells[51]. This open the way for the so-called hot carrier solar cells[52].

Perovskite solar cells have demonstrated exceptional properties, with an ultraslow cooling of hot carriers, that have made them a potential candidate for hot carrier solar cells[53].

Hot carriers in perovskite solar cells were first described by Xing *et al*. They reported the slow formation of the ground state bleach (GSB) associated with the band edge, which was assigned to carrier cooling to the band edge (**Figure 1.6.A**)[54]. The most typical observation of the hot carriers in the perovskite and the calculation of their temperature is done following the formation of a high energy tail of the GSB in the early times after photogeneration(**Figure 1.6.B**)[55–58]. This broadening is associated with the presence of a non-equilibrium carrier distribution. Additionally, the description of a photo-induced absorption (PIA) at 1.58 eV was associated to the presence of hot carriers[55,58,59].

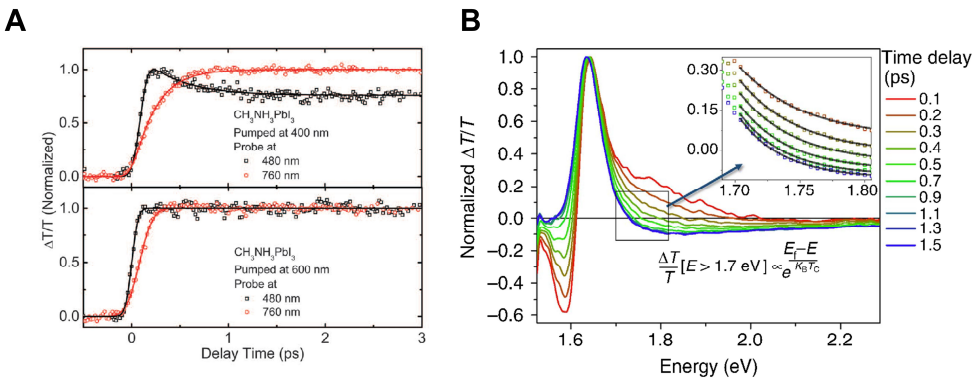

Figure 1.6. (A) Normalized bleaching kinetics at 480 nm and 760 nm which show the slow formation of the GSB at 760 nm after excitation at 400 nm (top) and 600 nm (bottom). Reprinted with permission from Xing, G.; Mathews, N.; Sun, S.; Lim, S. S.; Lam, Y. M.; Gratzel, M.; Mhaisalkar, S.; Sum, T. C. Science 2013, 342 (6156), 344–347 Copyright © 2013, American Association for the Advancement of Science. **(B)** Spectral broadening of the GSB to higher energies after the excitation at 2.25 eV. Reprinted with permission from Price, M. B.; Butkus, J.; Jellicoe, T. C.; Sadhanala, A.; Briane, A.; Halpert, J. E.; Broch, K.; Hodgkiss, J. M.; Friend, R. H.; Deschler, F. Nat. Commun. 2015, 6 (May), 8420 Copyright © 2015, Springer Nature.

1.3.7. Charge carrier relaxation

In a typical semiconductor, an incident photon with an energy higher than the band-gap energy are absorbed, they generate carriers in higher excited states causing a non-thermal carrier distribution. Then, very rapidly, these carriers form a thermal energy distribution, following the Fermi-Dirac statistics. This process, denominated thermalization, is done by carrier-carrier scattering (electron-electron or hole-hole)[49,60]. After thermalization, carriers present a much higher temperature compared to the lattice temperature, reason why they are referred as hot carriers. Richter *et al.*[61] directly observed this process using 2D electronic spectroscopy, and they found a carrier thermalization time between 10 and 85 fs.

Next, a slower cooling, through carrier interactions with the lattice, mainly via carrier-optical phonons interactions. Carriers reduce their temperature until they reach the lattice temperature. This process, carrier cooling, is exceptionally slow in lead halide perovskite, which have made them

a possible candidate for hot carrier solar cells[39,60,62,63]. **Figure 1.7** summarizes the thermalization process.

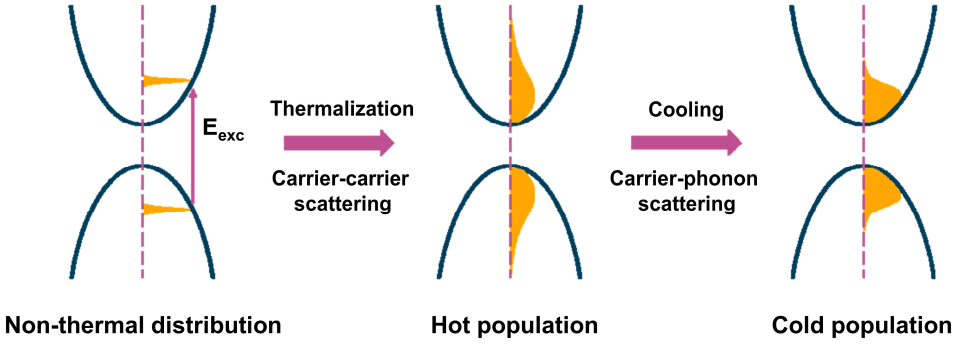

Figure 1.7. Scheme showing the different stages on the carrier relaxation process. Adapted with permission from Richter, J. M.; Branchi, F.; Valduga de Almeida Camargo, F.; Zhao, B.; Friend, R. H.; Cerullo, G.; Deschler, F. Nat. Commun. 2017, 8 (1), 376. Copyright © 2017, Springer Nature

Different mechanisms have been proposed to explain which properties make perovskites present such slow carrier cooling times.

Among the slow hot carrier cooling mechanisms, it has been proposed the hot phonon bottleneck effect, described by Yang *et al.*[56]. This process occurs at high excitation densities, when a non-equilibrium phonon population is created. Here, the probability of an electron absorbing a phonon increases, reducing the cooling rate of carriers, and thus extending the hot carrier lifetime[49,56,64].

Together with the hot-phonon bottleneck, the Auger heating effect can extend carrier cooling times even longer. In this process, the energy of the electron-hole recombination is transferred to another carrier, promoting it to higher excited states[49,57]. This process is observed also in high carrier excitation densities regimes.

Due to the ionic nature of perovskites, the formation of large polarons is one of the mechanisms suggested for slow hot carrier cooling. A polaron quasi-particle is a charge carrier localized in a generated potential due to the

polar response of the lattice[65]. The formation of polarons has been proposed by Zhu and co-workers[66–68]. It has been suggested that the formation of large polarons is due to the deformation of the PbI_3^- inorganic lattice, rather than the cation[66,69]. Also, recently, Batignani *et al.* using impulsive vibrational spectroscopy determined the phonon modes that provide the lattice modification upon photogeneration, and that proves the polaronic nature of perovskites[70]. Frost *et al.* suggested that at low carrier density, the formation of polarons is predominant, while at $n \geq 10^{18}$ cm^{-3} polarons start to overlap, which favors the formation of the hot-phonon bottleneck effect[65]. The formation of large polarons screens the interaction of charge carriers with phonons, with charge defects, and with other charges, obtaining longer hot carrier cooling times[66].

At high charge carrier densities, there are many body effects and state filling effects that also affect the charge carriers dynamics. It is possible to study these effects with transient absorption techniques. Just after photoexcitation, when it exists the hot population, a band-gap renormalization observable as a red-shift of the band edge is detected. This is caused by photoinduced carriers that force the band-gap to shrink[39,55,56]. As carriers thermalize, they occupy states at the band edges which results in state filling, thus, only higher energy states are available for optical transitions. This effect is known as state-filling or Burstein-Moss effect, and it is detected in perovskites as a blue-shift of the band-gap with increasing carrier densities[39,55,56,71].

1.3.8. Charge carrier injection

The extraction of photogenerated charge carriers is of paramount importance for efficient perovskite solar cells. Thus, the use of carrier selective contacts, either hole or electron transport materials is needed in order to facilitate the carrier transport to the corresponding electrode. Some requirements are to possess a high LUMO level in the case of HTMs and a low

HOMO level for ETMs, to act also as carrier blocking layer and avoid back-injection; they should also have energy levels matching the VBM and CBM of the perovskite[72]. Although it seems favorable for charge carrier injection to have an energy offset between the perovskite VBM and HOMO level of the HTM for hole injection, and also between the perovskite CBM and the LUMO level of the ETM for electron injection, this is not the case in perovskite solar cells, as these will introduce a non-radiative recombination component that will affect the final device V_{OC}[73]. The recombination of charge carriers in perovskite will be commented in depth in the following sections.

The determination of charge carrier injection is still a matter of debate. Different techniques, such as femtosecond transient absorption or reflection spectroscopy[74–80], time resolved microwave conductivity[81–83], or time resolved terahertz spectroscopy[84] have been employed, and a wide range of charge injection timescales, from sub-picosecond to several nanoseconds, have been proposed.

Grancini *et al.* determined the electron injection following the spectroscopic features associated with the electrons in the TiO_2 layer with the observation of a PIA in the near-IR region. The formation of this peak was completed in the first picosecond after photoexcitation, therefore, ultrafast electron-transfer was observed[85]. Piatkowski *et al.* followed a similar approach, obtaining similar conclusions, with electron injection taking place on the first 200 fs[74]. In this timescale, the electron injection competes with the electron thermalization in the perovskite layer.

The mechanism of hole injection has not been very well understood yet. In samples containing spiro-OMeTAD as HTM, a broad range of hole injection times have been reported, from sub-ps injection[74,77,85–88] to the nanosecond timescale[54,81,89]. Apart from spiro-OMeTAD, the hole injection into other molecules has been reported. For a series of semiconductor

polymers, such as P3HT, PTAA, and PCPDTBT, Brauer *et al.* reported injection times on the ns timescale[75]. However, Ishioka *et al.*[79] suggested that hole injection in the PTAA occurs orders of magnitude faster, between 1-2 ps. In this timescale, they also assigned the hole injection to PEDOT:PSS. The injection in NiO was identified at 40 ps, which is in contrast with the values deduced by Corani *et al.*[84], which identified sup-ps hole injection timescales. Very recently, Droseros *et al.* studied hole injection in a series of organic HTMs with different ionization energies (IE). They found that hole injection happens in the sub-ps timescale independently of the IE of these molecules[78].

In summary, the reported values indicate that in those timescales, hot carrier injection might be feasible in perovskite solar cells. Also, the variability of the values reported for the carrier injection can be explained in terms of film quality, and, of course, the use of different materials leads to differences in carrier injection rates.

1.3.9. Charge carrier recombination

Charge carrier recombination in photovoltaic devices has a very important role. The extraction of charges competes with carrier recombination, therefore, long carrier lifetimes are desirable to obtain efficient devices[39,90]. In a typical semiconductor, carrier recombination rates are obtained with the following equation:

$$\frac{dn}{dt} = - k_1 n - k_2 n^2 - k_3 n^3 \qquad (1.1)$$

In **Equation 1.1** n is the charge carrier density, k_1 is the rate associated with the trap-assisted Shockley-Read-Hall (SRH) recombination, k_2 is the bimolecular charge carrier recombination rate, and finally k_3 is related to the Auger recombination. The predominant recombination mechanism is ruled by the photoexcitation carrier density. At low carrier densities ($<10^{15}$ cm^{-3}), trap-assisted recombination will dominate. At intermediate carrier densities (10^{15} –

10^{17} cm^{-3}), after all the trap states are filled, the dominant recombination mechanism is the band-to-band bimolecular recombination. At even higher carrier densities, it is Auger recombination the dominant recombination mechanism[39]. The three different recombination mechanisms are summarized in **Figure 1.8**.

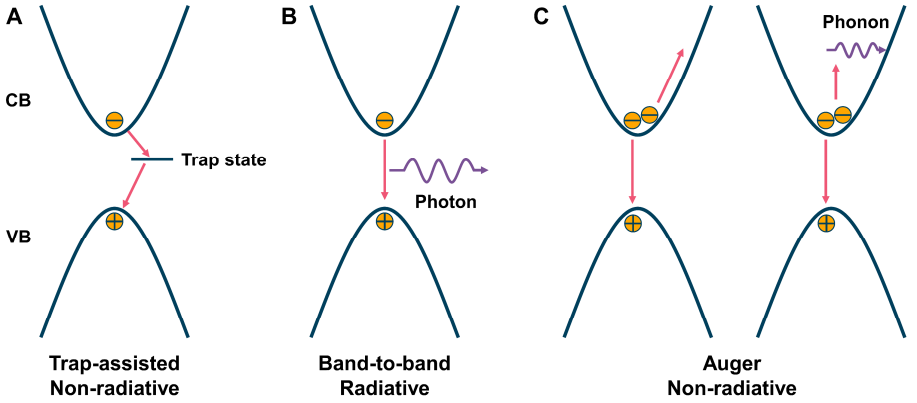

Figure 1.8. Recombination mechanisms in perovskite. **(A)** Trap-assisted recombination, **(B)** band-to-band bimolecular radiative recombination, and **(C)** Auger recombination, which involves a third component, the energy of recombination is transfer to another carrier and it is also possible to be assisted by phonons.

Recombination in the bulk of the perovskite

The case of perovskite is exceptional, as its properties (high trap density and strong light absorption) do not explain the long carrier lifetimes reported for this class of materials[90]. However, just a small amount of these traps are actually active[91]. Also, following the detailed balance principle, large recombination rates are expected from strong absorption coefficients. However, there are some processes happening at the perovskite that can extend their carrier lifetimes, what makes long carrier lifetimes in perovskite, actually expected, and not surprising[90]. This issue was addressed in a recent review by DeQuilettes *et al.*[90], they reached the conclusion that carrier lifetimes in perovskite are so long due to the photon recycling effect and the presence of polarons, while the continuous trapping and detrapping of carriers,

and the Rashba effect, which is a direct-indirect band-gap behavior, do not have a strong influence extending carrier lifetimes.

Shockley-Read-Hall trap assisted non-radiative recombination

Shockley-Read-Hall (SRH) trap-assisted recombination[92,93] is a one particle process, either an electron in the conduction band, a hole in the valence band, or an exciton. In perovskite materials, there is agreement that at room temperature only free carriers are generated. Thus, it is expected that the monomolecular decay consists on an electron or a hole lying on trap-states, from where they recombine non-radiatively to the valence band[94]. Solar cells at 1 Sun conditions operate in the low carrier density regime, where trap-assisted recombination is the predominant. For this reason, the passivation of these trap states has been the focus of attention for many research groups, obtaining longer charge carrier lifetimes[95,96] and better efficiencies[32,97].

These trap states are created by point defects of the perovskite lattice. Meggiolaro *et al.*[91] determined for $MAPbI_3$ that the only stable and active trap states are the interstitial iodine defects, although interstitial methylammonium and lead vacancies are the most common point defects in this perovskite configuration. Interstitial iodine introduces both electron and hole deep traps, however, the latter appear to be the only ones with detrimental effects. In addition, the hole traps can be deactivated by exposure to mild oxidative conditions and/or by halide mixing. All of this would explain the defect tolerance of perovskites[91]. Park *et al.*[98] also determined that those interstitial iodine defects segregate to grain boundaries, where it is possible to find high defect concentration, which act as trap recombination centers. Thus, passivation of grain boundaries reduces trap density in the perovskite obtaining extended lifetimes.

It is important to note that for non-radiative trap mediated recombination to occur, carriers should exchange their energy with the lattice

via the emission of phonons. The low energy phonons present in polar materials, as it is perovskite, make them to suppress non-radiative recombination by many orders of magnitude[99]. This effect is even more pronounced if the trap states are shallow defects, which is the case in most of perovskite point defects[90,99].

Band-to-band radiative recombination

This type of recombination involves two particles of different charge (electron and hole) that recombine radiatively. The energy of the emitted photon depends on the band-gap energy. It can also be described as the inverse process of light absorption[94,100].

Following the principle of detailed balance[101], the radiative recombination is equal to the carrier generation. As we have already appointed, perovskites feature a strong absorption, thus, high radiative recombination rates are expected[100,102]. Besides, charge carrier diffusion lengths are calculated to be already in the micron regime[23], which is larger than the average thickness of perovskite solar cell devices, where a thin layer around 500 - 600 nm is used. In summary, for photovoltaic devices, which operate in a low carrier density regime, it is favorable to have higher absorption coefficients, although this suppose high radiative recombination rates[102].

In contrast, usually the radiative recombination rates are not in accordance with the detailed balance principle. However, this long recombination rates can be justified if photon recycling is taken into account. Also, it has been suggested that the presence of polarons can extend the radiative rate, while other processes such as the Rashba effect is not having such an important effect over radiative recombination rates[90].

Auger recombination

Auger recombination is a many-body recombination type, in which an electron and a hole recombine non-radiatively transferring their energy to a

third carrier, electron in the conduction band, hole in the valence band, or exciton, that it is excited to higher excited states. Most probably, this process is also phonon assisted, via the absorption or emission of phonons[39,103,104].

For solar cells application, Auger recombination presents little importance over carrier recombination rates, as it is only operative in high carrier density regimes (> 10^{17} cm^{-3}) which is far from the carrier densities for photovoltaic applications (10^{15} – 10^{16} cm^{-3}). Yet, it presents high importance for other semiconductor applications which operate at higher carrier densities, such as LEDs or lasers.

Interfacial recombination

Apart from trap-assisted recombination, another source of non-radiative recombination is the interfacial or surface recombination, which strongly affects to the overall perovskite solar cell performance.

The interfacial recombination occurs across the interface between the absorber perovskite and the carrier selective contacts. At each interface, perovskite/ETM and perovskite/HTM, the majority carriers are in the selective contacts, while the minority carriers, which are the limiting species in this process, are in the perovskite[105]. The selectivity of a contact is defined by the capability of injection and extraction of majority carriers while recombination of minority carriers is as inefficient as possible[73,102].

The interfacial recombination losses in functional devices induces both V_{OC} and fill-factor (FF) losses. Thus, it is important to understand the origin and mechanism of interfacial recombination to obtain highly efficient solar cells[106].

Although non-radiative recombination in the bulk of the perovskite introduces losses that affects the V_{OC}, it has been suggested that the limiting factor determining the final V_{OC} of a perovskite solar cell is the interfacial

recombination, being the least selective layer the one setting the final V_{OC}[73,106–108]. The introduction of thin interfacial layers between the absorber and the selective contacts reduces interfacial recombination, obtaining higher V_{OC} values[106,107,109].

Additionally, to maximize the V_{OC}, an energy alignment between the perovskite and the selective contact is desirable, as an energetic offset assists in obtaining increased interfacial recombination[73,110]. Also, it has been seen that materials with a high-doping density increases carrier recombination, as they can act as recombination centers[105,111,112]. Thus, reduced doping density is required to obtain higher performances, which compromise the mobility in the selective contacts. To compensate the reduced mobility, thinner layers should be used[112].

Another parameter which affects importantly interfacial carrier recombination is the ionic presence at the interfaces, which has been associated with the hysteresis observed in perovskite solar cells[113,114]. Ions accumulated at the interfaces create space charged layers where a higher concentration of minority carriers increases carrier recombination. The presence of ions and how they affect carrier recombination have been the matter of study of many research groups[109,112,115–121]. In case of solar cells that claim no hysteresis, the presence of moving ions is not suppressed, but it has been suggested that fast ions can screen the electric field inside of the solar cell[121], or that carrier recombination is reduced, resulting in an efficient charge collection[118].

1.3.10. Ion migration

Although lead halide perovskites have received much attention due to their electronic properties, it is known that they are mixed ionic-electronic conductors[122,123]. Actually, direct measurements of ionic conductivity in perovskites were done in the 1980s[124,125]. However, the ionic conduction did

not receive much attention until the first report of current-voltage hysteresis appeared[113]. From that moment, the presence of moving ions received much attention and it has also been linked to the different processes, such as the switchable photovoltaic effect[126], light induced halide redistribution[127] or phase separation in mixed halide perovskites[128], to cite a few.

Ion migration in lead halide perovskite should occur via defects in the perovskite film, which can be either vacancies (Schottky defects) or by interstitials (Frenkel defects)[122,123,129,130], and any of the ions conforming the perovskite can migrate. The calculation of the activation energy (E_A) determines how easy ions can migrate[122,123,129–131]. There is a large discrepancy between the reported values for the E_A of the defects, but there is agreement that the lowest E_A is found for I^- ions, followed by MA^+, and Pb^{2+} for $MAPbI_3$ perovskite, which is the most extensively studied perovskite [123,130–132]. It is also known that I^- are the most mobile species, with diffusion coefficients orders of magnitude higher than that of the MA^+ species, making I^- defects to diffuse to the electrodes in the μs timescale, while the diffusion of MA^+ is in the order of tens of ms to minutes[123,130,131,133]. Likewise, it should be highlighted the role of grain boundaries on ion migration, as it is described that ion migration through grain boundaries is faster than in the bulk of the perovskite[122,123,134]. Direct observation of ionic migration is possible using Kelvin Probe Force Microscopies techniques, as reported by Birkhold *et al.*[135,136] and Weber *et al.*[137].

Among the reported effects associated with ionic migration, the most important and studied one is the presence of current-voltage hysteresis. There is agreement that the presence of ions at the interfaces cause the observed hysteresis[114,132,138,139]. However, which ions cause this effect is matter of debate. I^- ions accumulate at the interface, which can cause the hysteresis observed in devices[123]. Nevertheless, the reported diffusion values and activation energies for I^- suggest that these species are too fast to have an influence in the current-

voltage curves. Some authors suggest that the slower cations in the perovskite, mainly MA^+, are responsible of the hysteresis observed, as they migrate in the same timescale the hysteresis is observed[130,131]. Another interesting approach was given by Weber *et al.*[137]. Using Kelvin Probe Force Microscopy, they suggest that instead of the slow migration of ions, an interfacial charge layer is formed by the adsorption of ions, mostly related with I^- ions. The slow release of this interfacial layer modifies the charge extraction in the device and it dominates the hysteresis behavior in perovskite solar cells.

1.4. References

(1) International Energy Agency. Global Energy & CO2 Status Report. *Glob. Energy CO2 Status Rep.* **2018**, No. March, 1–15.

(2) A. E. Becquerel. Memoire Sur Les Effects d'Electriques Produits Sous l'Influence Des Rayons Solaires. *Comptes Rendus l'Academie des Sci.* **1839**, *9*, 561–567.

(3) Grylls, A. W.; Day, R. E. IX. The Action of Light on Selenium. *Philos. Trans. R. Soc. London* **1877**, *167*, 313–349. https://doi.org/10.1098/rstl.1877.0009.

(4) Fritts, C. E. On a New Form of Selenium Cell, and Some Electrical Discoveries Made by Its Use. *Am. J. Sci.* **1883**, *s3-26* (156), 465–472. https://doi.org/10.2475/ajs.s3-26.156.465.

(5) Chapin, D. M.; Fuller, C. S.; Pearson, G. L. A New Silicon P-n Junction Photocell for Converting Solar Radiation into Electrical Power. *J. Appl. Phys.* **1954**, *25* (5), 676–677. https://doi.org/10.1063/1.1721711.

(6) O'Regan, B.; Grätzel, M. A Low-Cost, High-Efficiency Solar Cell Based on Dye-Sensitized Colloidal TiO_2 Films. *Nature* **1991**, *353* (6346), 737–740. https://doi.org/10.1038/353737a0.

(7) NREL Efficiency Chart (https://www.nrel.gov/pv/assets/pdfs/best-research-cell-efficiencies.20190923.pdf).

(8) Rose, G. Beschreibung Einiger Neuen Mineralien Des Urals. *Ann. der Phys. und Chemie* **1839**, *124* (12), 551–573. https://doi.org/10.1002/andp.18391241205.

(9) Wells, H. L. Über Die Cäsium- Und Kalium-Bleihalogenide. *Zeitschrift für Anorg. Chemie* **1893**, *3* (1), 195–210. https://doi.org/10.1002/zaac.18930030124.

(10) Møller, C. K. Crystal Structure and Photoconductivity of Cæsium Plumbohalides. *Nature* **1958**, *182* (4647), 1436–1436. https://doi.org/10.1038/1821436a0.

(11) Weber, D. $CH_3NH_3PbX_3$, Ein Pb(II)-System Mit Kubischer Perowskitstruktur / $CH_3NH_3PbX_3$, a Pb(II)-System with Cubic Perovskite Structure. *Zeitschrift für Naturforsch. B* **1978**, *33* (12), 1443–1445. https://doi.org/10.1515/znb-1978-1214.

(12) Mitzi, D. B. Synthesis, Crystal Structure, and Optical and Thermal Properties of $(C_4H_9NH_3)_2MI_4$ (M = Ge, Sn, Pb). *Chem. Mater.* **1996**, *8* (3), 791–800. https://doi.org/10.1021/cm9505097.

(13) Ishihara, T.; Takahashi, J.; Goto, T. Exciton State in Two-Dimensional

Perovskite Semiconductor $(C_{10}H_{21}NH_3)_2PbI_4$. *Solid State Commun.* **1989**, *69* (9), 933–936. https://doi.org/10.1016/0038-1098(89)90935-6.

(14) Mitzi, D. B. Templating and Structural Engineering in Organic–Inorganic Perovskites. *J. Chem. Soc. Dalt. Trans.* **2001**, No. 1, 1–12. https://doi.org/10.1039/b007070j.

(15) Papavassiliou, G. C.; Koutselas, I. B. Structural, Optical and Related Properties of Some Natural Three- and Lower-Dimensional Semiconductor Systems. *Synth. Met.* **1995**, *71* (1–3), 1713–1714. https://doi.org/10.1016/0379-6779(94)03017-Z.

(16) Kagan, C. R. Organic-Inorganic Hybrid Materials as Semiconducting Channels in Thin-Film Field-Effect Transistors. *Science* **1999**, *286* (5441), 945–947. https://doi.org/10.1126/science.286.5441.945.

(17) Mitzi, D. B.; Chondroudis, K.; Kagan, C. R. Organic-Inorganic Electronics. *IBM J. Res. Dev.* **2001**, *45* (1), 29–45. https://doi.org/10.1147/rd.451.0029.

(18) Kojima, A.; Teshima, K.; Shirai, Y.; Miyasaka, T. Organometal Halide Perovskites as Visible-Light Sensitizers for Photovoltaic Cells. *J. Am. Chem. Soc.* **2009**, *131* (17), 6050–6051. https://doi.org/10.1021/ja809598r.

(19) Im, J.-H.; Lee, C.-R.; Lee, J.-W.; Park, S.-W.; Park, N.-G. 6.5% Efficient Perovskite Quantum-Dot-Sensitized Solar Cell. *Nanoscale* **2011**, *3* (10), 4088. https://doi.org/10.1039/c1nr10867k.

(20) Kim, H.-S.; Lee, C.-R.; Im, J.-H.; Lee, K.-B.; Moehl, T.; Marchioro, A.; Moon, S.-J.; Humphry-Baker, R.; Yum, J.-H.; Moser, J. E.; et al. Lead Iodide Perovskite Sensitized All-Solid-State Submicron Thin Film Mesoscopic Solar Cell with Efficiency Exceeding 9%. *Sci. Rep.* **2012**, *2* (1), 591. https://doi.org/10.1038/srep00591.

(21) Bach, U.; Lupo, D.; Comte, P.; Moser, J. E.; Weissörtel, F.; Salbeck, J.; Spreitzer, H.; Grätzel, M. Solid-State Dye-Sensitized Mesoporous TiO_2 Solar Cells with High Photon-to-Electron Conversion Efficiencies. *Nature* **1998**, *395* (6702), 583–585. https://doi.org/10.1038/26936.

(22) Lee, M. M.; Teuscher, J.; Miyasaka, T.; Murakami, T. N.; Snaith, H. J. Efficient Hybrid Solar Cells Based on Meso-Superstructured Organometal Halide Perovskites. *Science* **2012**, *338* (6107), 643–647. https://doi.org/10.1126/science.1228604.

(23) Stranks, S. D.; Eperon, G. E.; Grancini, G.; Menelaou, C.; Alcocer, M. J. P.; Leijtens, T.; Herz, L. M.; Petrozza, A.; Snaith, H. J. Electron-Hole Diffusion Lengths Exceeding 1 Micrometer in an Organometal Trihalide Perovskite Absorber. *Science* **2013**, *342* (6156), 341–344.

https://doi.org/10.1126/science.1243982.

(24) Xing, G.; Mathews, N.; Sun, S.; Lim, S. S.; Lam, Y. M.; Gratzel, M.; Mhaisalkar, S.; Sum, T. C. Long-Range Balanced Electron- and Hole-Transport Lengths in Organic-Inorganic CH3NH3PbI3. *Science* **2013**, *342* (6156), 344–347. https://doi.org/10.1126/science.1243167.

(25) Burschka, J.; Pellet, N.; Moon, S.-J.; Humphry-Baker, R.; Gao, P.; Nazeeruddin, M. K.; Grätzel, M. Sequential Deposition as a Route to High-Performance Perovskite-Sensitized Solar Cells. *Nature* **2013**, *499* (7458), 316–319. https://doi.org/10.1038/nature12340.

(26) Chen, Q.; Zhou, H.; Hong, Z.; Luo, S.; Duan, H.-S.; Wang, H.-H.; Liu, Y.; Li, G.; Yang, Y. Planar Heterojunction Perovskite Solar Cells via Vapor-Assisted Solution Process. *J. Am. Chem. Soc.* **2014**, *136* (2), 622–625. https://doi.org/10.1021/ja411509g.

(27) Liu, M.; Johnston, M. B.; Snaith, H. J. Efficient Planar Heterojunction Perovskite Solar Cells by Vapour Deposition Many Different Photovoltaic Technologies Are Being Developed for Large-Scale Solar Energy Conversion. *Nature* **2013**, *501* (7467), 395–398. https://doi.org/10.1038/nature12509.

(28) Jeon, N. J.; Noh, J. H.; Kim, Y. C.; Yang, W. S.; Ryu, S.; Seok, S. Il. Solvent Engineering for High-Performance Inorganic–Organic Hybrid Perovskite Solar Cells. *Nat Mater* **2014**, *13* (9), 897–903.

(29) Jesper Jacobsson, T.; Correa-Baena, J.-P.; Pazoki, M.; Saliba, M.; Schenk, K.; Grätzel, M.; Hagfeldt, A. Exploration of the Compositional Space for Mixed Lead Halogen Perovskites for High Efficiency Solar Cells. *Energy Environ. Sci.* **2016**, *9* (5), 1706–1724. https://doi.org/10.1039/C6EE00030D.

(30) Saliba, M.; Matsui, T.; Seo, J.-Y.; Domanski, K.; Correa-Baena, J.-P.; Nazeeruddin, M. K.; Zakeeruddin, S. M.; Tress, W.; Abate, A.; Hagfeldt, A.; et al. Cesium-Containing Triple Cation Perovskite Solar Cells: Improved Stability, Reproducibility and High Efficiency. *Energy Environ. Sci.* **2016**, *9* (6), 1989–1997. https://doi.org/10.1039/C5EE03874J.

(31) Hu, Y.; Hutter, E. M.; Rieder, P.; Grill, I.; Hanisch, J.; Aygüler, M. F.; Hufnagel, A. G.; Handloser, M.; Bein, T.; Hartschuh, A.; et al. Understanding the Role of Cesium and Rubidium Additives in Perovskite Solar Cells: Trap States, Charge Transport, and Recombination. *Adv. Energy Mater.* **2018**, *8* (16), 1703057. https://doi.org/10.1002/aenm.201703057.

(32) Jiang, Q.; Zhao, Y.; Zhang, X.; Yang, X.; Chen, Y.; Chu, Z.; Ye, Q.; Li, X.;

Yin, Z.; You, J. Surface Passivation of Perovskite Film for Efficient Solar Cells. *Nat. Photonics* **2019**, *13* (7), 460–466. https://doi.org/10.1038/s41566-019-0398-2.

(33) Sun, S.; Buonassisi, T.; Correa-Baena, J. P. State-of-the-Art Electron-Selective Contacts in Perovskite Solar Cells. *Adv. Mater. Interfaces* **2018**, *5* (22), 1–9. https://doi.org/10.1002/admi.201800408.

(34) Rodríguez-Seco, C.; Cabau, L.; Vidal-Ferran, A.; Palomares, E. Advances in the Synthesis of Small Molecules as Hole Transport Materials for Lead Halide Perovskite Solar Cells. *Acc. Chem. Res.* **2018**, *51* (4), 869–880. https://doi.org/10.1021/acs.accounts.7b00597.

(35) Saliba, M.; Correa-Baena, J.-P.; Wolff, C. M.; Stolterfoht, M.; Phung, N.; Albrecht, S.; Neher, D.; Abate, A. How to Make over 20% Efficient Perovskite Solar Cells in Regular (n–i–p) and Inverted (p–i–n) Architectures. *Chem. Mater.* **2018**, *30* (13), 4193–4201. https://doi.org/10.1021/acs.chemmater.8b00136.

(36) Jung, E. H.; Jeon, N. J.; Park, E. Y.; Moon, C. S.; Shin, T. J.; Yang, T.-Y.; Noh, J. H.; Seo, J. Efficient, Stable and Scalable Perovskite Solar Cells Using Poly(3-Hexylthiophene). *Nature* **2019**, *567* (7749), 511–515. https://doi.org/10.1038/s41586-019-1036-3.

(37) Saliba, M.; Correa-Baena, J.-P.; Grätzel, M.; Hagfeldt, A.; Abate, A. Perovskite Solar Cells: From the Atomic Level to Film Quality and Device Performance. *Angew. Chemie Int. Ed.* **2018**, *57* (10), 2554–2569. https://doi.org/10.1002/anie.201703226.

(38) Stolterfoht, M.; Caprioglio, P.; Wolff, C. M.; Márquez, J. A.; Nordmann, J.; Zhang, S.; Rothhardt, D.; Hörmann, U.; Amir, Y.; Redinger, A.; et al. The Impact of Energy Alignment and Interfacial Recombination on the Internal and External Open-Circuit Voltage of Perovskite Solar Cells. *Energy Environ. Sci.* **2019**, *12* (9), 2778–2788. https://doi.org/10.1039/C9EE02020A.

(39) Herz, L. M. Charge-Carrier Dynamics in Organic-Inorganic Metal Halide Perovskites. *Annu. Rev. Phys. Chem.* **2016**, *67* (1), 65–89. https://doi.org/10.1146/annurev-physchem-040215-112222.

(40) Mosconi, E.; Amat, A.; Nazeeruddin, M. K.; Grätzel, M.; De Angelis, F. First-Principles Modeling of Mixed Halide Organometal Perovskites for Photovoltaic Applications. *J. Phys. Chem. C* **2013**, *117* (27), 13902–13913. https://doi.org/10.1021/jp4048659.

(41) Even, J.; Pedesseau, L.; Jancu, J.-M.; Katan, C. Importance of Spin–Orbit Coupling in Hybrid Organic/Inorganic Perovskites for Photovoltaic Applications. *J. Phys. Chem. Lett.* **2013**, *4* (17), 2999–3005.

https://doi.org/10.1021/jz401532q.

(42) Brivio, F.; Walker, A. B.; Walsh, A. Structural and Electronic Properties of Hybrid Perovskites for High-Efficiency Thin-Film Photovoltaics from First-Principles. *APL Mater.* **2013**, *1* (4), 042111. https://doi.org/10.1063/1.4824147.

(43) Even, J.; Pedesseau, L.; Katan, C. Analysis of Multivalley and Multibandgap Absorption and Enhancement of Free Carriers Related to Exciton Screening in Hybrid Perovskites. *J. Phys. Chem. C* **2014**, *118* (22), 11566–11572. https://doi.org/10.1021/jp503337a.

(44) Even, J.; Pedesseau, L.; Katan, C.; Kepenekian, M.; Lauret, J. S.; Sapori, D.; Deleporte, E. Solid-State Physics Perspective on Hybrid Perovskite Semiconductors. *J. Phys. Chem. C* **2015**, *119* (19), 10161–10177. https://doi.org/10.1021/acs.jpcc.5b00695.

(45) Grosso, G.; Parravicini, G. P. Geometrical Description of Crystals: Direct and Reciprocal Lattices. In *Solid State Physics*; Elsevier, 2014; pp 67–105. https://doi.org/10.1016/B978-0-12-385030-0.00002-5.

(46) Marongiu, D.; Saba, M.; Quochi, F.; Mura, A.; Bongiovanni, G. The Role of Excitons in 3D and 2D Lead Halide Perovskites. *J. Mater. Chem. C* **2019**, *1* (207890), 3777. https://doi.org/10.1039/C9TC04292J.

(47) Huang, J.; Yuan, Y.; Shao, Y.; Yan, Y. Understanding the Physical Properties of Hybrid Perovskites for Photovoltaic Applications. *Nat. Rev. Mater.* **2017**, *2*. https://doi.org/10.1038/natrevmats.2017.42.

(48) Grancini, G.; Srimath Kandada, A. R.; Frost, J. M.; Barker, A. J.; De Bastiani, M.; Gandini, M.; Marras, S.; Lanzani, G.; Walsh, A.; Petrozza, A. Role of Microstructure in the Electron–Hole Interaction of Hybrid Lead Halide Perovskites. *Nat. Photonics* **2015**, *9* (10), 695–701. https://doi.org/10.1038/nphoton.2015.151.

(49) Li, M.; Fu, J.; Xu, Q.; Sum, T. C. Slow Hot-Carrier Cooling in Halide Perovskites: Prospects for Hot-Carrier Solar Cells. *Adv. Mater.* **2019**, *1802486*, 1802486. https://doi.org/10.1002/adma.201802486.

(50) König, D.; Casalenuovo, K.; Takeda, Y.; Conibeer, G.; Guillemoles, J. F.; Patterson, R.; Huang, L. M.; Green, M. A. Hot Carrier Solar Cells: Principles, Materials and Design. *Phys. E Low-dimensional Syst. Nanostructures* **2010**, *42* (10), 2862–2866. https://doi.org/10.1016/j.physe.2009.12.032.

(51) Shockley, W.; Queisser, H. J. Detailed Balance Limit of Efficiency of p-n Junction Solar Cells. *J. Appl. Phys.* **1961**, *32* (3), 510–519. https://doi.org/10.1063/1.1736034.

(52) König, D.; Casalenuovo, K.; Takeda, Y.; Conibeer, G.; Guillemoles, J. F.; Patterson, R.; Huang, L. M.; Green, M. A. Hot Carrier Solar Cells: Principles, Materials and Design. *Phys. E Low-dimensional Syst. Nanostructures* **2010**, *42* (10), 2862–2866. https://doi.org/10.1016/j.physe.2009.12.032.

(53) Joshi, P. P.; Maehrlein, S. F.; Zhu, X. Dynamic Screening and Slow Cooling of Hot Carriers in Lead Halide Perovskites. *Adv. Mater.* **2019**, 1803054. https://doi.org/10.1002/adma.201803054.

(54) Xing, G.; Mathews, N.; Sun, S.; Lim, S. S.; Lam, Y. M.; Gratzel, M.; Mhaisalkar, S.; Sum, T. C. Long-Range Balanced Electron- and Hole-Transport Lengths in Organic-Inorganic $CH_3NH_3PbI_3$. *Science* **2013**, *342* (6156), 344–347. https://doi.org/10.1126/science.1243167.

(55) Price, M. B.; Butkus, J.; Jellicoe, T. C.; Sadhanala, A.; Briane, A.; Halpert, J. E.; Broch, K.; Hodgkiss, J. M.; Friend, R. H.; Deschler, F. Hot-Carrier Cooling and Photoinduced Refractive Index Changes in Organic–Inorganic Lead Halide Perovskites. *Nat. Commun.* **2015**, *6* (1), 8420. https://doi.org/10.1038/ncomms9420.

(56) Yang, Y.; Ostrowski, D. P.; France, R. M.; Zhu, K.; van de Lagemaat, J.; Luther, J. M.; Beard, M. C. Observation of a Hot-Phonon Bottleneck in Lead-Iodide Perovskites. *Nat. Photonics* **2016**, *10* (1), 53–59. https://doi.org/10.1038/nphoton.2015.213.

(57) Fu, J.; Xu, Q.; Han, G.; Wu, B.; Huan, C. H. A.; Leek, M. L.; Sum, T. C. Hot Carrier Cooling Mechanisms in Halide Perovskites. *Nat. Commun.* **2017**, *8* (1), 1300. https://doi.org/10.1038/s41467-017-01360-3.

(58) Trinh, M. T.; Wu, X.; Niesner, D.; Zhu, X.-Y. Many-Body Interactions in Photo-Excited Lead Iodide Perovskite. *J. Mater. Chem. A* **2015**, *3* (17), 9285–9290. https://doi.org/10.1039/C5TA01093D.

(59) Guo, Z.; Wan, Y.; Yang, M.; Snaider, J.; Zhu, K.; Huang, L. Long-Range Hot-Carrier Transport in Hybrid Perovskites Visualized by Ultrafast Microscopy. *Science* **2017**, *356* (6333), 59–62. https://doi.org/10.1126/science.aam7744.

(60) Kahmann, S.; Loi, M. A. Hot Carrier Solar Cells and the Potential of Perovskites for Breaking the Shockley–Queisser Limit. *J. Mater. Chem. C* **2019**, *7* (9), 2471–2486. https://doi.org/10.1039/C8TC04641G.

(61) Richter, J. M.; Branchi, F.; Valduga de Almeida Camargo, F.; Zhao, B.; Friend, R. H.; Cerullo, G.; Deschler, F. Ultrafast Carrier Thermalization in Lead Iodide Perovskite Probed with Two-Dimensional Electronic Spectroscopy. *Nat. Commun.* **2017**, *8* (1), 376. https://doi.org/10.1038/s41467-017-00546-z.

(62) Li, M.; Bhaumik, S.; Goh, T. W.; Kumar, M. S.; Yantara, N.; Grätzel, M.; Mhaisalkar, S.; Mathews, N.; Sum, T. C. Slow Cooling and Highly Efficient Extraction of Hot Carriers in Colloidal Perovskite Nanocrystals. *Nat. Commun.* **2017**, *8* (1), 14350. https://doi.org/10.1038/ncomms14350.

(63) Wright, A. D.; Verdi, C.; Milot, R. L.; Eperon, G. E.; Pérez-Osorio, M. A.; Snaith, H. J.; Giustino, F.; Johnston, M. B.; Herz, L. M. Electron–Phonon Coupling in Hybrid Lead Halide Perovskites. *Nat. Commun.* **2016**, *7* (1), 11755. https://doi.org/10.1038/ncomms11755.

(64) Ridley FRS, B. K. Hot Phonons. In *Quantum Processes in Semiconductors*; Oxford University Press, 2013; pp 379–393. https://doi.org/10.1093/acprof:oso/9780199677214.003.0014.

(65) Frost, J. M.; Whalley, L. D.; Walsh, A. Slow Cooling of Hot Polarons in Halide Perovskite Solar Cells. *ACS Energy Lett.* **2017**, *2* (12), 2647–2652. https://doi.org/10.1021/acsenergylett.7b00862.

(66) Miyata, K.; Meggiolaro, D.; Tuan Trinh, M.; Joshi, P. P.; Mosconi, E.; Jones, S. C.; De Angelis, F.; Zhu, X. Y. Large Polarons in Lead Halide Perovskites. *Sci. Adv.* **2017**, *3* (8), e1701217. https://doi.org/10.1126/sciadv.1701217.

(67) Zhu, X. Y.; Podzorov, V. Charge Carriers in Hybrid Organic-Inorganic Lead Halide Perovskites Might Be Protected as Large Polarons. *J. Phys. Chem. Lett.* **2015**, *6* (23), 4758–4761. https://doi.org/10.1021/acs.jpclett.5b02462.

(68) Chen, Y.; Yi, H. T.; Wu, X.; Haroldson, R.; Gartstein, Y. N.; Rodionov, Y. I.; Tikhonov, K. S.; Zakhidov, A.; Zhu, X. Y.; Podzorov, V. Extended Carrier Lifetimes and Diffusion in Hybrid Perovskites Revealed by Hall Effect and Photoconductivity Measurements. *Nat. Commun.* **2016**, *7*. https://doi.org/10.1038/ncomms12253.

(69) Bretschneider, S. A.; Ivanov, I.; Wang, H. I.; Miyata, K.; Zhu, X.; Bonn, M. Quantifying Polaron Formation and Charge Carrier Cooling in Lead-Iodide Perovskites. *Adv. Mater.* **2018**, *30* (29), 1–8. https://doi.org/10.1002/adma.201707312.

(70) Batignani, G.; Fumero, G.; Srimath Kandada, A. R.; Cerullo, G.; Gandini, M.; Ferrante, C.; Petrozza, A.; Scopigno, T. Probing Femtosecond Lattice Displacement upon Photo-Carrier Generation in Lead Halide Perovskite. *Nat. Commun.* **2018**, *9* (1), 1971. https://doi.org/10.1038/s41467-018-04367-6.

(71) Manser, J. S.; Kamat, P. V. Band Filling with Free Charge Carriers in Organometal Halide Perovskites. *Nat. Photonics* **2014**, *8* (9), 737–743.

https://doi.org/10.1038/nphoton.2014.171.

(72) Zhao, X.; Wang, M. Organic Hole-Transporting Materials for Efficient Perovskite Solar Cells. *Mater. Today Energy* **2018**, *7*, 208–220. https://doi.org/10.1016/j.mtener.2017.09.011.

(73) Stolterfoht, M.; Caprioglio, P.; Wolff, C. M.; Márquez, J. A.; Nordmann, J.; Zhang, S.; Rothhardt, D.; Hörmann, U.; Amir, Y.; Redinger, A.; et al. The Impact of Energy Alignment and Interfacial Recombination on the Internal and External Open-Circuit Voltage of Perovskite Solar Cells. *Energy Environ. Sci.* **2019**, *12* (9), 2778–2788. https://doi.org/10.1039/C9EE02020A.

(74) Piatkowski, P.; Cohen, B.; Javier Ramos, F.; Di Nunzio, M.; Nazeeruddin, M. K.; Grätzel, M.; Ahmad, S.; Douhal, A. Direct Monitoring of Ultrafast Electron and Hole Dynamics in Perovskite Solar Cells. *Phys. Chem. Chem. Phys.* **2015**, *17* (22), 14674–14684. https://doi.org/10.1039/c5cp01119a.

(75) Brauer, J. C.; Lee, Y. H.; Nazeeruddin, M. K.; Banerji, N. Charge Transfer Dynamics from Organometal Halide Perovskite to Polymeric Hole Transport Materials in Hybrid Solar Cells. *J. Phys. Chem. Lett.* **2015**, *6* (18), 3675–3681. https://doi.org/10.1021/acs.jpclett.5b01698.

(76) Marchioro, A.; Brauer, J. C.; Teuscher, J.; Grätzel, M.; Moser, J.-E. Photoinduced Processes in Lead Iodide Perovskite Solid-State Solar Cells. *Phys. Chem. Interfaces Nanomater.* **2013**, *8811*, 881108. https://doi.org/10.1117/12.2023003.

(77) Brauer, J. C.; Lee, Y. H.; Nazeeruddin, M. K.; Banerji, N. Ultrafast Charge Carrier Dynamics in $CH_3NH_3PbI_3$: Evidence for Hot Hole Injection into Spiro-OMeTAD. *J. Mater. Chem. C* **2016**, *4* (25), 5922–5931. https://doi.org/10.1039/C6TC00763E.

(78) Droseros, N.; Dänekamp, B.; Tsokkou, D.; Boix, P. P.; Banerji, N. Charge Injection and Trapping at Perovskite Interfaces with Organic Hole Transporting Materials of Different Ionization Energies. *APL Mater.* **2019**, *7* (4), 041115. https://doi.org/10.1063/1.5086692.

(79) Ishioka, K.; Barker, B. G.; Yanagida, M.; Shirai, Y.; Miyano, K. Direct Observation of Ultrafast Hole Injection from Lead Halide Perovskite by Differential Transient Transmission Spectroscopy. *J. Phys. Chem. Lett.* **2017**, *8* (16), 3902–3907. https://doi.org/10.1021/acs.jpclett.7b01663.

(80) O'Keeffe, P.; Catone, D.; Paladini, A.; Toschi, F.; Turchini, S.; Avaldi, L.; Martelli, F.; Agresti, A.; Pescetelli, S.; Del Rio Castillo, A. E.; et al. Graphene-Induced Improvements of Perovskite Solar Cell Stability: Effects on Hot-Carriers. *Nano Lett.* **2019**, *19* (2), 684–691.

https://doi.org/10.1021/acs.nanolett.8b03685.

(81) Hutter, E. M.; Hofman, J.-J.; Petrus, M. L.; Moes, M.; Abellón, R. D.; Docampo, P.; Savenije, T. J. Charge Transfer from Methylammonium Lead Iodide Perovskite to Organic Transport Materials: Efficiencies, Transfer Rates, and Interfacial Recombination. *Adv. Energy Mater.* **2017**, *7* (13), 1602349. https://doi.org/10.1002/aenm.201602349.

(82) Petrus, M. L.; Schutt, K.; Sirtl, M. T.; Hutter, E. M.; Closs, A. C.; Ball, J. M.; Bijleveld, J. C.; Petrozza, A.; Bein, T.; Dingemans, T. J.; et al. New Generation Hole Transporting Materials for Perovskite Solar Cells: Amide-Based Small-Molecules with Nonconjugated Backbones. *Adv. Energy Mater.* **2018**, *8* (32), 1–11. https://doi.org/10.1002/aenm.201801605.

(83) Habisreutinger, S. N.; Noel, N. K.; Larson, B. W.; Reid, O. G.; Blackburn, J. L. Rapid Charge-Transfer Cascade through SWCNT Composites Enabling Low-Voltage Losses for Perovskite Solar Cells. *ACS Energy Lett.* **2019**, 1872–1879. https://doi.org/10.1021/acsenergylett.9b01041.

(84) Corani, A.; Li, M. H.; Shen, P. S.; Chen, P.; Guo, T. F.; El Nahhas, A.; Zheng, K.; Yartsev, A.; Sundström, V.; Ponseca, C. S. Ultrafast Dynamics of Hole Injection and Recombination in Organometal Halide Perovskite Using Nickel Oxide as P-Type Contact Electrode. *J. Phys. Chem. Lett.* **2016**, *7* (7), 1096–1101. https://doi.org/10.1021/acs.jpclett.6b00238.

(85) Grancini, G.; Viola, D.; Lee, Y.; Saliba, M.; Paek, S.; Cho, K. T.; Orlandi, S.; Cavazzini, M.; Fungo, F.; Hossain, M. I.; et al. Femtosecond Charge-Injection Dynamics at Hybrid Perovskite Interfaces. *ChemPhysChem* **2017**, *18* (17), 2381–2389. https://doi.org/10.1002/cphc.201700492.

(86) Marchioro, A.; Teuscher, J.; Friedrich, D.; Kunst, M.; van de Krol, R.; Moehl, T.; Grätzel, M.; Moser, J.-E. Unravelling the Mechanism of Photoinduced Charge Transfer Processes in Lead Iodide Perovskite Solar Cells. *Nat. Photonics* **2014**, *8* (3), 250–255. https://doi.org/10.1038/nphoton.2013.374.

(87) Ponseca, C. S.; Tian, Y.; Sundström, V.; Scheblykin, I. G. Excited State and Charge-Carrier Dynamics in Perovskite Solar Cell Materials. *Nanotechnology* **2016**, *27* (8), 082001. https://doi.org/10.1088/0957-4484/27/8/082001.

(88) Ponseca, C. S.; Hutter, E. M.; Piatkowski, P.; Cohen, B.; Pascher, T.; Douhal, A.; Yartsev, A.; Sundström, V.; Savenije, T. J. Mechanism of Charge Transfer and Recombination Dynamics in Organo Metal Halide Perovskites and Organic Electrodes, PCBM, and Spiro-OMeTAD: Role of Dark Carriers. *J. Am. Chem. Soc.* **2015**, *137* (51), 16043–16048.

https://doi.org/10.1021/jacs.5b08770.

(89) Pydzińska, K.; Karolczak, J.; Kosta, I.; Tena-Zaera, R.; Todinova, A.; Idígoras, J.; Anta, J. A.; Ziółek, M. Determination of Interfacial Charge-Transfer Rate Constants in Perovskite Solar Cells. *ChemSusChem* **2016**, *9* (13), 1647–1659. https://doi.org/10.1002/cssc.201600210.

(90) deQuilettes, D. W.; Frohna, K.; Emin, D.; Kirchartz, T.; Bulovic, V.; Ginger, D. S.; Stranks, S. D. Charge-Carrier Recombination in Halide Perovskites. *Chem. Rev.* **2019**, *119* (20), 11007–11019. https://doi.org/10.1021/acs.chemrev.9b00169.

(91) Meggiolaro, D.; Motti, S. G.; Mosconi, E.; Barker, A. J.; Ball, J.; Andrea Riccardo Perini, C.; Deschler, F.; Petrozza, A.; De Angelis, F. Iodine Chemistry Determines the Defect Tolerance of Lead-Halide Perovskites. *Energy Environ. Sci.* **2018**, *11* (3), 702–713. https://doi.org/10.1039/c8ee00124c.

(92) Shockley, W.; Read, W. T. Statistics of the Recombinations of Holes and Electrons. *Phys. Rev.* **1952**, *87* (5), 835–842. https://doi.org/10.1103/PhysRev.87.835.

(93) Hall, R. N. Electron-Hole Recombination in Germanium. *Phys. Rev.* **1952**, *87* (2), 387–387. https://doi.org/10.1103/PhysRev.87.387.

(94) Johnston, M. B.; Herz, L. M. Hybrid Perovskites for Photovoltaics: Charge-Carrier Recombination, Diffusion, and Radiative Efficiencies. *Acc. Chem. Res.* **2016**, *49* (1), 146–154. https://doi.org/10.1021/acs.accounts.5b00411.

(95) Dequilettes, D. W.; Koch, S.; Burke, S.; Paranji, R. K.; Shropshire, A. J.; Ziffer, M. E.; Ginger, D. S. Photoluminescence Lifetimes Exceeding 8 Ms and Quantum Yields Exceeding 30% in Hybrid Perovskite Thin Films by Ligand Passivation. *ACS Energy Lett.* **2016**, *1* (2), 438–444. https://doi.org/10.1021/acsenergylett.6b00236.

(96) Abdi-Jalebi, M.; Andaji-Garmaroudi, Z.; Cacovich, S.; Stavrakas, C.; Philippe, B.; Richter, J. M.; Alsari, M.; Booker, E. P.; Hutter, E. M.; Pearson, A. J.; et al. Maximizing and Stabilizing Luminescence from Halide Perovskites with Potassium Passivation. *Nature* **2018**, *555* (7697), 497–501. https://doi.org/10.1038/nature25989.

(97) Zheng, X.; Chen, B.; Dai, J.; Fang, Y.; Bai, Y.; Lin, Y.; Wei, H.; Zeng, X. C.; Huang, J. Defect Passivation in Hybrid Perovskite Solar Cells Using Quaternary Ammonium Halide Anions and Cations. *Nat. Energy* **2017**, *2* (7), 17102. https://doi.org/10.1038/nenergy.2017.102.

(98) Park, J.-S.; Calbo, J.; Jung, Y.-K.; Whalley, L. D.; Walsh, A. Accumulation of Deep Traps at Grain Boundaries in Halide Perovskites. *ACS Energy*

Lett. **2019**, 1321–1327. https://doi.org/10.1021/acsenergylett.9b00840.

(99) Kirchartz, T.; Markvart, T.; Rau, U.; Egger, D. A. Impact of Small Phonon Energies on the Charge-Carrier Lifetimes in Metal-Halide Perovskites. *J. Phys. Chem. Lett.* **2018**, *9* (5), 939–946. https://doi.org/10.1021/acs.jpclett.7b03414.

(100) Davies, C. L.; Filip, M. R.; Patel, J. B.; Crothers, T. W.; Verdi, C.; Wright, A. D.; Milot, R. L.; Giustino, F.; Johnston, M. B.; Herz, L. M. Bimolecular Recombination in Methylammonium Lead Triiodide Perovskite Is an Inverse Absorption Process. *Nat. Commun.* **2018**, *9* (1), 293. https://doi.org/10.1038/s41467-017-02670-2.

(101) Bridgman, P. W. Note on the Principle of Detailed Balancing. *Phys. Rev.* **1928**, *31* (1), 101–102. https://doi.org/10.1103/PhysRev.31.101.

(102) Kirchartz, T.; Krückemeier, L.; Unger, E. L. Research Update: Recombination and Open-Circuit Voltage in Lead-Halide Perovskites. *APL Mater.* **2018**, *6* (10), 100702. https://doi.org/10.1063/1.5052164.

(103) Trinh, M. T.; Wu, X.; Niesner, D.; Zhu, X. Y. Many-Body Interactions in Photo-Excited Lead Iodide Perovskite. *J. Mater. Chem. A* **2015**, *3* (17), 9285–9290. https://doi.org/10.1039/c5ta01093d.

(104) Wolf, C.; Cho, H.; Kim, Y.-H.; Lee, T.-W. Polaronic Charge Carrier-Lattice Interactions in Lead Halide Perovskites. *ChemSusChem* **2017**, *10* (19), 3705–3711. https://doi.org/10.1002/cssc.201701284.

(105) Kirchartz, T. High Open-Circuit Voltages in Lead-Halide Perovskite Solar Cells: Experiment, Theory and Open Questions. *Philos. Trans. R. Soc. A Math. Phys. Eng. Sci.* **2019**, *377* (2152), 20180286. https://doi.org/10.1098/rsta.2018.0286.

(106) Stolterfoht, M.; Wolff, C. M.; Márquez, J. A.; Zhang, S.; Hages, C. J.; Rothhardt, D.; Albrecht, S.; Burn, P. L.; Meredith, P.; Unold, T.; et al. Visualization and Suppression of Interfacial Recombination for High-Efficiency Large-Area Pin Perovskite Solar Cells. *Nat. Energy* **2018**, *3* (10), 847–854. https://doi.org/10.1038/s41560-018-0219-8.

(107) Wolff, C. M.; Zu, F.; Paulke, A.; Toro, L. P.; Koch, N.; Neher, D. Reduced Interface-Mediated Recombination for High Open-Circuit Voltages in CH 3 NH 3 PbI 3 Solar Cells. *Adv. Mater.* **2017**, *29* (28), 1700159. https://doi.org/10.1002/adma.201700159.

(108) Liu, Z.; Krückemeier, L.; Krogmeier, B.; Klingebiel, B.; Márquez, J. A.; Levcenko, S.; Öz, S.; Mathur, S.; Rau, U.; Unold, T.; et al. Open-Circuit Voltages Exceeding 1.26 V in Planar Methylammonium Lead Iodide Perovskite Solar Cells. *ACS Energy Lett.* **2018**, *7*, 110–117. https://doi.org/10.1021/acsenergylett.8b01906.

(109) Tress, W. Perovskite Solar Cells on the Way to Their Radiative Efficiency Limit - Insights Into a Success Story of High Open-Circuit Voltage and Low Recombination. *Adv. Energy Mater.* **2017**, *7* (14), 1602358. https://doi.org/10.1002/aenm.201602358.

(110) Caprioglio, P.; Stolterfoht, M.; Wolff, C. M.; Unold, T.; Rech, B.; Albrecht, S.; Neher, D. On the Relation between the Open-Circuit Voltage and Quasi-Fermi Level Splitting in Efficient Perovskite Solar Cells. *Adv. Energy Mater.* **2019**, *1901631*, 1901631. https://doi.org/10.1002/aenm.201901631.

(111) Correa-Baena, J. P.; Tress, W.; Domanski, K.; Anaraki, E. H.; Turren-Cruz, S. H.; Roose, B.; Boix, P. P.; Grätzel, M.; Saliba, M.; Abate, A.; et al. Identifying and Suppressing Interfacial Recombination to Achieve High Open-Circuit Voltage in Perovskite Solar Cells. *Energy Environ. Sci.* **2017**, *10* (5), 1207–1212. https://doi.org/10.1039/c7ee00421d.

(112) Du, T.; Xu, W.; Daboczi, M.; Kim, J.; Xu, S.; Lin, C.-T.; Kang, H.; Lee, K.; Heeney, M. J.; Kim, J.-S.; et al. P-Doping of Organic Hole Transport Layers in p–i–n Perovskite Solar Cells: Correlating Open-Circuit Voltage and Photoluminescence Quenching. *J. Mater. Chem. A* **2019**, *7* (32), 18971–18979. https://doi.org/10.1039/C9TA03896E.

(113) Snaith, H. J.; Abate, A.; Ball, J. M.; Eperon, G. E.; Leijtens, T.; Noel, N. K.; Stranks, S. D.; Wang, J. T.-W.; Wojciechowski, K.; Zhang, W. Anomalous Hysteresis in Perovskite Solar Cells. *J. Phys. Chem. Lett.* **2014**, *5* (9), 1511–1515. https://doi.org/10.1021/jz500113x.

(114) Richardson, G.; O'Kane, S. E. J.; Niemann, R. G.; Peltola, T. A.; Foster, J. M.; Cameron, P. J.; Walker, A. B. Can Slow-Moving Ions Explain Hysteresis in the Current-Voltage Curves of Perovskite Solar Cells? *Energy Environ. Sci.* **2016**, *9* (4), 1476–1485. https://doi.org/10.1039/c5ee02740c.

(115) Jacobs, D. A.; Shen, H.; Pfeffer, F.; Peng, J.; White, T. P.; Beck, F. J.; Catchpole, K. R. The Two Faces of Capacitance: New Interpretations for Electrical Impedance Measurements of Perovskite Solar Cells and Their Relation to Hysteresis. *J. Appl. Phys.* **2018**, *124* (22), 225702. https://doi.org/10.1063/1.5063259.

(116) Moia, D.; Gelmetti, I.; Calado, P.; Fisher, W.; Stringer, M.; Game, O.; Hu, Y.; Docampo, P.; Lidzey, D.; Palomares, E.; et al. Ionic-to-Electronic Current Amplification in Hybrid Perovskite Solar Cells: Ionically Gated Transistor-Interface Circuit Model Explains Hysteresis and Impedance of Mixed Conducting Devices. *Energy Environ. Sci.* **2019**, *12* (4), 1296–1308. https://doi.org/10.1039/C8EE02362J.

(117) Calado, P.; Burkitt, D.; Yao, J.; Troughton, J.; Watson, T. M.; Carnie, M. J.; Telford, A. M.; Regan, B. C. O.; Nelson, J.; Barnes, P. R. F. Identifying Dominant Recombination Mechanisms in Perovskite Solar Cells by Measuring the Transient Ideality Factor. *Phys. Rev. Appl.* **2019**, *10* (1), 1. https://doi.org/10.1103/PhysRevApplied.11.044005.

(118) Calado, P.; Telford, A. M.; Bryant, D.; Li, X.; Nelson, J.; O'Regan, B. C.; Barnes, P. R. F. Evidence for Ion Migration in Hybrid Perovskite Solar Cells with Minimal Hysteresis. *Nat. Commun.* **2016**, *7*, 13831.

(119) Pockett, A.; Carnie, M. J. Ionic Influences on Recombination in Perovskite Solar Cells. *ACS Energy Lett.* **2017**, *2* (7), 1683–1689. https://doi.org/10.1021/acsenergylett.7b00490.

(120) Pockett, A.; Eperon, G. E.; Sakai, N.; Snaith, H. J.; Peter, L. M.; Cameron, P. J. Microseconds, Milliseconds and Seconds: Deconvoluting the Dynamic Behaviour of Planar Perovskite Solar Cells. *Phys. Chem. Chem. Phys.* **2017**, *19* (8), 5959–5970. https://doi.org/10.1039/C6CP08424A.

(121) Bertoluzzi, L.; Belisle, R. A.; Bush, K. A.; Cheacharoen, R.; McGehee, M. D.; O'Regan, B. C. In Situ Measurement of Electric-Field Screening in Hysteresis-Free PTAA/$FA_{0.83}Cs_{0.17}Pb(I_{0.83}Br_{0.17})_3$/$C_{60}$ Perovskite Solar Cells Gives an Ion Mobility of ~3 × 10^{-7} cm^2/(V s), 2 Orders of Magnitude Faster than Reported for Metal-Oxide-Contacted. *J. Am. Chem. Soc.* **2018**, *140* (40), 12775–12784. https://doi.org/10.1021/jacs.8b04405.

(122) Walsh, A.; Stranks, S. D. Taking Control of Ion Transport in Halide Perovskite Solar Cells. *ACS Energy Lett.* **2018**, *3* (8), 1983–1990. https://doi.org/10.1021/acsenergylett.8b00764.

(123) Eames, C.; Frost, J. M.; Barnes, P. R. F.; O'Regan, B. C.; Walsh, A.; Islam, M. S. Ionic Transport in Hybrid Lead Iodide Perovskite Solar Cells. *Nat. Commun.* **2015**, *6* (1), 7497. https://doi.org/10.1038/ncomms8497.

(124) Mizusaki, J.; Arai, K.; Fueki, K. Ionic Conduction of the Perovskite-Type Halides. *Solid State Ionics* **1983**, *11* (3), 203–211. https://doi.org/10.1016/0167-2738(83)90025-5.

(125) Narayan, R. L.; Sarma, M. V. S.; Suryanarayana, S. V. Ionic Conductivity of $CsPbCl_3$ and $CsPbBr_3$. *J. Mater. Sci. Lett.* **1987**, *6* (1), 93–94. https://doi.org/10.1007/BF01729441.

(126) Xiao, Z.; Yuan, Y.; Shao, Y.; Wang, Q.; Dong, Q.; Bi, C.; Sharma, P.; Gruverman, A.; Huang, J. Giant Switchable Photovoltaic Effect in Organometal Trihalide Perovskite Devices. *Nat. Mater.* **2015**, *14* (2), 193–197. https://doi.org/10.1038/nmat4150.

(127) deQuilettes, D. W.; Zhang, W.; Burlakov, V. M.; Graham, D. J.; Leijtens,

T.; Osherov, A.; Bulović, V.; Snaith, H. J.; Ginger, D. S.; Stranks, S. D. Photo-Induced Halide Redistribution in Organic–Inorganic Perovskite Films. *Nat. Commun.* **2016**, *7* (1), 11683. https://doi.org/10.1038/ncomms11683.

(128) Hoke, E. T.; Slotcavage, D. J.; Dohner, E. R.; Bowring, A. R.; Karunadasa, H. I.; McGehee, M. D. Reversible Photo-Induced Trap Formation in Mixed-Halide Hybrid Perovskites for Photovoltaics. *Chem. Sci.* **2015**, *6* (1), 613–617. https://doi.org/10.1039/c4sc03141e.

(129) Yuan, Y.; Huang, J. Ion Migration in Organometal Trihalide Perovskite and Its Impact on Photovoltaic Efficiency and Stability. *Acc. Chem. Res.* **2016**, *49* (2), 286–293. https://doi.org/10.1021/acs.accounts.5b00420.

(130) Azpiroz, J. M.; Mosconi, E.; Bisquert, J.; De Angelis, F. Defect Migration in Methylammonium Lead Iodide and Its Role in Perovskite Solar Cell Operation. *Energy Environ. Sci.* **2015**, *8* (7), 2118–2127. https://doi.org/10.1039/c5ee01265a.

(131) Futscher, M. H.; Lee, J. M.; McGovern, L.; Muscarella, L. A.; Wang, T.; Haider, M. I.; Fakharuddin, A.; Schmidt-Mende, L.; Ehrler, B. Quantification of Ion Migration in $CH_3NH_3PbI_3$ Perovskite Solar Cells by Transient Capacitance Measurements. *Mater. Horizons* **2019**, *6* (7), 1497–1503. https://doi.org/10.1039/C9MH00445A.

(132) Leguy, A. M. A.; Frost, J. M.; McMahon, A. P.; Sakai, V. G.; Kockelmann, W.; Law, C.; Li, X.; Foglia, F.; Walsh, A.; O'Regan, B. C.; et al. The Dynamics of Methylammonium Ions in Hybrid Organic–Inorganic Perovskite Solar Cells. *Nat. Commun.* **2015**, *6* (1), 7124. https://doi.org/10.1038/ncomms8124.

(133) Senocrate, A.; Moudrakovski, I.; Kim, G. Y.; Yang, T.-Y.; Gregori, G.; Grätzel, M.; Maier, J. The Nature of Ion Conduction in Methylammonium Lead Iodide: A Multimethod Approach. *Angew. Chemie Int. Ed.* **2017**, *56* (27), 7755–7759. https://doi.org/10.1002/anie.201701724.

(134) Shao, Y.; Fang, Y.; Li, T.; Wang, Q.; Dong, Q.; Deng, Y.; Yuan, Y.; Wei, H.; Wang, M.; Gruverman, A.; et al. Grain Boundary Dominated Ion Migration in Polycrystalline Organic–Inorganic Halide Perovskite Films. *Energy Environ. Sci.* **2016**, *9* (5), 1752–1759. https://doi.org/10.1039/C6EE00413J.

(135) Birkhold, S. T.; Precht, J. T.; Liu, H.; Giridharagopal, R.; Eperon, G. E.; Schmidt-Mende, L.; Li, X.; Ginger, D. S. Interplay of Mobile Ions and Injected Carriers Creates Recombination Centers in Metal Halide Perovskites under Bias. *ACS Energy Lett.* **2018**, *3* (6), 1279–1286.

https://doi.org/10.1021/acsenergylett.8b00505.

(136) Birkhold, S. T.; Precht, J. T.; Giridharagopal, R.; Eperon, G. E.; Schmidt-Mende, L.; Ginger, D. S. Direct Observation and Quantitative Analysis of Mobile Frenkel Defects in Metal Halide Perovskites Using Scanning Kelvin Probe Microscopy. *J. Phys. Chem. C* **2018**, *122* (24), 12633–12639. https://doi.org/10.1021/acs.jpcc.8b03255.

(137) Weber, S. A. L.; Hermes, I. M.; Turren-Cruz, S.-H.; Gort, C.; Bergmann, V. W.; Gilson, L.; Hagfeldt, A.; Graetzel, M.; Tress, W.; Berger, R. How the Formation of Interfacial Charge Causes Hysteresis in Perovskite Solar Cells. *Energy Environ. Sci.* **2018**, *11* (9), 2404–2413. https://doi.org/10.1039/C8EE01447G.

(138) Tress, W.; Marinova, N.; Moehl, T.; Zakeeruddin, S. M.; Nazeeruddin, M. K.; Grätzel, M. Understanding the Rate-Dependent J–V Hysteresis, Slow Time Component, and Aging in CH 3 NH 3 PbI 3 Perovskite Solar Cells: The Role of a Compensated Electric Field. *Energy Environ. Sci.* **2015**, *8* (3), 995–1004. https://doi.org/10.1039/C4EE03664F.

(139) Belisle, R. A.; Nguyen, W. H.; Bowring, A. R.; Calado, P.; Li, X.; Irvine, S. J. C.; McGehee, M. D.; Barnes, P. R. F.; O'Regan, B. C. Interpretation of Inverted Photocurrent Transients in Organic Lead Halide Perovskite Solar Cells: Proof of the Field Screening by Mobile Ions and Determination of the Space Charge Layer Widths. *Energy Environ. Sci.* **2017**, *10* (1), 192–204. https://doi.org/10.1039/C6EE02914K.

Chapter 2

Motivation and Aims

In order to satisfy the increasing energy demand around the world, it is necessary to look into the different energy resources that are available. Photovoltaic technologies are one of the most promising renewable energy sources to produce electricity. They can directly transform the sunlight energy into electrical energy without the use of any intermediates. Silicon is still the most used material to fabricate solar panels to produce electricity. Although the production costs are getting lower and lower, silicon still presents some disadvantages, such as the high energy required in their production or the impossibility of being implemented into flexible substrates, which made researchers look for alternatives to silicon.

From the emerging photovoltaic technologies, lead halide perovskites have received the focus of many research groups since their implementation as light harvesters in 2009. Huge efforts were directed into developing fabrication methods and techniques to get higher power conversion efficiencies. These efforts have been very fruitful, as efficiencies have increased from 3.8% to a very recent 25.2% in just ten years. To obtain such high efficiencies, it is of paramount importance to understand the processes happening in perovskite devices. Although many of these processes have been described theoretically and confirmed experimentally, there is not a complete consensus in the research community. Thus, more research is needed to fully understand the working mechanisms and the physics that govern perovskite solar cells.

The principal aim of this thesis is to shed light on the charge carrier processes that take place at different timescales, from the charge carrier generation to the charge carrier recombination. For this purpose, it is necessary first to develop efficient solar cells based on lead halide perovskites. Once this is accomplished, a complete physical-chemical characterization of the material should be carried out. After having characterized both films and devices, we

moved on the study using advanced characterization techniques, such as transient photovoltage (TPV), transient photocurrent (TPC), and charge extraction (CE) for complete devices; and femtosecond transient absorption spectroscopy (fsTA). We use these techniques to study charge carrier processes in the bulk of the perovskite material and the different perovskite/selective contacts interfaces.

In this Chapter, the objectives and contents of every chapter will be briefly described.

Chapter 1 includes an introduction to perovskite solar cells, and a description of the state-of-the-art of the fabrication of perovskite solar cells. A timeline describing the different charge carrier processes, starting from the femtosecond timescale with the description of charge carrier generation to the second timescale. Finally, the description of the influence of ionic migration on perovskites is given.

Chapter 3 gives a detailed description of the experimental procedures for the fabrication of perovskite-based solar cells. All the characterization techniques used in this thesis are described focusing on the advanced characterization techniques (TPV, TPC, CE, and fsTA).

Chapter 4 is focused on the charge carrier processes happening at the interface perovskite/hole transporting material (HTM). With this purpose, we used a series of semiconductor polymers, namely PTB7, P3HT, and PCPDTBT, widely used in organic solar cells, and compared them to the standard HTM, spiro-OMeTAD. In the first part, we fabricated and characterized perovskite solar cells with different HTM. Using transient optoelectronic techniques, we studied which processes govern the final open-circuit voltage. In the second part, in collaboration with Prof. Dirk M. Guldi and Dr. Bianka M.D. Puscher from the Friedrich-Alexander Universität at Erlangen (Germany), as part of my

research fellowship, we studied the charge transfer processes at the interface perovskite/HTM using fsTA spectroscopy.

Chapter 5 reflects the results obtained from the study of the other interface, perovskite/ETM. Here, we modified the interface TiO_2/perovskite with the deposition of a thin layer of C_{60} fullerene. Again, first, complete devices were prepared and characterized. Using fullerenes was early showed as a strategy to reduce the current-voltage hysteresis observed in perovskite solar cells. In this Chapter, again in collaboration with Prof. Guldi and Dr. Puscher, we studied how fullerene derivatives have an influence over charge carrier processes at different timescales.

In the next chapter, **Chapter 6**, charge carrier processes in the bulk of the perovskite are described. We monitored the influence of the aging of perovskite solar cells in dry air conditions (< 10% H_2O) on the photovoltaic parameters and charge carrier recombination kinetics. With this purpose, we used transient optoelectronic techniques (TPV, TPC, and CE) and a modification of TPV, which is called transient of the transient photovoltage (TROTTR).

Finally, **Chapter 7** summarizes the main conclusions obtained in the previous chapters.

Chapter 3

Experimental procedures and characterization techniques

CHAPTER 3: EXPERIMENTAL PROCEDURES AND CHARACTERIZATION TECHNIQUES 51

3.1. Solar Cell Fabrication 55
3.1.1. Substrate cleaning 56
3.1.2 Bottom selective contacts 56
3.1.3. Perovskite layer 58
3.1.4. Top selective contacts 61
3.1.5. Metal electrode 62

3.2. Characterization techniques 63
3.2.1. Measurement of solar cell efficiency 63
3.2.2 V_{OC} and J_{SC} dependence with light intensity 65
3.2.3. V_{OC} stabilization 67
3.2.4. UV-Vis absorbance spectroscopy 68
3.2.5. Photoluminiscence spectroscopy 69
3.2.6. X-Ray Diffraction 70
3.2.7 Scanning electron microscopy 70
3.2.8. Atomic Force Microscopy 71
3.2.9. Mobility measurements 71

3.3. Advanced Characterization techniques 72
3.3.1. Femtosecond Transient Absorption Spectroscopy 72
3.3.2. Optoelectronic transient techniques 76

3.1. Solar Cell Fabrication

One of the biggest focus in Perovskite Solar Cells (PSC) research has been the development solar cell fabrication procedures. Many different strategies have been suggested over the course of the years, from solution processing methods, using one[1–3] or two step spin coating processes, or by dip coating[4], to cite some examples. Additionally, it has been described ultra-high vacuum deposition procedures[5], or even, solid state reaction for perovskite preparation[6,7].

In the period of this thesis, many of these approaches have been adapted to our initial procedure, with the corresponding increase in both efficiency and stability of this kind of solar cells.

In this section, it will be described the fabrication procedure of regular n-i-p perovskite architectures, which is the most employed architecture, and the one that has been used during this thesis. The different layers in this architecture are: FTO/ETM/perovskite/HTM/Metal Contact (**Figure 3.1**).

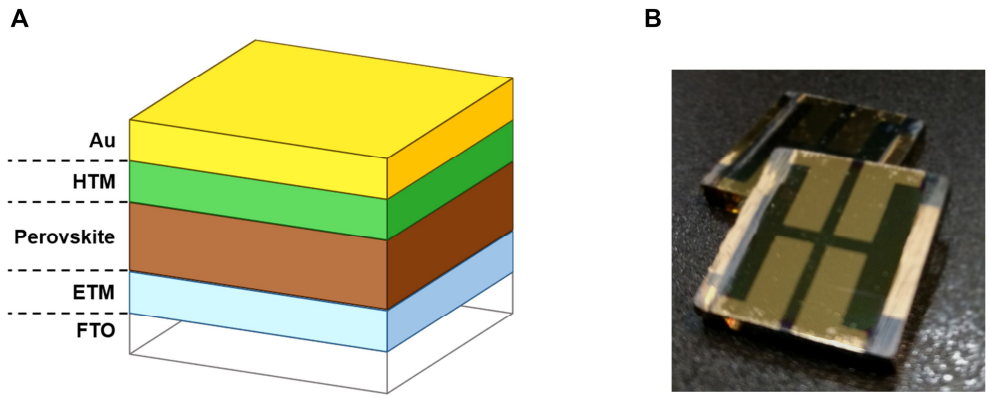

Figure 3.1. **(A)** Scheme with the different layers of a n-i-p type perovskite solar cell. **(B)** Picture of a complete solar cell view from the Au electrode side.

It will be described the procedure for different electron transport materials (ETM), alongside with the description of different deposition procedures for the perovskite layer, and, finally, the deposition of the hole

transporting materials. In the following Chapters, the differences from the procedures described here will be commented in detail in every chapter.

3.1.1. Substrate cleaning

For regular n-i-p PSC, we used pre-patterned 1.5 x 1.5 cm FTO substrates (7 Ω/sq, Pilkington TEC7, XinYan Technology Ltd.). The cleaning of the substrates is a very basic step, but it should be done carefully, as it could lead to detrimental consequences in the final operation of the device.

First, the substrates are brushed energetically with a diluted solution of Hellmanex™ and H_2O, taking care of not damaging the FTO layer. The substrates are then placed into a container with the same Hellmanex™/H_2O solution and they are ultrasonicated for 15 minutes. The substrates are rinsed with H_2O and acetone, placed again in a container with acetone, and ultrasonicated again for 15 minutes. We repeat the rinsing step, but this time with acetone and isopropanol. Once more, the substrates are ultrasonicated, this time in isopropanol for 15 minutes. Finally, they are dried with a strong airflow.

Before the deposition of the bottom contact, the substrates are treated with UV/O_3 for 30 minutes. Right after, the bottom selective contacts are deposited.

3.1.2 Bottom selective contacts

In the case of regular n-i-p perovskite architectures, the ETM will act as bottom selective contacts. The most common ETM is TiO_2, but it presents several drawbacks, reason why there have been many attempts to replace it for other metallic oxides (SnO_2, ZnO), other inorganic compounds or organic ETMs[8].

In this thesis, TiO_2 was employed in the case of mesoscopic ETM, while either TiO_2 or SnO_2 was chosen for planar devices. In this section, both procedures are shown.

TiO_2 as Electron Transporting Material

First, a compact TiO_2 ($cTiO_2$) layer is formed by spin coating 30 µl of a 0.3 M $Ti(iPrO)_2(acac)_2$ solution in 2-propanol using 4000 rpm, 1000 rpm/s for 25 s. The substrates are then dried at 120 ºC for 5 minutes and calcined at 450 ºC for 30 minutes.

Once the substrates cool down, they are immersed into a 40 mM $TiCl_4$ bath at 70 ºC for 30 minutes. After that, they are rinsed with water and EtOH and dried with a strong airflow. If the deposition of the mesoporous TiO_2 layer is done just after finishing this step, is not needed to make a calcination step. If that is not the case, the calcination at 450 ºC for 30 minutes is needed.

To deposit the mesoporous TiO_2 ($mTiO_2$) layer, a solution with a 30 nm particle size is prepared by diluting a commercial paste (30NR-D, Greatcell) in a 1:7 weight ratio in EtOH. 40 µl of this solution are spin coated at 6000 rpm, with 1000 rpm/s for 30 s. The substrates are then dried at 120 ºC for 5 minutes and calcined at 450 ºC for 30 minutes. If they are going to be used after the calcination, they should be transferred to the glovebox while they are still warm (remove them from the hot plate at 150 ºC approximately) to avoid humidity. If the substrates will be used in another moment, they should be heated up to 150 ºC for around 30 minutes prior to be transferred to the glovebox.

SnO_2 as Electron Transporting Material

SnO_2 layer was grown by chemical bath deposition (CBD) technique on top of the FTO substrates following the procedure by Anaraki *et al.*[9] . The solution is prepared dissolving first 0.5 g of urea in 40 ml of deionized H_2O. Then, 10 ml of mercaptopropionic acid and 0.5 ml of HCl (37 wt%) are added.

Finally, $SnCl_2 \cdot 2H_2O$ was added to the solution to a final concentration of 0.012 M. The solution is stirred for 2 minutes and transferred to a glass container where the substrates are immersed vertically. The deposition is made by putting them in a lab oven at 70 ºC for 3 hours. Then, the substrates are transferred to another glass container with H_2O, and they are ultrasonicated for 2 minutes in order to remove any loosely bound material. Then, the substrates are dried and annealed at 180 ºC for 1 hour. Prior to perovskite deposition, SnO_2 films must be treated with UV/O_3 for 30 minutes.

3.1.3. Perovskite layer

The formation of the perovskite layer is the most critical step in the fabrication of solar cells of this kind. When checking literature, it is possible to find many different techniques to deposit the perovskite layer, most of them claiming high efficiency and highly reproducible devices. What you will not find in those papers is that perovskite deposition is not something trivial and easy-to-do. There are many things and aspects to take into consideration and it requires skills until you obtain decent perovskite devices.

In this section, one-step and two-step methods will be described, both for $MAPbI_3$ perovskite and the triple cation containing perovskite, $Cs_x(FAMA)_{1-x}PbI_{3-y}Br_y$.

All the steps for perovskite deposition are made into a N_2-filled glove-box, both solution preparation, spin coating, and annealing. Additionally, is very important to maintain the glove-box atmosphere as clean as possible, as the solvent vapors (DMF and DMSO) affect dramatically the perovskite surface. We observed that the first samples always looked nicer than the last ones prepared for every batch. For this reason, we always work with a continuous N_2-flow, that we achieved by putting the glove-box in quick purge mode. In addition, we remove the cover-lid from the spin-coater, as the solvents remained there, affecting the perovskite surface. Additionally, we

protect the spin-coater walls with aluminum foil and it should be changed at the beginning of every set of devices. We also recommend changing it once the deposition of perovskite solution is finished and prior to deposition of the top selective contact.

One-Step Perovskite Deposition

This method is the easiest one, and the first one I tried when this thesis started. It does not require many skills, but the main disadvantage, which is the reason why this method has been abandoned, is that we obtain a rough perovskite top surface, which affects the final open-circuit voltage (V_{OC}) of the device, and, consequently, the final power conversion efficiency.

In this case, 1 M solution of both PbI_2 and MAI are dissolved in DMF. To help dissolution, it is heated up to 60 ºC while stirring. The solution is then filtered and 80 µl are dispensed on top of the substrate. It is spin coated at 2000 rpm, with 2000 rpm/s for 60 s. The substrates are then annealed at 100 ºC for 1 h.

Then, the substrates were cooled down before top selective contact deposition.

Two-Step Perovskite Deposition

As we already commented, the morphology of the perovskite surface is a very important parameter that determines the overall efficiency. In this case, using a two-step approach allows us to have a better control of the perovskite surface. There have been many reports were the first step consisted in spin coating a layer of PbI_2 while the second is the dipping into a methylammonium iodide (MAI) solution. This method presents two major problems, the first one is to obtain the complete conversion of PbI_2 and the second one is the control of the morphology of the film surface due to the rapid crystallization process.

To overcome this, we adapted a two spin coating procedure by Mao *et al.*[10]. First, 80 µl of 1 M PbI_2 solution dissolved in DMF:DMSO (90:10, vol%) is spin coated at 2000 rpm, with 2000 rpm/s for 90 s. DMSO forms a $PbI_2(DMSO)_x$ complex that retards the crystallization process[11]. Then, 100 µl of a 50 mg/ml MAI solution in 2-propanol is deposited on the spinning substrate 30 seconds before the spinning process ends. Then, the substrate is annealed at 100 ºC for 45 minutes. All the solutions were filtered before deposition.

This process results in devices with a smooth surface that lead to great efficiencies. The main disadvantage of this procedure is the control of the final stoichiometry in mixed cation perovskite.

Antisolvent Perovskite Deposition

The use of antisolvents has become the most extended way to fabricate PSC. The most commonly used solvents are toluene, chlorobenzene, and diethyl ether, although other different solvents have been tested. The use of antisolvents enhances crystallinity and allows us to have a better control of the perovskite morphology[11,12].

With this method, we prepared the triple cation Cs containing perovskite, which has become one of the most used perovskite configuration due to its better film quality, stability, and overall performance[13]. On the other hand, this kind of perovskite requires a fine control of the stoichiometry, reason why it has not been used with the two-step procedure.

In order to prepare the triple cation perovskite with a stoichiometry $Cs_{0.1}(FA_{0.85}MA_{0.15})Pb(I_{0.85}Br_{0.15})_3$, a solution containing 1.2 M of PbI_2, 1.04 M of formamidinium iodide (FAI), 0.16 M $PbBr_2$, 0.16 M methylammonium bromide (MABr), and 0.1 M of CsI was prepared in DMF:DMSO (4:1, vol%). To help the dissolution of the reagents, it is stirred at 60 ºC for 30 minutes. Then, the solution is filtered and 40 µl are spin coated using a two-step program. The first step, a spreading step, consists on 2000 rpm, with 2000 rpm/s for 12 s.

Then, the process accelerates to 5000 rpm, with 2000 rpm/s and 25 s. The antisolvent step is done 10 s before the spinning process ends by spin coating 100 µl of chlorobenzene on top of the substrate. Finally, the samples are annealed at 100 ºC for 1 h.

With this method, high quality films with a smooth surface, detected with a mirror effect in the films. Also, it should be noticed that this method requires practice, as the antisolvent step is the most important when preparing the perovskite layer. It should be done not too fast neither too slow[14].

3.1.4. Top selective contacts

In PSC, the most common HTM in n-i-p configuration is spiro-OMeTAD. The best efficiencies have been obtained for spiro-OMeTAD based devices, or, alternatively, PTAA as HTM. Spiro-OMeTAD presents major drawbacks (doping, tedious synthetic route...), and huge efforts have been made in order to find new HTM as an alternative to it[15]. Some of the newly synthesized HTM have achieved similar performances as spiro-OMeTAD. Nevertheless, it has not been replaced by any of these new HTM and continue to be the most employed.

This step is done in a N_2-fillled glove-box. It is very important that we have a clean atmosphere before the deposition of the HTM. For this reason, it is recommended to change the aluminum foil protecting the spin coater before the deposition step and working with a constant N_2 flow.

To deposit the HTM layer, a 60 mM spiro-OMeTAD solution in chlorobenzene is prepared just before the deposition step. A series of dopants are employed in order to enhance spiro-OMeTAD properties as HTM. The dopants used are 4-tert-butylpyridine (TBP), LiTFSI (from a 1.8 M stock solution in acetonitrile), and Co(III) TFSI (from a 0.25 M stock solution in acetonitrile). The molar ratio used is 1 spiro-OMeTAD : 3.3 TBP : 0.5 LiTFSI : 0.05 Co(III) TFSI. In some cases, not all the dopants have been used, as the use

of Co(III) TFSI was not implemented until quite recently. 30 µl of the solution are spin coated dynamically at 4000 rpm for 30 s.

The surface should look uniform and without the presence of spots, which are associated with either aggregates or LiTFSI that has been hydrated. To eliminate the possibility of aggregates or dust in the solution, it is recommended to filter the solution before spin coating.

Once this process is finished, the substrates are keep overnight in dark and air conditions with controlled humidity below 10 %.

The following day, the sides of the substrates are cleaned to deposit the electrode also on top of the FTO, closing the circuit. After trying different methods, our recommendation is to clean just once, at the end of the fabrication, first with a sharp razor, and, secondly, if there is some remaining material, using a cotton swab with DMF, but keeping it as dry as possible, as DMF vapors can damage the solar cell.

3.1.5. Metal electrode

Last, the metal contact is deposited on top of the different layers. 80 nm of gold are deposited using thermal evaporation and employing ultra-high vacuum ($1 \cdot 10^{-6}$ mbar). A shadowing mask is used to deposit the metal contacts with the desired pattern. The whole procedure is shown in **Figure 3.2**.

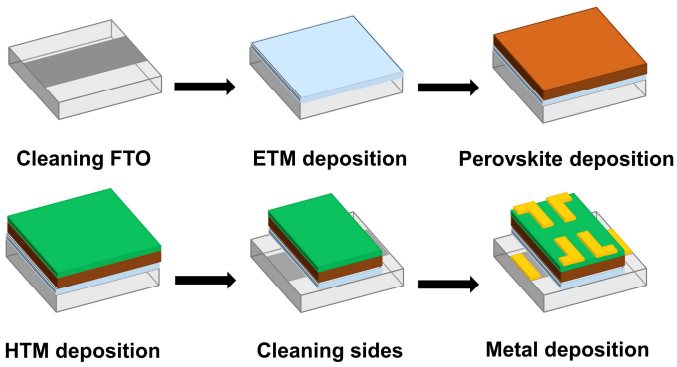

Figure 3.2. Scheme summarizing the different device fabrication steps.

3.2. Characterization techniques

In this section, a description of the methods and techniques employed in this thesis will be given. Both solar cell characterization techniques and film characterization techniques will be explained.

3.2.1. Measurement of solar cell efficiency

The most fundamental characterization for solar cell devices is the measurement of solar cell efficiency. The solar cell efficiency or Power Conversion Efficiency (PCE) is the ratio between the maximum electrical power output and the incident light power density under standard conditions. In other words, we estimate the electrical energy generated by the solar cell when it is irradiated[16].

It is calculated from the current density-voltage (JV) curve under 1 Sun standard conditions (100 mW/cm^2, AM 1.5) using a solar simulator (ABET 11000 Sun 2000) calibrated with a Si photodiode. These standard conditions, Air Mass 1.5 (AM 1.5), refer to the solar radiation spectrum at mid-latitudes, corresponding to the solar spectrum at a solar zenith angle of 48.2º. In order to measure the JV curve, the current that the solar cell generates under solar irradiation is measured while a variable voltage is applied to the solar cell with a source meter (Keithley 2400). The JV curve allows us to calculate the photovoltaic parameters, open-circuit voltage (V_{OC}), short-circuit current (J_{SC}), fill factor (FF), and power conversion efficiency (PCE)[17] (**Figure 3.3**).

- **Open-circuit voltage (V_{OC}):** Is the maximum voltage of a solar cell and it occurs with a zero net current through the device.
- **Short-circuit current (J_{SC}):** Current when the voltage in the cell is zero. It depends of different factors such as the area of the solar cell, which is the reason why it is normally given as current density, or the spectrum of the incident light.

- **Fill factor (FF):** Is the ratio between the maximum power output and the product of V_{OC} and J_{SC} (**Equation 3.1.**). The point in the JV curve where the fill factor is found is called maximum power point (MPP).

$$FF = \frac{P_m}{V_{OC} \cdot J_{SC}} = \frac{V_{MPP} \cdot J_{MPP}}{V_{OC} \cdot J_{SC}} \qquad (3.1)$$

- **Power Conversion Efficiency (PCE) :** As discussed above, the power conversion efficiency is the ratio between the output electrical power generated by the solar cell and the incident light power density (P_{in}, 100 mW/cm^2) (**Equation 3.2.**). It is normally expressed as a percentage.

$$PCE = \frac{P_m}{P_{in}} = \frac{V_{OC} \cdot J_{SC} \cdot FF}{P_{in}} \qquad (3.2)$$

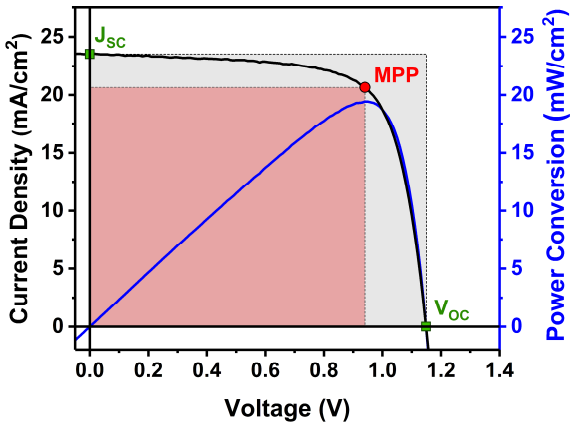

Figure 3.3. Typical JV curve of a perovskite solar cell (black line) and its power conversion output (blue line). It is also shown the MPP (red), V_{OC}, and J_{SC} (green). The ratio between the red and grey rectangles areas is the fill factor.

The measurement of the JV curve can be done with two different scan sweeps, forward, which means from J_{SC} to V_{OC} conditions, and reverse, from V_{OC} to J_{SC}. In PSC, it is important to perform the JV measurement in both ways, forward and reverse, as this kind of cells present the so-called JV hysteresis[18] mainly associated with ionic influences (it will be further discussed in the following chapters) giving very different PCE depending on the scan direction

(**Figure 3.4.A**). For the same reason, it is important to choose a proper scan rate (**Figure 3.4.B**)[19]. If not stated, we used 40 mV/s for every scan.

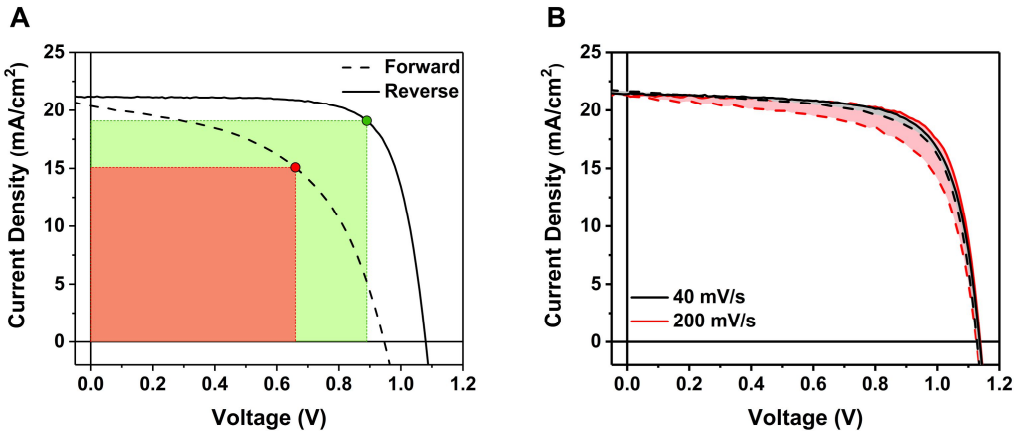

Figure 3.4. (A) JV curve measured on forward (dashed) and reverse (solid line) conditions. This cell presents high degree of hysteresis, which is corroborated by the difference between the areas of the FF on forward (red area) and reverse (green area) conditions. **(B)** Influence of the scan speed on the JV performance for a same solar cell, which presents negligible hysteresis at 40 mV/s, while some degree of hysteresis is observed at 200 mV/s. The shadowed areas indicate the difference of the forward and reverse JV curves.

3.2.2 V_{OC} and J_{SC} dependence with light intensity

Another possible analysis by means of current-voltage characteristics is to determine the V_{OC} and J_{SC} dependence with light intensity (Φ). The different light intensities employed for these measurements are obtained with different optical filters that allow more or less light to pass through them. These measurements are done measuring the different JV curves under different light intensities (**Figure 3.5**).

From the JV curves, V_{OC} and J_{SC} values at each light intensity are extracted. In the case of J_{SC}, it is fitted to a power law dependence with the light intensity, $J_{SC} \alpha \Phi^{\alpha}$, and it is possible to evaluate if there are photocurrent losses at short-circuit conditions. If $\alpha = 1$, there are no photocurrent losses at short-circuit conditions[20] (**Figure 3.6.A**).

From the V_{OC} dependence with the light intensity, we can calculate the ideality factor (n_{id}). The ideality factor shows how much the solar cell deviates from the ideal diode behavior. It presents a value $n_{id} = 1 – 2$, where $n_{id} = 1$ means band-to-band recombination and $n_{id} = 2$ suggests that the Shockley-Read-Hall (SRH) recombination or trap mediated is the predominant[21,22]. The non-ideal diode equation including the net current (J) is in **Equation 3.3.**

$$J = J_{SC} - J_0 \left(e^{\frac{q\,V}{n_{id}\,K_B\,T}} - 1 \right) \qquad (3.3)$$

Where J_0 is a constant, q is the elementary charge, K_B the Boltzmann constant and T is the device temperature. At open-circuit conditions, net current, J = 0, so **Equation 3.3.** can be approximated to **Equation 3.4.**

$$J_{SC} = J_0 \left(e^{\frac{q\,V_{oc}}{n_{id}\,K_B\,T}} - 1 \right) \qquad (3.4)$$

As the J_{SC} increments linearly with the light intensity (Φ), we can make a final approximation to derivate the ideality factor, n_{id} (**Equation 3.5.**). In **Figure 3.6.B** it is plotted the fitting for a typical perovskite solar cell where it is obtained n_{id}.

$$V_{OC} = \frac{K_B\,T}{n_{id}\,q} \ln \Phi \qquad (3.5)$$

It should be highlighted that the presence of mobile ions at the interface can lead to errors in the n_{id} calculation. An alternative has been suggested by Calado *et al.*[23] where they calculate a transient ideality factor with different voltage preconditioning periods in order to obtain information about the recombination mechanisms.

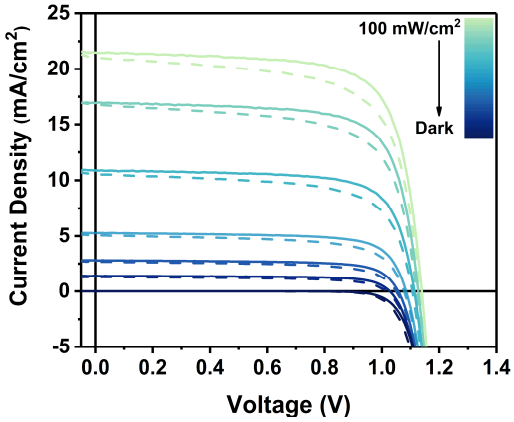

Figure 3.5. JV curves measured under different light intensitites from 1 Sun to dark (100, 81.3, 51.5, 25.2, 12.6, and 5.1 mW/cm^2) on forward (dashed) and reverse (solid) conditions.

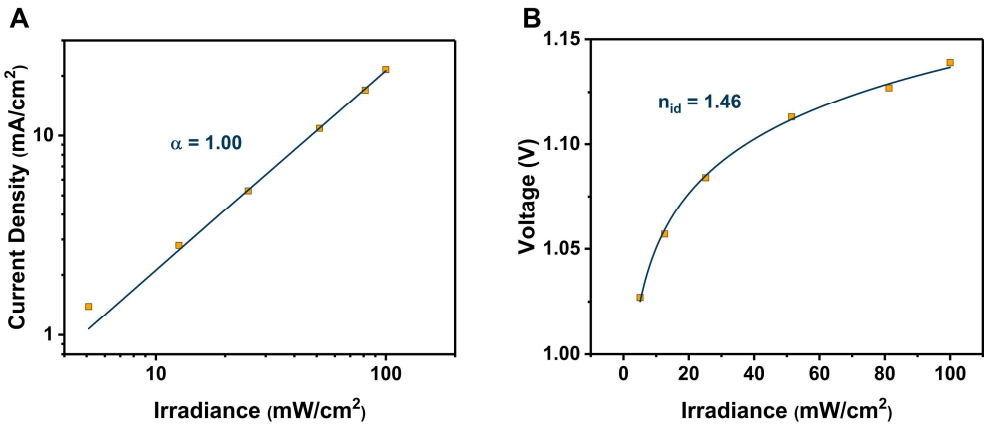

Figure 3.6. (A) J_{SC} dependence with the light intensity obtained from the reverse JV curves on **Figure 3.5**. obtaining a linear increment of J_{SC} with Φ. **(B)** V_{OC} dependence with Φ obtained from **Figure 3.5**. The n_{id} found suggests a recombination regime ranging from interfacial to bulk recombination.

3.2.3. V_{OC} stabilization

The measurement of V_{OC} stabilization time is very useful, mostly in cells with n-i-p configuration, which show great degree of hysteresis. It is often observed a slow rise in V_{OC}, associated with the ionic movement. A model explaining this behavior will be shown in **Chapter 6**.

This measurement is done keeping the cell in open-circuit and dark conditions. After few seconds in dark, the cell is illuminated at 1 Sun conditions and the evolution of the V_{OC} growth is registered.

3.2.4. UV-Vis absorbance spectroscopy

When ultraviolet and visible radiation (UV-Vis) is absorbed by a semiconductor solid, this radiation is used to promote electrons from the valence band to the conduction band.

In the case of perovskites, we work in the solid state, thus, we can use UV-Vis spectroscopy to find the position of the valence band of the lead halide perovskites. For example, in methylammonium lead iodide perovskite, $MAPbI_3$, the typical UV-Vis spectra show two distinguishable bands, one at 760 nm approximately and the second one at 480 nm (**Figure 3.7**)[24,25]. The presence of these two bands and their origin has been the topic of discussion and will be further commented on **Chapter 4.**

These measurements were done in an Agilent Cary 60 UV-Vis Spectrophotometer, equipped with two silicon detectors, double beam optics, Czerny-Turner monochromator, 190-1100 nm range and the light source is a Xenon Flash Lamp (80 Hz).

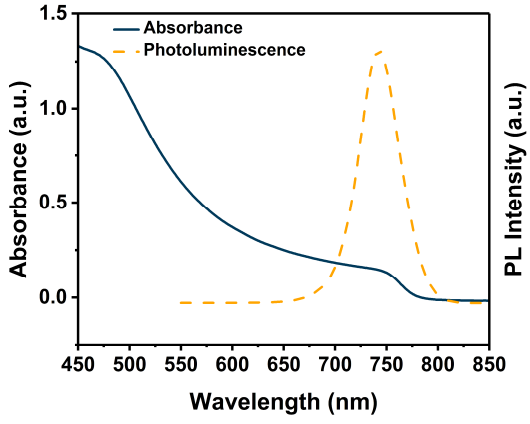

Figure 3.7. UV-Vis absorption spectra of the $MAPbI_3$ perovskite. It is clearly observed the two different absorbance features at 760 and 480 nm.

It is also possible to measure the oxidized and/or reduced absorption spectrum by applying a potential (either positive or negative) with a potentiostat, while measuring the absorption spectra of a system. In this case, it will be observed the reduction of the peaks previously observed in the steady state, while the formation of new peaks associated with the newly formed species will appear. Spectroelectrochemistry measurements were done in solution, using a three-neck cell in argon-purged solutions. A three-electrode system was used, with a platinum gauze working electrode, a platinum wire counter electrode, and a silver wire pseudo reference electrode. The potentials were applied using an FRA 2 mAutolab Type III potentiostat (Metrohm). Absorption measurements were made with a Cary 5000 spectrometer (Varian) equipped with a PMT detector, double beam and a range from 175 to 1300 nm.

3.2.5. Photoluminescence spectroscopy

In this technique, we examine the possible paths of radiative recombination in the form of light emission of semiconductors. When a photon is absorbed by a semiconductor, an electron is excited from its ground state (HOMO level for molecules or valence band in the case of solid semiconductors) to higher excited states (LUMO or conduction band respectively). The electron will recombine radiatively to its ground state with the emission of photons, which energy will be dependent with the energy of the band-gap of the semiconductor[26,27].

For lead halide perovskites, the steady state photoluminescence (PL) spectra shows a peak in the region around 760 nm (**Figure 3.7**). The emission peak maximum will differ depending on the perovskite composition. It is also possible to study the lifetime of the radiative recombination via Time Correlated Single Photon Counting (TCSPC), which is a technique based on the detection of single emitted photons over the time of the luminescence decay[28]. The measured PL lifetime of perovskites has been shown to be really

large (> 1 μs)[29–31], being the focus of study to explain which perovskite properties make them present these long PL lifetimes, which was previously explain in **Chapter 1**.

Steady state measurements were performed in a Fluorolog Horiba Jobin Yvon spectrofluorimeter equipped with a photomultiplier (PMT) detector, double monochromator and Xenon light source. The PL lifetime was measured on a Edinburgh Instruments LifeSpec-II based on Time Correlated Single Photon Counting (TCSPC technique), equipped with a PMT detector, double subtractive monochromator and picosecond pulsed diode lasers (470 nm was the most employed).

3.2.6. X-Ray Diffraction

The crystalline structure of perovskite has been determined using X-Ray Diffraction (XRD). The incident X-ray beam interact with the atoms in the crystalline structure, creating constructive interferences from waves reflected from the ordered layers of atoms. Every plane of the crystalline structure presents a characteristic angle of diffraction that follows Bragg's law: $n \cdot \lambda = 2 \cdot d \cdot \sin \theta$, being λ the incident wavelength, d the interplanar distance, and θ the angle of diffraction[32].

These measurements were made with samples deposited on glass substrates using a Siemens D5000 diffractometer (Bragg-Brentano monochromator, incident and diffracted – beam Soller slits, a 0.06º receiving slit and scintillation counter as a detector. The angular 2θ diffraction range was between 5 and 70º. The data were collected with an angular step of 0.05º at 3 s per step and sample rotation. CuKα radiation was obtained from a copper X-ray tube operated at 40 kV and 30 mA.

3.2.7 Scanning electron microscopy

Scanning Electron Microscopy (SEM) and Environmental Scanning Electron Microscopy (ESEM) were used to study perovskite film's morphology.

More precisely, we used SEM to make cross-sectional studies to observe all the layers in a complete device, while ESEM was used from top-view, to study the surface morphology of the films.

Electrons interact with the samples. Although different kinds of signals are produced, in SEM we are interested in back-scattered electrons, which are electrons reflected from the sample with an elastic interference. The detection of these scattered electrons forms a 3D image that is quite simple to interpret. This measurements needs ultra-high vacuum, so long time is required until the adequate vacuum is reached. For this reason, if we do not need high resolution, ESEM can be used. This technique was designed for working in low vacuum, which make it an easier and faster approach to obtain SEM images[33,34].

SEM microscopy was performed in a JEOL JSM-6400 microscopy. ESEM images were obtained with a FEI Quanta 600 microscopy.

3.2.8. Atomic Force Microscopy

Atomic Force Microscopy (AFM) was also used to study the surface morphology of the perovskite or the materials deposited on top of it.

An AFM image is obtained with a sharp tip (probe) that is brought into the surface proximity, generating forces between the tip and the surface that cause the tip to deflect. This force is is derived from the Hooke's law: $F = -k \cdot z$, where k is the stiffness of the tip and z is the distance that the tip is deflected. Normally, the distance of the tip is controlled with a laser pointing on the top of the tip, reaching a detector, and processing this signal into the final image[35].

AFM images were obtained with a Pico SPM II instrument. The images were processed with the WSxM software[36].

3.2.9. Mobility measurements

Carrier mobility is measured with a method based on Space Charge Limited Current (SCLC). To measure hole mobility, hole-only devices were

prepared, with a configuration of ITO/Pedot:PSS/HTM/Au, and measuring current-voltage characteristics from 0 to 4-5 V. These high voltages enable current-voltage characteristic to be only ohmic, therefore conductivity only depends on mobility and carrier concentration. The electric field dependent SCLC mobility was estimated from Mott-Gurney's law[37] (**Equation 3.6**):

$$J = \frac{9}{8}\varepsilon_r\varepsilon_0\mu_h\frac{V^2}{L^3} \qquad (3.6)$$

Where J is the current density, ε_r is the relative permittivity of the material, ε_0 is the electric constant, μ_h is the hole mobility, V the effective voltage in the device and L the device thickness.

3.3. Advanced Characterization techniques

3.3.1. Femtosecond Transient Absorption Spectroscopy

Principles

Femto-second transient absorption spectroscopy (fsTA) has been demonstrated as a high-powered technique in the field of photovoltaics. It helps to understand ultrafast photoinduced carrier processes in excited electronic states. In PSC, there has been huge research using fsTA to understand the nature of carrier generation, carrier protection and carrier injection.

fsTA is a pump-probe technique. The pump (λ_{exc}) is selectively promoting an electronic transition to a higher excited state by a vertical Franck Condon transition. Only a fraction of the molecules is excited. On the other hand, a weak probe pulse (λ_{probe}) is sent to the sample with a delay (τ) compared to the pump. A difference absorption spectrum (ΔA) is then calculated, which means the absorption spectra in the excited state minus the absorption spectra in the ground state. Registering the ΔA at different delay

times, it is possible to construct a ΔA profile depending on the wavelength and the delay time ΔA (λ, τ) that contains information about the system under study[38,39].

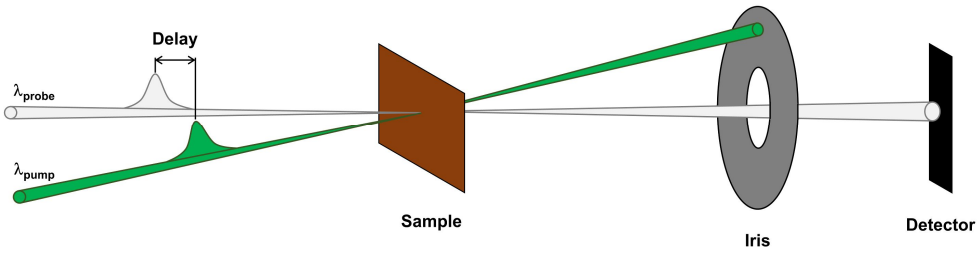

Figure 3.8. Scheme of the transient absorption principle.

It is possible to obtain both positive and negative signals associated with different processes[39]:

1) *Ground state bleach*: A fraction of the molecules have been excited due to the action of the pump pulse; therefore, the ground state is depopulated. For this reason, a negative signal for the ΔA is observed.

2) *Stimulated Emission*: The molecules in the excited state can relax with the emission of light to the ground state. This process will occur when the probe light passes through the sample and will have a shape similar to the fluorescence of the system. Stimulated emission is observable as a negative signal due to an increase of light in the detected signal. As one photon of the incident probe induces the emission of another photon of the sample that is emitted in the same direction as the probe, a bigger amount of light arrives at the detector.

3) *Excited-state absorption*: It is possible that the probe light promotes allowed transitions from the excited state to higher excited states.

Thus, absorption at these certain wavelengths will occur with the corresponding positive signal in the ΔA spectra.

4) *Absorption of new photoproducts*: Finally, it is also possible the formation of new products or reactions involving the excited states. Some examples are the charge transfer to another molecule, triplet states, or isomerized states.

Setup

Generally speaking, a fsTA spectrometer consists on a laser, an optical parametric amplifier (OPA), a delay line, a chopper, and a detector (**Figure 3.9.** and **Figure 3.10**).

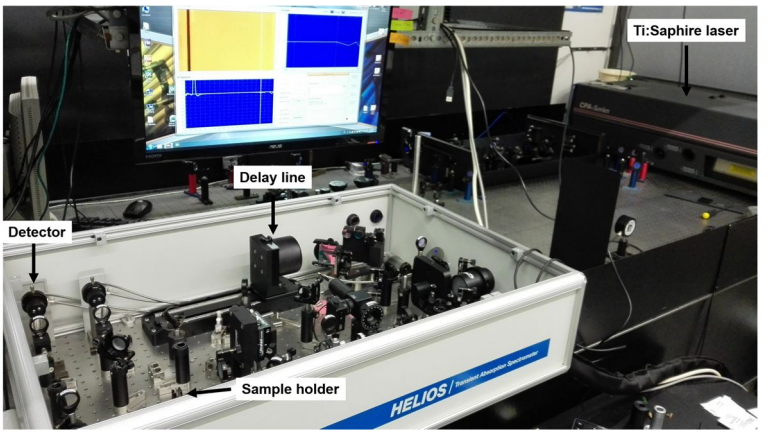

Figure 3.9. Picture of a fsTA spectrometer with the main components highlighted.

As the laser source, in this thesis we have used a Ti:Sapphire laser (Clark MXR) with an output of 775 nm, 1 kHz of repetition rate, a full width at half maximum (FWHM) of 150 fs. The laser pulse is divided into two beams that will act as the pump and the probe of the measurement.

To shift the wavelength of the pump pulse, an OPA or non-collinear OPA (NOPA) is used (NOPA Plus – Clark MXR). These systems allow us to obtain all the wavelengths from UV to mid-IR, with relatively high energetic pulses.

The other laser beam, used as the probe pulse, is concentrated in a sapphire or CaF_2 plate, generating a white-light continuum. This pulse is sent through an optical delay line that permits the measurement from the femtosecond to the nanosecond timescale. Then, it is focused on the sample with a spot overlapped to the pump pulse and using a slightly smaller spot.

Before the pump pulse reaches the sample holder, it passes through a mechanical chopper. Therefore, it is measured alternatively the excited and the non-excited spectra, allowing the measurement of the ΔA spectra.

Finally, the probe pulse reaches the detector (HELIOS, Ultrafast systems LLC). It is based on a charge coupled device (CCD) for the UV-Vis range and for the near-IR detection an InGaS sensor[38,39].

The whole setup is depicted in Figure 3.10.

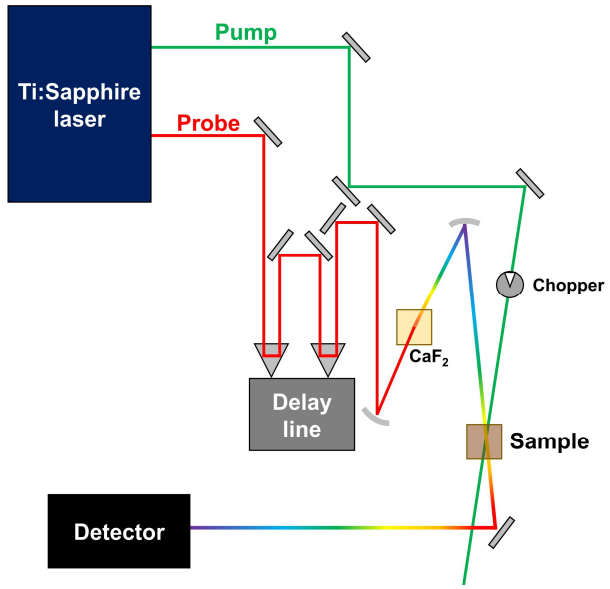

Figure 3.10. Schematic description of the fsTA spectrometer setup.

3.3.2. Optoelectronic transient techniques

In this section, the description of transient techniques, such as charge extraction (CE), transient photovoltage (TPV), and transient photocurrent (TPC) will be given. Those are powerful tools to study both carrier transport, accumulation and recombination kinetics under close to *operando* conditions.

They can be divided into small and large perturbations techniques, if a small laser perturbation is studied or the light is switched on and off correspondingly. In every case, voltage or current is registered before and after the perturbation is applied. The data collected should be treated and analyzed carefully, in order to extract the correct information.

Charge extraction (CE)

Charge Extraction (CE) is a technique designed to quantify the charge stored in the solar cell under operational conditions[40]. In order to do so, the device is illuminated while it is kept at open-circuit conditions until a stable V_{OC} is obtained. Then, at the same time, the device is switched to short-circuit and the light is switched off. The current transient obtained from the discharge of the device is integrated in order to obtain the charge in the device[41]. **Figure 3.11** summarizes the measurement process. Doing the measurement at different light intensities, it is possible to obtain the charge stored in the device at different V_{OC}[42].

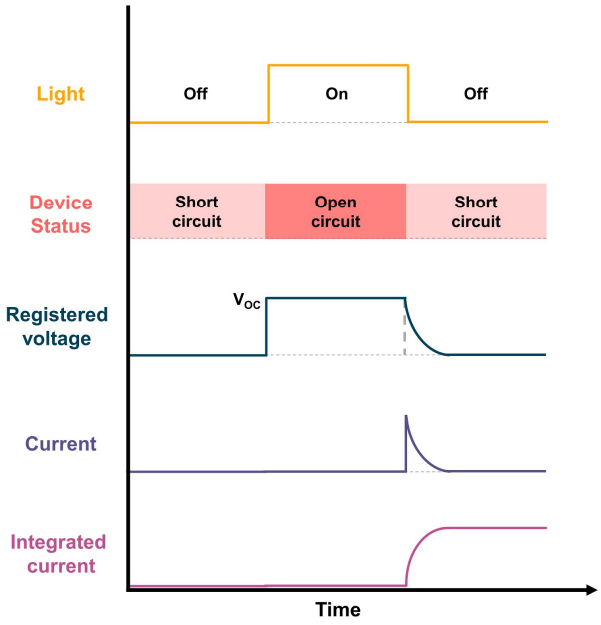

Figure 3.11. Scheme summarizing the CE measurement process.

As shown in **Figure 3.11**, the solar cell is kept under constant illumination at open circuit conditions until a stable V_{OC} is obtained. The white-light source is a LED array (LED from LUXEON Lumileds and powered by an Aim-TTi PLH120-P power supply) that allows us to use different light intensities that determine the device V_{OC}. As explained in **section 3.2.3**, V_{OC} stabilization in the case of PSC takes long time because of the presence of mobile ions, which means that longer illumination times are required in this kind of solar cells. Once steady state is reached, the light is switched off, and, at the same time, the device is short circuited through a small and known resistance (R = 50 Ω). The system is connected to an oscilloscope (Yokogawa DLM2052 with an internal resistance of 1 MΩ) that measures the voltage drop across the resistance. Using Ohm's law, it is possible to obtain the charge in the device integrating the transient voltage over time[41,42] (**Equation 3.7**).

$$Q = \frac{1}{R}\int_{t=0}^{t=t} V(t)\,dt \qquad (3.7)$$

Where Q is the charge, R is the small 50 Ω resistance, and V(t) is the voltage at every time. Measuring the device under different light intensities it is possible to obtain the charge stored in the device at different values of V_{OC}, so we can plot the dependence of the charge with the V_{OC} (**Figure 3.12**).

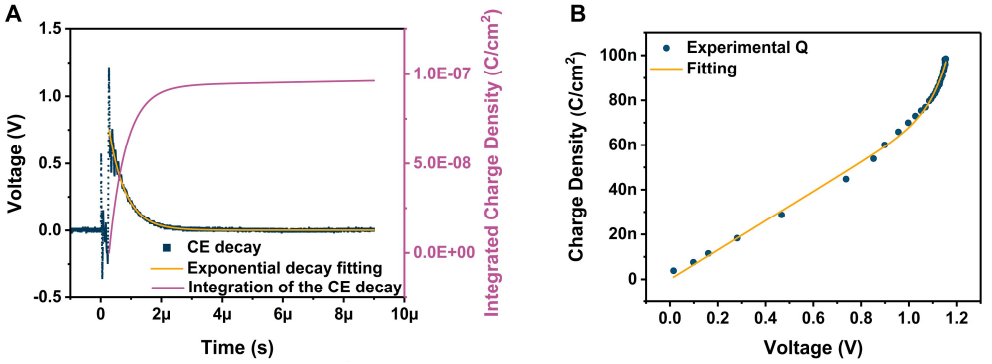

Figure 3.12. (A) CE decay from a perovskite device (blue), the exponential fit (orange), and the integrated charge density (pink). **(B)** Charge density obtained from the integration at different light intensities plot as a function of the voltage and fitting to **Equation 3.10**.

In **Figure 3.12.B** two different regions are observed. In the linear part, the geometrical capacitance C_{geo}, already described in both organic solar cells (OSC)[42,43] and PSC[44,45] can be observed. It is assigned to the accumulation of charges in the selective contacts and the electrodes. It follows a parallel plate capacitor model and grows linearly with the voltage (**Equation 3.8**).

$$Q = C_{geo}\, V = \frac{\varepsilon_0\, \varepsilon_r\, A}{d}\, V \qquad (3.8)$$

Where ε_0 is the electric constant, ε_r the relative permittivity, A the active area of the plate of the capacitor, and d is the distance between the two plates.

The second regime observed, the exponential part, is associated with the chemical capacitance in the solar cell. At higher illumination intensities, the selective contacts are depleted, and thus, the charges start accumulating in the perovskite bulk[44]. The charge extracted grows exponentially with voltage, following the Maxwell-Boltzmann distribution[46] (**Equation 3.9**).

$$Q = Q_0 \left[\exp\left(\frac{q\,V}{m\,K_B\,T}\right) - 1\right] \qquad (3.9)$$

Where Q_0 is the charge density in equilibrium, K_BT/q is the thermal voltage and m is a factor related with the deviation from the thermal voltage. With the subtraction of 1 to the exponential factor we obtain zero charge for zero voltage[47].

Combining **Equation 3.8** and **Equation 3.9** we obtain an expression for the charge extraction as a function of the voltage (**Equation 3.10**).

$$Q = C_{geo}\ V + Q_0 \left[\exp\left(\frac{q\,V}{m\,K_B\,T}\right) - 1\right] \qquad (3.10)$$

Transient photovoltage (TPV)

Transient photovoltage (TPV) is a technique that has been previously applied in dye sensitized solar cells (DSSC)[48,49] and OSC[42,50,51] to study carrier recombination. In PSC it has also been applied, although there is still debate about the interpretation of the data, as it seems that many factors, for example the ionic nature of perovskite, can lead to a misinterpretation of the data[52–54]. It is based on the application of a laser pulse while the device is kept at open circuit conditions under constant illumination. The laser pulse induces a small perturbation in the V_{OC}, generating a small amount of charges, directly related with a small perturbation in the *quasi*-Fermi level. Then, we observe the decay of the V_{OC} to its steady state value associated with the light illumination. From the kinetics associated with this decay, we can obtain the carrier lifetime that it is associated with the major recombination rate in the solar cell[42].

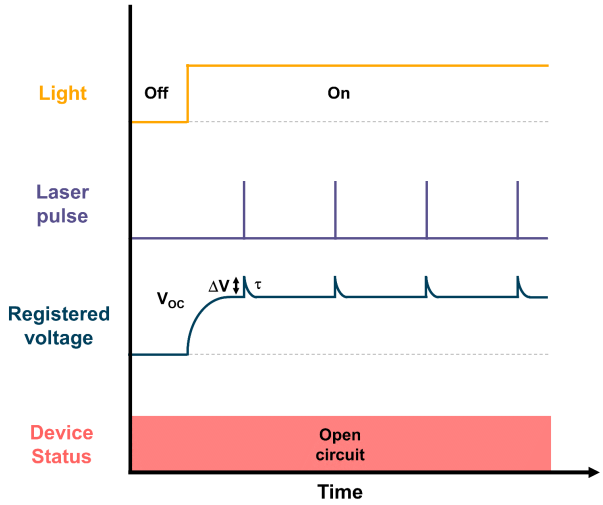

Figure 3.13. Scheme summarizing the TPV measurement process.

In order to perform a measurement (**Figure 3.13**), the solar cell is kept under constant illumination using a white LED array, the same one used for CE, that allows the use of different light illuminations and keep a constant and stable V_{OC}. The solar cell is kept at open circuit conditions to ensure no current flowing in the device. In order to do so, it is connected to an oscilloscope with a large internal resistance (1 MΩ) that also registers the V_{OC} evolution. After reaching a stable V_{OC}, a laser pulse is applied that generates the small perturbation on the $V_{OC}(\Delta V)$. We use a nanosecond nitrogen laser (PTI GL-3300) that allows a tunable excitation wavelength with the use of different organic dyes. Unless it is stated, the excitation wavelength employed is 590 nm using the emission of Rhodamine 6G (R6G). The pulse is triggered using an Aim-TTi TG330 analog function generator that generates a square wave pulse with a duration of 1.5 ns. The intensity of the laser pulse is filtered to ensure a small perturbation regime using a semitransparent optical filter. The extra carriers generated with the laser pulse are forced to recombine as the device is in open circuit conditions and they cannot be extracted. The small perturbation lifetime ($\tau_{\Delta n}$) is obtained from the monoexponential fitting of the transient decay (**Figure 3.14.A**), and it is associated with the recombination

rate. In some cases, biexponential decays have been described[55]. It is important to highlight that, as the light intensity increase, the V_{OC} increase as well and $\tau_{\Delta n}$ decreases. It is possible to compare $\tau_{\Delta n}$ with the V_{OC} (**Figure 3.14.B**), fitted with an exponential decay[56–58] (**Equation 3.11**).

$$\tau_{\Delta n} = \tau_{\Delta n0} \exp\left(-\frac{q\, V_{OC}}{\theta\, K_B\, T}\right) \qquad (3.11)$$

Where $\tau_{\Delta n0}$ is the equilibrium carrier lifetime, θ is the deviation from the thermal voltage (K_BT/q).

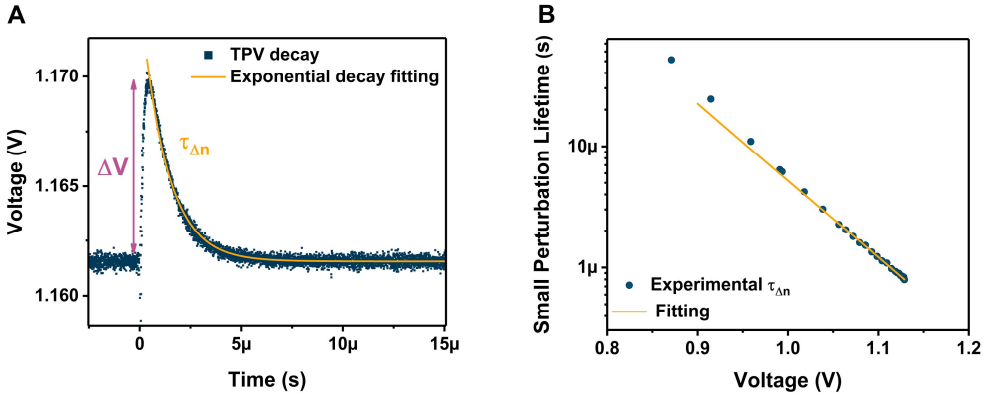

Figure 3.14. (A) Example of a TPV decay (blue) and the monoexponential fit (orange). We obtain from this decay $\tau_{\Delta n}$ and the intensity of the small perturbation, ΔV. **(B)** $\tau_{\Delta n}$ as a function of the different photovoltage obtained (blue) and the exponential fit to **Equation 3.11** (orange).

Although the comparison of Q can be useful to compare devices, as carrier recombination kinetics depend on the charge density, it is convenient to compare $\tau_{\Delta n}$ obtained from the TPV measurement with the charge density obtained under the same illumination conditions[42]. The charge density can be obtained from the CE method or transient photocurrent (TPC) that will be explained in detail below.

Transient of Transient Photovoltage (TROTTR)

This technique is a variation of TPV, introduced by Calado *et al.*[53] and Pockett *et al.*[59]. With this technique it is possible to study the evolution of the TPV decays as the V_{OC} of the solar cell stabilizes. V_{OC} stabilization in n-i-p PSC

is very slow (up to hundreds of seconds) due to the presence of ions at the perovskite interfaces in dark conditions and their redistribution once the cell is illuminated. We observe anomalous TPV decays, as a negative transient deflection appears when the TPV decay is measured while the V_{OC} is not stable. The intensity of this negative deflection decreases as the V_{OC} approaches to its final V_{OC} value. The negative peak is associated with an increased recombination at the interface due to the presence of ions[23,53,59]. This behavior will be explained and analyzed in detail in **Chapter 6**.

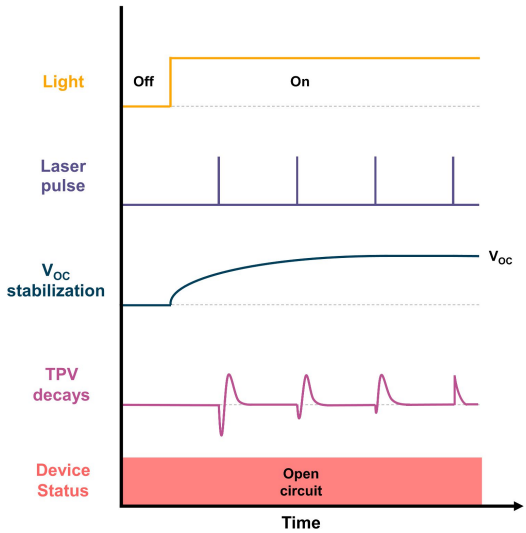

Figure 3.15. Scheme summarizing the TROTTR measurement process.

To do this measurement, it is necessary to register individual TPV decays while the V_{OC} is stabilizing. The rest of the setup is the same as TPV. A summary of TROTTR is shown in **Figure 3.15.**

Transient Photocurrent (TPC) and Differential Capacitance (DiffCap)

Transient photocurrent (TPC) is a technique that allows us to estimate the extra carriers generated by the small perturbation induced with the laser pulse (ΔQ)[43,60–62].

The setup for a TPC measurement is very similar to the one used for TPV, with the exception that the solar cell is kept at short circuit conditions, connected to a small resistor (50 Ω). The laser pulse generates a small perturbation in the device current that is measured on the oscilloscope as a voltage drop over the resistor that is easily converted into a transient current using Ohm's law. This transient current is measured and integrated over time to calculate the amount of charges generated by the laser pulse (ΔQ). **Figure 3.16** summarizes the measurement process.

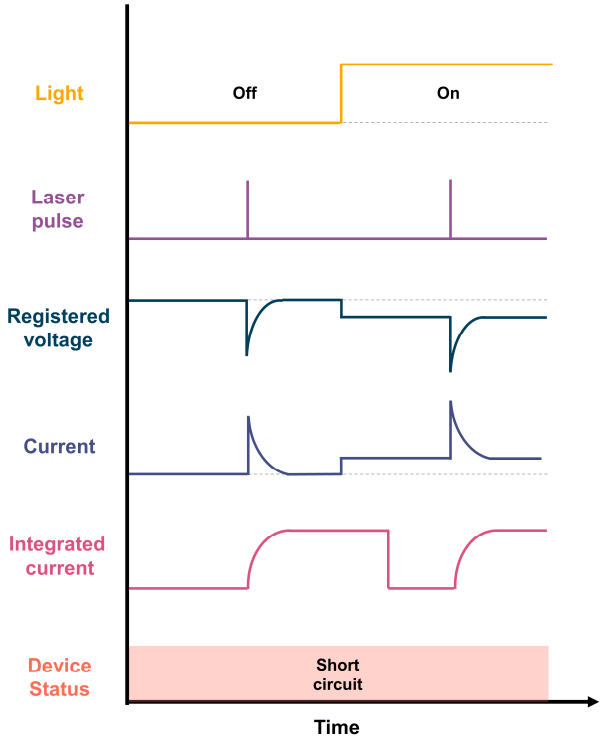

Figure 3.16. Scheme summarizing the TPC measurement process.

However, TPC presents some limitations because it is only valid when charge carrier losses are negligible at short circuit conditions, so, the charge collection process is not affected by carrier recombination. In order to prove it, three different measurements must be checked[42]:

1. The Jsc dependence with the light intensity (**section 3.2.2**) must fit to a power law ($J_{SC}\ \alpha\ \Phi^{\alpha}$) where $\alpha = 1$, as shown in **Figure 3.6.A**, which implies that there are not major carrier losses at short circuit.
2. The TPC decays must be similar under different light irradiation conditions. The extra carriers generated by the laser pulse must be independent on the background light intensity.
3. TPC decay must be faster than the TPV decay, meaning that carrier collection is faster than carrier recombination.

If all these requirements are accomplished, TPC can be used to estimate the charge density in the solar cell via the differential capacitance (DiffCap) method. DiffCap is an alternative to CE, which combines the data obtained from TPV and TPC measurements to estimate the charge density in the solar cell[60,61]. From the TPC we obtain the charges generated by the laser pulse (ΔQ) that, as we already stated, should be the same at the different light intensities. From the TPV we obtain the intensity of the perturbation created by the laser pulse at every light intensity (ΔV) (see **Figure 3.14**). Therefore, DiffCap allows us to measure the capacitance of the device at different light biases (**Equation 3.12**).

$$C(V_{oc}) = \frac{\Delta Q}{\Delta V} \qquad (3.12)$$

DiffCap can be also defined as the ability of a solar cell to store the extra charges (ΔQ) generated by the laser pulse, which creates a small perturbation in the voltage (ΔV) under different light conditions. An example of a DiffCap plot is found in **Figure 3.17.A**. Two different regimes are observed, first, a constant part, associated with the geometric capacitance (C_{geo})[57,58,61] which was previously described in CE. Once the contacts are depleted with charges, they start accumulating in the perovskite bulk, and it follows an exponential trend. This second regime is the chemical capacitance[57].

Finally, the integration of DiffCap at every voltage (**Equation 3.13**) gives us an estimation of the charges stored in the solar cell (**Figure 3.17.C**).

$$Q\,(V_{oc}) = \int_{0}^{V_{OC}} C(V_{oc})\, dV_{oc} \qquad (3.13)$$

As we did in CE, the charge in the solar cell can be correlated with the increasing voltage using **Equation 3.10**. As we will discuss further below, in some cases, it is very useful to eliminate C_{geo} from the DiffCap plot in order to study the charge density just in the bulk of the perovskite[52] (**Figure 3.17.B and Figure 3.17.D**).

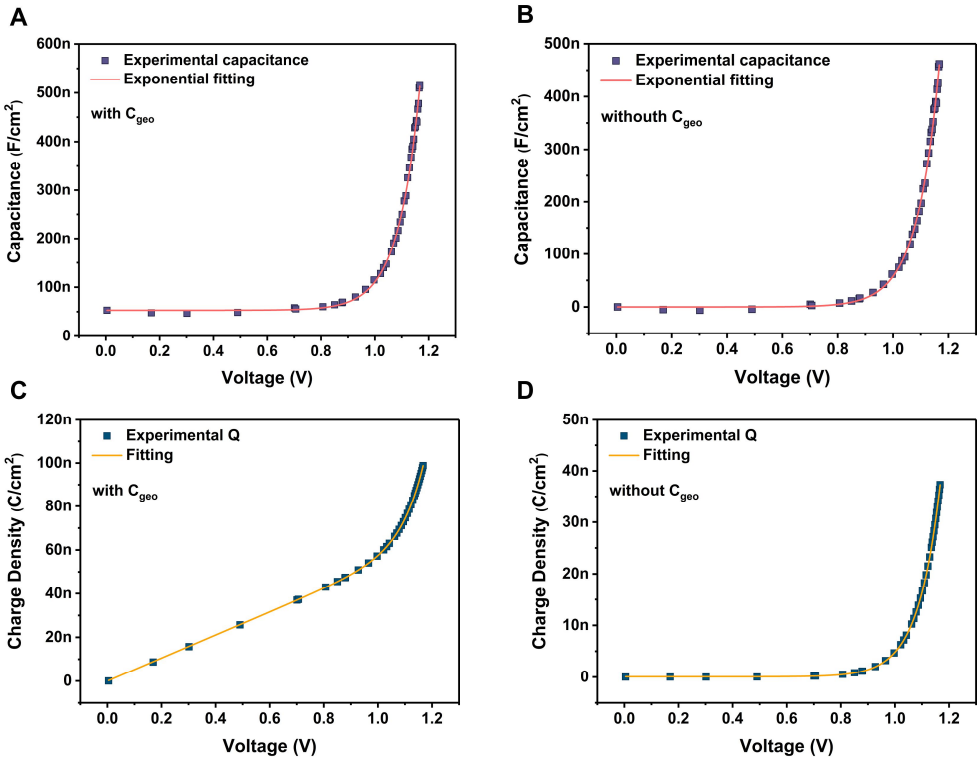

Figure 3.17. **(A)** Differential Capacitance plot obtained from a combination of TPV and TPC decays at different light intensities as a function of the light bias. The pink line shows the exponential fit. **(B)** Differential Capacitance plot as a function of the light bias after the subtraction of the C_{geo}. The pink line shows the exponential fit **(C)** Charge density as a function of the light bias obtained from the integration of the differential capacitance. The orange line shows the fit using equation 3.10. **(D)** Charge density as a function of the light bias obtained from the integration of the differential capacitance after the subtraction of C_{geo}. The orange line shows the fit using equation 3.10.

DiffCap and CE offer different alternatives to the estimation of charge density, using small and large perturbation techniques respectively. However, in the case of PSC, both techniques have resulted in different values for the charge density estimated, contrary to what was obtained in both DSSC and OSC[54]. This behavior is dependent on the perovskite composition: higher charge recombination, as it is in the case of $MAPbI_3$ showed larger differences, compared to CsFAMAPbIBr (**Figure 3.18**).

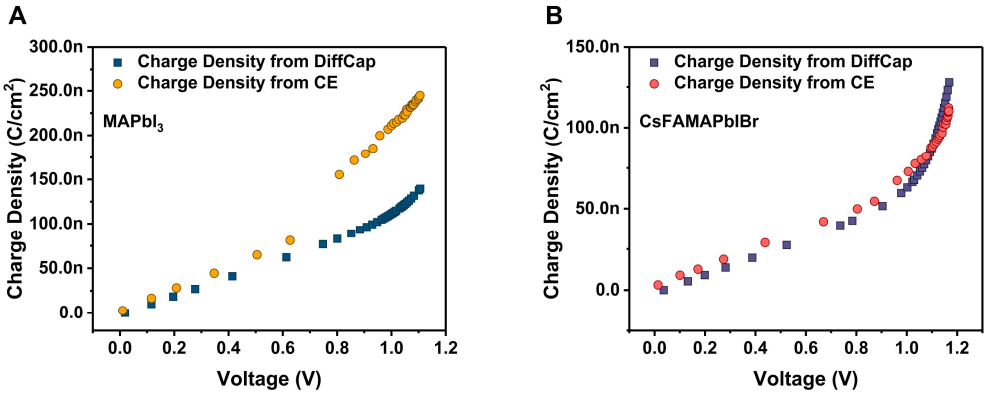

Figure 3.18. (A) Comparison for charge density obtained from the CE and DC methods for $MAPbI_3$ perovskite. **(B)** Comparison for the charge density obtained from the CE and DC methods for CsFAMAPbIBr perovskite.

TPV as a function of the charge density

The comparison of the small perturbation lifetime obtained from the TPV experiments, with the charge density, obtained from the CE or DiffCap experiments, allows us to make a fair comparison between different devices. Additionally, from this experiment, it is possible to obtain the recombination order (δ) that allows us to calculate the total carrier lifetime (τ)[56,57].

Figure 3.19.A shows the comparison of the small perturbation lifetime as a function of the charge density obtained from the DiffCap method. To obtain the recombination order, we compare the values of small perturbation lifetime around 1 Sun and we fit it with a power law dependence (**Equation 3.14**).

$$\tau_{\Delta n} = \tau_{\Delta n0} \left(\frac{Q}{Q_0}\right)^{-\lambda} \qquad (3.14)$$

Where λ is a parameter that describes the slope of the power law and is correlate with the recombination order (δ) as $\delta = \lambda + 1$ [56]; Q_0 is the charge density in the equilibrium and $\tau_{\Delta n0}$ is the equilibrium small perturbation lifetime. If C_{geo} is taken into account, in some cases, odd values of carrier recombination are obtained. For this reason, we use the charge density after the subtraction of C_{geo}. This ensures that we are studying processes in the bulk of the perovskite (**Figure 3.19.B**).

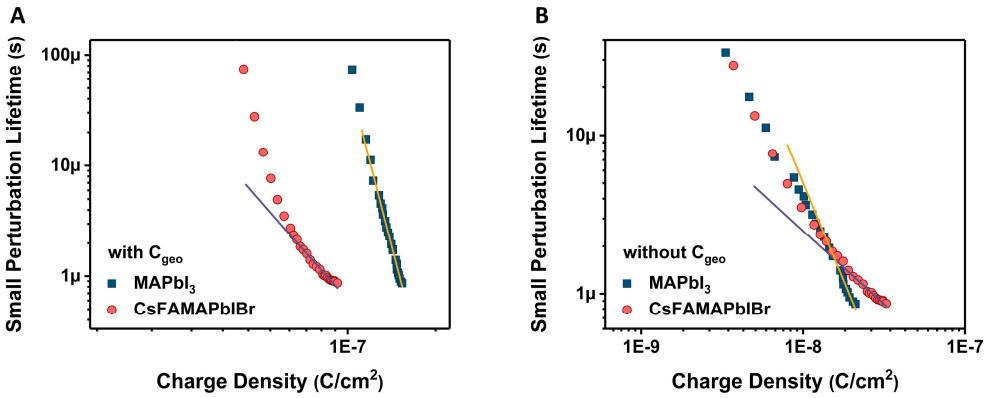

Figure 3.19. (A) Small perturbation lifetime as a function of the charge density obtained from the DiffCap method. **(B)** Small perturbation lifetime as a function of the charge density obtained from the DiffCap method after the subtraction of C_{geo}. In pink it is shown the experimental data for the CsFAMAPbIBr perovskite with the power law fitting as a purple line, and blue shows the experimental data from the $MAPbI_3$ perovskite and the orange line the power law fitting.

Then, the small perturbation lifetime ($\tau_{\Delta n}$) can be converted to the total carrier lifetime (τ) using the recombination order, $\tau = \tau_{\Delta n} \cdot \delta$ **(Figure 3.20)**[56]. From the total carrier lifetime values, it is possible to obtain meaningful comparison of recombination rates between different devices.

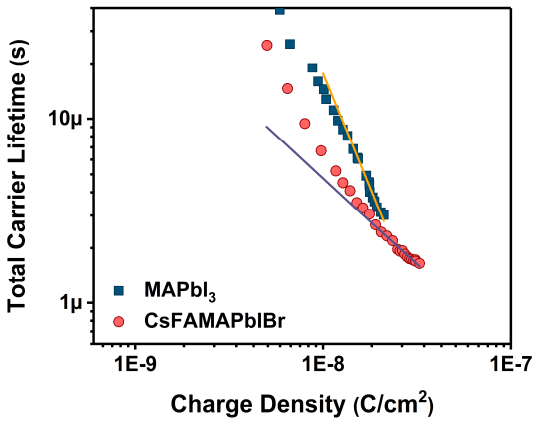

Figure 3.20. Total carrier lifetime obtained from the correction of the small perturbation lifetime with the recombination order as a function of the charge density obtained from the DiffCap method. The fittings are the power law which present the same slope as in **Figure 3.18.B.**

Finally, we take into consideration one limitation for TPV that was recently pointed out by Kiermasch *et al.*[45,52] In these publications, it was described a capacitive component in small perturbation lifetimes obtained from TPV decays (τ_{cap}). It is associated with the release of free charges accumulated at the perovskite contacts that can shorten the decay time constants. In order to check if the small perturbation lifetime that we are studying is corresponding to bulk carrier recombination dynamics, or, it is related with this capacitive component, it is possible to calculate its associated lifetime, τ_{cap} (**Equation 3.15**, **Figure 3.21**).

$$\tau_{cap} = \frac{n_{id}\ K_B\ T\ C_{geo}}{q\ J_{sc}(V_{oc})} \qquad (3.15)$$

Where n_{id} is the ideality factor, obtained from **Equation 3.5**, K_BT/q is the thermal voltage, C_{geo} is the geometric capacitance, obtained from the intercept of the DiffCap plot (**Figure 3.17.A**) and $J_{SC}(V_{OC})$ is a relationship described by Tvingstedt *et al.*[63]. Additionally, to be completely sure that the lifetimes we are comparing are correlated with bulk perovskite dynamics, we eliminate C_{geo} to the charge density calculations, and we compare the lifetimes obtained around 1 Sun light intensities, where the capacitive effect is negligible.

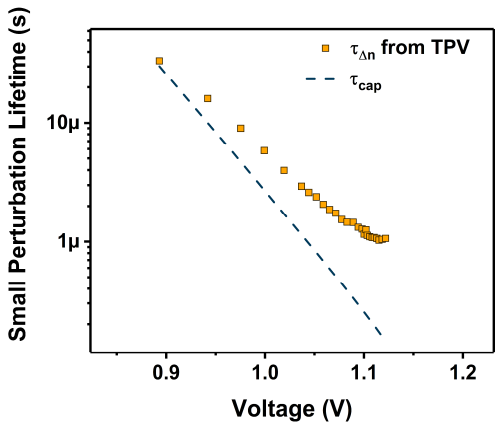

Figure 3.21. Small perturbation as a function of the light bias in the region around 1 Sun (orange) and calculated τ_{cap} using **Equation 3.15** that confirms that we are measuring lifetimes corresponding to bulk dynamics.

3.4. References

(1) Kojima, A.; Teshima, K.; Shirai, Y.; Miyasaka, T. Organometal Halide Perovskites as Visible-Light Sensitizers for Photovoltaic Cells. *J. Am. Chem. Soc.* **2009**, *131* (17), 6050–6051. https://doi.org/10.1021/ja809598r.

(2) Lee, M. M.; Teuscher, J.; Miyasaka, T.; Murakami, T. N.; Snaith, H. J. Efficient Hybrid Solar Cells Based on Meso-Superstructured Organometal Halide Perovskites. *Science* **2012**, *338* (6107), 643–647. https://doi.org/10.1126/science.1228604.

(3) Kim, H.-S.; Lee, C.-R.; Im, J.-H.; Lee, K.-B.; Moehl, T.; Marchioro, A.; Moon, S.-J.; Humphry-Baker, R.; Yum, J.-H.; Moser, J. E.; et al. Lead Iodide Perovskite Sensitized All-Solid-State Submicron Thin Film Mesoscopic Solar Cell with Efficiency Exceeding 9%. *Sci. Rep.* **2012**, *2* (1), 591. https://doi.org/10.1038/srep00591.

(4) Burschka, J.; Pellet, N.; Moon, S.-J. J.; Humphry-Baker, R.; Gao, P.; Nazeeruddin, M. K.; Grätzel, M. Sequential Deposition as a Route to High-Performance Perovskite-Sensitized Solar Cells. *Nature* **2013**, *499* (7458), 316–319. https://doi.org/10.1038/nature12340.

(5) Liu, M.; Johnston, M. B.; Snaith, H. J. Efficient Planar Heterojunction Perovskite Solar Cells by Vapour Deposition Many Different Photovoltaic Technologies Are Being Developed for Large-Scale Solar Energy Conversion. *Nature* **2013**, *501* (7467), 395–398. https://doi.org/10.1038/nature12509.

(6) Prochowicz, D.; Yadav, P.; Saliba, M.; Kubicki, D. J.; Tavakoli, M. M.; Zakeeruddin, S. M.; Lewiński, J.; Emsley, L.; Grätzel, M. One-Step Mechanochemical Incorporation of an Insoluble Cesium Additive for High Performance Planar Heterojunction Solar Cells. *Nano Energy* **2018**, *49* (May), 523–528. https://doi.org/10.1016/j.nanoen.2018.05.010.

(7) Palazon, F.; El Ajjouri, Y.; Bolink, H. J. Making by Grinding: Mechanochemistry Boosts the Development of Halide Perovskites and Other Multinary Metal Halides. *Adv. Energy Mater.* **2019**, *1902499*, 1902499. https://doi.org/10.1002/aenm.201902499.

(8) Schulz, P.; Cahen, D.; Kahn, A. Halide Perovskites: Is It All about the Interfaces? *Chem. Rev.* **2019**, *119* (5), 3349–3417. https://doi.org/10.1021/acs.chemrev.8b00558.

(9) Anaraki, E. H.; Kermanpur, A.; Steier, L.; Domanski, K.; Matsui, T.; Tress, W.; Saliba, M.; Abate, A.; Grätzel, M.; Hagfeldt, A.; et al. Highly Efficient and Stable Planar Perovskite Solar Cells by Solution-Processed Tin Oxide. *Energy Environ. Sci.* **2016**, *9* (10), 3128–3134.

https://doi.org/10.1039/C6EE02390H.

(10) Mao, P.; Zhou, Q.; Jin, Z.; Li, H.; Wang, J. Efficiency-Enhanced Planar Perovskite Solar Cells via an Isopropanol/Ethanol Mixed Solvent Process. *ACS Appl. Mater. Interfaces* **2016**, *8* (36), 23837–23843. https://doi.org/10.1021/acsami.6b08863.

(11) Jeon, N. J.; Noh, J. H.; Kim, Y. C.; Yang, W. S.; Ryu, S.; Seok, S. Il. Solvent Engineering for High-Performance Inorganic–Organic Hybrid Perovskite Solar Cells. *Nat Mater* **2014**, *13* (9), 897–903.

(12) Paek, S.; Schouwink, P.; Athanasopoulou, E. N.; Cho, K. T.; Grancini, G.; Lee, Y.; Zhang, Y.; Stellacci, F.; Nazeeruddin, M. K.; Gao, P. From Nano- to Micrometer Scale: The Role of Antisolvent Treatment on High Performance Perovskite Solar Cells. *Chem. Mater.* **2017**, *29* (8), 3490–3498. https://doi.org/10.1021/acs.chemmater.6b05353.

(13) Saliba, M.; Matsui, T.; Seo, J.-Y.; Domanski, K.; Correa-Baena, J.-P.; Nazeeruddin, M. K.; Zakeeruddin, S. M.; Tress, W.; Abate, A.; Hagfeldt, A.; et al. Cesium-Containing Triple Cation Perovskite Solar Cells: Improved Stability, Reproducibility and High Efficiency. *Energy Environ. Sci.* **2016**, *9* (6), 1989–1997. https://doi.org/10.1039/C5EE03874J.

(14) Saliba, M.; Correa-Baena, J.-P.; Wolff, C. M.; Stolterfoht, M.; Phung, N.; Albrecht, S.; Neher, D.; Abate, A. How to Make over 20% Efficient Perovskite Solar Cells in Regular (n–i–p) and Inverted (p–i–n) Architectures. *Chem. Mater.* **2018**, *30* (13), 4193–4201. https://doi.org/10.1021/acs.chemmater.8b00136.

(15) Rodríguez-Seco, C.; Cabau, L.; Vidal-Ferran, A.; Palomares, E. Advances in the Synthesis of Small Molecules as Hole Transport Materials for Lead Halide Perovskite Solar Cells. *Acc. Chem. Res.* **2018**, *51* (4), 869–880. https://doi.org/10.1021/acs.accounts.7b00597.

(16) Solar Cell Efficiency https://www.pveducation.org/pvcdrom/solar-cell-operation/solar-cell-efficiency.

(17) Nelson, J. *The Physics of Solar Cells*; 2003. https://doi.org/10.1142/p276.

(18) Snaith, H. J.; Abate, A.; Ball, J. M.; Eperon, G. E.; Leijtens, T.; Noel, N. K.; Stranks, S. D.; Wang, J. T.-W.; Wojciechowski, K.; Zhang, W. Anomalous Hysteresis in Perovskite Solar Cells. *J. Phys. Chem. Lett.* **2014**, *5* (9), 1511–1515. https://doi.org/10.1021/jz500113x.

(19) Tress, W.; Marinova, N.; Moehl, T.; Zakeeruddin, S. M.; Nazeeruddin, M. K.; Grätzel, M. Understanding the Rate-Dependent J–V Hysteresis, Slow Time Component, and Aging in $CH_3NH_3PbI_3$ Perovskite Solar Cells: The Role of a Compensated Electric Field. *Energy Environ. Sci.*

2015, *8* (3), 995–1004. https://doi.org/10.1039/C4EE03664F.

(20) Koster, L. J. A. A.; Mihailetchi, V. D.; Ramaker, R.; Blom, P. W. M. M. Light Intensity Dependence of Open-Circuit Voltage of Polymer:Fullerene Solar Cells. *Appl. Phys. Lett.* **2005**, *86* (12), 123509. https://doi.org/10.1063/1.1889240.

(21) Wetzelaer, G.-J. A. H.; Scheepers, M.; Sempere, A. M.; Momblona, C.; Ávila, J.; Bolink, H. J. Trap-Assisted Non-Radiative Recombination in Organic-Inorganic Perovskite Solar Cells. *Adv. Mater.* **2015**, *27* (11), 1837–1841. https://doi.org/10.1002/adma.201405372.

(22) Kim, H. Do; Ohkita, H.; Benten, H.; Ito, S. Photovoltaic Performance of Perovskite Solar Cells with Different Grain Sizes. *Adv. Mater.* **2016**, *28* (5), 917–922. https://doi.org/10.1002/adma.201504144.

(23) Calado, P.; Burkitt, D.; Yao, J.; Troughton, J.; Watson, T. M.; Carnie, M. J.; Telford, A. M.; Regan, B. C. O.; Nelson, J.; Barnes, P. R. F. Identifying Dominant Recombination Mechanisms in Perovskite Solar Cells by Measuring the Transient Ideality Factor. *Phys. Rev. Appl.* **2019**, *10* (1), 1. https://doi.org/10.1103/PhysRevApplied.11.044005.

(24) Xing, G.; Mathews, N.; Sun, S.; Lim, S. S.; Lam, Y. M.; Gratzel, M.; Mhaisalkar, S.; Sum, T. C. Long-Range Balanced Electron- and Hole-Transport Lengths in Organic-Inorganic $CH_3NH_3PbI_3$. *Science* **2013**, *342* (6156), 344–347. https://doi.org/10.1126/science.1243167.

(25) Sum, T. C.; Mathews, N.; Xing, G.; Lim, S. S.; Chong, W. K.; Giovanni, D.; Dewi, H. A. Spectral Features and Charge Dynamics of Lead Halide Perovskites: Origins and Interpretations. *Acc. Chem. Res.* **2016**, *49* (2), 294–302. https://doi.org/10.1021/acs.accounts.5b00433.

(26) Yu, P. Y.; Cardona, M. *Fundamentals of Semiconductors*; Graduate Texts in Physics; Springer Berlin Heidelberg: Berlin, Heidelberg, 2010. https://doi.org/10.1007/978-3-642-00710-1.

(27) C. N. R. Rao Achim Müller A. K. Cheetham. *The Chemistry of Nanomaterials*; Rao, C. N. R., Müller, A., Cheetham, A. K., Eds.; Wiley, 2004. https://doi.org/10.1002/352760247X.

(28) Phillips, D. V. O. and D. *Time-Correlated Single Photon Counting*; Elsevier, 1984. https://doi.org/10.1016/B978-0-12-524140-3.X5001-1.

(29) Dequilettes, D. W.; Koch, S.; Burke, S.; Paranji, R. K.; Shropshire, A. J.; Ziffer, M. E.; Ginger, D. S. Photoluminescence Lifetimes Exceeding 8 Ms and Quantum Yields Exceeding 30% in Hybrid Perovskite Thin Films by Ligand Passivation. *ACS Energy Lett.* **2016**, *1* (2), 438–444. https://doi.org/10.1021/acsenergylett.6b00236.

(30) deQuilettes, D. W.; Frohna, K.; Emin, D.; Kirchartz, T.; Bulovic, V.; Ginger, D. S.; Stranks, S. D. Charge-Carrier Recombination in Halide Perovskites. *Chem. Rev.* **2019**, *119* (20), 11007–11019. https://doi.org/10.1021/acs.chemrev.9b00169.

(31) Dong, Q.; Fang, Y.; Shao, Y.; Mulligan, P.; Qiu, J.; Cao, L.; Huang, J. Electron-Hole Diffusion Lengths > 175 μm in Solution-Grown $CH_3NH_3PbI_3$ Single Crystals. *Science* **2015**, *347* (6225), 967–970. https://doi.org/10.1126/science.aaa5760.

(32) Accordingly, V.; Boxes, I. Principles of X-Ray Diffraction. In *Thin Film Analysis by X-Ray Scattering*; Wiley-VCH Verlag GmbH & Co. KGaA: Weinheim, FRG, 2006; pp 1–40. https://doi.org/10.1002/3527607595.ch1.

(33) Goldstein, J. I.; Newbury, D. E.; Echlin, P.; Joy, D. C.; Lyman, C. E.; Lifshin, E.; Sawyer, L.; Michael, J. R. *Scanning Electron Microscopy and X-Ray Microanalysis*; Springer US: Boston, MA, 2003. https://doi.org/10.1007/978-1-4615-0215-9.

(34) Flegler, S. L.; Heckman, J. W.; Klomparens, K. L. Scanning and Transmission Electron Microscopy: An Introduction. *Choice Rev. Online* **1994**, *31* (08), 31-4353-31–4353. https://doi.org/10.5860/CHOICE.31-4353.

(35) nanoScience Instruments. Atomic Force Microscopy https://www.nanoscience.com/techniques/atomic-force-microscopy/.

(36) Horcas, I.; Fernández, R.; Gómez-Rodríguez, J. M.; Colchero, J.; Gómez-Herrero, J.; Baro, A. M. WSXM: A Software for Scanning Probe Microscopy and a Tool for Nanotechnology. *Rev. Sci. Instrum.* **2007**, *78* (1), 013705. https://doi.org/10.1063/1.2432410.

(37) Kirchartz, T. Influence of Diffusion on Space-Charge-Limited Current Measurements in Organic Semiconductors. *Beilstein J. Nanotechnol.* **2013**, *4* (1), 180–188. https://doi.org/10.3762/bjnano.4.18.

(38) Ruckebusch, C.; Sliwa, M.; Pernot, P.; de Juan, A.; Tauler, R. Comprehensive Data Analysis of Femtosecond Transient Absorption Spectra: A Review. *J. Photochem. Photobiol. C Photochem. Rev.* **2012**, *13* (1), 1–27. https://doi.org/10.1016/j.jphotochemrev.2011.10.002.

(39) Berera, R.; van Grondelle, R.; Kennis, J. T. M. Ultrafast Transient Absorption Spectroscopy: Principles and Application to Photosynthetic Systems. *Photosynth. Res.* **2009**, *101* (2–3), 105–118. https://doi.org/10.1007/s11120-009-9454-y.

(40) Duffy, N. W.; Peter, L. M.; Rajapakse, R. M. G.; Wijayantha, K. G. U.

Investigation of the Kinetics of the Back Reaction of Electrons with Tri-Iodide in Dye-Sensitized Nanocrystalline Photovoltaic Cells. *J. Phys. Chem. B* **2000**, *104* (38), 8916–8919. https://doi.org/10.1021/jp001185z.

(41) Barnes, P. R. F.; Anderson, A. Y.; Juozapavicius, M.; Liu, L.; Li, X.; Palomares, E.; Forneli, A.; O'Regan, B. C. Factors Controlling Charge Recombination under Dark and Light Conditions in Dye Sensitised Solar Cells. *Phys. Chem. Chem. Phys.* **2011**, *13* (8), 3547–3558. https://doi.org/10.1039/C0CP01855D.

(42) Ryan, J. W.; Palomares, E. Photo-Induced Charge Carrier Recombination Kinetics in Small Molecule Organic Solar Cells and the Influence of Film Nanomorphology. *Adv. Energy Mater.* **2017**, *7* (10). https://doi.org/10.1002/aenm.201601509.

(43) Credgington, D.; Liu, S. W.; Nelson, J.; Durrant, J. R. In Situ Measurement of Energy Level Shifts and Recombination Rates in Subphthalocyanine/C_{60} Bilayer Solar Cells. *J. Phys. Chem. C* **2014**, *118* (40), 22858–22864. https://doi.org/10.1021/jp505297u.

(44) Gelmetti, I.; Montcada, N. F.; Pérez-Rodríguez, A.; Barrena, E.; Ocal, C.; García-Benito, I.; Molina-Ontoria, A.; Martín, N.; Vidal-Ferran, A.; Palomares, E. Energy Alignment and Recombination in Perovskite Solar Cells: Weighted Influence on the Open Circuit Voltage. *Energy Environ. Sci.* **2019**, *12* (4), 1309–1316. https://doi.org/10.1039/c9ee00528e.

(45) Kiermasch, D.; Gil-Escrig, L.; Baumann, A.; Bolink, H. J.; Dyakonov, V.; Tvingstedt, K. Unravelling Steady-State Bulk Recombination Dynamics in Thick Efficient Vacuum-Deposited Perovskite Solar Cells by Transient Methods. *J. Mater. Chem. A* **2019**, *7* (24), 14712–14722. https://doi.org/10.1039/C9TA04367E.

(46) Kirchartz, T.; Nelson, J. Meaning of Reaction Orders in Polymer:Fullerene Solar Cells. *Phys. Rev. B - Condens. Matter Mater. Phys.* **2012**, *86* (16), 1–12. https://doi.org/10.1103/PhysRevB.86.165201.

(47) Gelmetti, I. Advanced Characterization and Modelling of Charge Transfer in Perovskite Solar Cells, 2019.

(48) Barnes, P. R. F.; Miettunen, K.; Li, X.; Anderson, A. Y.; Bessho, T.; Gratzel, M.; O'Regan, B. C. Interpretation of Optoelectronic Transient and Charge Extraction Measurements in Dye-Sensitized Solar Cells. *Adv. Mater.* **2013**, *25* (13), 1881–1922. https://doi.org/10.1002/adma.201201372.

(49) Walker, A. B.; Peter, L. M.; Lobato, K.; Cameron, P. J. Analysis of Photovoltage Decay Transients in Dye-Sensitized Solar Cells. *J. Phys. Chem. B* **2006**, *110* (50), 25504–25507.

https://doi.org/10.1021/jp064860z.

(50) Sánchez-Díaz, A.; Burtone, L.; Riede, M.; Palomares, E. Measurements of Efficiency Losses in Blend and Bilayer-Type Zinc Phthalocyanine/C_{60} High-Vacuum-Processed Organic Solar Cells. *J. Phys. Chem. C* **2012**, *116* (31), 16384–16390. https://doi.org/10.1021/jp3054422.

(51) Montcada, N. F.; Domínguez, R.; Pelado, B.; Cruz, P. de la; Palomares, E.; Langa, F. High Photocurrent in Oligo-Thienylenevinylene-Based Small Molecule Solar Cells with 4.9% Solar-to-Electrical Energy Conversion. *J. Mater. Chem. A* **2015**, *3* (21), 11340–11348. https://doi.org/10.1039/C5TA01632K.

(52) Kiermasch, D.; Baumann, A.; Fischer, M.; Dyakonov, V.; Tvingstedt, K. Revisiting Lifetimes from Transient Electrical Characterization of Thin Film Solar Cells; a Capacitive Concern Evaluated for Silicon, Organic and Perovskite Devices. *Energy Environ. Sci.* **2018**, *11* (3), 629–640. https://doi.org/10.1039/C7EE03155F.

(53) Calado, P.; Telford, A. M.; Bryant, D.; Li, X.; Nelson, J.; O'Regan, B. C.; Barnes, P. R. F. Evidence for Ion Migration in Hybrid Perovskite Solar Cells with Minimal Hysteresis. *Nat. Commun.* **2016**, *7*, 1–10. https://doi.org/10.1038/ncomms13831.

(54) Montcada, N. F.; Méndez, M.; Cho, K. T.; Nazeeruddin, M. K.; Palomares, E. Photo-Induced Dynamic Processes in Perovskite Solar Cells: The Influence of Perovskite Composition in the Charge Extraction and the Carrier Recombination. *Nanoscale* **2018**, *10* (13), 6155–6158. https://doi.org/10.1039/C8NR00180D.

(55) Montcada, N. F.; Marín-Beloqui, J. M.; Cambarau, W.; Jiménez-López, J.; Cabau, L.; Cho, K. T.; Nazeeruddin, M. K.; Palomares, E. Analysis of Photoinduced Carrier Recombination Kinetics in Flat and Mesoporous Lead Perovskite Solar Cells. *ACS Energy Lett.* **2017**, *2* (1), 182–187. https://doi.org/10.1021/acsenergylett.6b00600.

(56) Shuttle, C. G.; O'Regan, B.; Ballantyne, A. M.; Nelson, J.; Bradley, D. D. C.; de Mello, J.; Durrant, J. R. Experimental Determination of the Rate Law for Charge Carrier Decay in a Polythiophene: Fullerene Solar Cell. *Appl. Phys. Lett.* **2008**, *92* (9), 093311. https://doi.org/10.1063/1.2891871.

(57) Du, T.; Kim, J.; Ngiam, J.; Xu, S.; Barnes, P. R. F.; Durrant, J. R.; McLachlan, M. A. Elucidating the Origins of Subgap Tail States and Open-Circuit Voltage in Methylammonium Lead Triiodide Perovskite Solar Cells. *Adv. Funct. Mater.* **2018**, *28* (32), 1801808. https://doi.org/10.1002/adfm.201801808.

(58) Wheeler, S.; Bryant, D.; Troughton, J.; Kirchartz, T.; Watson, T.; Nelson,

J.; Durrant, J. R. Transient Optoelectronic Analysis of the Impact of Material Energetics and Recombination Kinetics on the Open-Circuit Voltage of Hybrid Perovskite Solar Cells. *J. Phys. Chem. C* **2017**, *121* (25), 13496–13506. https://doi.org/10.1021/acs.jpcc.7b02411.

(59) Pockett, A.; Carnie, M. J. Ionic Influences on Recombination in Perovskite Solar Cells. *ACS Energy Lett.* **2017**, *2* (7), 1683–1689. https://doi.org/10.1021/acsenergylett.7b00490.

(60) Maurano, A.; Shuttle, C. G.; Hamilton, R.; Ballantyne, A. M.; Nelson, J.; Zhang, W.; Heeney, M.; Durrant, J. R. Transient Optoelectronic Analysis of Charge Carrier Losses in a Selenophene/Fullerene Blend Solar Cell. *J. Phys. Chem. C* **2011**, *115* (13), 5947–5957. https://doi.org/10.1021/jp109697w.

(61) O'Regan, B. C.; Barnes, P. R. F.; Li, X.; Law, C.; Palomares, E.; Marin-Beloqui, J. M. Optoelectronic Studies of Methylammonium Lead Iodide Perovskite Solar Cells with Mesoporous TiO_2: Separation of Electronic and Chemical Charge Storage, Understanding Two Recombination Lifetimes, and the Evolution of Band Offsets during J – V Hysteresis. *J. Am. Chem. Soc.* **2015**, *137* (15), 5087–5099. https://doi.org/10.1021/jacs.5b00761.

(62) O'Regan, B. C.; Scully, S.; Mayer, A. C.; Palomares, E.; Durrant, J. The Effect of Al_2O_3 Barrier Layers in TiO_2/Dye/CuSCN Photovoltaic Cells Explored by Recombination and DOS Characterization Using Transient Photovoltage Measurements. *J. Phys. Chem. B* **2005**, *109* (10), 4616–4623. https://doi.org/10.1021/jp0468049.

(63) Tvingstedt, K.; Deibel, C. Temperature Dependence of Ideality Factors in Organic Solar Cells and the Relation to Radiative Efficiency. *Adv. Energy Mater.* **2016**, *6* (9), 1502230. https://doi.org/10.1002/aenm.201502230.

Chapter 4

Charge carrier interfacial processes at the perovskite/hole transporting material interface

CHAPTER 4: CHARGE CARRIER INTERFACIAL PROCESSES AT THE PEROVSKITE/HOLE TRANSPORTING MATERIAL INTERFACE..... 97

4.1. Abstract 101

4.2. Introduction 101

4.3. Device Fabrication 103

4.4 Results and discussion 104
4.4.1. Surface characterization 104
4.4.2. Current-Voltage Characteristics 106
4.4.3. Photoluminescence analysis 109
4.4.4. Carrier storage and recombination using optoelectronic transient techniques 112
4.4.5. Spectroscopic findings in $MAPbI_3$ 119
4.4.6. Electron and hole injection at the $MAPbI_3/TiO_2$ and $MAPbI_3$/HTM interfaces 121
4.4.7. Hot electron injection 130

4.5. Conclusions 132

4.1. Abstract

In this chapter, we studied charge carrier processes happening at the perovskite/hole transporting material (HTM) interface. For this purpose, several low band gap semiconductor polymers, widely used as donor materials in Organic Solar Cells[1–3], were implemented in complete devices.

First, perovskite solar cells with the different polymers were prepared and characterized. Later on, to gain insight into the carrier processes happening at this interface, the devices were characterized with optoelectronic techniques, such as TPV, TPC, and CE (described in **Chapter 3**), finding out that, independently of the energy levels of the HTM, there are other processes that governs the device V_{OC}.

Thereafter, we moved forward on the study of carrier processes at early stages after photogeneration using fsTA in collaboration with Prof. Guldi group from the Friedrich-Alexander University (FAU) at Erlangen (Germany). We investigated interfacial charge transfer between the perovskite and the different HTMs. Interestingly, we identified a carrier loss process, which has an impact on the photocurrent of the studied devices.

4.2. Introduction

Since the rise of perovskite solar cells (PSC)[4], great efforts have been directed to the synthesis and implementation into devices of new HTMs[5]. Nevertheless, only few of them, *e.g.* PTAA or P3HT, have been capable of replacing spiro-OMeTAD in n-i-p perovskite solar cells. Apart from high production costs and difficult synthetic routes, spiro-OMeTAD is not suitable for long term stability due to the need of chemical dopants to enhance its hole mobility[6,7].

Despite the enormous advances in perovskite solar cells, there is am ongoing debate about the working principles of PSC. Many different techniques, such as terahertz spectroscopy[8], time-resolved

photoluminescence[9] or laser transient absorption spectroscopy[10–14] have been used to analyze the nature of charge carriers, charge carrier injection into the selective contacts, and the lifetime of charge carriers[15–21].

In addition to that, the origin of carrier losses and different strategies to overcome them have also been the matter of study[22–24]. The main carrier losses in PSC are radiative, trap mediated, and interfacial recombination[13,25]. Different techniques, such as transient optoelectronic techniques or impedance spectroscopy have been very useful to find out carrier losses[24,26–28].

In this chapter, we prepare PSC with several low band gap semiconductor polymers, poly[[4,8-bis[(2-ethylhexyl)oxy]benzo[1,2-b:4,5-b']dithiophene-2,6-diyl][3-fluoro-2-[(2-ethylhexyl)carbonyl]thieno[3,4-b]thiophenediyl]] (**PTB7**) poly(3-hexylthiophene-2,5-diyl) (**P3HT**), and poly[2,6-(4,4-bis-(2-ethylhexyl)-4H-cyclopenta[2,1-b;3,4-b′]dithiophene)-alt-4,7(2,1,3-benzothiadiazole)] (**PCPDTBT**) (**Scheme 4.1**). These polymers have been widely applied as donor materials in organic solar cells. We will implement them as efficient HTM in n-i-p PSC.

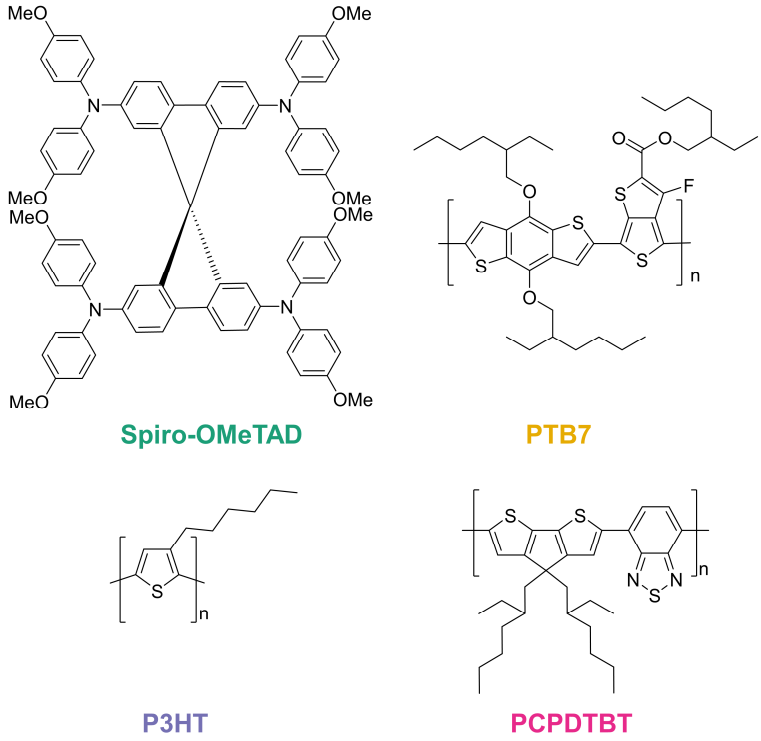

Scheme 4.1. Molecular structure of the different HTM employed in this chapter.

Efficient PSC have been obtained with these polymers. However, we obtained different photovoltaic parameters when compared them to spiro-OMeTAD. Therefore, we investigated which processes were limiting the efficiency in this kind of devices. Using different techniques that cover a wide range of timescales, from the femtosecond, studying carrier injection into the different HTMs, to the microsecond timescale on the analysis of the carrier recombination.

4.3. Device Fabrication

Solar cell devices were prepared following the procedure described for the 2-step $MAPbI_3$ perovskite in **Chapter 3**. TiO_2, both compact and mesoporous, was used as electron transporting material (ETM). Spiro-OMeTAD doped with TBP and LiTFSI was employed as the reference HTM, and the conditions for the polymers studied were as follows.

The concentrations for the semiconductor polymers solutions were 20 mg/ml in chlorobenzene for PTB7 (1-Material), and P3HT (Rieke Metals Inc.), while 30 mg/ml was employed for PCPDTBT (1-Material). The solutions were spin coated at 3000 rpm with 1500 rpm/s for 30 seconds.

For the fs-TAS measurements, films containing ETM/$MAPbI_3$ or $MAPbI_3$/HTM were prepared on glass substrates. Additionally, the perovskite deposition procedure needed to be adapted to obtain samples thin enough to allow the probe light to pass through the sample and reach the detector. For this purpose, 1 M solution of PbI_2 was spin coated at 8000 rpm with 2000 rpm/s for 90 s. In a second step, 50 mg/ml MAI solution was spin coated 30 seconds before the end of the spinning process, obtaining approximately 200 nm thickness of the perovskite layer. Finally, the films were encapsulated in N_2 atmosphere to avoid degradation due to air exposure and humidity using Meltonix 1170-60PF and a cover slide on top of it.

4.4 Results and discussion

4.4.1. Surface characterization

High quality perovskite films were prepared as it can be observed from the XRD and AFM measurements (**Figure 4.1.**). The XRD pattern was obtained from Burda et al.[29] We assigned all the peaks to the different crystallographic planes. On the AFM image of $MAPbI_3$, relatively big perovskite crystal grains are observed. In the case of the AFM images of $MAPbI_3$ covered with the different HTMs under study, spiro-OMeTAD, PTB7, P3HT, and PCPDTBT, all of them presented a complete coverage. Nevertheless, we observed different film roughness for each one of them, which is correlated with the different thicknesses employed. Spiro-OMeTAD, with the thickest layer, presents the smoothest layer, the different organic HTM present different ways of crystallization.

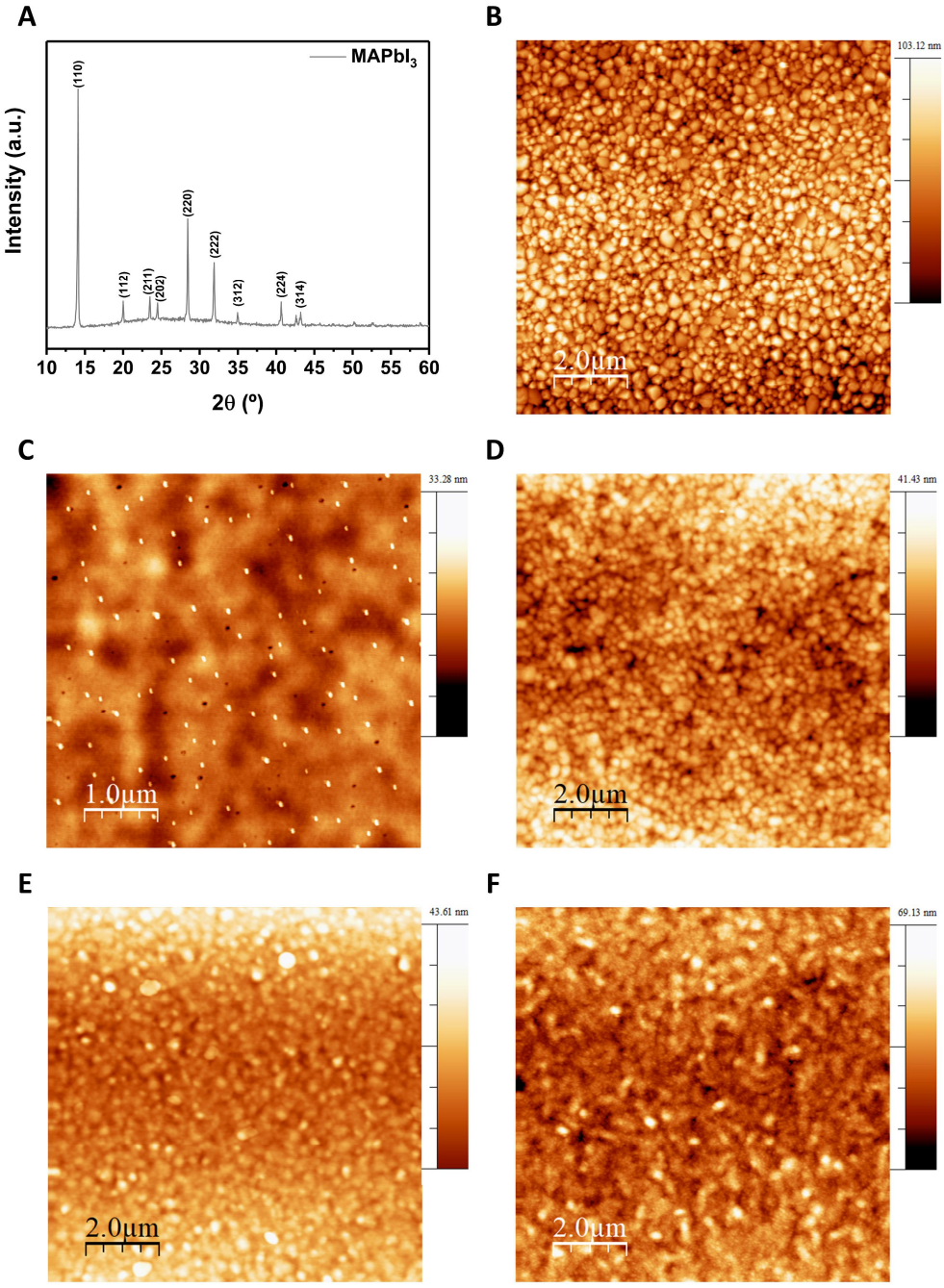

Figure 4.1. **(A)** XRD pattern of $MAPbI_3$ perovskite. AFM images of $MAPbI_3$ **(B)** and $MAPbI_3$ covered with the different HTM under study, spiro-OMeTAD **(C)**, PTB7 **(D)**, P3HT **(E)**, and PCPDTBT **(F)**.

4.4.2. Current-Voltage Characteristics

Then, $MAPbI_3$ perovskite solar cells were prepared and characterized measuring first the current density voltage characteristics under 1 Sun conditions (AM 1.5G, 100 mW/cm^2). JV curves of the best performing devices (reverse scan) and the statistic distribution of photovoltaic parameters obtained are shown in **Figure 4.2, Figure 4.3**, and **Table 4.1**. All cells present high degree of hysteresis in the JV curves (**Figure 4.3** and **Figure 4.4**) leading to differences in photovoltaic parameters depending on the direction of the JV scan[30,31], which has been attributed to the presence of mobile ions[32,33].

From the cells studied, it is evident that both V_{OC} and J_{SC} values for spiro-OMeTAD are much greater compared to the polymers, PTB7, P3HT, and PCPDTBT. If these values are compared with the HOMO levels of the HTM, depicted in **Figure 4.2.B**, it is obvious that the differences in V_{OC} of the cells are not only due to the differences in the HOMO levels, as they are very similar. In this Chapter we will try to discern which factors make polymer-based perovskite solar cells not as efficient as they are when spiro-OMeTAD is used as HTM. Compared to other results in bibliography, we find that, nowadays, efficiencies using some of these polymers, especially P3HT[34], have increased considerably. It is also worthy to mention that these efficiencies are greatly affected by the molecular weight of the polymer that has been chosen for the device fabrication[35,36]. Nevertheless, for the time this research was conducted, the power conversion efficiency (PCE) obtained for PCPDTBT surpassed the previous record reported in literature[37].

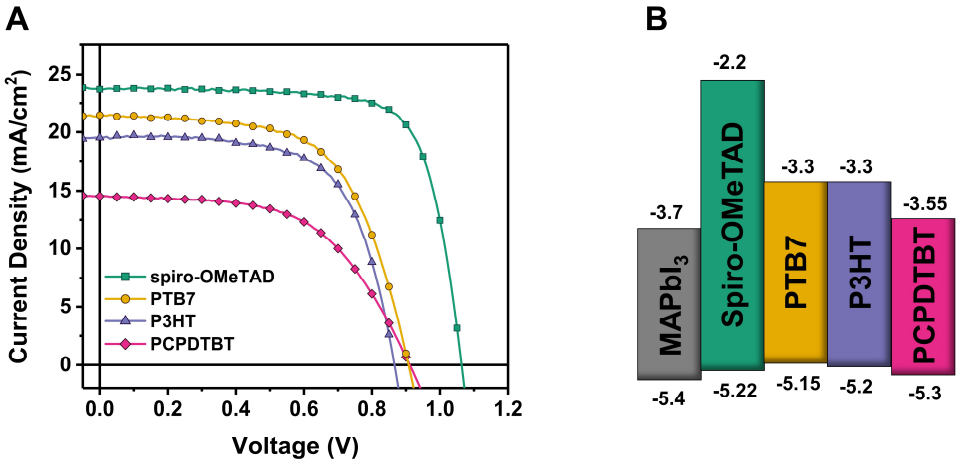

Figure 4.2. **(A)** JV curves of the best performing devices on reverse scan (V_{OC} to J_{SC}) under 1 Sun conditions. **(B)** Scheme containing the energetic levels of the different HTM compared to $MAPbI_3$.

Table 4.1. Photovoltaic parameters obtained from the JV curves in **Figure 4.2**. In parentheses, the average and the standard deviation is shown for the efficiency of all the devices.

HTM	Sweep	V_{OC} (V)	J_{SC} (mA/cm²)	FF	PCE (%)
Spiro-OMeTAD	Forward	0.936	24.4	0.55	**12.6 (9.0 ± 1.5)**
	Reverse	1.068	24.3	0.74	**19.1 (14.9 ± 2.0)**
PTB7	Forward	0.856	21.3	0.45	**8.2 (7.2 ± 1.2)**
	Reverse	0.908	21.4	0.62	**12.0 (10.8 ± 1.2)**
P3HT	Forward	0.807	17.8	0.34	**4.9 (4.8 ± 0.8)**
	Reverse	0.866	19.6	0.65	**11.0 (10.2 ± 0.9)**
PCPDTBT	Forward	0.853	13.4	0.43	**4.9 (4.6 ± 0.6)**
	Reverse	0.911	14.6	0.56	**7.4 (6.5 ± 1.0)**

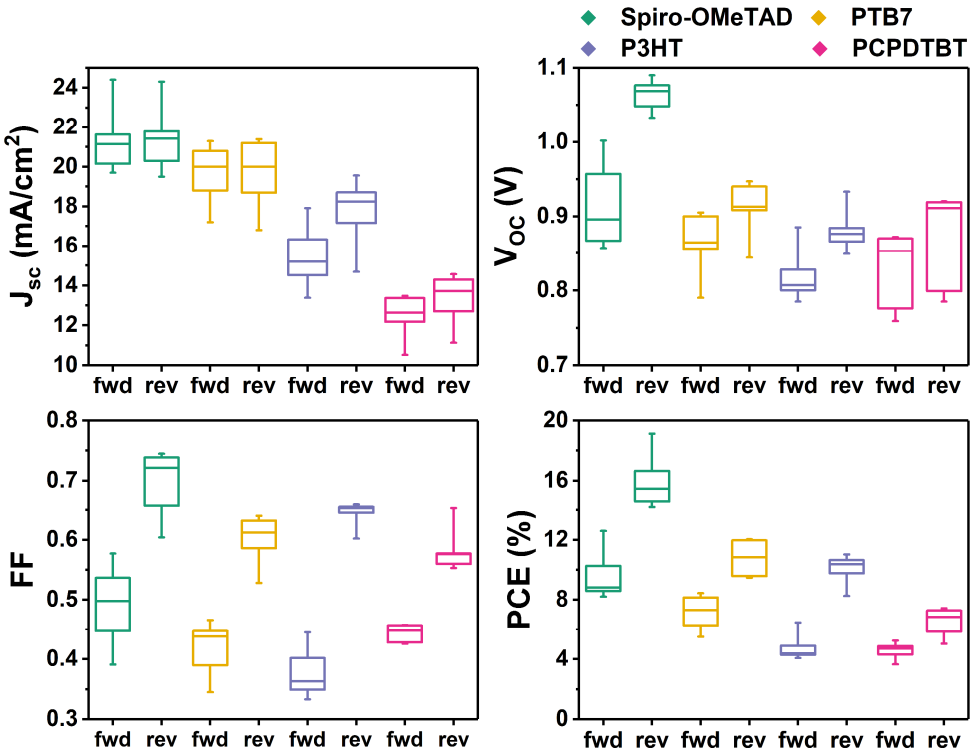

Figure 4.3. Statistical distribution of the photovoltaic parameters obtained from the JV curves measured under 1 Sun Conditions. The box limits show the 25 and 75 percentile while the whiskers show the maximum and minimum value obtained.

Then, we measured the J_{SC} dependence with the light intensity (Φ)(**Figure 4.4.A**). As already described in **Chapter 3**, it follows a power law dependency, J_{SC} proportional to Φ^{α}, and α close to 1 for each HTM ($\alpha_{spiro\text{-}OMeTAD}$ = 0.98; α_{PTB7} = 0.97; α_{P3HT} = 0.92; $\alpha_{PCPDTBT}$ = 0.94). This behavior indicates that there is minimal light intensity dependence for charge collection, so, there are no photocurrent losses at short-circuit conditions[38].

In addition, we evaluated the V_{OC} dependence with Φ. We use the values obtained from the reverse scans of the JV curves, as it is also coincident with the value of V_{OC} obtained in the optoelectronic transient techniques (TPV, TPC, and CE; **Chapter 4.4.4**). After the analysis of V_{OC} dependence with Φ, and, as we already explained in **Chapter 3**, we obtain an approximation of the

ideality factor (n_{id}) that shows how much the solar cell deviates from the ideal diode behavior (**Equation 4.1**).

$$V_{oc} = \frac{K_B T}{n_{id} q} \ln \Phi \qquad (4.1)$$

Where the n_{id} presents values between 1 and 2, being n_{id} = 1 band-to-band recombination, while n_{id} = 2 suggests that trap-assisted recombination is the predominant in the device[39,40]. In this case, it seems that the recombination mechanism is through deep traps, as values close or even bigger than 2 are obtained ($n_{id,spiro\text{-}OMeTAD}$ = 2.2; $n_{id,P3HT}$ = 2.2; $n_{id,PCPDTBT}$ = 1.7) except for PTB7 ($n_{id,PTB7}$ =1.4).

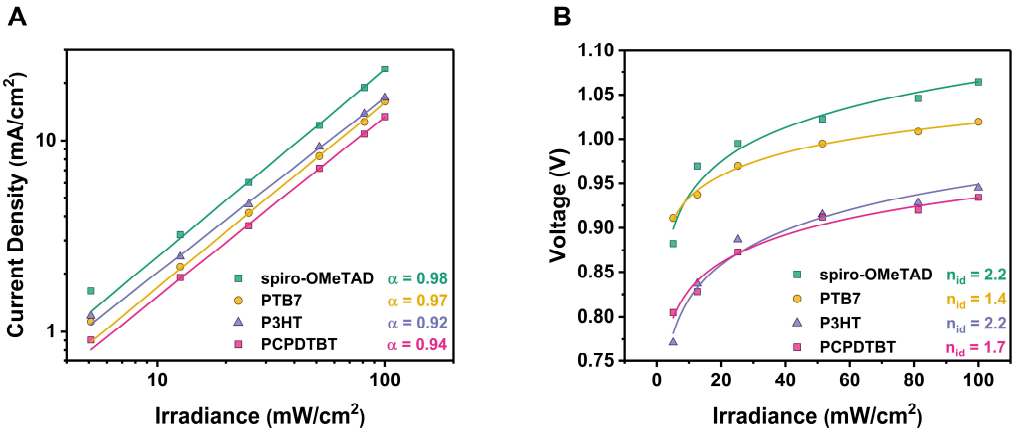

Figure 4.4. (**A**) Light intensity dependence with Jsc and (**B**) V_{OC} for the different HTM under study.

4.4.3. Photoluminescence analysis

Then, we moved on the study of the photoluminescence (PL) characteristics of the $MAPbI_3$ perovskite, and how it is affected by the implementation of the different HTMs[10,41,42]. To analyze the radiative recombination dynamics, we employed time-resolved photoluminescence (TRPL), which was acquired with Time Correlated Single Photon Counting (TCSPC) technique.

The PL spectrum of the perovskite/HTM films deposited on top of a glass substrate (**Figure 4.5.A**) shows a single emission peak centered around 750 nm, with negligible differences between samples. Additionally, the dynamics were acquired and fitted to a bi-exponential function[41,42] (**Equation 4.2**).

$$y = y_0 + A_1 e^{-(t/\tau_1)} + A_2 e^{-(t/\tau_2)} \qquad (4.2)$$

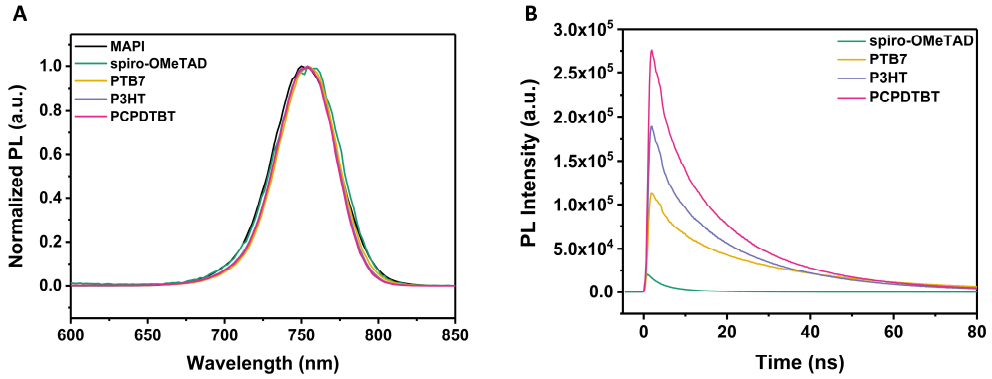

Figure 4.5. (**A**) Normalized PL spectra of the $MAPbI_3$ and $MAPbI_3$/HTM films. (**B**) PL decay dynamics of the perovskite/HTM films. Both measurements were obtained after an excitation at 470 nm.

In **Equation 4.2**, A_1 and A_2 are the amplitude of the respective components, while τ_1 and τ_2 are the lifetimes from the fast and the slow component, respectively. As already described before, perovskite recombination mechanisms are governed by trap assisted recombination, thus Shockley-Read-Hall (SRH) recombination. Therefore, in a PL decay, the fast component (τ_1) has been related to the filling of those traps, while the slow component (τ_2) is related with the radiative recombination in the perovskite bulk[10,42]. These measurements have been performed in $MAPbI_3$/HTM films, so, we correlate the fast component of the PL decay to carrier transfer processes from the perovskite to the HTM, having in mind that, as it has been described, carrier injection happens in earlier timescales.

Table 4.2. TRPL lifetimes obtained from the fitting of PL decays in **Figure 4.5.B** to a bi-exponential fitting.

HTM	τ_1 (ns)	τ_2 (ns)
Spiro-OMETAD	3.2	9.0
PTB7	4.8	30.8
P3HT	3.8	21.8
PCPDTBT	4.4	20.2

Comparing the lifetimes of the films with $MAPbI_3$/HTM, faster lifetimes are obtained (**Figure 4.5.B** and **Table 4.2**), both for τ_1 and τ_2, compared with films with just $MAPbI_3$ (τ_1 = 47.4 ns and τ_2 = 232.5 ns). This behavior suggests that we have an efficient carrier transfer to the HTM, and a faster recombination is expected due to the lower amount of available carriers.

In **Figure 4.5.B** TRPL was measured at the same acquisition time for each HTM shown that is the reason behind the different PL intensities for every decay. As can be seen, in the case of PCPDTBT, which is the HTM that leads to the lowest device efficiency, the perovskite luminescence is the highest. This behavior implies that the hole transfer from the perovskite to the HTM does not occur efficiently. Thus, the sequence of the efficiency for the hole transfer, PCPDTBT < PTB7 < P3HT < spiro-OMeTAD, is in agreement with the efficiencies obtained in working devices, described in **Table 4.1.**

4.4.4. Charge storage and recombination using optoelectronic transient techniques

We moved into the characterization with optoelectronic transient techniques, such as transient photovoltage (TPV), transient photocurrent (TPC), and charge extraction (CE), already described in **Chapter 3**. These techniques are really useful to gain insight into carrier recombination and charge storage in working devices, close to *operando* conditions[23,43–45].

Although CE has been demonstrated as a reliable method to estimate charge density in different kind of solar cells, in perovskite solar cells, in particular with $MAPbI_3$ devices, the measured charge is overestimated[46]. This behavior was already described by O'Regan *et al.*[47], and as an alternative, they suggested to estimate charge density *via* the integration of differential capacitance (DiffCap) that was also demonstrated as a reliable method in both Organic Solar Cells and Dye Sensitized Solar Cells[44,45]. DiffCap measurement and interpretation has been already described in **Chapter 3**. In contrast to other photovoltaic devices, in perovskite devices, especially $MAPbI_3$, CE, and DiffCap led to a very different estimation of charge stored in the solar cell (**Figure 4.9**).

For DiffCap, we need to know the amplitude of the laser pulse that induces the generation of extra carriers. This is obtained from the TPV, which also allows us to study carrier recombination processes in the device, as also explained in **Chapter 3**. All of our TPV decays show a mono-exponential behavior (**Figure 4.6**) which has been previously linked to a very good coverage of the perovskite layer on top of the TiO_2[48]. Having a good perovskite coverage avoids a direct recombination path between the HTM and the TiO_2 layer, avoiding bi-exponential TPV decays[49].

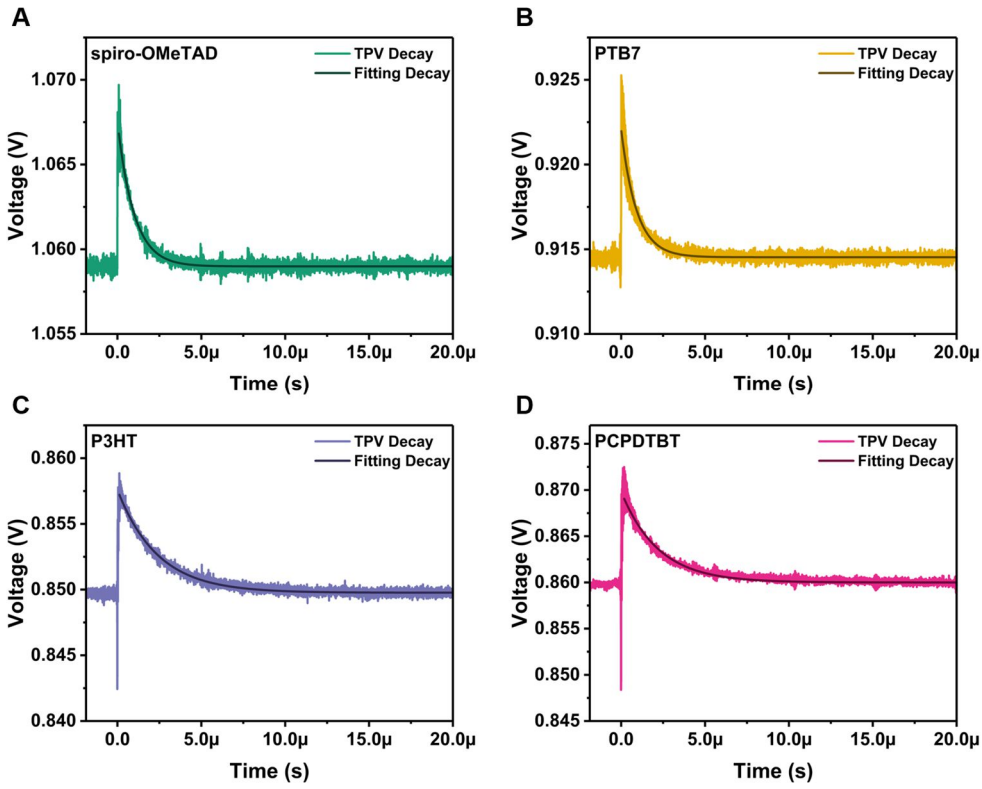

Figure 4.6. TPV decays measured under 1 Sun conditions for all the studied devices, (**A**) spiro-OMeTAD, (**B**) PTB7, (**C**) P3HT, and (**D**) PCPDTBT. It is also shown the mono-exponential fitting to obtain the perturbation lifetime.

It is possible to obtain the TPV lifetime at different V_{OC} measuring under different light intensities. Then, the perturbation lifetime decreases with the increment of V_{OC} (**Figure 4.7**), following the equation 4.3.

$$\tau_{\Delta n} = \tau_{\Delta n_0} e^{-\frac{q V_{oc}}{\theta K_B T}} \qquad (4.3)$$

Where $\tau_{\Delta n0}$ is the equilibrium lifetime and θ is the deviation from the thermal voltage K_BT/q. We observed that at 1 Sun illumination conditions (**Figure 4.6** and **4.7**) spiro-OMeTAD and PTB7 presented the fastest lifetimes, approximately 1 μs, while for P3HT and PCPDTBT is more than 2 μs. From the θ parameter, it was also observed that the bigger deviation from the thermal voltage leads to worse performance.

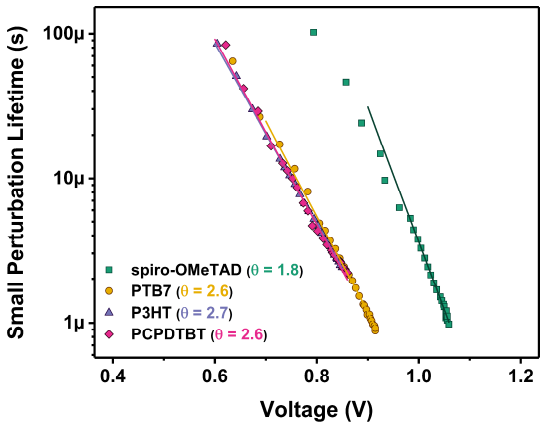

Figure 4.7. Perturbation lifetime obtained from the TPV decays as a function of the voltage generated at different light intensities.

After that, using the DiffCap technique that combines TPV and TPC, we obtained an estimation of the capacitance of the cell. For that, we used the definition of the capacitance $C = \Delta Q/\Delta V$, so, the carriers generated with a variation of voltage in the device. The variation of voltage is the small perturbation generated by the laser pulse. The intensity of the laser pulse that generates this small perturbation ΔV is obtained from the TPV decay, being dependent from the light bias, while the carriers generated by the laser pulse ΔQ is obtained from TPC decays, that should be independent of the light bias.

Figure 4.8 shows the DiffCap measured under different light intensities that led to different V_{OC}. Two different regimes were observed in the capacitance plots. The constant part at lower voltages, obtained at lower light intensities, is associated with the charge stored in the contacts. This term of the capacitance is called geometric capacitance, C_{geo}, and it is associated with a parallel plate capacitor, so its value is dependent on the electric permittivity, ε, the area of the capacitor, a, and the distance separating the two plates, d, with the relation $C_{geo} = \varepsilon\, {}^{a}/_{d}$. The second regime, the exponential part, is related to the accumulation of charges in the active layer, in this case

the perovskite layer. Therefore, subtracting C_{geo} (**Figure 4.8.B**) we obtained information about charge in the perovskite layer.

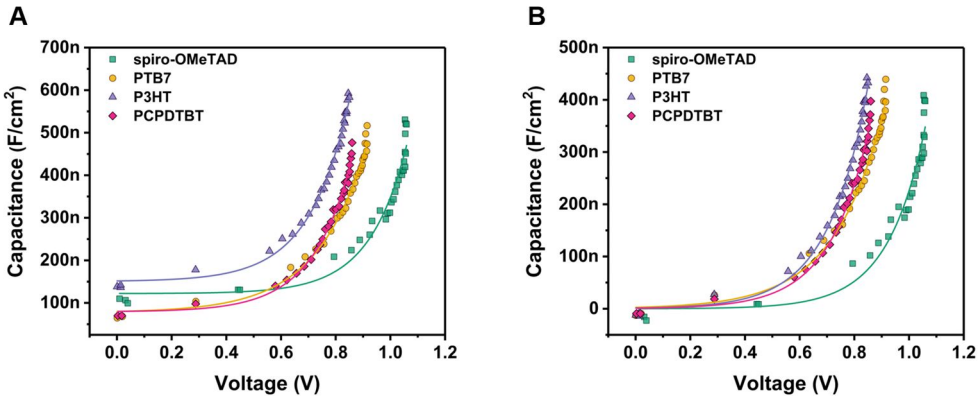

Figure 4.8. **(A)** Differential Capacitance plot as a function of the V_{OC} for the different HTM used including the geometric capacitance. **(B)** Differential Capacitance after subtracting the geometric capacitance.

From **Figure 4.8** the most characteristic feature is the difference observed in the exponential part comparing the spiro-OMeTAD with the rest of the semiconducting polymers. While this shift agrees with the V_{OC} values obtained for these devices, it is not correlated with the HOMO (**Figure 4.2.B**) reported from cyclic voltammetry in solution[50]. The V_{OC} will increment with the Quasi Fermi Level Splitting (QFLS) with the increasing illumination intensity until the depletion layers at each interface are filled and the charges start accumulating at the bulk of the perovskite. We expected that the QFLS will be correlated with the HOMO levels of the HTMs, but we observed that this is not the case. Very recently, Stolterfoht *et al.* suggested that some polymers, such as P3HT, suffer from band bending, with a much larger effect over the V_{OC} rather than the QFLS[22].

An estimation of the charge density of the devices is obtained with the integration of the DiffCap plots. As it is shown in **Figure 4.9**, it is possible to observe the influence of the geometric capacitance over the total charge density. Additionally we plotted in **Figure 4.9.C** the charge density estimation

from the CE technique. It is clear when we compared the DC method, that CE overestimates the charge density in this perovskite composition.

Furthermore, we compared the perturbation lifetime at every charge density obtained from DiffCap, shown in **Figure 4.10**. Carrier lifetime as a function of the voltage gave us longer lifetimes for spiro-OMeTAD compared to the rest of the semiconducting polymers (**Figure 4.7**). In contrast, we observe for the same amount of charge in the device spiro-OMeTAD presents the slowest lifetime. This scenario changes completely if we remove C_{geo}. Recently, Kiermasch *et al.* described a capacitive component that affects to the carrier lifetime, therefore, it would be an optimal approximation to remove C_{geo} in order to study bulk carrier lifetime[51,52]. In this case, the fastest lifetimes were found for spiro-OMeTAD devices, but, it should also be noted that the slope of both spiro-OMeTAD and PTB7 were quite similar, and their lifetimes increased rapidly with the decrease of charge, which was not the case for P3HT, and PCPDTBT.

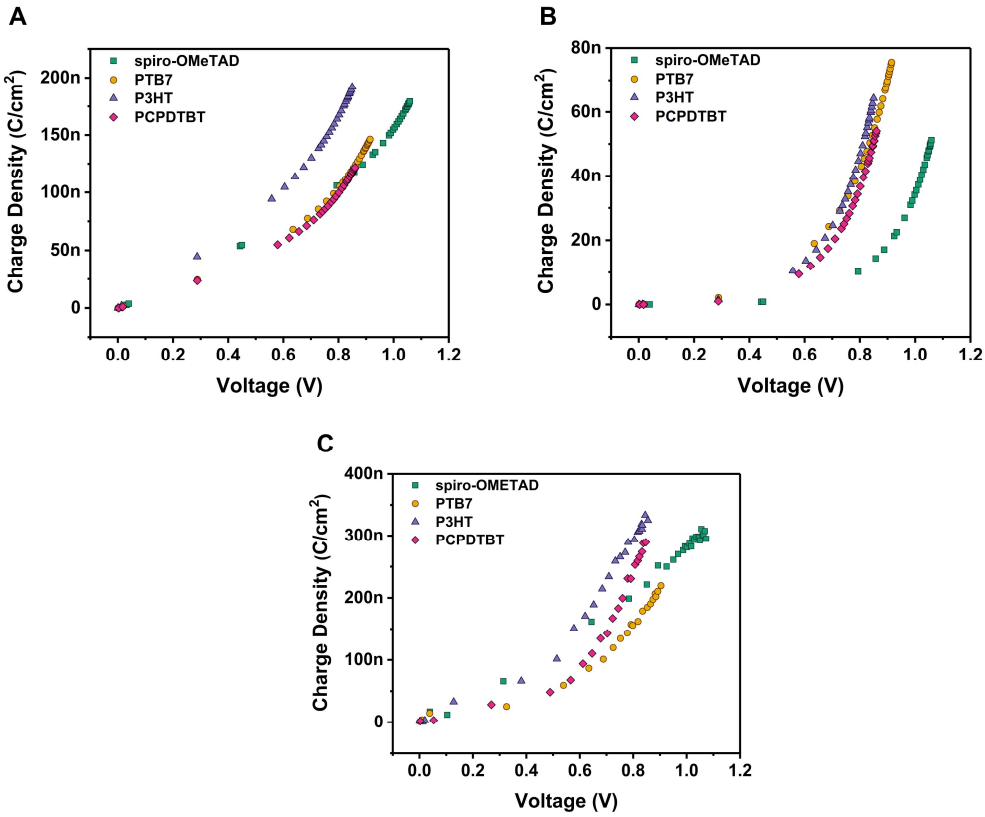

Figure 4.9. **(A)** Charge density obtained from the integration of the differential capacitance at the same voltages. **(B)** Charge density obtained after the subtraction of the geometrical capacitance, reflecting the charge stored in the perovskite bulk. **(C)** Charge density obtained from the CE method.

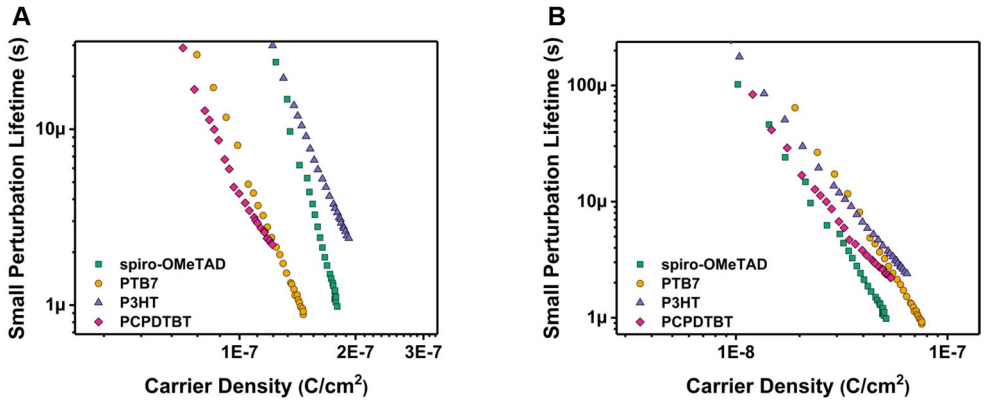

Figure 4.10. **(A)** Carrier lifetime as a function of the charge density in the device considering the geometric capacitance and **(B)** after the subtraction of the geometric capacitance.

Finally, we measured the hole mobility of the HTM using the space charge limited current (SCLC) method. In order to apply the SCLC there should be just one type of carrier present, the current is not trap limited, the current is drift only, and the electric field at the contacts is zero[53]. The JV curves of the hole only devices prepared for the measurements (with the architecture ITO/PEDOT:PSS/HTM/Au) are shown in **Figure 4.11**. We obtained hole mobility values that are in accordance with values reported previously in literature[54–56]. In addition, these results confirmed that doped spiro-OMeTAD present a better hole mobility $1.5 \cdot 10^{-3}$ $cm^2\,V^{-1}\,s^{-1}$ compared to the rest of the HTMs ($2.0 \cdot 10^{-4}$ $cm^2\,V^{-1}\,s^{-1}$ for PTB7, $1.9 \cdot 10^{-4}$ $cm^2\,V^{-1}\,s^{-1}$ for P3HT, and $3.5 \cdot 10^{-4}$ $cm^2\,V^{-1}\,s^{-1}$ for PCPDTBT).

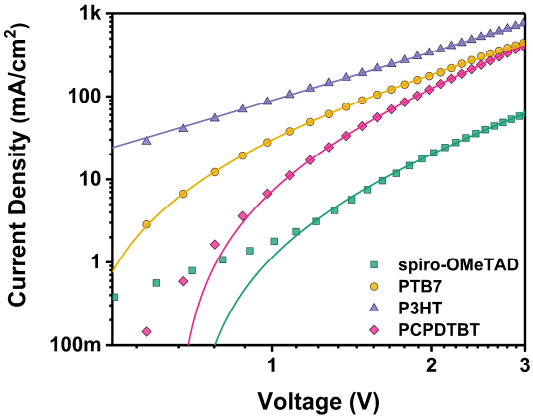

Figure 4.11. JV measurements of the hole only devices for each HTM under study. The lines correspond to the fitting of the SCLC method.

4.4.5. Spectroscopic findings in $MAPbI_3$

In this second part of the Chapter, we used femtosecond transient absorption spectroscopy (fsTA) to study carrier processes happening at the interface $MAPbI_3$/HTM in the early stages after photoexcitation.

Following the absorption spectra of thin $MAPbI_3$ (**Figure 4.12**), we selected 460 nm and 695 nm as excitation wavelengths (λ_{exc}). The use of these wavelengths allows us to study the differences when exciting at the two valence bands (VB) described for the perovskite, VB_1 at 760 nm, which has been associated with the band gap transition, and the VB_2 at 480 nm according to Sum *et al.*[57].

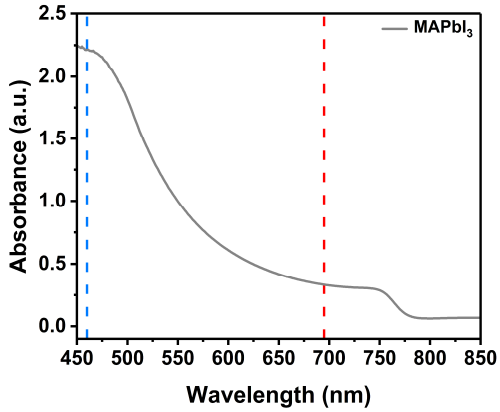

Figure 4.12. UV-Vis absorption spectra of the $MAPbI_3$ film. The dashed vertical lines indicate the excitation wavelengths in the fsTA experiments, 460 nm (blue), and 695 nm (red).

Figure 4.13 shows the fsTA of the $MAPbI_3$ film. It is characterized by two ground-state bleaching (GSB) at 480 and 760 nm, which corresponds to the characteristics observed in the steady state absorption spectra (**Figure 4.12**). Additionally, a broad photo-induced absorption (PIA) between the two GSB, as well as in the near—infrared (NIR) region are detected. There are many studies that assign the two GSB to the depopulation to two valence bands (VB_1 and VB_2)[10,57–60]. Another study, by Even *et al.*[61] raised the possibility that the 760 nm and 480 nm GSB are caused by photoexcitation at the R and M high

symmetry points of the perovskite cubic phase. Photogenerated electron-hole pairs at the M point (480 nm) can relax to the R valley, assisted by the emission of phonons. From now on, we will refer to the 480 nm GSB as the depopulation of the VB_2, although the conclusion is applicable to the excitation across the M point.

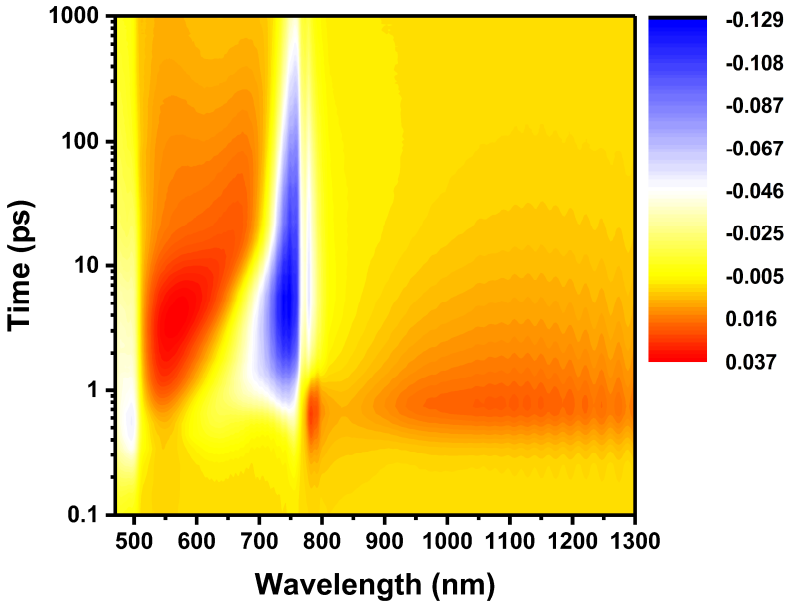

Figure 4.13. FsTA spectra in the visible and NIR of $MAPbI_3$ films using λ_{exc} = 460 nm and a laser fluence of 130 $\mu J/cm^2$.

Independently of the excitation wavelength employed, both GSB are present. The differences observed rely on the kinetics. When using excitation wavelengths of higher energy than VB_2 (480 nm), the kinetics at 480 nm were much faster than those registered for 760 nm (**Figure 4.14**).

Another important spectroscopic feature observed in $MAPbI_3$ films is the presence of hot electrons that are typically registered as a weak PIA at 780 nm on the sub-ps timescale[12,19,62] (**Figure 4.13**), before the GSB forms. Hot carriers are clearly observed when there is an excess energy, obtained with λ_{exc} that allows excitation above the conduction band of the perovskite. Therefore,

we observed this peak with λ_{exc} = 460 nm but not in the case of 695 nm. In literature, hot carriers have also been identified in the broadening of the GSB at 760 nm.

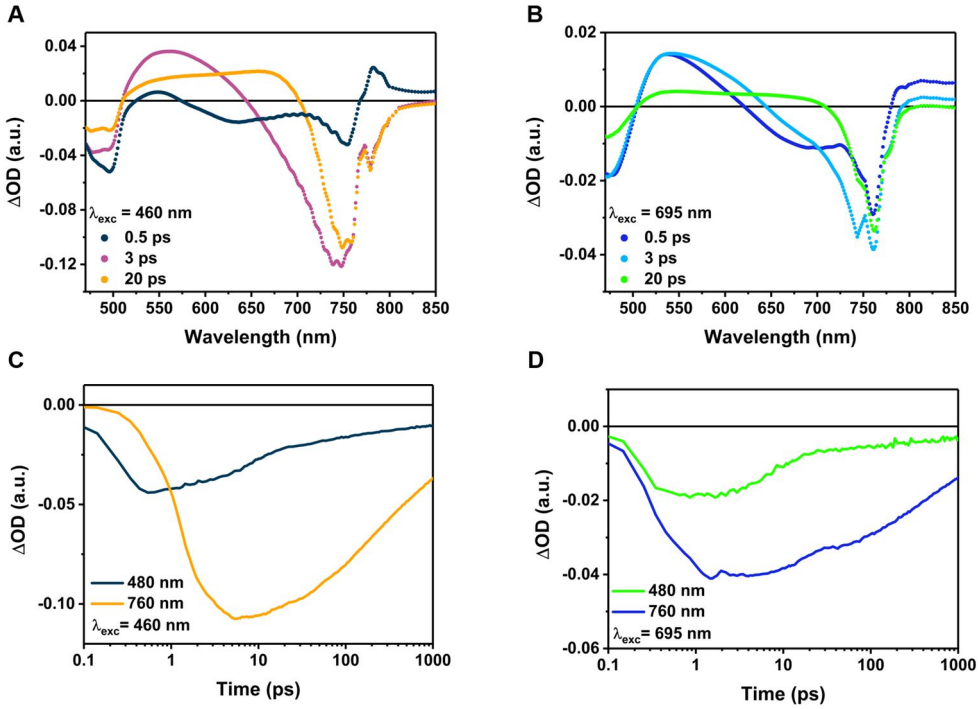

Figure 4.14. (A) Differential absorption spectra of $MAPbI_3$ with time delays of 0.5 ps (blue), 3 ps (purple), and 20 ps (orange) using λ_{exc} = 460 nm and a laser fluence of 130 μJ/cm² **(B) (A)** Differential absorption spectra of $MAPbI_3$ with time delays of 0.5 ps (blue), 3 ps (cyan), and 20 ps (green) using λ_{exc} = 695 nm nm and a laser fluence of 130 μJ/cm². **(C)** Time absorption profiles of $MAPbI_3$ at 480 nm (blue) and 760 nm (orange) using λ_{exc} = 460 nm and a laser fluence of 130 μJ/cm² **(D)** Time absorption profiles of $MAPbI_3$ at 480 nm (green) and 760 nm (blue) using λ_{exc} = 695 nm and a laser fluence of 130 μJ/cm².

4.4.6. Electron and hole injection at the $MAPbI_3/TiO_2$ and $MAPbI_3$/HTM interfaces

After identifying the principal spectroscopic features assigned to $MAPbI_3$, we continued using a mesoporous TiO_2 layer as ETM. In this case, the electron injection into the mesoporous layer is associated with the growth of a PIA in the NIR region with a maximum at 970 nm (**Figure 4.15**). The maximum of this peak appears after 0.5 ps, much faster than the carrier relaxation, what

makes possible to associate it with hot electron injection[58,63]. However, this will be commented with more detail in **Chapter 5**.

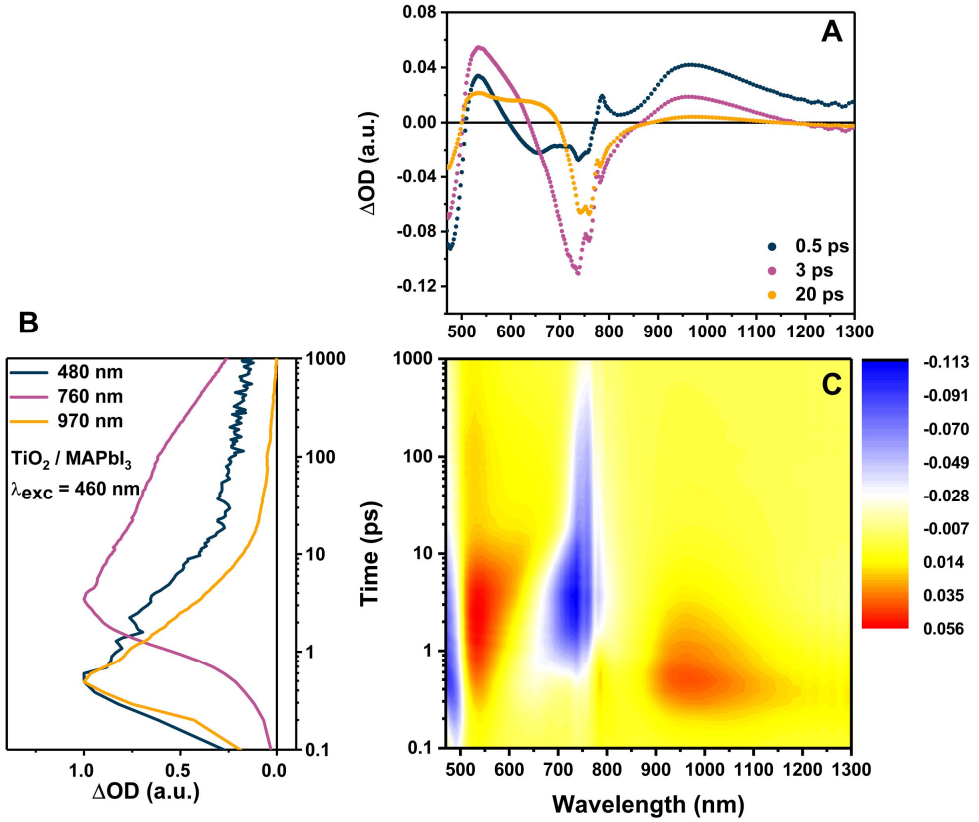

Figure 4.15. FsTA spectra of TiO_2/$MAPbI_3$ films with λ_{exc} = 460 nm. Differential absorption spectra **(A)** with time delays of 0.5 ps (blue), 3 ps (purple), and 20 ps (orange). Time absorption profiles **(B)** at 480 nm (blue), 760 nm (purple), and 970 nm (orange) showing the electron injection into the TiO_2 layer.

Now, we will focus our study into the processes happening at the $MAPbI_3$/HTM interface. The HTMs under study were the same used in the previous sections, spiro-OMeTAD, PTB7, P3HT, and PCPDTBT. **Figure 4.16** shows the UV-Vis absorption spectra of the different $MAPbI_3$/HTM and HTM films.

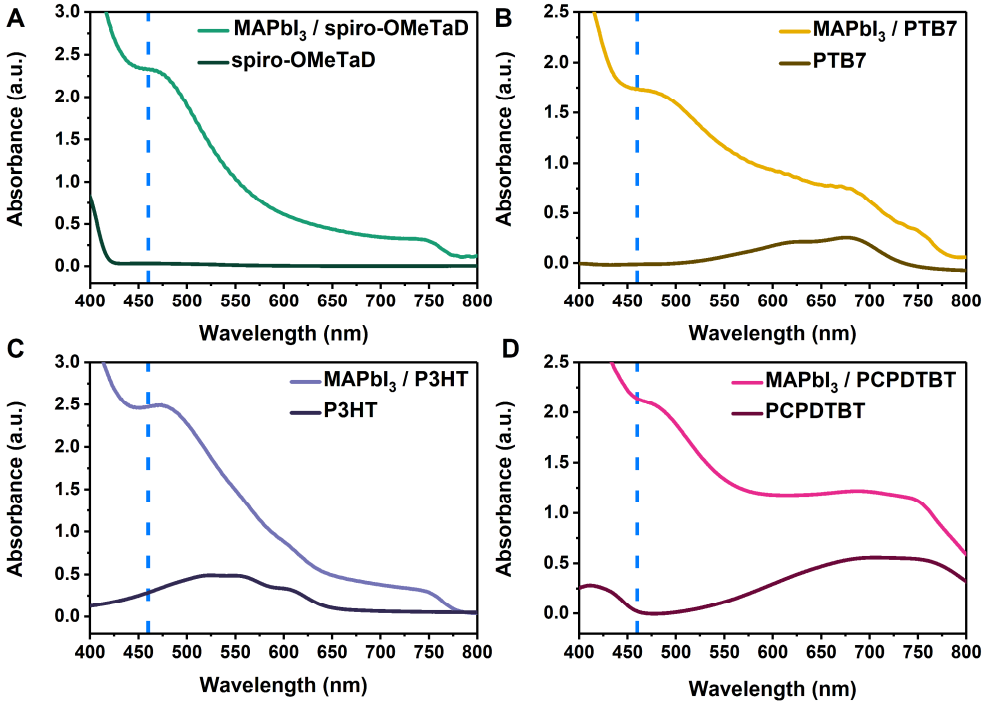

Figure 4.16. UV-Vis absorption spectra of the different $MAPbI_3$/HTM and HTM films. **(A)** $MAPbI_3$/spiro-OMeTAD and spiro-OMeTAD films; **(B)** $MAPbI_3$/PTB7 and PTB7; **(C)** $MAPbI_3$/P3HT and P3HT; and **(D)** $MAPbI_3$/PCPDTBT and PCPDTBT. The dashed blue line indicates the excitation wavelength in the fsTA experiments.

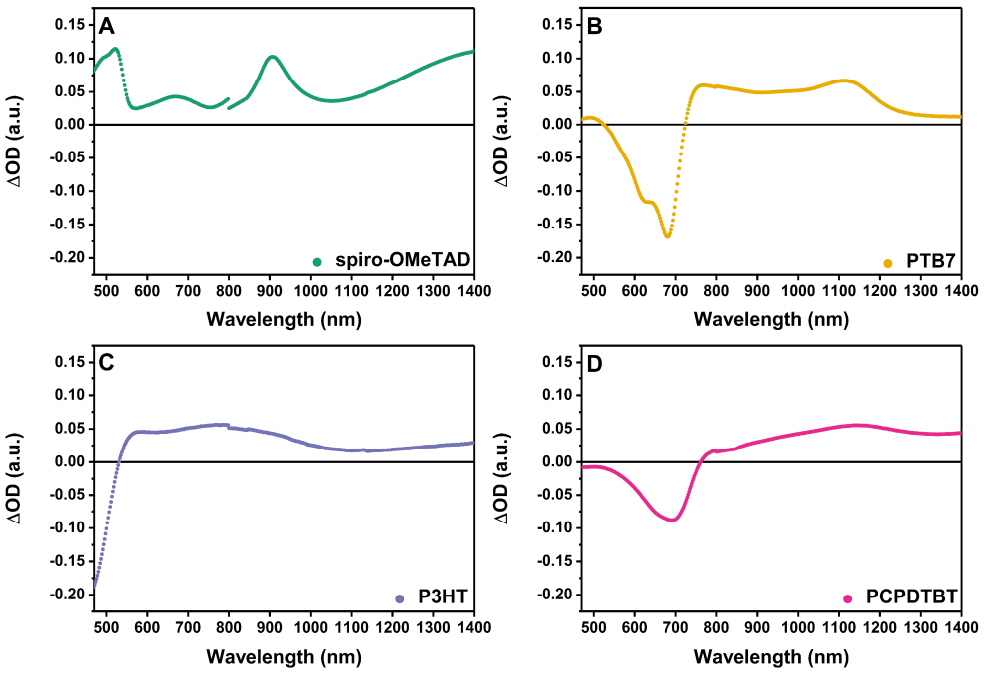

Figure 4.17. Differential absorption spectra obtained by spectroelectrochemical oxidation at different voltages for spiro-OMeTAD ($V_{spiro\text{-}OMeTAD}$ = +0.27 V) **(A)**, PTB7 (V_{PTB7} = +1.52 V) **(B)**, P3HT (V_{P3HT} = +1.07 V) **(C)**, and PCPDTBT ($V_{PCPDTBT}$ = +0.07 V) **(D).** All potentials vs Fc/Fc^+.

In order to study both charge injection and carrier lifetime at this interface, we will follow the polaron spectral features of every HTM[58,64,65]. The different polaron signatures are determined measuring the spectroelectrochemistry of the different materials in chlorobenzene. The differential absorption spectra of the oxidized HTMs were identified upon chemical oxidation which reveals the polaron features in the NIR region (**Figure 4.17**). It should be noted that these measurements are red-shifted in the fsTA due to the aggregation in thin films.

Next, we measured fsTA of $MAPbI_3$/HTM thin films using spiro-OMeTAD (150 nm thick), PTB7 (90 nm), P3HT (90 nm), and PCPDTBT (110 nm) as HTM. We used 460 nm as excitation wavelength (blue dashed line in **Figure 4.16**) as it is one of the wavelengths available that allows us to excite selectively the perovskite layer, and not the HTM layers, as we excite from the $MAPbI_3$ side. With the excitation of the $MAPbI_3$ layer we observed the

depopulation of VB_1 and VB_2[66], as well as the charge transfer processes across the different $MAPbI_3$/HTM interfaces.

Comparing $MAPbI_3$ and $MAPbI_3$/HTM films, we found differences in the fsTA, especially in the NIR region (**Figure 4.18**). The characteristics features correlated with $MAPbI_3$ were observed, but, newly developed characteristics were observed in the NIR. These characteristics are in agreement with the spectroelectrochemical findings of the HTMs under oxidative conditions, taking into account the red-shift due to the aggregation in thin film. The spectroscopic features found for the HTMs are corroborated in literature[67–69]. Thereby, the presence of the HTM polarons, which are products from the hole transfer from the $MAPbI_3$ to the HTM is confirmed.

We studied the charge injection kinetics analyzing the time absorption profiles from the HTM polaron spectral characteristics. The charge injection rates were obtained from the fast component of the oxidized HTM transient decay (**Figure 4.19** and **Table 4.3**). In every case, we observed an ultrafast hole injection, between 1 and 2 ps, which is in agreement with previous reports in literature. Spiro-OMeTAD appears as the most efficient hole extracting semiconducting material with the fastest charge injection rate. We consider the "apparent driving force" for charge injection as the difference between the valence band maximum of the perovskite and the HOMO level of the HTM[70,71]. It increases going from PCPDTBT < spiro-OMeTAD < P3HT < PTB7, which goes in accordance with the hole transfer rates. However, we can conclude from here that hole injection rate is not a key factor for solar cell efficiency because PCPDTBT, which presents similar hole injection rates compared with spiro-OMeTAD, reveals the lowest power conversion efficiency of all the devices[24,72].

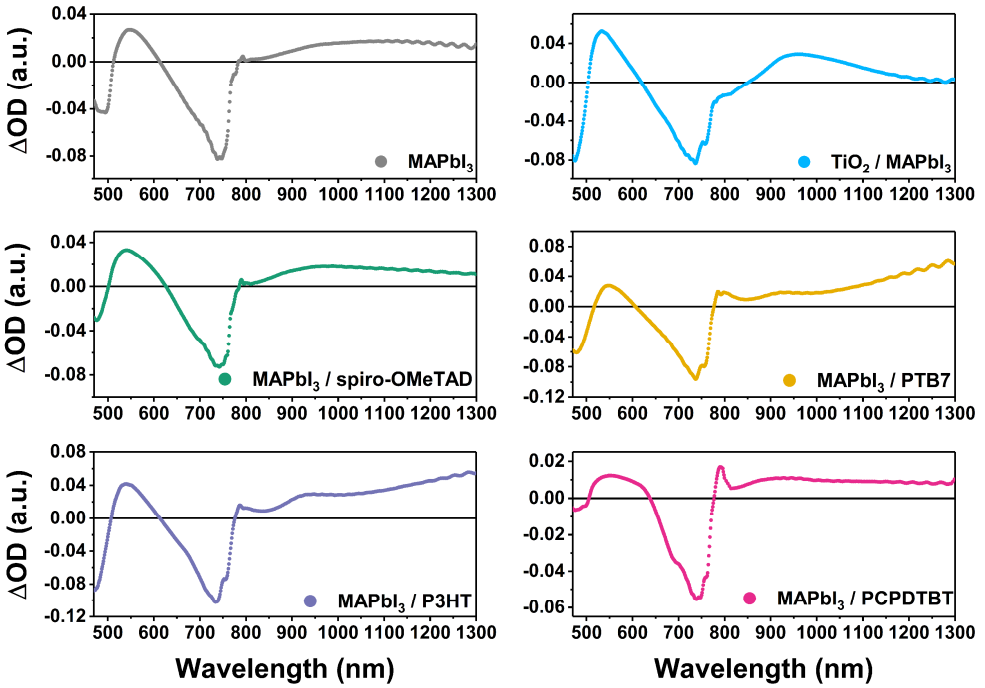

Figure 4.18. Comparison of the differential absorption spectra in the visible and NIR region of the different films, $MAPbI_3$, $TiO_2/MAPbI_3$, $MAPbI_3$/spiro-OMeTAD, $MAPbI_3$/PTB7, $MAPbI_3$/P3HT, and $MAPbI_3$/PCPDTBT at 1.2 ps with λ_{exc} = 460 nm and a laser fluence of 130 $\mu J/cm^2$.

Table 4.3. HOMO and LUMO values of the different HTMs, hole injection rates derived from the fastest component in the kinetic traces of the oxidized species of the HTMs, and power conversion efficiencies obtained from **Table 4.1** on the reverse sweep conditions.

HTM	HOMO values (eV)	LUMO values (eV)	Charge injection rate 10^{12} (s^{-1})	PCE (%)
spiro-OMeTAD	-5.22	-2.2	0.82 ± 0.03	14.9 ± 2.0
PTB7	-5.15	-3.3	5.9 ± 1.1	10.8 ± 1.2
P3HT	-5.2	-3.3	4.2 ± 0.8	10.2 ± 0.9
PCPDTBT	-5.3	-3.55	1.00 ± 0.05	6.5 ± 1.0

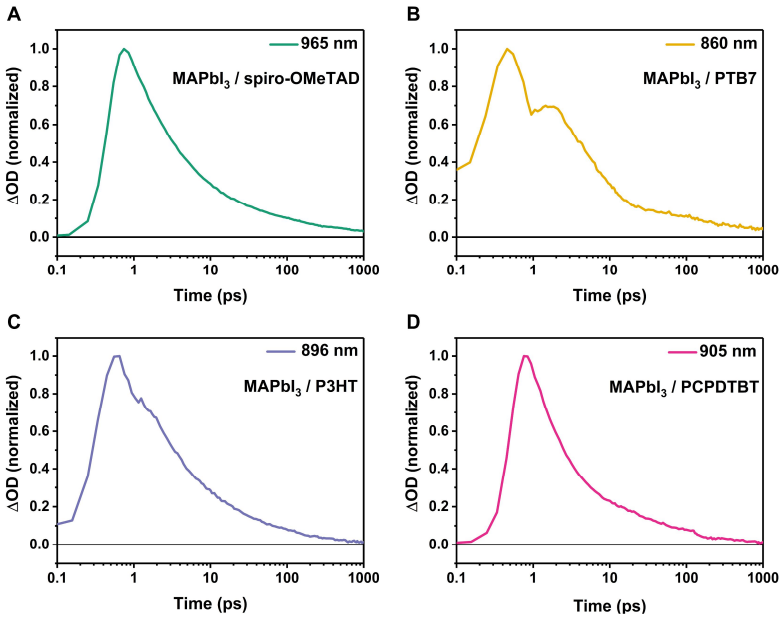

Figure 4.19. Time absorption profiles obtained at the maximum of the polaron features for every HTM: **(A)** spiro-OMeTAD, **(B)** PTB7, **(C)** P3HT, and **(D)** PCPDTBT. The fast component of the decay is associated with hole injection.

From now on, we will focus on the comparison between $MAPbI_3$/spiro-OMeTAD and $MAPbI_3$/PCPDTBT, which correspond to the best and the worst device efficiency, respectively. From the kinetic analysis, we have not reached any round conclusion that justify this behavior. It is important to highlight that even using low pump fluences, we have measured in a range between 26-191 $\mu J/cm^2$, it is possible to observe the characteristic polaron signature for every HTM (**Figure 4.20** and **Figure 4.21**). In **Figure 4.20**, the fsTA spectra acquired with a time delay of 0.5 ps using a laser fluence of 64 $\mu J/cm^2$ is shown and the spiro-OMeTAD polaron feature is observed as a PIA at 965 nm, while in the case of PCPDTBT the PIA is at 905 nm. This make us suggest that the formation of the PIA peak associated with the hole injection and its detection is not affected by the pump fluence. Additionally, we have highlighted the signal associated with the hot carriers, which will be commented later. Also, the dependence of the HTM polaron signal as a function on the laser fluence is shown in **Figure 4.22**.

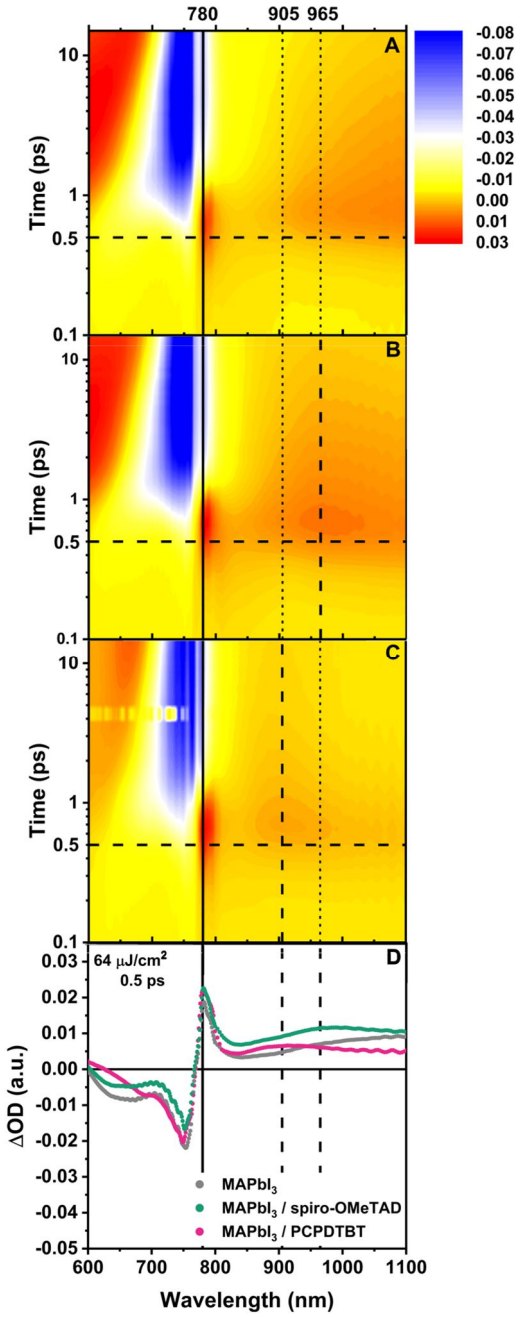

Figure 4.20. (A-C) FsTA spectra in the visible and NIR (600-1100 nm) of $MAPbI_3$ **(A)**, $MAPbI_3$/spiro-OMeTAD **(B)**, and $MAPbI_3$/PCPDTBT **(C)** using λ_{exc} = 460 nm and a laser fluence of 64 μJ/cm². **(D)** Differential absorption spectra with a time delay of 0.5 ps for $MAPbI_3$ (grey), $MAPbI_3$/spiro-OMeTAD (green), and $MAPbI_3$/PCPDTBT (pink). Solid lines were added to highlight the PIA signals of hot carriers (780 nm). Vertical dashed lines highlight the polaron of spiro-OMeTAD at 965 nm and PCPDTBT at 905 nm. Horizontal dashed lines indicate the time delay of 0.5 ps.

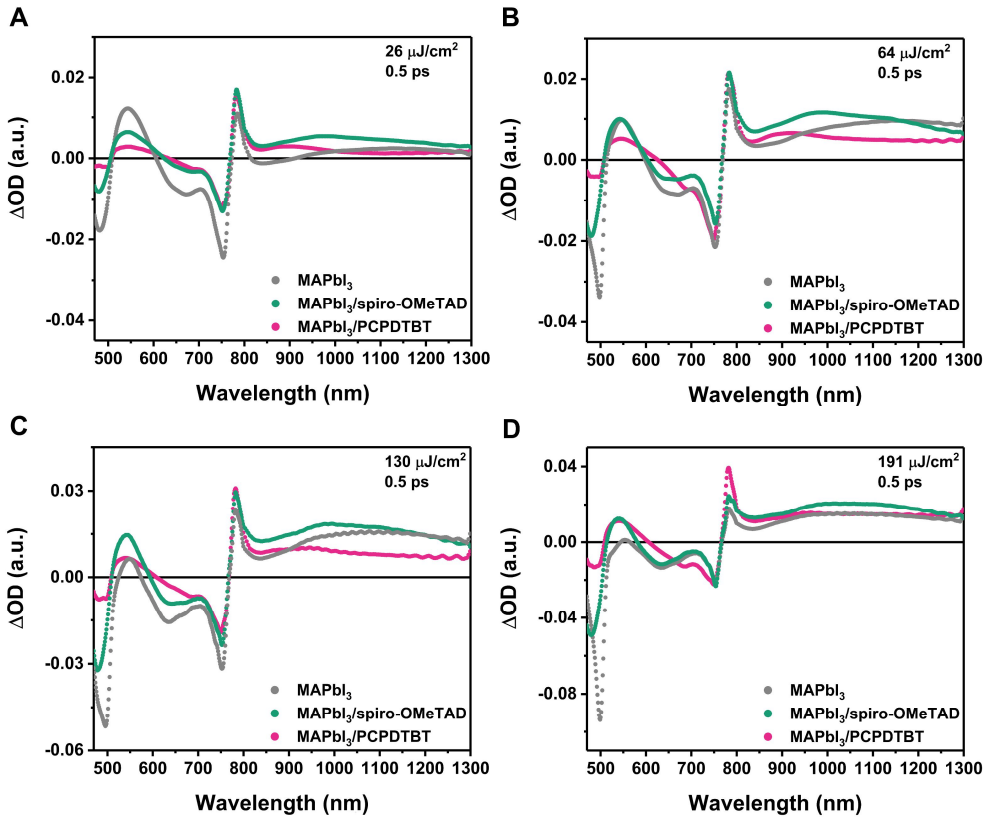

Figure 4.21. Comparison of differential absorption spectra at 0.5 ps with λ_{exc} = 460 nm and laser fluences of 26 μJ/cm² **(A)**, 64 μJ/cm² **(B)**, 130 μJ/cm² **(C)**, and 191 μJ/cm² **(D)** of $MAPbI_3$ (grey). $MAPbI_3$/spiro-OMeTAD (green), and $MAPbI_3$/PCPDTBT (pink).

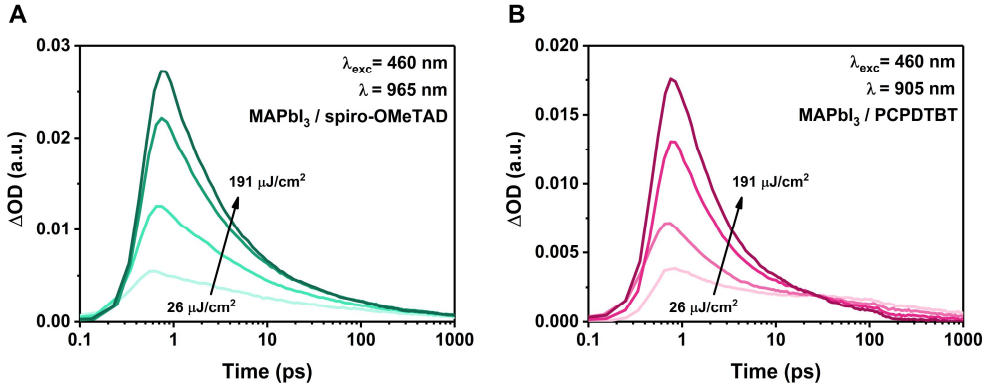

Figure 4.22. Time absorption profiles of spiro-OMeTAD **(A)** and PCPDTBT **(B)** polaron signals at 965 nm and 905 nm, respectively with increasing laser fluences 26, 64, 130, and 191 μJ/cm².

4.4.7. Hot electron injection

In the last part of the Chapter, we focused on the study of the hot electrons in $MAPbI_3$ when the different HTMs are present. As already described in the previous sections, the spectroscopic feature associated to the hot electrons is a PIA at 780 nm that is only observable at early times. These hot electrons, which are located in higher energetic states in the conduction band of the perovskite, are cooled via the emission of the longitudinal optical (LO) phonons[12,19,62]. Because of the relaxation to the conduction band minimum, the PIA evolves into a GSB.

Figure 4.23.A shows the 780 nm PIA kinetics for the $MAPbI_3$, $MAPbI_3$/spiro-OMeTAD, $MAPbI_3$/PCPDTBT, and TiO_2/ $MAPbI_3$ films using λ_{exc} = 460 nm. As we have previously stated, mTiO_2 films are capable of hot electron quenching, and therefore, this behavior is observed in the PIA at 780 nm. Surprisingly, we also observed the quenching of the 780 nm PIA in $MAPbI_3$/PCPDTBT films. This behavior is not expected, as PCPDTBT acts as a HTM rather than an ETM. Therefore, there is a competition for hot electron injection into the TiO_2 layer or into low LUMO level semiconductors polymers, as it is PCPDTBT. On the other hand, spiro-OMeTAD, which presents a high LUMO level, acts as an electron blocking layer, and, thus, there is not a hot electron injection competition.

If both holes and electrons are injected into the HTM, there are two plausible scenarios: In the first one, electrons and holes recombine in the HTM resulting in radiative recombination, the fluorescence coming from the polymer. Yet, we did not appreciate any spectroscopic feature associated with the fluorescence of the polymer, making this scenario not possible. In the other scenario, those electrons in the PCPDTBT are transferred back to the $MAPbI_3$ layer.

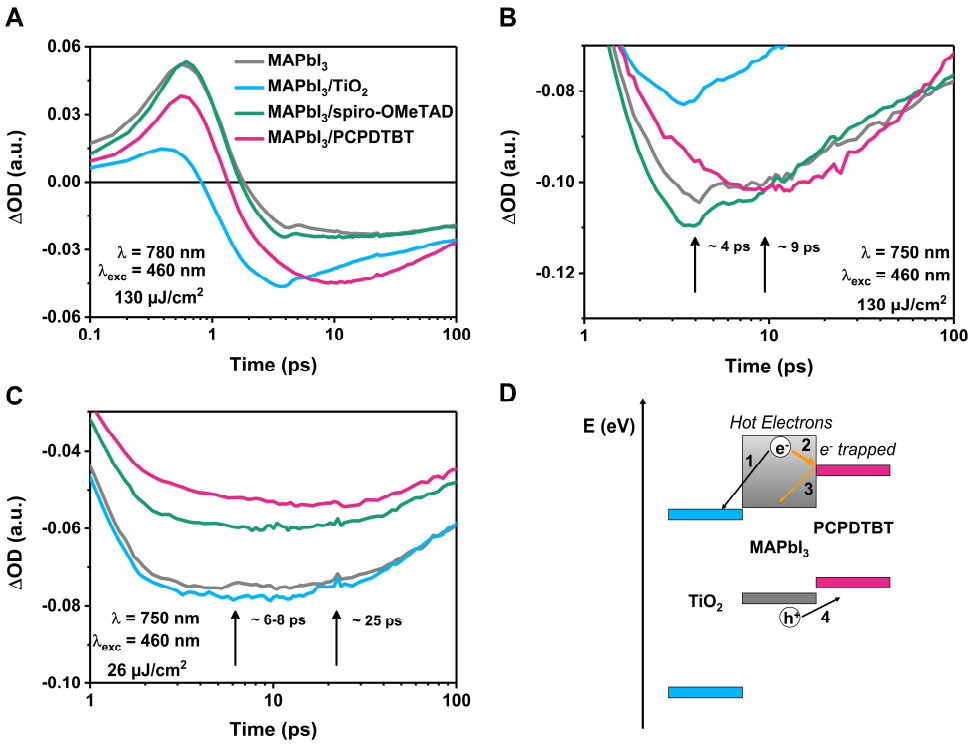

Figure 4.23. Kinetic traces obtained for $MAPbI_3$ (grey), $TiO_2/MAPbI_3$ (blue), $MAPbI_3$/spiro-OMeTAD (green), and $MAPbI_3$/PCPDTBT (pink) using λ_{exc} = 460 probing at 780 and a laser fluence of 130 μJ/cm^2 **(A)**. Kinetic traces probing at 750 nm and a laser fluence of 130 μJ/cm^2 **(B)** and a laser fluence of 26 μJ/cm^2 **(C)**. **(D)** Scheme showing the proposed mechanism. Hot electrons are either injected into TiO_2 (1) and/or PCPDTBT (2). The electrons injected into PCPDTBT are transferred back to $MAPbI_3$ (3). Additionally, there is the hole injection into the HTM (4).

The back transfer of electrons from the PCPDTBT to the $MAPbI_3$ layer was confirmed following the kinetics of the GSB correlated with VB_1 at 750 nm (**Figure 4.23.B**). The GSB maximum peaks at approximately 4 ps with $MAPbI_3$, $TiO_2/MAPbI_3$, and $MAPbI_3$/spiro-OMeTAD films. If the injected hot electrons into PCPDTBT are later back injected into $MAPbI_3$, the maximum of the GSB should be delayed to longer time delays. In fact, the maximum of the GSB is found at 9 ps, which confirmed our hypothesis (**Figure 4.23.B**). This behavior was also observed when using low pump fluences, where we found that the maximum of the GSB is delayed even more, reaching its maximum at around 25 ps, while for the rest of the samples it is found at 6-8 ps approximately

(**Figure 4.23.C**). The demonstrated hot electron injection competition and the subsequent back electron injection, summarize in **figure 4.23.D,** suppose a charge carrier loss pathway that affects to the final power conversion efficiency in complete devices.

4.5. Conclusions

In the first part of the chapter, we fabricated efficient perovskite solar cells using a series of semiconductor polymers with similar HOMO values and they have been compared to the standard spiro-OMeTAD. From the results, we conclude that there is no correlation between the HTM HOMO level and the final V_{OC} of the device. Also, from the measurement of the perovskite photoluminescence, spiro-OMeTAD presents the most efficient hole transfer, while PCPDTBT is the less efficient. Indeed, the photoluminescence quenching is directly correlated with the final efficiency of the perovskite solar cells.

From the DiffCap measurements, we find a clear shift in voltage between spiro-OMeTAD and the polymers that justify the V_{OC} obtained. This confirms the fact that V_{OC} is not dependent on the HOMO level of the HTM. In addition, we obtained the mobility values for all the HTM. Spiro-OMeTAD presents the best charge mobility values.

Then, in the second part of the chapter, using fsTA we have identified and analyzed the spectroscopic features associated with the $MAPbI_3$, as well as the charge carrier transfer processes happening at the interface $MAPbI_3$/HTM. We have found the spectroscopic signatures of the polarons in the HTM, which are formed after the injection of hole carriers into the HTM layer. Hole carrier injection into the organic HTM happens in the subpicosecond to 2 ps range, which is coincident with previous reports. Moreover, we have documented a new loss pathway for hot electrons which are close to the $MAPbI_3$/HTM interface. Instead of being transferred to TiO_2, they are injected into the low LUMO level organic semiconductor. The injection of hot electrons into the

HTM represents an unexpected carrier loss pathway, which has detrimental effects on complete devices, as it was demonstrated in the first part of the chapter.

In summary, for the future design of novel HTM for perovskite solar cells, high LUMO level should be considered to avoid these losses.

4.6. References

(1) Kim, Y.; Choulis, S. A.; Nelson, J.; Bradley, D. D. C.; Cook, S.; Durrant, J. R. Device Annealing Effect in Organic Solar Cells with Blends of Regioregular Poly(3-Hexylthiophene) and Soluble Fullerene. *Appl. Phys. Lett.* **2005**, *86* (6), 1–3. https://doi.org/10.1063/1.1861123.

(2) Liao, S. H.; Jhuo, H. J.; Cheng, Y. S.; Chen, S. A. Fullerene Derivative-Doped Zinc Oxide Nanofilm as the Cathode of Inverted Polymer Solar Cells with Low-Bandgap Polymer (PTB7-Th) for High Performance. *Adv. Mater.* **2013**, *25* (34), 4766–4771. https://doi.org/10.1002/adma.201301476.

(3) Li, G.; Zhu, R.; Yang, Y. Polymer Solar Cells. *Nat. Photonics* **2012**, *6* (3), 153–161. https://doi.org/10.1038/nphoton.2012.11.

(4) Kojima, A.; Teshima, K.; Shirai, Y.; Miyasaka, T. Organometal Halide Perovskites as Visible-Light Sensitizers for Photovoltaic Cells. *J. Am. Chem. Soc.* **2009**, *131* (17), 6050–6051. https://doi.org/10.1021/ja809598r.

(5) Rodríguez-Seco, C.; Cabau, L.; Vidal-Ferran, A.; Palomares, E. Advances in the Synthesis of Small Molecules as Hole Transport Materials for Lead Halide Perovskite Solar Cells. *Acc. Chem. Res.* **2018**, *51* (4), 869–880. https://doi.org/10.1021/acs.accounts.7b00597.

(6) Salim, T.; Sun, S.; Abe, Y.; Krishna, A.; Grimsdale, A. C.; Lam, Y. M. Perovskite-Based Solar Cells: Impact of Morphology and Device Architecture on Device Performance. *J. Mater. Chem. A* **2015**, *3* (17), 8943–8969. https://doi.org/10.1039/C4TA05226A.

(7) Hou, Y.; Zhang, H.; Chen, W.; Chen, S.; Quiroz, C. O. R.; Azimi, H.; Osvet, A.; Matt, G. J.; Zeira, E.; Seuring, J.; et al. Inverted, Environmentally Stable Perovskite Solar Cell with a Novel Low-Cost and Water-Free PEDOT Hole-Extraction Layer. *Adv. Energy Mater.* **2015**, *5* (15), 1500543. https://doi.org/10.1002/aenm.201500543.

(8) Johnston, M. B.; Herz, L. M. Hybrid Perovskites for Photovoltaics: Charge-Carrier Recombination, Diffusion, and Radiative Efficiencies. *Acc. Chem. Res.* **2016**, *49* (1), 146–154. https://doi.org/10.1021/acs.accounts.5b00411.

(9) Stranks, S. D.; Eperon, G. E.; Grancini, G.; Menelaou, C.; Alcocer, M. J. P.; Leijtens, T.; Herz, L. M.; Petrozza, A.; Snaith, H. J. Electron-Hole Diffusion Lengths Exceeding 1 Micrometer in an Organometal Trihalide Perovskite Absorber. *Science* **2013**, *342* (6156), 341–344. https://doi.org/10.1126/science.1243982.

(10) Xing, G.; Mathews, N.; Sun, S.; Lim, S. S.; Lam, Y. M.; Gratzel, M.; Mhaisalkar, S.; Sum, T. C. Long-Range Balanced Electron- and Hole-Transport Lengths in Organic-Inorganic $CH_3NH_3PbI_3$. *Science* **2013**, *342* (6156), 344–347. https://doi.org/10.1126/science.1243167.

(11) Manser, J. S.; Kamat, P. V. Band Filling with Free Charge Carriers in Organometal Halide Perovskites. *Nat. Photonics* **2014**, *8* (9), 737–743. https://doi.org/10.1038/nphoton.2014.171.

(12) Price, M. B.; Butkus, J.; Jellicoe, T. C.; Sadhanala, A.; Briane, A.; Halpert, J. E.; Broch, K.; Hodgkiss, J. M.; Friend, R. H.; Deschler, F. Hot-Carrier Cooling and Photoinduced Refractive Index Changes in Organic–Inorganic Lead Halide Perovskites. *Nat. Commun.* **2015**, *6* (1), 8420. https://doi.org/10.1038/ncomms9420.

(13) Marchioro, A.; Teuscher, J.; Friedrich, D.; Kunst, M.; Van De Krol, R.; Moehl, T.; Grätzel, M.; Moser, J.-E. E. Unravelling the Mechanism of Photoinduced Charge Transfer Processes in Lead Iodide Perovskite Solar Cells. *Nat. Photonics* **2014**, *8* (3), 250–255. https://doi.org/10.1038/nphoton.2013.374.

(14) Yang, Y.; Yang, M.; Moore, D. T.; Yan, Y.; Miller, E. M.; Zhu, K.; Beard, M. C. Top and Bottom Surfaces Limit Carrier Lifetime in Lead Iodide Perovskite Films. *Nat. Energy* **2017**, *2* (2), 16207. https://doi.org/10.1038/nenergy.2016.207.

(15) Zhu, X. Y.; Podzorov, V. Charge Carriers in Hybrid Organic-Inorganic Lead Halide Perovskites Might Be Protected as Large Polarons. *J. Phys. Chem. Lett.* **2015**, *6* (23), 4758–4761. https://doi.org/10.1021/acs.jpclett.5b02462.

(16) Zhu, H.; Miyata, K.; Fu, Y.; Wang, J.; Joshi, P. P.; Niesner, D.; Williams, K. W.; Jin, S.; Zhu, X. Y. Screening in Crystalline Liquids Protects Energetic Carriers in Hybrid Perovskites. *Science* **2016**, *353* (6306), 1409–1413. https://doi.org/10.1126/science.aaf9570.

(17) Miyata, K.; Meggiolaro, D.; Tuan Trinh, M.; Joshi, P. P.; Mosconi, E.; Jones, S. C.; De Angelis, F.; Zhu, X. Y. Large Polarons in Lead Halide Perovskites. *Sci. Adv.* **2017**, *3* (8), e1701217. https://doi.org/10.1126/sciadv.1701217.

(18) Fu, J.; Xu, Q.; Han, G.; Wu, B.; Huan, C. H. A.; Leek, M. L.; Sum, T. C. Hot Carrier Cooling Mechanisms in Halide Perovskites. *Nat. Commun.* **2017**, *8* (1), 1300. https://doi.org/10.1038/s41467-017-01360-3.

(19) Guo, Z.; Wan, Y.; Yang, M.; Snaider, J.; Zhu, K.; Huang, L. Long-Range Hot-Carrier Transport in Hybrid Perovskites Visualized by Ultrafast Microscopy. *Science* **2017**, *356* (6333), 59–62.

https://doi.org/10.1126/science.aam7744.

(20) Piatkowski, P.; Cohen, B.; Ponseca, C. S.; Salado, M.; Kazim, S.; Ahmad, S.; Sundström, V.; Douhal, A. Unraveling Charge Carriers Generation, Diffusion, and Recombination in Formamidinium Lead Triiodide Perovskite Polycrystalline Thin Film. *J. Phys. Chem. Lett.* **2016**, *7* (1), 204–210. https://doi.org/10.1021/acs.jpclett.5b02648.

(21) Wu, X.; Tan, L. Z.; Shen, X.; Hu, T.; Miyata, K.; Tuan Trinh, M.; Li, R.; Coffee, R.; Liu, S.; Egger, D. A.; et al. Light-Induced Picosecond Rotational Disordering of the Inorganic Sublattice in Hybrid Perovskites. *Sci. Adv.* **2017**, *3* (7), e1602388. https://doi.org/10.1126/sciadv.1602388.

(22) Stolterfoht, M.; Caprioglio, P.; Wolff, C. M.; Márquez, J. A.; Nordmann, J.; Zhang, S.; Rothhardt, D.; Hörmann, U.; Amir, Y.; Redinger, A.; et al. The Impact of Energy Alignment and Interfacial Recombination on the Internal and External Open-Circuit Voltage of Perovskite Solar Cells. *Energy Environ. Sci.* **2019**, *12* (9), 2778–2788. https://doi.org/10.1039/C9EE02020A.

(23) Wheeler, S.; Bryant, D.; Troughton, J.; Kirchartz, T.; Watson, T.; Nelson, J.; Durrant, J. R. Transient Optoelectronic Analysis of the Impact of Material Energetics and Recombination Kinetics on the Open-Circuit Voltage of Hybrid Perovskite Solar Cells. *J. Phys. Chem. C* **2017**, *121* (25), 13496–13506. https://doi.org/10.1021/acs.jpcc.7b02411.

(24) Jiménez-López, J.; Cambarau, W.; Cabau, L.; Palomares, E. Charge Injection, Carriers Recombination and HOMO Energy Level Relationship in Perovskite Solar Cells. *Sci. Rep.* **2017**, *7* (1), 6101. https://doi.org/10.1038/s41598-017-06245-5.

(25) Contreras-Bernal, L.; Salado, M.; Todinova, A.; Calio, L.; Ahmad, S.; Idígoras, J.; Anta, J. A. Origin and Whereabouts of Recombination in Perovskite Solar Cells. *J. Phys. Chem. C* **2017**, *121* (18), 9705–9713. https://doi.org/10.1021/acs.jpcc.7b01206.

(26) Gelmetti, I.; Montcada, N. F.; Pérez-Rodríguez, A.; Barrena, E.; Ocal, C.; García-Benito, I.; Molina-Ontoria, A.; Martín, N.; Vidal-Ferran, A.; Palomares, E. Energy Alignment and Recombination in Perovskite Solar Cells: Weighted Influence on the Open Circuit Voltage. *Energy Environ. Sci.* **2019**, *12* (4), 1309–1316. https://doi.org/10.1039/C9EE00528E.

(27) Correa-Baena, J. P.; Tress, W.; Domanski, K.; Anaraki, E. H.; Turren-Cruz, S. H.; Roose, B.; Boix, P. P.; Grätzel, M.; Saliba, M.; Abate, A.; et al. Identifying and Suppressing Interfacial Recombination to Achieve High Open-Circuit Voltage in Perovskite Solar Cells. *Energy Environ. Sci.*

2017, *10* (5), 1207–1212. https://doi.org/10.1039/c7ee00421d.

(28) Yoo, S.-M.; Yoon, S. J.; Anta, J. A.; Lee, H. J.; Boix, P. P.; Mora-Seró, I. An Equivalent Circuit for Perovskite Solar Cell Bridging Sensitized to Thin Film Architectures. *Joule* **2019**, 1–15. https://doi.org/10.1016/j.joule.2019.07.014.

(29) Guo, X.; McCleese, C.; Kolodziej, C.; Samia, A. C. S.; Zhao, Y.; Burda, C. Identification and Characterization of the Intermediate Phase in Hybrid Organic–Inorganic $MAPbI_3$ Perovskite. *Dalt. Trans.* **2016**, *45* (9), 3806–3813. https://doi.org/10.1039/C5DT04420K.

(30) Kim, H.-S.; Park, N.-G. Parameters Affecting I – V Hysteresis of $CH_3NH_3PbI_3$ Perovskite Solar Cells: Effects of Perovskite Crystal Size and Mesoporous TiO_2 Layer. *J. Phys. Chem. Lett.* **2014**, *5* (17), 2927–2934. https://doi.org/10.1021/jz501392m.

(31) Tress, W.; Marinova, N.; Moehl, T.; Zakeeruddin, S. M.; Nazeeruddin, M. K.; Grätzel, M. Understanding the Rate-Dependent J–V Hysteresis, Slow Time Component, and Aging in $CH_3NH_3PbI_3$ Perovskite Solar Cells: The Role of a Compensated Electric Field. *Energy Environ. Sci.* **2015**, *8* (3), 995–1004. https://doi.org/10.1039/C4EE03664F.

(32) Belisle, R. A.; Nguyen, W. H.; Bowring, A. R.; Calado, P.; Li, X.; Irvine, S. J. C.; McGehee, M. D.; Barnes, P. R. F.; O'Regan, B. C. Interpretation of Inverted Photocurrent Transients in Organic Lead Halide Perovskite Solar Cells: Proof of the Field Screening by Mobile Ions and Determination of the Space Charge Layer Widths. *Energy Environ. Sci.* **2017**, *10* (1), 192–204. https://doi.org/10.1039/C6EE02914K.

(33) Moia, D.; Gelmetti, I.; Calado, P.; Fisher, W.; Stringer, M.; Game, O.; Hu, Y.; Docampo, P.; Lidzey, D.; Palomares, E.; et al. Ionic-to-Electronic Current Amplification in Hybrid Perovskite Solar Cells: Ionically Gated Transistor-Interface Circuit Model Explains Hysteresis and Impedance of Mixed Conducting Devices. *Energy Environ. Sci.* **2019**, *12* (4), 1296–1308. https://doi.org/10.1039/C8EE02362J.

(34) Jung, E. H.; Jeon, N. J.; Park, E. Y.; Moon, C. S.; Shin, T. J.; Yang, T.-Y.; Noh, J. H.; Seo, J. Efficient, Stable and Scalable Perovskite Solar Cells Using Poly(3-Hexylthiophene). *Nature* **2019**, *567* (7749), 511–515. https://doi.org/10.1038/s41586-019-1036-3.

(35) Nia, N. Y.; Matteocci, F.; Cina, L.; Di Carlo, A. High-Efficiency Perovskite Solar Cell Based on Poly(3-Hexylthiophene): Influence of Molecular Weight and Mesoscopic Scaffold Layer. *ChemSusChem* **2017**, *10* (19), 3854–3860. https://doi.org/10.1002/cssc.201700635.

(36) Yaghoobi Nia, N.; Méndez, M.; di Carlo, A.; Palomares, E. Energetic

Disorder in Perovskite/Polymer Solar Cells and Its Relationship with the Interfacial Carrier Losses. *Philos. Trans. R. Soc. A Math. Phys. Eng. Sci.* **2019**, *377* (2152), 20180315. https://doi.org/10.1098/rsta.2018.0315.

(37) Heo, J. H.; Im, S. H.; Noh, J. H.; Mandal, T. N.; Lim, C.-S.; Chang, J. A.; Lee, Y. H.; Kim, H.; Sarkar, A.; Nazeeruddin, M. K.; et al. Efficient Inorganic–Organic Hybrid Heterojunction Solar Cells Containing Perovskite Compound and Polymeric Hole Conductors. *Nat. Photonics* **2013**, *7* (6), 486–491. https://doi.org/10.1038/nphoton.2013.80.

(38) Koster, L. J. A.; Mihailetchi, V. D.; Xie, H.; Blom, P. W. M. Origin of the Light Intensity Dependence of the Short-Circuit Current of Polymer/Fullerene Solar Cells. *Appl. Phys. Lett.* **2005**, *87* (20), 203502. https://doi.org/10.1063/1.2130396.

(39) Wetzelaer, G.-J. A. H.; Scheepers, M.; Sempere, A. M.; Momblona, C.; Ávila, J.; Bolink, H. J. Trap-Assisted Non-Radiative Recombination in Organic-Inorganic Perovskite Solar Cells. *Adv. Mater.* **2015**, *27* (11), 1837–1841. https://doi.org/10.1002/adma.201405372.

(40) Kim, H. Do; Ohkita, H.; Benten, H.; Ito, S. Photovoltaic Performance of Perovskite Solar Cells with Different Grain Sizes. *Adv. Mater.* **2016**, *28* (5), 917–922. https://doi.org/10.1002/adma.201504144.

(41) Bi, D.; Yi, C.; Luo, J.; Décoppet, J. D.; Zhang, F.; Zakeeruddin, S. M.; Li, X.; Hagfeldt, A.; Grätzel, M. Polymer-Templated Nucleation and Crystal Growth of Perovskite Films for Solar Cells with Efficiency Greater than 21%. *Nat. Energy* **2016**, *1* (10), 1–5. https://doi.org/10.1038/nenergy.2016.142.

(42) Jang, I.-H.; Yoo, P. J.; Park, N.-G.; Kim, D.; Son, D.-Y.; Choi, Y. J.; Lee, S.; Shin, H.; Lee, J.-W.; Ahn, N.; et al. Self-Formed Grain Boundary Healing Layer for Highly Efficient $CH_3NH_3PbI_3$ Perovskite Solar Cells. *Nat. Energy* **2016**, *1* (7), 1–8. https://doi.org/10.1038/nenergy.2016.81.

(43) Guerrero, A.; Montcada, N. F.; Ajuria, J.; Etxebarria, I.; Pacios, R.; Garcia-Belmonte, G.; Palomares, E. Charge Carrier Transport and Contact Selectivity Limit the Operation of PTB7-Based Organic Solar Cells of Varying Active Layer Thickness. *J. Mater. Chem. A* **2013**, *1* (39), 12345–12354. https://doi.org/10.1039/c3ta12358h.

(44) Barnes, P. R. F.; Miettunen, K.; Li, X.; Anderson, A. Y.; Bessho, T.; Gratzel, M.; O'Regan, B. C. Interpretation of Optoelectronic Transient and Charge Extraction Measurements in Dye-Sensitized Solar Cells. *Adv. Mater.* **2013**, *25* (13), 1881–1922. https://doi.org/10.1002/adma.201201372.

(45) Maurano, A.; Shuttle, C. G.; Hamilton, R.; Ballantyne, A. M.; Nelson, J.;

Zhang, W.; Heeney, M.; Durrant, J. R. Transient Optoelectronic Analysis of Charge Carrier Losses in a Selenophene/Fullerene Blend Solar Cell. *J. Phys. Chem. C* **2011**, *115* (13), 5947–5957. https://doi.org/10.1021/jp109697w.

(46) Montcada, N. F.; Méndez, M.; Cho, K. T.; Nazeeruddin, M. K.; Palomares, E. Photo-Induced Dynamic Processes in Perovskite Solar Cells: The Influence of Perovskite Composition in the Charge Extraction and the Carrier Recombination. *Nanoscale* **2018**, *10* (13), 6155–6158. https://doi.org/10.1039/C8NR00180D.

(47) O'Regan, B. C.; Barnes, P. R. F. F.; Li, X.; Law, C.; Palomares, E.; Marin-Beloqui, J. M. Optoelectronic Studies of Methylammonium Lead Iodide Perovskite Solar Cells with Mesoporous TiO_2: Separation of Electronic and Chemical Charge Storage, Understanding Two Recombination Lifetimes, and the Evolution of Band Offsets during J – V Hy. *J. Am. Chem. Soc.* **2015**, *137* (15), 5087–5099. https://doi.org/10.1021/jacs.5b00761.

(48) Montcada, N. F.; Marín-Beloqui, J. M.; Cambarau, W.; Jiménez-López, J.; Cabau, L.; Cho, K. T.; Nazeeruddin, M. K.; Palomares, E. Analysis of Photoinduced Carrier Recombination Kinetics in Flat and Mesoporous Lead Perovskite Solar Cells. *ACS Energy Lett.* **2017**, *2* (1), 182–187. https://doi.org/10.1021/acsenergylett.6b00600.

(49) Wang, F.; Shimazaki, A.; Yang, F.; Kanahashi, K.; Matsuki, K.; Miyauchi, Y.; Takenobu, T.; Wakamiya, A.; Murata, Y.; Matsuda, K. Highly Efficient and Stable Perovskite Solar Cells by Interfacial Engineering Using Solution-Processed Polymer Layer. *J. Phys. Chem. C* **2017**, *121* (3), 1562–1568. https://doi.org/10.1021/acs.jpcc.6b12137.

(50) Wright, M.; Uddin, A. Organic-Inorganic Hybrid Solar Cells: A Comparative Review. *Sol. Energy Mater. Sol. Cells* **2012**, *107*, 87–111. https://doi.org/10.1016/j.solmat.2012.07.006.

(51) Kiermasch, D.; Baumann, A.; Fischer, M.; Dyakonov, V.; Tvingstedt, K. Revisiting Lifetimes from Transient Electrical Characterization of Thin Film Solar Cells; a Capacitive Concern Evaluated for Silicon, Organic and Perovskite Devices. *Energy Environ. Sci.* **2018**, *11* (3), 629–640. https://doi.org/10.1039/C7EE03155F.

(52) Kiermasch, D.; Gil-Escrig, L.; Baumann, A.; Bolink, H. J.; Dyakonov, V.; Tvingstedt, K. Unravelling Steady-State Bulk Recombination Dynamics in Thick Efficient Vacuum-Deposited Perovskite Solar Cells by Transient Methods. *J. Mater. Chem. A* **2019**, *7* (24), 14712–14722. https://doi.org/10.1039/c9ta04367e.

(53) Kirchartz, T. Influence of Diffusion on Space-Charge-Limited Current Measurements in Organic Semiconductors. *Beilstein J. Nanotechnol.* **2013**, *4* (1), 180–188. https://doi.org/10.3762/bjnano.4.18.

(54) Snaith, H. J.; Grätzel, M. Enhanced Charge Mobility in a Molecular Hole Transporter via Addition of Redox Inactive Ionic Dopant: Implication to Dye-Sensitized Solar Cells. *Appl. Phys. Lett.* **2006**, *89* (26), 262114. https://doi.org/10.1063/1.2424552.

(55) Chiguvare, Z.; Dyakonov, V. Trap-Limited Hole Mobility in Semiconducting Poly(3-Hexylthiophene). *Phys. Rev. B* **2004**, *70* (23), 235207. https://doi.org/10.1103/PhysRevB.70.235207.

(56) Liang, Y.; Xu, Z.; Xia, J.; Tsai, S.-T.; Wu, Y.; Li, G.; Ray, C.; Yu, L. For the Bright Future-Bulk Heterojunction Polymer Solar Cells with Power Conversion Efficiency of 7.4%. *Adv. Mater.* **2010**, *22* (20), E135–E138. https://doi.org/10.1002/adma.200903528.

(57) Sum, T. C.; Mathews, N.; Xing, G.; Lim, S. S.; Chong, W. K.; Giovanni, D.; Dewi, H. A. Spectral Features and Charge Dynamics of Lead Halide Perovskites: Origins and Interpretations. *Acc. Chem. Res.* **2016**, *49* (2), 294–302. https://doi.org/10.1021/acs.accounts.5b00433.

(58) Piatkowski, P.; Cohen, B.; Javier Ramos, F.; Di Nunzio, M.; Nazeeruddin, M. K.; Grätzel, M.; Ahmad, S.; Douhal, A. Direct Monitoring of Ultrafast Electron and Hole Dynamics in Perovskite Solar Cells. *Phys. Chem. Chem. Phys.* **2015**, *17* (22), 14674–14684. https://doi.org/10.1039/c5cp01119a.

(59) Leguy, A. M. A. A.; Azarhoosh, P.; Alonso, M. I.; Campoy-Quiles, M.; Weber, O. J.; Yao, J.; Bryant, D.; Weller, M. T.; Nelson, J.; Walsh, A.; et al. Experimental and Theoretical Optical Properties of Methylammonium Lead Halide Perovskites. *Nanoscale* **2016**, *8* (12), 6317–6327. https://doi.org/10.1039/C5NR05435D.

(60) Davies, C. L.; Filip, M. R.; Patel, J. B.; Crothers, T. W.; Verdi, C.; Wright, A. D.; Milot, R. L.; Giustino, F.; Johnston, M. B.; Herz, L. M. Bimolecular Recombination in Methylammonium Lead Triiodide Perovskite Is an Inverse Absorption Process. *Nat. Commun.* **2018**, *9* (1), 293. https://doi.org/10.1038/s41467-017-02670-2.

(61) Even, J.; Pedesseau, L.; Katan, C. Analysis of Multivalley and Multibandgap Absorption and Enhancement of Free Carriers Related to Exciton Screening in Hybrid Perovskites. *J. Phys. Chem. C* **2014**, *118* (22), 11566–11572. https://doi.org/10.1021/jp503337a.

(62) Li, M.; Fu, J.; Xu, Q.; Sum, T. C. Slow Hot-Carrier Cooling in Halide Perovskites: Prospects for Hot-Carrier Solar Cells. *Adv. Mater.* **2018**,

1802486, 1–17. https://doi.org/10.1002/adma.201802486.

(63) Li, M.; Bhaumik, S.; Goh, T. W.; Kumar, M. S.; Yantara, N.; Grätzel, M.; Mhaisalkar, S.; Mathews, N.; Sum, T. C. Slow Cooling and Highly Efficient Extraction of Hot Carriers in Colloidal Perovskite Nanocrystals. *Nat. Commun.* **2017**, *8* (May), 14350. https://doi.org/10.1038/ncomms15299.

(64) Brauer, J. C.; Lee, Y. H.; Nazeeruddin, M. K.; Banerji, N. Ultrafast Charge Carrier Dynamics in $CH_3NH_3PbI_3$: Evidence for Hot Hole Injection into Spiro-OMeTAD. *J. Mater. Chem. C* **2016**, *4* (25), 5922–5931. https://doi.org/10.1039/C6TC00763E.

(65) Brauer, J. C.; Lee, Y. H.; Nazeeruddin, M. K.; Banerji, N. Charge Transfer Dynamics from Organometal Halide Perovskite to Polymeric Hole Transport Materials in Hybrid Solar Cells. *J. Phys. Chem. Lett.* **2015**, *6* (18), 3675–3681. https://doi.org/10.1021/acs.jpclett.5b01698.

(66) Trinh, M. T.; Wu, X.; Niesner, D.; Zhu, X. Y. Many-Body Interactions in Photo-Excited Lead Iodide Perovskite. *J. Mater. Chem. A* **2015**, *3* (17), 9285–9290. https://doi.org/10.1039/c5ta01093d.

(67) Sharma, R.; Lee, H.; Gupta, V.; Kim, H.; Kumar, M.; Sharma, C.; Chand, S.; Yoo, S.; Gupta, D. Photo-Physics of PTB7, PCBM and ICBA Based Ternary Solar Cells. *Org. Electron.* **2016**, *34*, 111–117. https://doi.org/10.1016/j.orgel.2016.04.022.

(68) Ogata, Y.; Kawaguchi, D.; Tanaka, K. An Effect of Molecular Motion on Carrier Formation in a Poly(3-Hexylthiophene) Film. *Sci. Rep.* **2015**, *5* (1), 8436. https://doi.org/10.1038/srep08436.

(69) Grancini, G.; Maiuri, M.; Fazzi, D.; Petrozza, A.; Egelhaaf, H. J.; Brida, D.; Cerullo, G.; Lanzani, G. Hot Exciton Dissociation in Polymer Solar Cells. *Nat. Mater.* **2013**, *12* (1), 29–33. https://doi.org/10.1038/nmat3502.

(70) Ryu, S.; Noh, J. H.; Jeon, N. J.; Chan Kim, Y.; Yang, W. S.; Seo, J.; Seok, S. Il. Voltage Output of Efficient Perovskite Solar Cells with High Open-Circuit Voltage and Fill Factor. *Energy Environ. Sci.* **2014**, *7* (8), 2614–2618. https://doi.org/10.1039/c4ee00762j.

(71) Polander, L. E.; Pahner, P.; Schwarze, M.; Saalfrank, M.; Koerner, C.; Leo, K. Hole-Transport Material Variation in Fully Vacuum Deposited Perovskite Solar Cells. *APL Mater.* **2014**, *2* (8), 81503. https://doi.org/10.1063/1.4889843.

(72) Droseros, N.; Dänekamp, B.; Tsokkou, D.; Boix, P. P.; Banerji, N. Charge Injection and Trapping at Perovskite Interfaces with Organic Hole Transporting Materials of Different Ionization Energies. *APL Mater.* **2019**, *7* (4), 041115. https://doi.org/10.1063/1.5086692.

Chapter 5

Charge carrier interfacial processes at the perovskite/electron transporting material interface

CHAPTER 5: CHARGE CARRIER INTERFACIAL PROCESSES AT THE PEROVSKITE/ELECTRON TRANSPORTING MATERIAL INTERFACE..... 143

5.1. Abstract 147

5.2. Introduction 147

5.3 Device Fabrication 148

5.4 Results and discussion 149
5.4.1 Hysteresis reduction 149
5.4.2. Trap passivation and charge carrier recombination 153
5.4.3. Ionic influences on charge carrier recombination 159
5.4.4. Charge carrier injection 161

5.5. Conclusions 168

5.6. References 169

5.1. Abstract

In **Chapter 5**, we will get a better understanding of the carrier processes happening at the interface perovskite/electron transporting material (ETM). For this purpose, we introduce C_{60}-fullerene (C_{60}) at the interface between TiO_2 and methyl ammonium lead iodide perovskite ($MAPbI_3$). Using fullerenes and their molecular derivatives assists the reduction of the current-voltage hysteresis and correlates with the interfacial carrier injection and the recombination processes that limit the power conversion efficiency of working devices.

Here, we thoroughly study the processes at different timescales, ranging from femtoseconds to seconds, and we observed that C_{60} influences on carrier lifetime, injection, and recombination. C_{60} has been capable of extracting hot carriers generated at the early stages after the photoexcitation, which makes C_{60} a suitable material for hot carrier solar cells.

5.2. Introduction

In Perovskite Solar Cells (PSCs), the right selection of n-type and p-type selective contacts, which result in a fast and efficient extraction of charge carriers, and reduce their recombination, is key to get better efficiencies. For this reason, the effects of the selective contacts over the processes that govern the PSCs solar cell efficiency have been extensively studied[1–7].

Many inorganic wide band gap semiconductors have been tested as n-type selective contacts (TiO_2, SnO_2, ZnO, $BaSnO_3$, etc)[8,9]. Among them, TiO_2 is the most used in highly efficient PSCs[7,10,11], while SnO_2 has been described in the most efficient PSCs to date[12]. With n-type organic semiconductors, the choice is concentrated in fullerene (C_{60}) and its molecular derivatives, like $PC_{61}BM$, $PC_{71}BM$, C_{60}-SAM (Self-Assembled Monolayer)[13–16]. They have been implemented either as Electron Transporting Material (ETM) in most cases covering the perovskite layer in the p-i-n architecture[15,17,18], or as an interfacial

modification between the inorganic n-type semiconductor and the perovskite layer in n-i-p architectures[19,20]. Fullerenes have shown not only electron transporting properties but also passivation effects on perovskite. First, using C_{60} and its derivatives reduce the trap density at the perovskite surface and at the grain boundaries, which, in turn, decreases the interface carrier recombination[17,21]. Second, fullerenes inhibit ion diffusion along the grain boundaries, which were described as the main ion migration channel under applied bias[18]. Hence, with fullerenes as ETM, the current-voltage hysteresis in PSCs is reduced[17].

In this Chapter, we prepared PSCs with and without a C_{60} interfacial modification layer (30 nm) between either compact or mesoporous TiO_2 and methyl ammonium iodide ($MAPbI_3$) perovskite. Rather than $PC_{61}BM$ and other fullerene derivatives that have a cascading energy level alignment when implemented between $MAPbI_3$ and TiO_2[18,20,22], we select C_{60} whose lowest unoccupied molecular orbital (LUMO) lies below the conduction band (CB) level of TiO_2. With this molecule there are no moieties increasing the disorder[3,14], and there are not anchoring groups influencing the interaction between C_{60} and TiO_2[20,22]. We observed a great reduction of the hysteresis in devices modified with C_{60} that is associated with an excellent electron transfer, despite the energy level misalignment, confirmed by differential capacitance measurements. Furthermore, we investigated the fast electron injection of photogenerated charge carriers using femtosecond transient absorption spectroscopy.

5.3 Device Fabrication

In this case, we used a n-i-p perovskite architecture in which the different layers are FTO/ETM/$MAPbI_3$/spiro-OMeTAD/Au, where ETM stands for compact TiO_2 ($cTiO_2$), mesoporous TiO_2 ($mTiO_2$), $cTiO_2/C_{60}$, or $mTiO_2/C_{60}$. In $mTiO_2$ devices prior to the mesoporous layer, a compact TiO_2

layer was also deposited. $cTiO_2$ and $mTiO_2$ layers were deposited following the protocol explained in **chapter 3.1.2**. Additionally, these layers were modified with a 30 nm thick layer of C_{60}, deposited using thermal evaporation, with a deposition rate of 0.2 Å/s.

$MAPbI_3$ was the perovskite composition employed. It was prepared using the two-step deposition protocol, as explained in **chapter 3.1.3**. Then, spiro-OMeTAD was the HTM employed and Au the metal contact.

In the case of the films prepared for femtosecond transient absorption spectroscopy (fsTA), we used the following architecture Glass/ETM/$MAPbI_3$. The perovskite layer was prepared using a 0.7 M PbI_2 solution in DMF/DMSO (90/10, vol%); 80 µl were deposited at 4000 rpm with 2000 rpm/s for 90 s. 100 µl of MAI solution (100 mg/ml in IPA) were deposited 30 s before the end of the spinning process. The samples were annealed at 100 ºC for 45 minutes. Finally, the films were encapsulated in a N_2-filled glovebox to avoid degradation with Meltonix 1170-60PF (Solaronix) and a cover slide on top of it.

5.4 Results and discussion

5.4.1 Hysteresis reduction

In this chapter, we will study the influences of C_{60} on both $cTiO_2$ and $mTiO_2$. The high-quality of the $MAPbI_3$ films on top of the ETM layer can be observed from the cross-section ESEM images that show full coverage and homogeneous layers along solar cell (**Figure 5.1**).

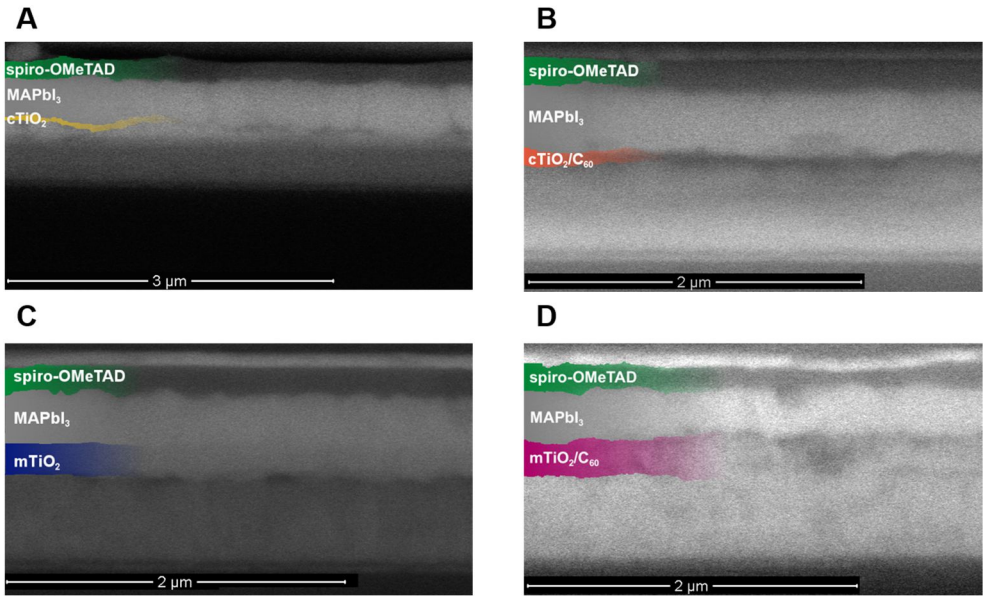

Figure 5.1. ESEM images of the four different architectures employed in this study **(A)** $cTiO_2$, **(B)** $cTiO_2/C_{60}$, **(C)** $mTiO_2$, and **(D)** $mTiO_2/C_{60}$.

First, current-voltage characteristics were obtained for these devices (**Figure 5.2**, **Figure 5.3**, and **Table 5.1**). From the analysis of the JV curves, it appears evident that the use of a C_{60} layer effectively reduces the hysteresis observed in the TiO_2 based devices. In **Figure 5.2**, the shadowed area indicates the difference between both scan directions, giving an idea of how hysteresis is reduced. Additionally, when C_{60} is employed, a better reproducibility of the results is obtained (**Figure 5.3**).

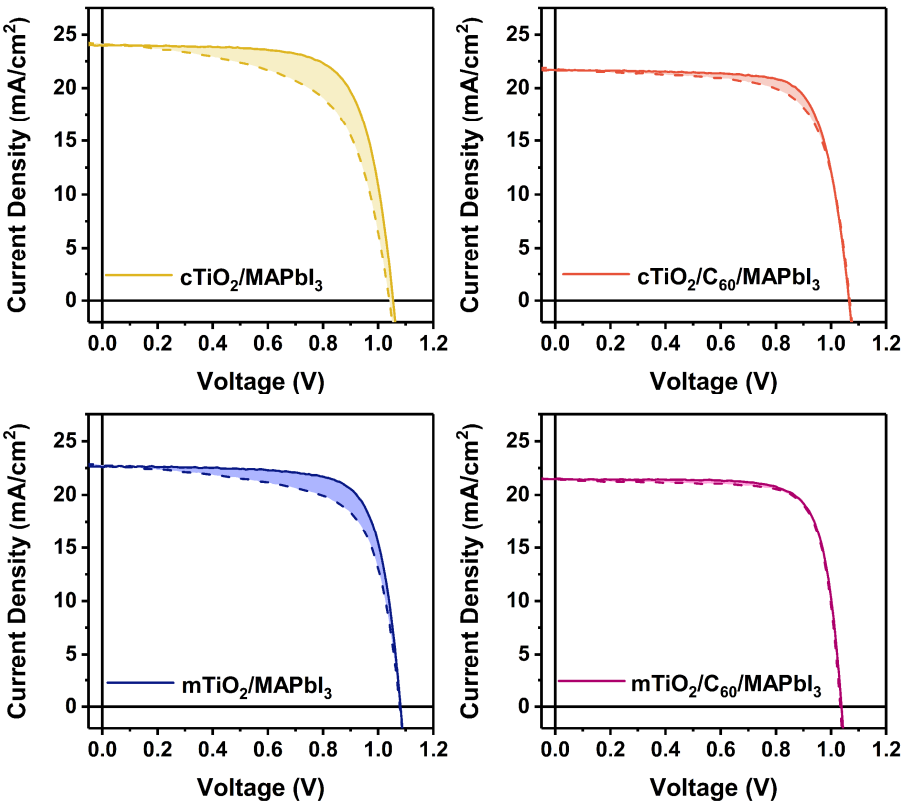

Figure 5.2. JV curves of the champion devices of the four different types of devices under study. Both forward (dashed lines) and reverse (solid lines) were measured under 1 Sun conditions (100 mW/cm^2, AM 1.5G) with a scan rate of 40 mV/s. The shadowed area shows the degree of hysteresis in every device.

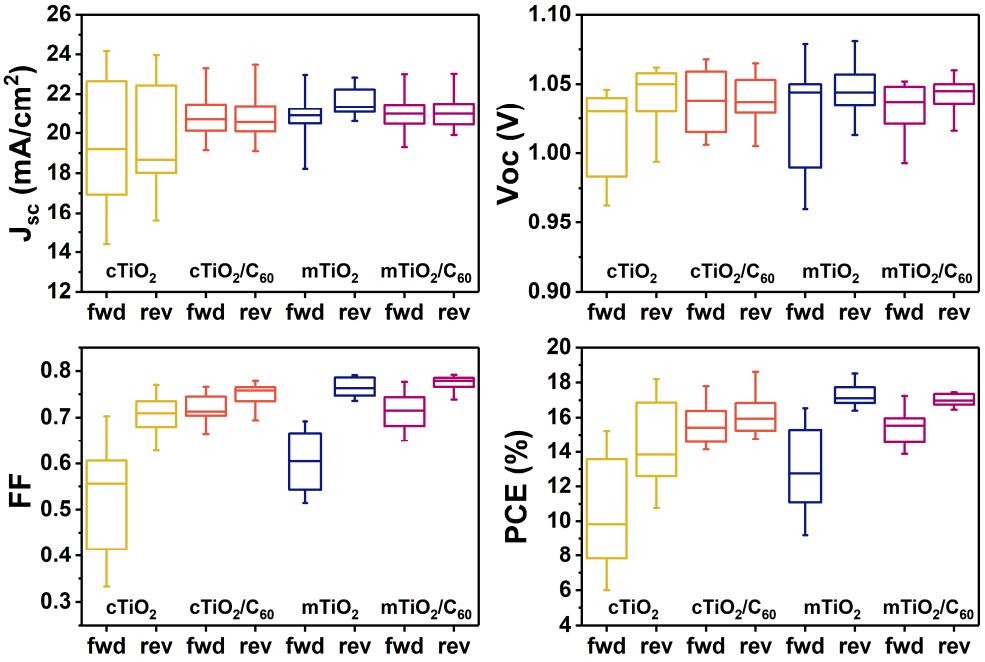

Figure 5.3. Photovoltaic parameters derived from the JV measurement in both forward and reverse conditions. All JV curves were measured under 1 Sun conditions (100 mW/cm^2, AM 1.5G) with a scan rate of 40 mV/s.

Table 5.1. Summary of the photovoltaic parameters obtained from the JV measurement under 1 Sun conditions. The given values are the mean and the standard deviations obtained for the different set of devices.

ETM	Sweep	J_{SC} (mA/cm^2)	V_{OC} (V)	FF	PCE (%)
cTiO$_2$	Fwd	19.3 ± 3.0	1.016 ± 0.029	0.53 ± 0.12	10.4 ± 3.1
	Rev	19.3 ± 2.6	1.041 ± 0.024	0.71 ± 0.04	14.3 ± 2.3
cTiO$_2$/C$_{60}$	Fwd	20.8 ± 1.1	1.037 ± 0.021	0.72 ± 0.03	15.5 ± 1.1
	Rev	20.7 ± 1.1	1.038 ± 0.018	0.75 ± 0.02	16.2 ± 1.1
mTiO$_2$	Fwd	20.8 ± 1.3	1.025 ± 0.041	0.60 ± 0.07	13.0 ± 2.3
	Rev	21.5 ± 0.7	1.048 ± 0.020	0.77 ± 0.02	17.3 ± 0.6
mTiO$_2$/C$_{60}$	Fwd	21.0 ± 0.9	1.034 ± 0.017	0.71 ± 0.04	15.5 ± 0.9
	Rev	21.1 ± 0.8	1.042 ± 0.011	0.77 ± 0.02	17.0 ± 0.3

The effect of fullerenes on perovskite solar cells has been extensively studied[3,13,23,24], focusing on which properties make fullerenes reduce the hysteresis observed in this kind of devices. Hysteresis has been linked to the presence of the mobile ions in the perovskite[25,26]. On the other side, fullerenes have been suggested to passivate trap states at the grain boundaries of the thin film perovskite[13,19], which are correlated with iodine vacancies at the grain boundaries[18,27]. Therefore, it seems that hysteresis in the devices studied is suppressed via the passivation of defects at the grain boundaries of the perovskite solar cell[13,18,19]. Fullerenes can diffuse along the bulk of the perovskite and reach the defects at the grain boundaries, where they will "block" the ionic movement[18]. However, they do not diffuse easily, but an annealing step will improve their diffusion kinetics[13]. As we deposit the C_{60} layer prior to the perovskite deposition, the annealing of the perovskite layer (100 ºC, 45 min) will also enhance the diffusion of C_{60}.

5.4.2. Trap passivation and charge carrier recombination

Even though the LUMO level of C_{60} is energetically below the CB of $MAPbI_3$, we still observe improved charge transfer into the TiO_2, and, in turn, an effectively reduced hysteresis in devices containing a thin C_{60} layer. In order to analyze the passivation effects when C_{60} is deposited on top of the TiO_2 layer, we made use of optoelectronic transient techniques, such as transient photovoltage (TPV), transient photocurrent (TPC), and differential capacitance (DiffCap)[28–31]. These techniques, as already explained in **Chapter 3**, give information about carrier energetics and carrier recombination kinetics.

All of them are based on the application of a small perturbation in voltage (ΔV) by means of a laser pulse that generates extra charge carriers (ΔQ). Keeping the device at open circuit conditions (TPV) the extra carriers generated by the laser pulse are forced to recombine with an associated lifetime ($\tau_{\Delta n}$). At short circuit conditions (TPC) the extra carriers are extracted before

they recombine. We obtain values at different V_{OC} measuring with different light intensities.

DiffCap is a combination of TPV and TPC that enables the calculation of the device capacitance at different V_{OC} values. We combine ΔQ, which is independent of the V_{OC}, and ΔV, the small perturbation in voltage created by the laser pulse at every V_{OC} (**Equation 5.1**).

$$C(V) = \frac{\Delta Q}{\Delta V} \qquad (5.1)$$

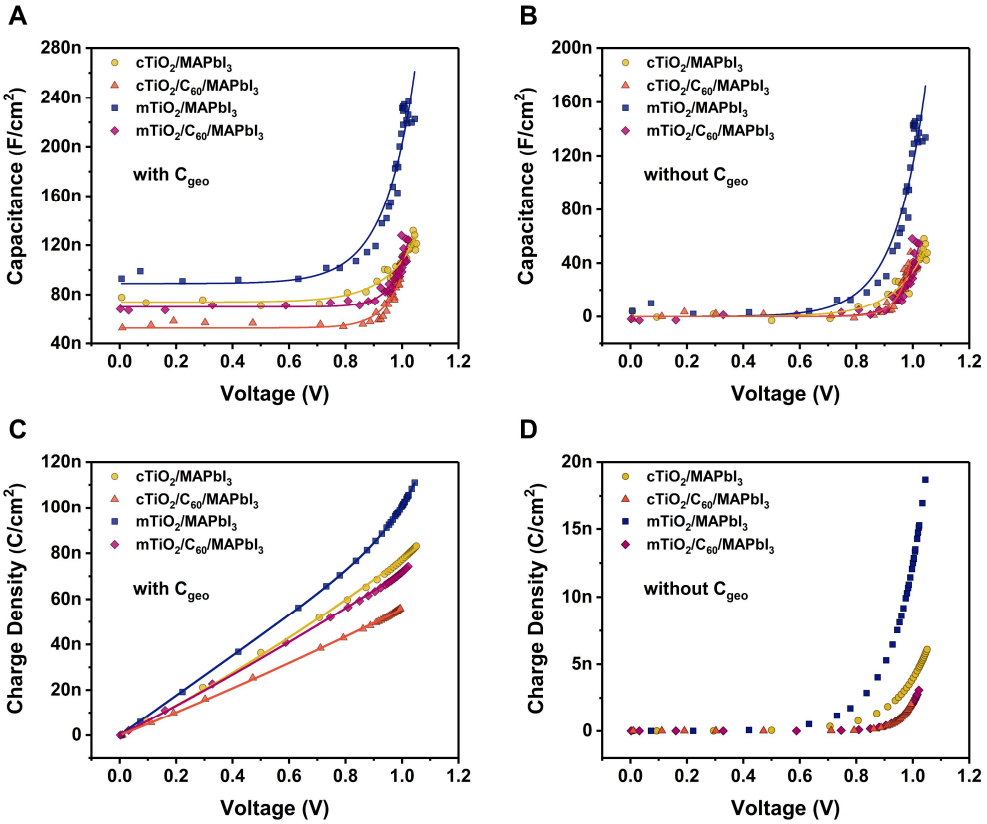

Figure 5.4. **(A)** DiffCap plotted as a function of the applied light bias. **(B)** DiffCap after subtracting C_{geo} (charge stored at the contacts). **(C)** Total charge density at different V_{OC} values, including charge in the bulk and the contacts. **(D)** Charge density in the perovskite bulk.

Figure 5.4.A shows the results obtained from the DiffCap at different light biases. Two regimes are observed in the DiffCap plots. First, a constant

part which is directly linked to the geometric capacitance (C_{geo}), that is, the charge stored in the electrodes[29–31]. C_{geo} depends on the electrical permittivity (ε), the area of the capacitor (a), and the thickness (d), $C_{geo} = \varepsilon\, a/d$. **Figure 5.4** underlines that devices containing a thin layer of C_{60} are linked to smaller capacitances. This is attributed to the difference in ε, as $\varepsilon(TiO_2) > \varepsilon(C_{60})$[32,33]. The larger specific surface area of mesoporous TiO_2 based devices ensure a larger capacitance compared to the planar TiO_2 based devices. The second regime, the exponential part, is correlated with the chemical capacitance of the perovskite layer, charge stored in the active layer as the photoinduced *quasi*-Fermi level splitting approaches to its valence band and conduction band edges[26,31].

The exponential part has also been linked to carrier accumulation in energetic states at the interface between perovskite and the selective contacts[30]. **Figure 5.4.B** shows the capacitance of the device after the subtraction of C_{geo}, which give us a direct estimation of the capacitance in the bulk of the perovskite. Then, it is possible to estimate the total charge density (Q) stored in the device upon the integration of the differential capacitance (**Equation 5.2**)

$$Q(V_{oc}) = \int C \, dV \qquad (5.2)$$

In **Figure 5.4.C**, the total charge density in the device is shown. It clearly reveals the influence of C_{geo} over the total charge density. Recently, it was suggested that the release of the carriers associated with C_{geo} may affect the interpretation of the data obtained from TPV[34,35]. Thus, we subtracted C_{geo} to compare the charge carriers, which are stored in the perovskite bulk, with their recombination kinetics. Charge density in **Figure 5.4.D** is fitted to **Equation 5.3**[36]**.**

$$Q = Q_0 \left(\exp \left(\frac{q V_{oc}}{m K_B T} \right) - 1 \right) \qquad (5.3)$$

Where Q_0 is the equilibrium charge density and m is the deviation from the thermal voltage (K_BT/q). In **Figure 5.4.D**, we compare the charge stored in the bulk of the perovskite. A very important characteristic is the voltage at which the exponential part of the plot is discernable. These differences account for changes in carriers stored in sub-bandgap tail states[30], which are been commonly referred as shallow trap states in perovskite solar cells. Such energy shifts can also be assigned to the energetic alignment differences between the materials when contacted with the perovskite[3]. As aforementioned, fullerenes passivate traps at the grain boundaries of the perovskite bulk[13,19]. Thus, we have a direct evidence for this effect from the observation of the exponential part of the charge density at much higher voltages when C_{60} layers are present. We correlate this shift to the carriers stored in the sub-bandgap states, normally associated with defects at the grain boundaries, which are the main ion migration channel[18,27].

In the next step, we compared carrier recombination in these devices. For this purpose, we used the small perturbation lifetime ($\tau_{\Delta n}$) obtained from the exponential fitting of the TPV decays. $\tau_{\Delta n}$ depends exponentially on the V_{OC} obtained under different light conditions (**Equation 5.4**).

$$\tau_{\Delta n} = \tau_{\Delta n_0} \exp \left(- \frac{q V_{oc}}{\theta K_B T} \right) \qquad (5.4)$$

In **Equation 5.4** $\tau_{\Delta n0}$ is the equilibrium carrier lifetime and θ is the deviation from the thermal voltage. The results are shown in **Figure 5.5.**

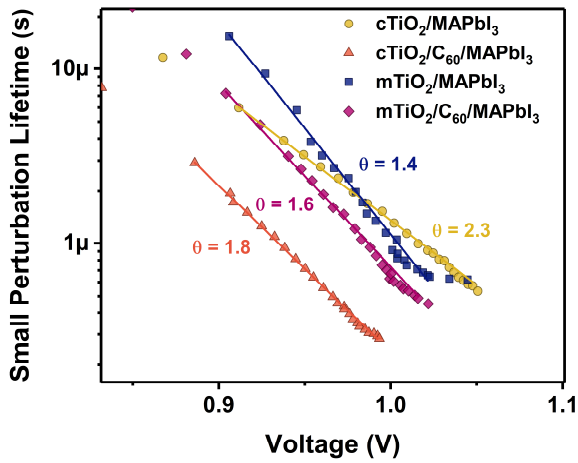

Figure 5.5. Small perturbation lifetime from TPV experiments as a function of the light bias. The lines relates to the exponential fit from **Equation 5.4.**

From **Figure 5.5**, we observed that faster $\tau_{\Delta n}$ are obtained around 1 Sun when C_{60} is present, that will be correlated with faster carrier recombination. Although we obtained valuable information from this plot, same voltages lead to different charge densities, therefore, it is better to compare $\tau_{\Delta n}$ as a function of the charge density. In order to perform a fair comparison of bulk carrier recombination, we compared the values of lifetime around 1 Sun, where the exponential part in **Figure 5.4** was visible. At low light intensities, were C_{geo} is predominant, the small perturbation is affected by a capacitive component due to the release of charge stored in the contacts[34,35]. In order to avoid the effect of the capacitive component, we compared the small perturbation lifetime obtained from the TPV as a function of the charge density without C_{geo} (**Figure 5.6.A**). **Figure 5.6.B** shows the comparison including C_{geo}.

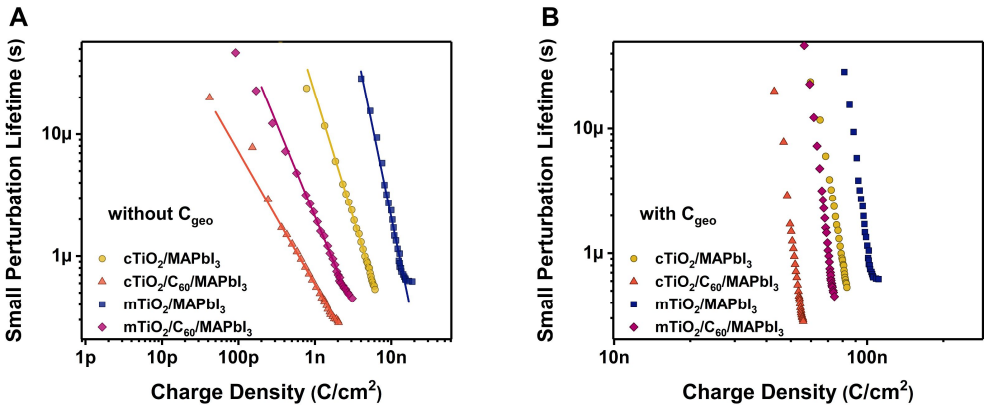

Figure 5.6. Small perturbation lifetime from TPV measurements as a function of the charge density in the devices after subtracting C_{geo} **(A)** and including C_{geo} **(B)**.

Figure 5.6.A is fitted to a power law dependence (**Equation 5.5**) with a slope, λ, which is correlated with the recombination order, δ, via $\delta = \lambda + 1$ [37]. From **Figure 5.6.A** we conclude that C_{60} reduces the recombination order: $\delta(cTiO_2) = 3.0$; $\delta(cTiO_2/C_{60}) = 2.1$; $\delta(mTiO_2) = 4.0$; $\delta(mTiO_2/C_{60}) = 2.5$.

$$\tau_{\Delta n} = \tau_{\Delta n_0} \left(\frac{Q}{Q_0}\right)^{-\lambda} \qquad (5.5)$$

Finally, the small perturbation lifetime is converted to the total carrier lifetime or pseudo-first order lifetime of total excess charge carriers (τ) via $\tau = \tau_{\Delta n}\delta$ [37]. Independently of the lifetime, the fitting to obtain the recombination order remains unchanged (**Figure 5.7**).

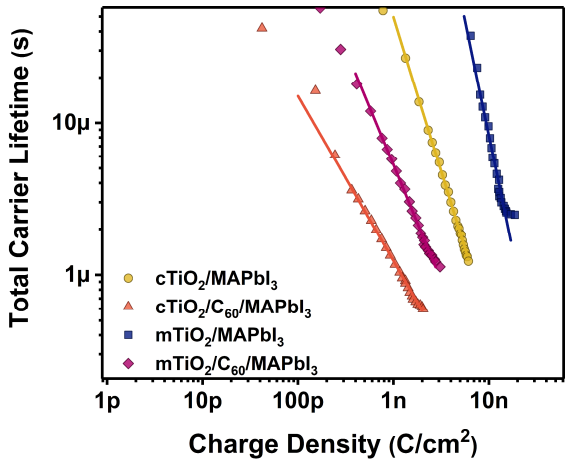

Figure 5.7. Carrier lifetime obtained from the TPV measurements as a function of the charge density based on the DiffCap method. The lines show the power law fitting used (**equation 5.5**) to estimate the recombination order.

5.4.3. Ionic influences on charge carrier recombination

Next, we turned to the study of the impact of the ionic process on the solar cells. Mobile ions are one of the most important factors that govern hysteresis in PSCs[25,26]. JV curves on **Figure 5.2** show that devices containing a C_{60} interfacial layer on top of the TiO_2 present reduced hysteresis, which suggest that C_{60} may have an influence over ionic motion. To confirm our hypothesis, we use a derivation of TPV, namely "transient of the transient photovoltage" (TROTTR)[38,39] which has been explained in **Chapter 3.3.2**. With this technique, we measure TPV decays before a stable V_{OC} is reached. PSCs with a n-i-p architecture usually present long V_{OC} stabilization times (**Figure 5.8**) due to the rearrangement of the ionic profile[40,41]. A model, which will be described in depth in **Chapter 6**, have been suggested by different authors to understand the influence of the mobile ions on the PSCs properties[25,40–44].

First, in dark conditions, a built-in voltage (V_{bi}) is generated to compensate the differences in the Fermi level of the contacts. An internal electric field is created and drives ions to the interfaces. Once at the interfaces, the internal electric field is canceled in the perovskite layer, but creates an ionic

charged layer at the interfaces. Once illuminated, the *quasi*-Fermi levels split, responsible of the V_{OC} observed. Subsequently, ions start to redistribute in order to cancel the photogenerated electric field. However, they do it slowly, so ions will remain at the interfaces for some time and the initial electric field will persist, forcing photogenerated carriers into the opposite direction of extraction, which will increase recombination at the interfaces, and, thus, lower V_{OC} values. Once ions redistribute and cancel the internal electric field, a stable V_{OC} is obtained.

In agreement with the model, we observed a slow V_{OC} stabilization in the case of TiO_2-based devices. On the other hand, an almost instant stabilization is observed when C_{60} is deposited on top of the TiO_2 suggesting that ionic motion is blocked (**Figure 5.8**).

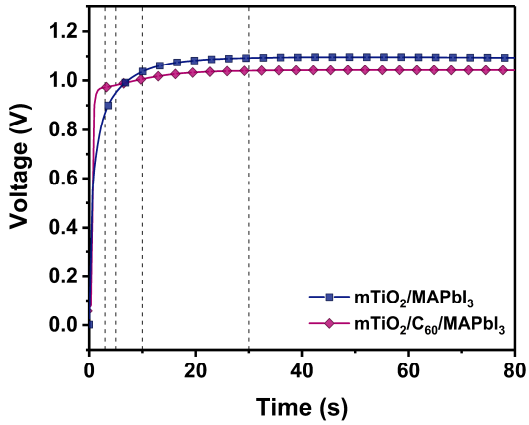

Figure 5.8. V_{OC} stabilization times for $mTiO_2/MAPbI_3$ and $mTiO_2/C_{60}/MAPbI_3$ devices. The dashed vertical lines indicate the times at which TPV transients were acquired in **Figure 5.9**.

To evaluate how the ionic motion influences carrier recombination, we measured TPV at the early stages of V_{OC} stabilization. TPV decays were measured after 3, 5, 10, and 30 s of light irradiation (dashed lines in **Figure 5.8**).

In **Figure 5.9** we show the results of TPV measurements after different illumination times, for $mTiO_2$ and $mTiO_2/C_{60}$ devices. A negative transient

deflection appears at early illumination times in TiO_2 based devices (**Figure 5.9.A**). This negative transient deflection is correlated with a higher degree of recombination due to carrier accumulation at the wrong interface based on the fact that ions remain at the interfaces. Yet, this is not the case with $mTiO_2/C_{60}$ devices (**Figure 5.9.B**) where no negative transient deflection is detected. We conclude that ionic motion is reduced through the action of C_{60} which passivates defects at the grain boundaries, reducing the main ion migration channels.

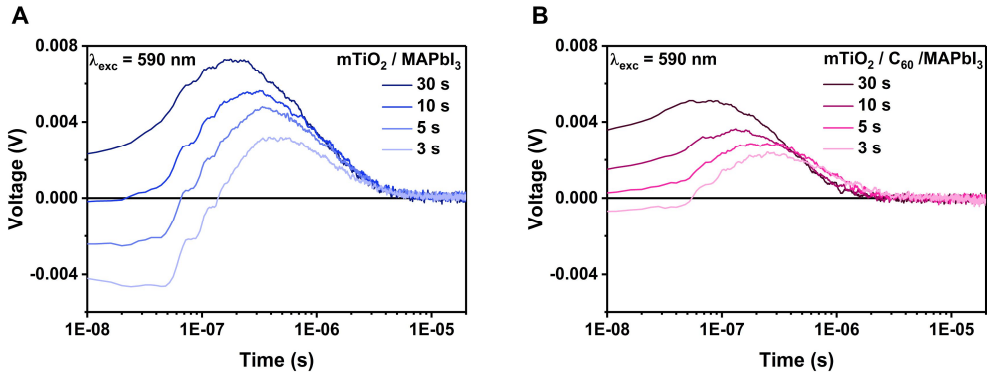

Figure 5.9. TPV transients measured after 3, 5, 10, and 30 s of illumination at 1 Sun conditions for $mTiO_2/MAPbI_3$ **(A)** and $mTiO_2/C_{60}/MAPbI_3$ **(B)** using a laser excitation wavelength of 590 nm.

5.4.4. Charge carrier injection

In this last section, we use femtosecond transient absorption spectroscopy (fsTA) to investigate the effects of C_{60} as interfacial layer at the $MAPbI_3$/ETM interface over the photogenerated charge carriers at the very early times. Several reports suggest that polycrystalline PCBM reduces the energy disorder compared to amorphous PCBM, and, additionally, more discrete states are potentially available for hot carrier extraction[3,45]. The properties and harvesting of hot carriers have been widely studied using spectroscopic techniques, as their extraction could greatly improve the final power conversion efficiency in devices[46–48].

By means of fsTA we studied the improved electron extraction when a C_{60} layer is deposited between $MAPbI_3$ and TiO_2. The most common feature described in literature for the identification of hot carriers in perovskite samples is following the broadening of the perovskite ground state bleaching (GSB) at 750 nm towards higher wavelengths in the sub-ps timescale[46,49]. Additionally, the photo-induced absorption (PIA) peak observed at 780 nm has been associated with the presence of hot carriers in perovskites when using laser excitation wavelengths with excess energy[47]. The excess energy was obtained using high excitation energies (460 nm) to excite above the conduction band minimum, and high laser fluences to obtain high density of photogenerated charge carriers.

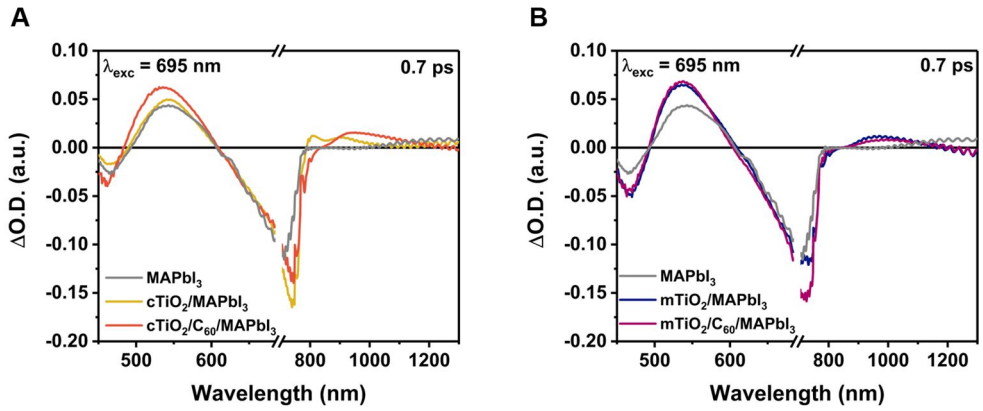

Figure 5.10. Differential absorption spectra at 0.7 ps of the different ETM/$MAPbI_3$ films with **(A)** $cTiO_2$ and $cTiO_2/C_{60}$; **(B)** $mTiO_2$ and $mTiO_2/C_{60}$ compared with the reference $MAPbI_3$ using λ_{exc} = 695 nm and a laser fluence of 64 μJ/cm^2.

The spectra obtained 0.7 ps after the photoexcitation with a 695 nm excitation wavelength (λ_{exc}) of the different ETM/$MAPbI_3$ films are shown in **Figure 5.10**. In $MAPbI_3$ reference films there is a PIA that peaks at 1200 nm is related to intraband transitions in the excited state[46,50]. Using λ_{exc} = 695 nm, the excess energy required for the generation of hot carriers is not accomplished and the corresponding signal at 780 nm is not observed[47]. In the case of $cTiO_2/MAPbI_3$ films (**Figure 5.10.A**), the signal associated with

electrons in the TiO_2 is observed as a PIA at 950 nm with its maximum after 0.7 ps [51]. This suggests a fast injection of a fraction of the electrons close to the interface. Contrary to the results obtained from $MAPbI_3$, $mTiO_2/MAPbI_3$, and as our previous work shown in **Chapter 4**, the PIA signal at 780 nm associated with hot carriers is observed in $cTiO_2/MAPbI_3$ films using λ_{exc} = 695 nm, which we attribute to charge carrier accumulation at the interface associated with a slow extraction of the remaining electrons. This peak at 780 nm is no longer observed when C_{60} is employed as interfacial layer, and, the signal of the electrons in the TiO_2 is even more noticeable. Similar features are observed in **Figure 5.10.B** for $mTiO_2/MAPbI_3$ and $mTiO_2/C_{60}/MAPbI_3$ films, with a pronounced signal of electrons in the TiO_2 (PIA in the NIR region), which reflects the better electron extraction properties of $mTiO_2$ compared to $cTiO_2$. The mesoporous layer creates a high surface area that gives a faster electron extraction. Additionally, no PIA is observed at 780 nm for $mTiO_2/MAPbI_3$ and $mTiO_2/C_{60}/MAPbI_3$ films. This confirms the better electron extraction and lack of carrier accumulation at the ETM/$MAPbI_3$ interface.

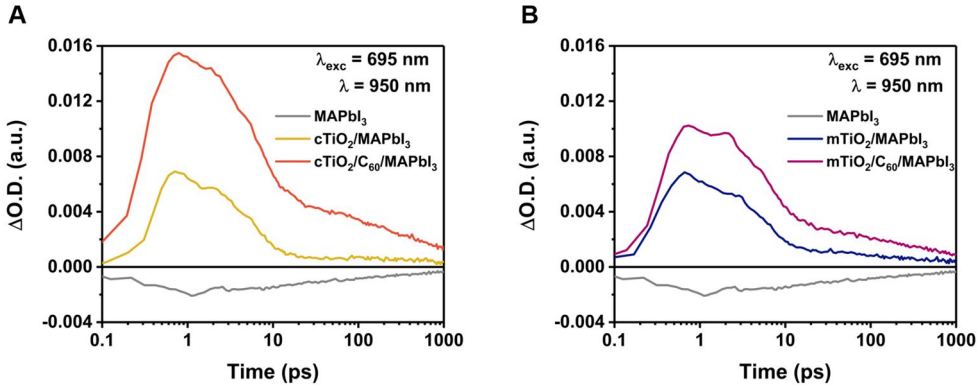

Figure 5.11. Kinetic traces probing at 950 nm of the different ETM/$MAPbI_3$ films with **(A)** $cTiO_2$ and $cTiO_2/C_{60}$ as well as **(B)** $mTiO_2$ and $mTiO_2/C_{60}$ compared with the reference $MAPbI_3$ using λ_{exc} = 695 nm and 64 μJ/cm^2 as laser fluence

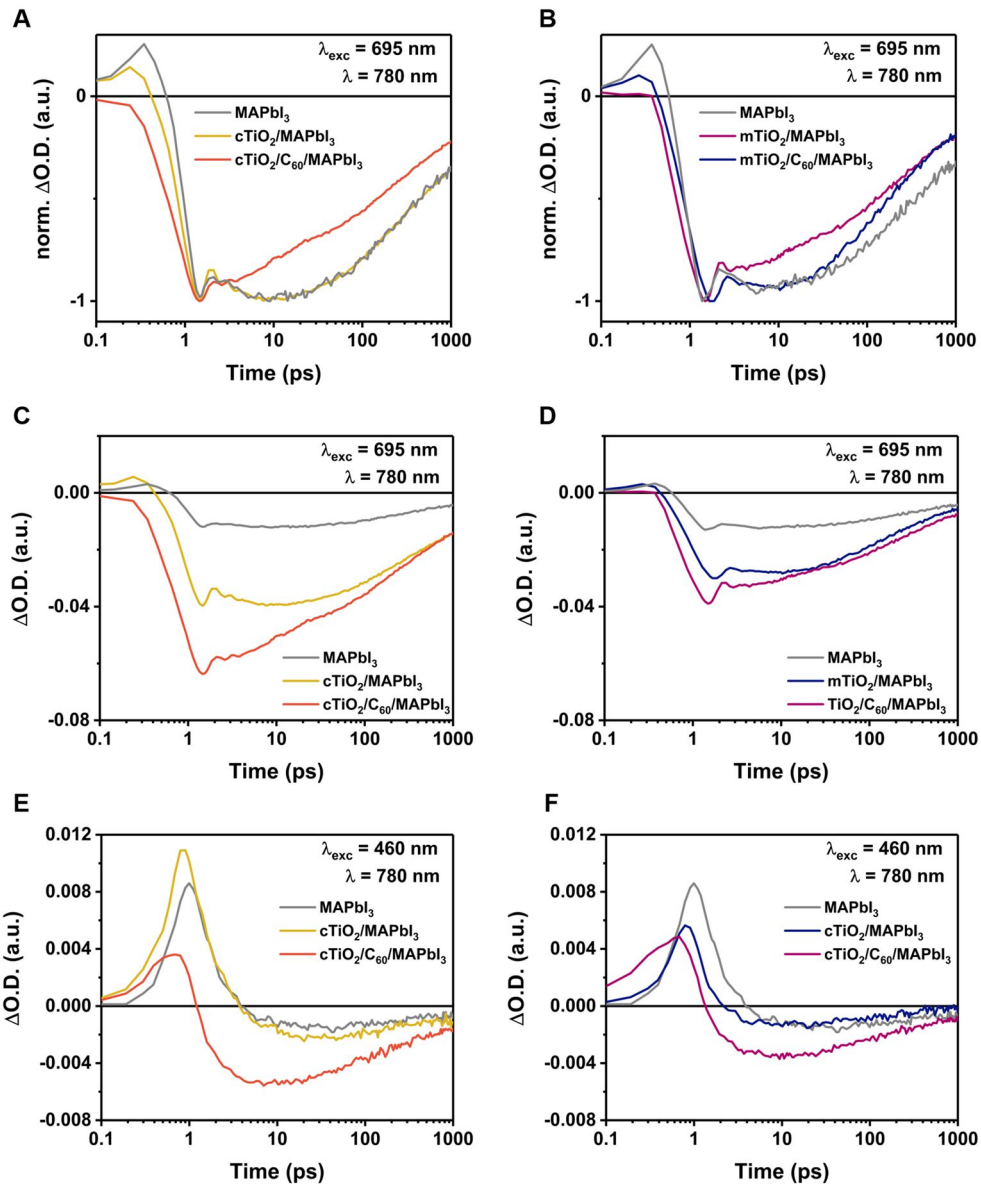

Figure 5.12. Normalized kinetic traces probing at 780 nm **(A, B)** and as-measured kinetic traces probing at 780 nm **(C-F)** of the different ETM/$MAPbI_3$ films with **(A, C, E)** $cTiO_2/C_{60}$, as well as **(B, D, F)** $mTiO_2$, and $mTiO_2/C_{60}$ compared with the reference $MAPbI_3$ using λ_{exc} = 695 **(A-D)** and 460 nm **(E,F)** using a laser fluence of 64 μJ/cm^2.

In **Figure 5.11** and **Figure 5.12** we analyze the increased electron density when C_{60} is employed on top of TiO_2 following the kinetics at λ = 780 nm and 950 nm.

The kinetics at 950 nm (**Figure 5.11**) reveal two decays for all the TiO_2 based films. A fast decay is observed until a time delay of 10 ps which evolves in a slow decay that extends in all the time window. While $mTiO_2/MAPbI_3$ films show a pronounced signal in both regimes, the PIA of $cTiO_2/MAPbI_3$ films is already reduced to ~10 % of its maximum intensity after 10 ps. This behavior reflects the lower electron density in the compact TiO_2 layer compared to the mesoporous film. Also, the use of C_{60} as interlayer with either the compact or mesoporous layer increases drastically the intensity of the PIA at 950 nm, especially with the $cTiO_2/C_{60}/MAPbI_3$ film.

We followed studying the kinetics at the 780 nm PIA (**Figure 5.12**) to study the charge carriers close to the interface. Starting at 1 ps, there is a contribution of the band-edge population and an intensification of the GSB because of the Stark effect, spectral changes in the presence of an external electric field[52]. For clarity, we compared the normalized kinetics (**Figure 5.12.A,** and **Figure 5.12.B**, not-normalized kinetics are shown in **Figure 5.12.C** and **Figure 5.12.D**). There is a red shift in the GSB minimum compared to the absorption profile of the perovskite which is caused by the band gap renormalization associated with free charge carriers, which are the primary photogenerated species in perovskite[49,53]. These photogenerated species thermalize slowly, with a band gap build up population that peaks at 10 ps. In **Figure 5.12.A**, we observed that both the thermalization and the decay are almost the same for $MAPbI_3$ and $cTiO_2/MAPbI_3$ films. This suggests that most of the charge carriers remain in the perovskite rather than being injected into the $cTiO_2$ layer. Contrary to that, $mTiO_2/MAPbI_3$ (**Figure 5.12.B**) presents a faster GSB regeneration. The extracted electrons seem to cancel the band gap renormalization. Most important is the effect of C_{60} in both cases because we did not observe any band gap population build up; instead, the GSB immediately decays.

From the analysis of the fsTA we conclude that $cTiO_2$ forms an interface with the perovskite that is not sufficient for carrier extraction because of its small surface area that does not ensure a fair electron transfer in the early stages of photogeneration. Although a small fraction of the photogenerated carriers are transferred to the $cTiO_2$ layer, most of them remain trapped at the interface in band valleys which are caused by ionic accumulation. The introduction of a C_{60} interlayer induces, first, the passivation of trap states; and second, the improvement in electron extraction. Also, we prevent band bending with its use. From the kinetic analysis, we observed ultrafast charge transfer when C_{60} is present. This suggests that hot carrier extraction might be possible.

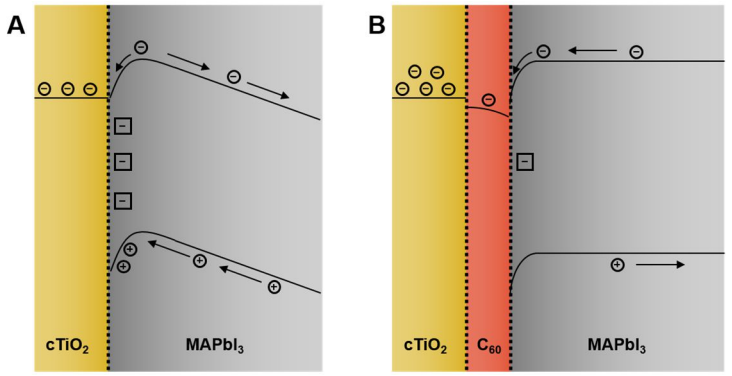

Scheme 5.1. Energy levels characteristics in the early stages of illumination. The presence of ions at the interface drives ions into the opposite direction of extraction **(A)**. The use of C_{60} layer mitigates this effect blocking ionic movement and improving carrier collection **(B)**.

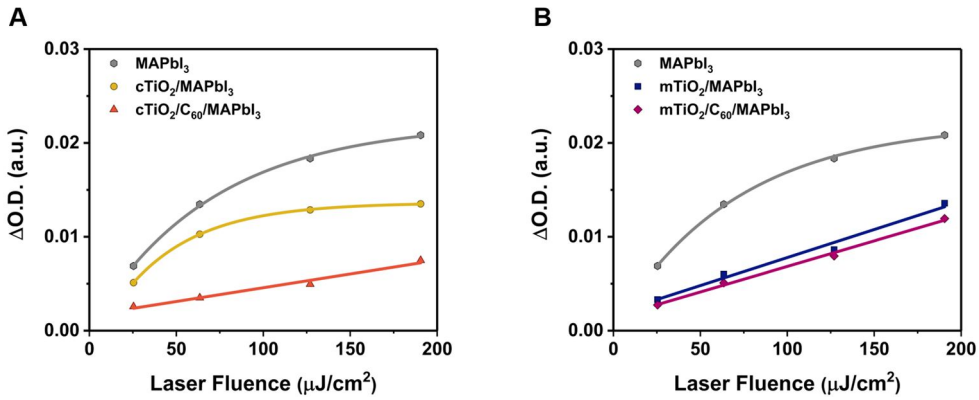

Figure 5.13. PIA intensity dependence probing at 780 nm and with λ_{exc} = 460 nm with the laser fluence ranging from 26 to 191 μJ/cm^2 which results in an exponential dependency for $MAPbI_3$ and $cTiO_2/MAPbI_3$ and linear dependency for $cTiO_2/C_{60}/MAPbI_3$ (**A**). The dependency is linear for $mTiO_2/MAPbI_3$ and $mTiO_2/C_{60}/MAPbI_3$ in (**B**).

In the last part of this Chapter, we explored the hot carrier extraction capabilities of the different ETM. To observe the presence of hot carriers, we excited the $MAPbI_3$ layer with λ_{exc} = 460 nm and laser fluences ranging between 26 and 191 μJ/cm^2 (**Figure 5.12.E, Figure 5.12.F** and **Figure 5.13**). This wavelength has the excess energy that is necessary to generate and observe the hot carriers. Similar to previous results, we observed the saturation at high laser fluence regimes of the PIA at 780 nm in the case of $MAPbI_3$ and $cTiO_2/MAPbI_3$ (**Figure 5.13**). This behavior is correlated with Pauli blocking effects, which means that the states associated with that transition are filled, thus, this transition is no longer available[54]. However, this situation was reversed when using $mTiO_2$ and/or C_{60} which results in a linear dependency with the laser fluence rather than the saturation observed before for $cTiO_2$. This make us to conclude that not only the electron extraction is enhanced with $mTiO_2$ and C_{60} but also hot electrons are harvested.

5.5. Conclusions

In this chapter we prepared and characterized efficient PSCs using a thin C_{60} interfacial layer between either compact or mesoporous TiO_2 and $MAPbI_3$. As a result, we decreased noticeably the hysteresis observed in the solar cells. Moreover, we carried out an in-depth analysis to understand which properties are making C_{60} reduce the hysteresis observed when implemented on top of the TiO_2 layer. This study expands from very slow kinetics (seconds), which is related with the ion migration within the perovskite layer to the nanosecond and microsecond timescale where the charge carrier recombination takes place. The measured kinetics fully agree with the proposed model on ionic redistribution following changes in internal electric fields upon illumination. Finally, using fsTA, we confirmed in the femtosecond to picosecond timescale the slow electron extraction in $cTiO_2$ films compared to the $mTiO_2$ or C_{60}, which causes carrier accumulation at the interfaces and subsequent band bending. Furthermore, we demonstrated the C_{60} capabilities for hot carrier extraction, which makes C_{60} a suitable prospect to be used in hot carrier solar cells to increase the final solar cell efficiency.

5.6. References

(1) Gelmetti, I.; Montcada, N. F.; Pérez-Rodríguez, A.; Barrena, E.; Ocal, C.; García-Benito, I.; Molina-Ontoria, A.; Martín, N.; Vidal-Ferran, A.; Palomares, E. Energy Alignment and Recombination in Perovskite Solar Cells: Weighted Influence on the Open Circuit Voltage. *Energy Environ. Sci.* **2019**, *12* (4), 1309–1316. https://doi.org/10.1039/C9EE00528E.

(2) Tao, C.; Van Der Velden, J.; Cabau, L.; Montcada, N. F.; Neutzner, S.; Srimath Kandada, A. R.; Marras, S.; Brambilla, L.; Tommasini, M.; Xu, W.; et al. Fully Solution-Processed n-i-p-Like Perovskite Solar Cells with Planar Junction: How the Charge Extracting Layer Determines the Open-Circuit Voltage. *Adv. Mater.* **2017**, *29* (15), 1604493. https://doi.org/10.1002/adma.201604493.

(3) Hou, Y.; Xie, C.; Radmilovic, V. V.; Puscher, B.; Wu, M.; Heumüller, T.; Karl, A.; Li, N.; Tang, X.; Meng, W.; et al. Assembling Mesoscale-Structured Organic Interfaces in Perovskite Photovoltaics. *Adv. Mater.* **2019**, *31* (8), 1806516. https://doi.org/10.1002/adma.201806516.

(4) Lee, M. M.; Teuscher, J.; Miyasaka, T.; Murakami, T. N.; Snaith, H. J. Efficient Hybrid Solar Cells Based on Meso-Superstructured Organometal Halide Perovskites. *Science* **2012**, *338* (6107), 643–647. https://doi.org/10.1126/science.1228604.

(5) Kim, H.-S.; Park, N.-G. Parameters Affecting I–V Hysteresis of $CH_3NH_3PbI_3$ Perovskite Solar Cells: Effects of Perovskite Crystal Size and Mesoporous TiO_2 Layer. *J. Phys. Chem. Lett.* **2014**, *5* (17), 2927–2934. https://doi.org/10.1021/jz501392m.

(6) Saliba, M.; Orlandi, S.; Matsui, T.; Aghazada, S.; Cavazzini, M.; Correa-Baena, J.-P.; Gao, P.; Scopelliti, R.; Mosconi, E.; Dahmen, K.-H.; et al. A Molecularly Engineered Hole-Transporting Material for Efficient Perovskite Solar Cells. *Nat. Energy* **2016**, *1* (2), 15017. https://doi.org/10.1038/nenergy.2015.17.

(7) Jung, E. H.; Jeon, N. J.; Park, E. Y.; Moon, C. S.; Shin, T. J.; Yang, T.-Y.; Noh, J. H.; Seo, J. Efficient, Stable and Scalable Perovskite Solar Cells Using Poly(3-Hexylthiophene). *Nature* **2019**, *567* (7749), 511–515. https://doi.org/10.1038/s41586-019-1036-3.

(8) Shin, S. S.; Lee, S. J.; Seok, S. Il. Metal Oxide Charge Transport Layers for Efficient and Stable Perovskite Solar Cells. *Adv. Funct. Mater.* **2019**, *1900455*, 1900455. https://doi.org/10.1002/adfm.201900455.

(9) Zhou, Y.; Li, X.; Lin, H. To Be Higher and Stronger—Metal Oxide Electron Transport Materials for Perovskite Solar Cells. *Small* **2019**, *1902579*, 1902579. https://doi.org/10.1002/smll.201902579.

(10) Saliba, M.; Matsui, T.; Seo, J.-Y.; Domanski, K.; Correa-Baena, J.-P.; Nazeeruddin, M. K.; Zakeeruddin, S. M.; Tress, W.; Abate, A.; Hagfeldt, A.; et al. Cesium-Containing Triple Cation Perovskite Solar Cells: Improved Stability, Reproducibility and High Efficiency. *Energy Environ. Sci.* **2016**, *9* (6), 1989–1997. https://doi.org/10.1039/C5EE03874J.

(11) Kogo, A.; Sanehira, Y.; Numata, Y.; Ikegami, M.; Miyasaka, T. Amorphous Metal Oxide Blocking Layers for Highly Efficient Low-Temperature Brookite TiO_2 -Based Perovskite Solar Cells. *ACS Appl. Mater. Interfaces* **2018**, *10* (3), 2224–2229. https://doi.org/10.1021/acsami.7b16662.

(12) Jiang, Q.; Zhao, Y.; Zhang, X.; Yang, X.; Chen, Y.; Chu, Z.; Ye, Q.; Li, X.; Yin, Z.; You, J. Surface Passivation of Perovskite Film for Efficient Solar Cells. *Nat. Photonics* **2019**. https://doi.org/10.1038/s41566-019-0398-2.

(13) Shao, Y.; Xiao, Z.; Bi, C.; Yuan, Y.; Huang, J. Origin and Elimination of Photocurrent Hysteresis by Fullerene Passivation in $CH_3NH_3PbI_3$ Planar Heterojunction Solar Cells. *Nat. Commun.* **2014**, *5* (1), 5784. https://doi.org/10.1038/ncomms6784.

(14) Shao, Y.; Yuan, Y.; Huang, J. Correlation of Energy Disorder and Open-Circuit Voltage in Hybrid Perovskite Solar Cells. *Nat. Energy* **2016**, *1* (1), 15001. https://doi.org/10.1038/nenergy.2015.1.

(15) Docampo, P.; Ball, J. M.; Darwich, M.; Eperon, G. E.; Snaith, H. J. Efficient Organometal Trihalide Perovskite Planar-Heterojunction Solar Cells on Flexible Polymer Substrates. *Nat. Commun.* **2013**, *4* (1), 2761. https://doi.org/10.1038/ncomms3761.

(16) Chiang, C.; Tseng, Z.; Wu, C. Planar Heterojunction Perovskite/$PC_{71}BM$ Solar Cells with Enhanced Open-Circuit Voltage via a (2/1)-Step Spin-Coating Process. *J. Mater. Chem. A* **2014**, *2* (38), 15897–15903. https://doi.org/10.1039/C4TA03674C.

(17) Wang, Q.; Shao, Y.; Dong, Q.; Xiao, Z.; Yuan, Y.; Huang, J. Large Fill-Factor Bilayer Iodine Perovskite Solar Cells Fabricated by a Low-Temperature Solution-Process. *Energy Environ. Sci.* **2014**, *7* (7), 2359–2365. https://doi.org/10.1039/C4EE00233D.

(18) Shao, Y.; Fang, Y.; Li, T.; Wang, Q.; Dong, Q.; Deng, Y.; Yuan, Y.; Wei, H.; Wang, M.; Gruverman, A.; et al. Grain Boundary Dominated Ion Migration in Polycrystalline Organic–Inorganic Halide Perovskite Films. *Energy Environ. Sci.* **2016**, *9* (5), 1752–1759. https://doi.org/10.1039/C6EE00413J.

(19) Xu, J.; Buin, A.; Ip, A. H.; Li, W.; Voznyy, O.; Comin, R.; Yuan, M.; Jeon,

S.; Ning, Z.; McDowell, J. J.; et al. Perovskite–Fullerene Hybrid Materials Suppress Hysteresis in Planar Diodes. *Nat. Commun.* **2015**, *6* (1), 7081. https://doi.org/10.1038/ncomms8081.

(20) Wojciechowski, K.; Stranks, S. D.; Abate, A.; Sadoughi, G.; Sadhanala, A.; Kopidakis, N.; Rumbles, G.; Li, C.-Z.; Friend, R. H.; Jen, A. K. Y.; et al. Heterojunction Modification for Highly Efficient Organic–Inorganic Perovskite Solar Cells. *ACS Nano* **2014**, *8* (12), 12701–12709. https://doi.org/10.1021/nn505723h.

(21) Shao, Y.; Xiao, Z.; Bi, C.; Yuan, Y.; Huang, J. Origin and Elimination of Photocurrent Hysteresis by Fullerene Passivation in $CH_3NH_3PbI_3$ Planar Heterojunction Solar Cells. *Nat. Commun.* **2014**, *5* (1), 5784. https://doi.org/10.1038/ncomms6784.

(22) Abrusci, A.; Stranks, S. D.; Docampo, P.; Yip, H.-L.; Jen, A. K.-Y.; Snaith, H. J. High-Performance Perovskite-Polymer Hybrid Solar Cells via Electronic Coupling with Fullerene Monolayers. *Nano Lett.* **2013**, *13* (7), 3124–3128. https://doi.org/10.1021/nl401044q.

(23) Xu, J.; Buin, A.; Ip, A. H.; Li, W.; Voznyy, O.; Comin, R.; Yuan, M.; Jeon, S.; Ning, Z.; McDowell, J. J.; et al. Perovskite–Fullerene Hybrid Materials Suppress Hysteresis in Planar Diodes. *Nat. Commun.* **2015**, *6* (1), 7081. https://doi.org/10.1038/ncomms8081.

(24) Fang, Y.; Bi, C.; Wang, D.; Huang, J. The Functions of Fullerenes in Hybrid Perovskite Solar Cells. *ACS Energy Lett.* **2017**, *2* (4), 782–794. https://doi.org/10.1021/acsenergylett.6b00657.

(25) Belisle, R. A.; Nguyen, W. H.; Bowring, A. R.; Calado, P.; Li, X.; Irvine, S. J. C.; McGehee, M. D.; Barnes, P. R. F.; O'Regan, B. C. Interpretation of Inverted Photocurrent Transients in Organic Lead Halide Perovskite Solar Cells: Proof of the Field Screening by Mobile Ions and Determination of the Space Charge Layer Widths. *Energy Environ. Sci.* **2017**, *10* (1), 192–204. https://doi.org/10.1039/C6EE02914K.

(26) Moia, D.; Gelmetti, I.; Calado, P.; Fisher, W.; Stringer, M.; Game, O.; Hu, Y.; Docampo, P.; Lidzey, D.; Palomares, E.; et al. Ionic-to-Electronic Current Amplification in Hybrid Perovskite Solar Cells: Ionically Gated Transistor-Interface Circuit Model Explains Hysteresis and Impedance of Mixed Conducting Devices. *Energy Environ. Sci.* **2019**, *12* (4), 1296–1308. https://doi.org/10.1039/C8EE02362J.

(27) Park, J.-S.; Calbo, J.; Jung, Y.-K.; Whalley, L. D.; Walsh, A. Accumulation of Deep Traps at Grain Boundaries in Halide Perovskites. *ACS Energy Lett.* **2019**, *4* (6), 1321–1327. https://doi.org/10.1021/acsenergylett.9b00840.

(28) Maurano, A.; Shuttle, C. G.; Hamilton, R.; Ballantyne, A. M.; Nelson, J.; Zhang, W.; Heeney, M.; Durrant, J. R. Transient Optoelectronic Analysis of Charge Carrier Losses in a Selenophene/Fullerene Blend Solar Cell. *J. Phys. Chem. C* **2011**, *115* (13), 5947–5957. https://doi.org/10.1021/jp109697w.

(29) O'Regan, B. C.; Barnes, P. R. F.; Li, X.; Law, C.; Palomares, E.; Marin-Beloqui, J. M. Optoelectronic Studies of Methylammonium Lead Iodide Perovskite Solar Cells with Mesoporous TiO_2 : Separation of Electronic and Chemical Charge Storage, Understanding Two Recombination Lifetimes, and the Evolution of Band Offsets during J – V Hysteresis. *J. Am. Chem. Soc.* **2015**, *137* (15), 5087–5099. https://doi.org/10.1021/jacs.5b00761.

(30) Du, T.; Kim, J.; Ngiam, J.; Xu, S.; Barnes, P. R. F.; Durrant, J. R.; McLachlan, M. A. Elucidating the Origins of Subgap Tail States and Open-Circuit Voltage in Methylammonium Lead Triiodide Perovskite Solar Cells. *Adv. Funct. Mater.* **2018**, *28* (32), 1801808. https://doi.org/10.1002/adfm.201801808.

(31) Wheeler, S.; Bryant, D.; Troughton, J.; Kirchartz, T.; Watson, T.; Nelson, J.; Durrant, J. R. Transient Optoelectronic Analysis of the Impact of Material Energetics and Recombination Kinetics on the Open-Circuit Voltage of Hybrid Perovskite Solar Cells. *J. Phys. Chem. C* **2017**, *121* (25), 13496–13506. https://doi.org/10.1021/acs.jpcc.7b02411.

(32) Zettergren, H.; Forsberg, B. O.; Cederquist, H. Are Single C_{60} Fullerenes Dielectric or Metallic? *Phys. Chem. Chem. Phys.* **2012**, *14* (47), 16360. https://doi.org/10.1039/c2cp42884a.

(33) Bally, A. R.; Korobeinikova, E. N.; Schmid, P. E.; Lévy, F.; Bussy, F. Structural and Electrical Properties of Fe-Doped Thin Films. *J. Phys. D. Appl. Phys.* **1998**, *31* (10), 1149–1154. https://doi.org/10.1088/0022-3727/31/10/004.

(34) Kiermasch, D.; Gil-Escrig, L.; Baumann, A.; Bolink, H. J.; Dyakonov, V.; Tvingstedt, K. Unravelling Steady-State Bulk Recombination Dynamics in Thick Efficient Vacuum-Deposited Perovskite Solar Cells by Transient Methods. *J. Mater. Chem. A* **2019**, *7* (24), 14712–14722. https://doi.org/10.1039/C9TA04367E.

(35) Kiermasch, D.; Baumann, A.; Fischer, M.; Dyakonov, V.; Tvingstedt, K. Revisiting Lifetimes from Transient Electrical Characterization of Thin Film Solar Cells; a Capacitive Concern Evaluated for Silicon, Organic and Perovskite Devices. *Energy Environ. Sci.* **2018**, *11* (3), 629–640. https://doi.org/10.1039/C7EE03155F.

(36) Kirchartz, T.; Nelson, J. Meaning of Reaction Orders in Polymer:Fullerene Solar Cells. *Phys. Rev. B - Condens. Matter Mater. Phys.* **2012**, *86* (16), 1–12. https://doi.org/10.1103/PhysRevB.86.165201.

(37) Shuttle, C. G.; O'Regan, B.; Ballantyne, A. M.; Nelson, J.; Bradley, D. D. C.; de Mello, J.; Durrant, J. R. Experimental Determination of the Rate Law for Charge Carrier Decay in a Polythiophene: Fullerene Solar Cell. *Appl. Phys. Lett.* **2008**, *92* (9), 093311. https://doi.org/10.1063/1.2891871.

(38) Calado, P.; Telford, A. M.; Bryant, D.; Li, X.; Nelson, J.; O'Regan, B. C.; Barnes, P. R. F. Evidence for Ion Migration in Hybrid Perovskite Solar Cells with Minimal Hysteresis. *Nat. Commun.* **2016**, *7*, 1–10. https://doi.org/10.1038/ncomms13831.

(39) Pockett, A.; Carnie, M. J. Ionic Influences on Recombination in Perovskite Solar Cells. *ACS Energy Lett.* **2017**, *2* (7), 1683–1689. https://doi.org/10.1021/acsenergylett.7b00490.

(40) Pockett, A.; Eperon, G. E.; Sakai, N.; Snaith, H. J.; Peter, L. M.; Cameron, P. J. Microseconds, Milliseconds and Seconds: Deconvoluting the Dynamic Behaviour of Planar Perovskite Solar Cells. *Phys. Chem. Chem. Phys.* **2017**, *19* (8), 5959–5970. https://doi.org/10.1039/C6CP08424A.

(41) Tress, W.; Marinova, N.; Moehl, T.; Zakeeruddin, S. M.; Nazeeruddin, M. K.; Grätzel, M. Understanding the Rate-Dependent J–V Hysteresis, Slow Time Component, and Aging in $CH_3NH_3PbI_3$ Perovskite Solar Cells: The Role of a Compensated Electric Field. *Energy Environ. Sci.* **2015**, *8* (3), 995–1004. https://doi.org/10.1039/C4EE03664F.

(42) van Reenen, S.; Kemerink, M.; Snaith, H. J. Modeling Anomalous Hysteresis in Perovskite Solar Cells. *J. Phys. Chem. Lett.* **2015**, *6* (19), 3808–3814. https://doi.org/10.1021/acs.jpclett.5b01645.

(43) Eames, C.; Frost, J. M.; Barnes, P. R. F.; O'Regan, B. C.; Walsh, A.; Islam, M. S. Ionic Transport in Hybrid Lead Iodide Perovskite Solar Cells. *Nat. Commun.* **2015**, *6* (1), 7497. https://doi.org/10.1038/ncomms8497.

(44) Richardson, G.; O'Kane, S. E. J.; Niemann, R. G.; Peltola, T. A.; Foster, J. M.; Cameron, P. J.; Walker, A. B. Can Slow-Moving Ions Explain Hysteresis in the Current-Voltage Curves of Perovskite Solar Cells? *Energy Environ. Sci.* **2016**, *9* (4), 1476–1485. https://doi.org/10.1039/c5ee02740c.

(45) Li, M.; Bhaumik, S.; Goh, T. W.; Kumar, M. S.; Yantara, N.; Grätzel, M.; Mhaisalkar, S.; Mathews, N.; Sum, T. C. Slow Cooling and Highly Efficient Extraction of Hot Carriers in Colloidal Perovskite Nanocrystals. *Nat. Commun.* **2017**, *8* (May), 14350. https://doi.org/10.1038/ncomms15299.

(46) Price, M. B.; Butkus, J.; Jellicoe, T. C.; Sadhanala, A.; Briane, A.; Halpert, J. E.; Broch, K.; Hodgkiss, J. M.; Friend, R. H.; Deschler, F. Hot-Carrier Cooling and Photoinduced Refractive Index Changes in Organic–Inorganic Lead Halide Perovskites. *Nat. Commun.* **2015**, *6* (1), 8420. https://doi.org/10.1038/ncomms9420.

(47) Guo, Z.; Wan, Y.; Yang, M.; Snaider, J.; Zhu, K.; Huang, L. Long-Range Hot-Carrier Transport in Hybrid Perovskites Visualized by Ultrafast Microscopy. *Science* **2017**, *356* (6333), 59–62. https://doi.org/10.1126/science.aam7744.

(48) Li, M.; Fu, J.; Xu, Q.; Sum, T. C. Slow Hot-Carrier Cooling in Halide Perovskites: Prospects for Hot-Carrier Solar Cells. *Adv. Mater.* **2019**, *1802486*, 1802486. https://doi.org/10.1002/adma.201802486.

(49) Yang, Y.; Ostrowski, D. P.; France, R. M.; Zhu, K.; van de Lagemaat, J.; Luther, J. M.; Beard, M. C. Observation of a Hot-Phonon Bottleneck in Lead-Iodide Perovskites. *Nat. Photonics* **2016**, *10* (1), 53–59. https://doi.org/10.1038/nphoton.2015.213.

(50) Zhai, Y.; Sheng, C. X.; Zhang, C.; Vardeny, Z. V. Ultrafast Spectroscopy of Photoexcitations in Organometal Trihalide Perovskites. *Adv. Funct. Mater.* **2016**, *26* (10), 1617–1627. https://doi.org/10.1002/adfm.201505115.

(51) Piatkowski, P.; Cohen, B.; Javier Ramos, F.; Di Nunzio, M.; Nazeeruddin, M. K.; Grätzel, M.; Ahmad, S.; Douhal, A. Direct Monitoring of Ultrafast Electron and Hole Dynamics in Perovskite Solar Cells. *Phys. Chem. Chem. Phys.* **2015**, *17* (22), 14674–14684. https://doi.org/10.1039/c5cp01119a.

(52) Roiati, V.; Mosconi, E.; Listorti, A.; Colella, S.; Gigli, G.; De Angelis, F. Stark Effect in Perovskite/TiO_2 Solar Cells: Evidence of Local Interfacial Order. *Nano Lett.* **2014**, *14* (4), 2168–2174. https://doi.org/10.1021/nl500544c.

(53) Price, M. B.; Butkus, J.; Jellicoe, T. C.; Sadhanala, A.; Briane, A.; Halpert, J. E.; Broch, K.; Hodgkiss, J. M.; Friend, R. H.; Deschler, F. Hot-Carrier Cooling and Photoinduced Refractive Index Changes in Organic-Inorganic Lead Halide Perovskites. *Nat. Commun.* **2015**, *6*, 9420. https://doi.org/10.1038/ncomms9420.

(54) Kalanoor, B. S.; Gouda, L.; Gottesman, R.; Tirosh, S.; Haltzi, E.; Zaban, A.; Tischler, Y. R. Third-Order Optical Nonlinearities in Organometallic Methylammonium Lead Iodide Perovskite Thin Films. *ACS Photonics* **2016**, *3* (3), 361–370. https://doi.org/10.1021/acsphotonics.5b00746.

Chapter 6

Charge carrier processes at the perovskite layer

CHAPTER 6: CHARGE CARRIER PROCESSES AT THE PEROVSKITE LAYER 175

6.1. Abstract 179

6.2. Introduction 179

6.3. Device Fabrication 181

6.4. Results and Discussion 181
6.4.1. Aging effects on solar cells performance 181
6.4.2. Ionic influences on carrier recombination 184
6.4.3. Aging effects on carrier recombination 188

6.5. Conclusions 195

6.6. References 196

6.1. Abstract

In this thesis chapter, we gain insight into the interfacial charge recombination kinetics in Perovskite Solar Cells, which is the source of one of the major carrier losses. Therefore, in order to increase the device photovoltaic efficiency, it is key to understand the origin of these losses and how they can be minimized.

With this purpose, we use transient photovoltage (TPV) to study carrier recombination under *operando* conditions. Interestingly, we observe a novel negative transient deflection when carrying out TPV measurements that has been related to ionic accumulation at the interfaces.

We monitor the evolution of this negative trace with the aging of the perovskite devices under dry air conditions. Importantly, we demonstrated that the negative signal changes with the aging of the solar cells, and this change can be related to the enhancement of the open circuit voltage and fill factor of the devices, and, thus, with the solar cell efficiency.

6.2. Introduction

Interfacial carrier recombination in lead halide perovskite solar cells (PSC) is a topic of growing interest[1–3]. Finding the major carrier losses is key to gain better efficiencies in solar cells[4]. Different techniques, performed in films[5–7] or working devices[8–10], have been used to study carrier recombination in PSC. From the different types of carrier recombination in PSC[11,12], it has been suggested that one of the major carrier losses is associated with carrier recombination at the interfaces between the perovskite layer and both selective contacts, the electron transporting material (ETM) and the hole transporting material (HTM)[13,14].

Transient photovoltage (TPV) has been used to study carrier recombination in solar cell devices, such as dye-sensitized solar cells (DSSC)[15,16], organic solar cells (OSC)[17,18], and also has been employed in PSC[2,19–

[23]. As previously explained in **chapter 4**, during the TPV experiment, the device is illuminated and kept at open circuit conditions. At the same time, a laser pulse generates a small perturbation with an associated extra number of generated carriers, which are forced to recombine as the device continues at open circuit conditions. Using different light intensities allows us to study the carrier recombination under different light biases.

A modification of this technique, called "transient of the transient photovoltage" (TROTTR) described by Calado *et al.*[24] and Pockett *et al.*[25] have been very useful to understand better ion migration in PSC. They studied the evolution of the TPV perturbations as the V_{OC} of the solar cell stabilizes. The stabilization of the V_{OC} in perovskite solar cell normally takes long times (up to hundreds of seconds), what has been assigned to the presence of ions at the perovskite interface in dark conditions and their redistribution when light irradiates the device[26].

Thus, TROTTR correlates ionic motion with carrier recombination. The most remarkable feature observed with this technique is the presence of a negative transient when the laser pulse is applied while the V_{OC} has not reached equilibrium. Calado *et al.*[24] modeled this negative transient by using the well-known Drift-Diffusion theory when they increased the recombination at the contact layers. Pockett *et al.*[25] also observed this negative signal and they attribute it to the presence of TiO_2 as ETM.

In this chapter, we have seek further in the disappearance of this negative transient and analyzed how the signal changes in correlation with the device aging and its relation with the hysteresis and the increase in the V_{OC} values of the triple cation PSC, $Cs_{0.1}(FA_{0.85}MA_{0.15})Pb(I_{0.85}Br_{0.15})_3$, herein referred as CsFAMAPbIBr (FA = $CH(NH_2)_2^+$; MA = $CH_3NH_3^+$). For this purpose, the solar cells were stored in N_2 and later and later on in air conditions with controlled humidity (<10% H_2O).

6.3. Device Fabrication

In this chapter, we employ the methods described in Chapter 4 for the fabrication of triple cation based, CsFAMAPbIBr perovskite solar cell, using a n-i-p configuration with the following architecture: FTO/TiO_2/CsFAMAPbIBr/Spiro-OMeTAD/Au.

Additionally, we have studied the influence of aging over these cells. In order to do it, the devices were stored under dry air conditions (<10% H_2O).

6.4. Results and Discussion

6.4.1. Aging effects on solar cells performance

We prepared PSC with nip configuration, using TiO_2 (compact and mesoporous layers) as ETM (n-type selective contact), and spiro-OMETAD as HTM (p-type selective contact). Photovoltaic parameters are listed in **Table 6.1** and the statistics are illustrated in **Figure 6.1**. For the sake of clarity, **Figure 6.1** only shows the results from day 3 and day 45 measurements. The most remarkable aspect in the performance of the solar cells is the reduction of the hysteresis with time, as it can be observed in **Table 6.1** and **Figure 6.2**.

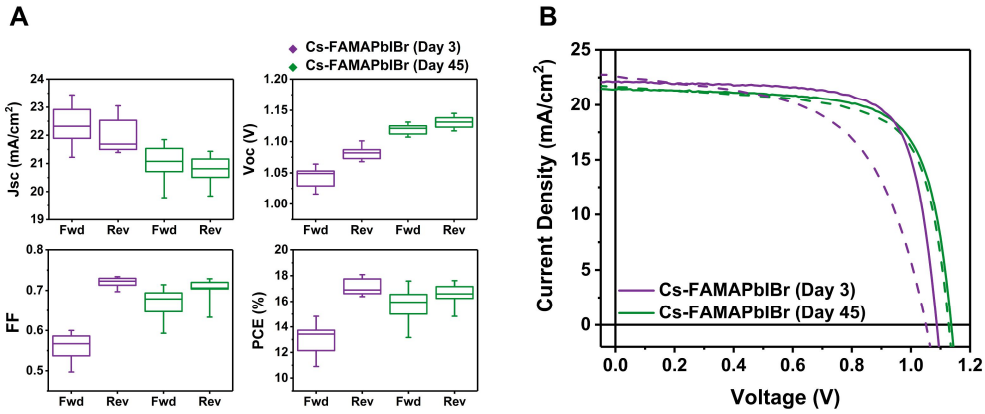

Figure 6.1. (A) Photovoltaic parameters obtained from the JV curves of the devices measured on day 3 and 45. **(B)** JV curves of the same device measured on day 3 and day 45. All the measurements were done at 1 Sun conditions (AM 1.5 G, 100 mW/cm^2) and a scan rate of 40 mv/s.

Table 6.1. Summary of the photovoltaic parameters of the cells tested in the study. The results were obtained under 1 Sun conditions (AM 1.5G, 100 mW/cm2) and a scan rate of 40 mV/s.

Day	Sweep	J_{sc} (mA/cm^2)	V_{OC} (V)	FF (%)	PCE (%)
1	Forward	21.3 ± 1.3	0.960 ± 0.026	50.6 ± 3.3	**10.3 ± 0.8**
	Reverse	21.1 ± 1.3	1.045 ± 0.008	69.9 ± 0.5	**15.4 ± 1.0**
2	Forward	21.2 ± 1.7	1.010 ± 0.025	54.7 ± 3.6	**11.7 ± 1.2**
	Reverse	20.8 ± 1.6	1.063 ± 0.011	69.7 ± 1.8	**15.4 ± 1.5**
3	Forward	22.4 ± 0.6	1.043 ± 0.015	55.8 ± 3.4	**13.0 ± 1.2**
	Reverse	22.0 ± 0.6	1.081 ± 0.010	72.1 ± 1.1	**17.1 ± 0.6**
21	Forward	22.2 ± 0.5	0.981 ± 0.039	58.9 ± 4.4	**12.9 ± 1.5**
	Reverse	22.4 ± 0.5	1.078 ± 0.014	71.8 ± 0.9	**17.3 ± 0.5**
30	Forward	21.8 ± 0.6	1.090 ± 0.007	64.0 ± 3.3	**15.3 ± 1.0**
	Reverse	21.2 ± 0.6	1.097 ± 0.008	69.2 ± 2.7	**16.1 ± 0.8**
45	Forward	21.0 ± 0.6	1.120 ± 0.009	67.1 ± 3.5	**15.8 ± 1.3**
	Reverse	20.8 ± 0.5	1.132 ± 0.009	70.6 ± 2.2	**16.6 ± 0.8**

We would like to point out that between days 3 and 21 the cells were stored in a N_2 filled glove-box, while the rest of the days, they were stored under air conditions with low humidity (<10 % H_2O).

The reduction of the hysteresis observed in the solar cells is even clearer when we compare the difference in the area under the curve (shadowed area, **Figure 6.2**) between the forward and reverse sweeps. A clear reduction of the hysteresis is observed when the devices were stored in air conditions, while the N_2 storage shows no evolution.

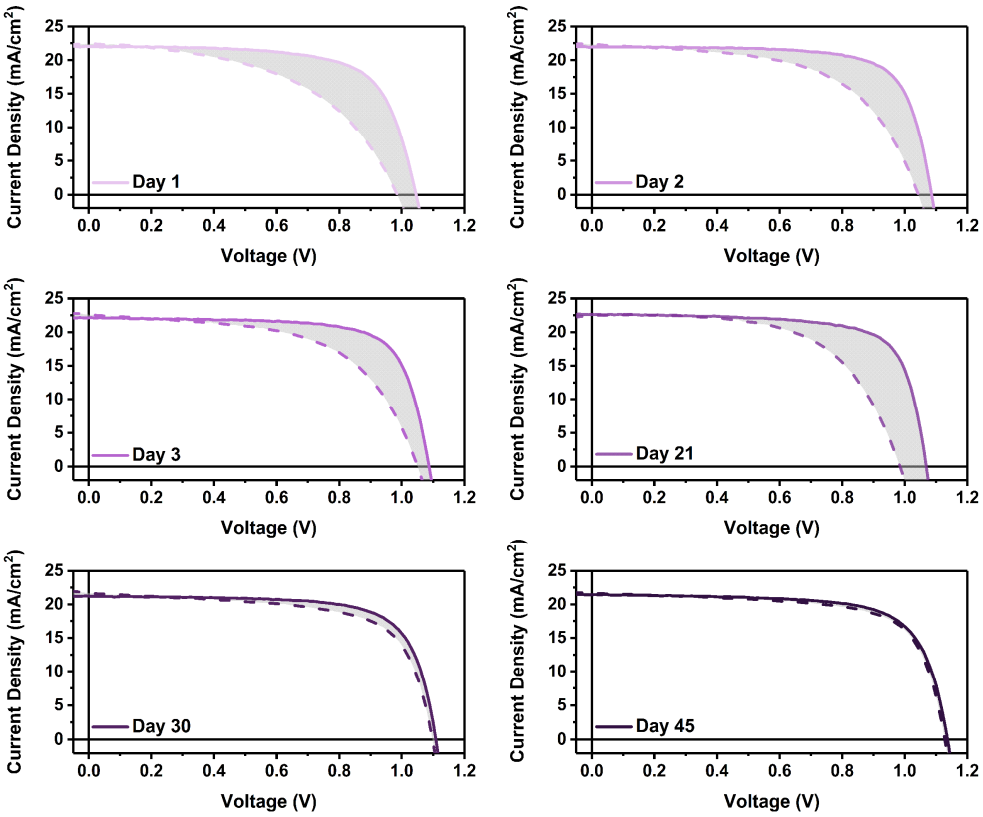

Figure 6.2. JV curves of the same solar cell measured on different days, while it was stored under air or N_2 conditions. The shadowed area shows the degree of hysteresis on the device.

Furthermore, from the analysis of the JV curves, we observe an increase in the V_{OC} over the different measurement days, V_{OC} (day 3) = 1.081 V; V_{OC} (day 45) = 1.132 V. Additionally, the V_{OC} values at forward and reverse sweeps reduce

their difference with aging time, $\Delta V = V_{OC}$ (rev) – V_{OC} (fwd) (ΔV(day 3) = 0.038 V; ΔV(day 45) = 0.012 V). These results suggest that carrier recombination is reduced over the different measurement days. It should also be appointed that the presence of ions at the interfaces has been attributed as the main responsible for hysteresis[27]. Therefore, we will analyze the role of ions in carrier recombination and check their correlation to the reduction of hysteresis and the increase in the V_{OC}.

6.4.2. Ionic influences on carrier recombination

As discussed before, we made use of TPV to study carrier recombination. More specifically, we used the TROTTR approach that combines TPV measurements with the V_{OC} stabilization kinetics. PSC show long stabilization times (**Figure 6.3**), so, to understand which processes are making this stabilization so slow[26,28], we applied laser pulses at different illumination times, corresponding to very different V_{OC} values. We measured the TPV at the following illumination times: 3 s, 5 s, 10 s, and 30 s. **Figure 6.3** shows the slow stabilization time for the cell measured in day 3, while the cell measured on day 45 shows an immediate stabilization.

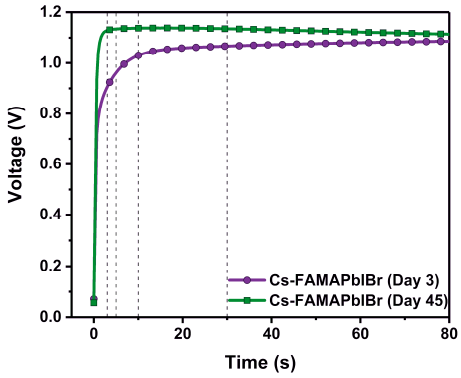

Figure 6.3. V_{OC} stabilization over time of the devices measured on days 3 and 45. Dashed lines show the times at which TPV pulses for TROTTR were registered.

A model to explain ionic movement have been suggested by different authors[26–31] in order to also explain the hysteresis observed in these solar cells. This model consists in the following:

1) In dark conditions, a built-in voltage (V_{bi}) is generated to compensate the difference in Fermi levels of both selective contacts (**Figure 6.4.a**). The internal electric field forces ions, normally iodide and its vacancies[30,32], to move to the interfaces until they screen the electric field. This process creates an ionic charged layer with band bending at each interface (**Figure 6.4.b**).

2) When light irradiates the solar cell, the photogenerated carriers originate a split of the Fermi levels, with the associated V_{OC}. The ions start moving to compensate the photogenerated electric field. Nevertheless, they do it slowly, so, the electric field associated with the ions at the interface will persist, driving carriers to the opposite direction of extraction, creating regions with accumulated carriers, band valleys (electrons at the HTM side and holes at the ETM side)[27]. It is expected that high degree of recombination will happen in these regions, thus reducing the V_{OC} (**Figure 6.4.c**).

3) This carrier accumulation will persist until ions redistribute, and the electric field that drives carriers in the opposite direction is canceled (**Figure 6.4.d**).

Then, the accumulation of ions at each interface explains the slow stabilization times for the cell measured on day 3. In the other case, where the stabilization is immediate, meaning that the internal electric field created by the ionic accumulation at the interfaces is screened immediately, and, as suggested by Bertoluzzi *et al.*[33] this behavior could be correlated with a fast ionic component to compensate the electric field.

As expected[24,25], TPV transients at early light illumination times, together with a slow stabilization (day 3 device, **Figure 6.3** and **Figure 6.5.a**) show a clear negative deflection in the transient. As we have already stated, this behavior was associated with increased recombination at the interfaces. When the laser pulse generates extra carriers, they move in the direction of the electric field generated by the ions, trying to compensate it.

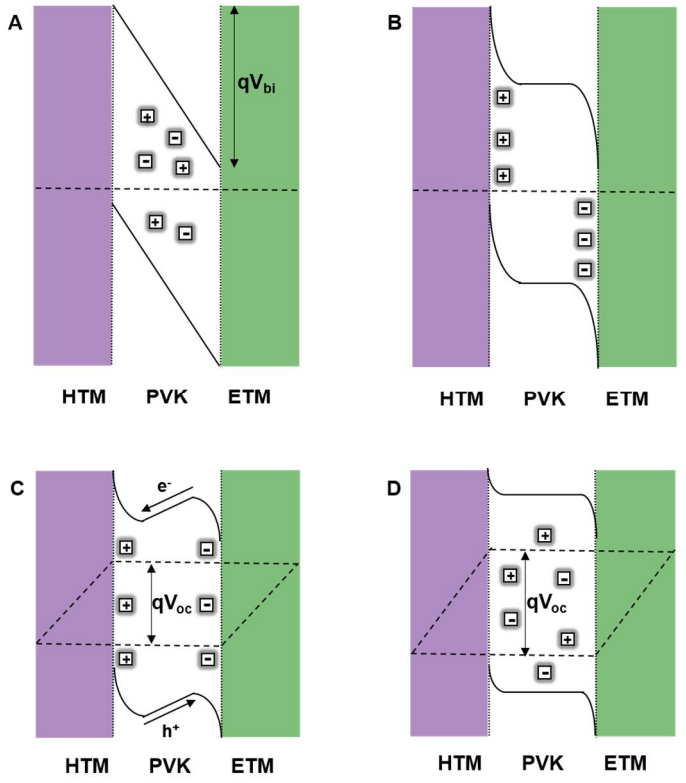

Figure 6.4. Scheme showing the possible band diagrams in different stages. Dashed lines show the Fermi levels, complete lines show the valence and conduction band of the perovskite, and the squared positive and negative symbols shoe the ions in the perovskite.

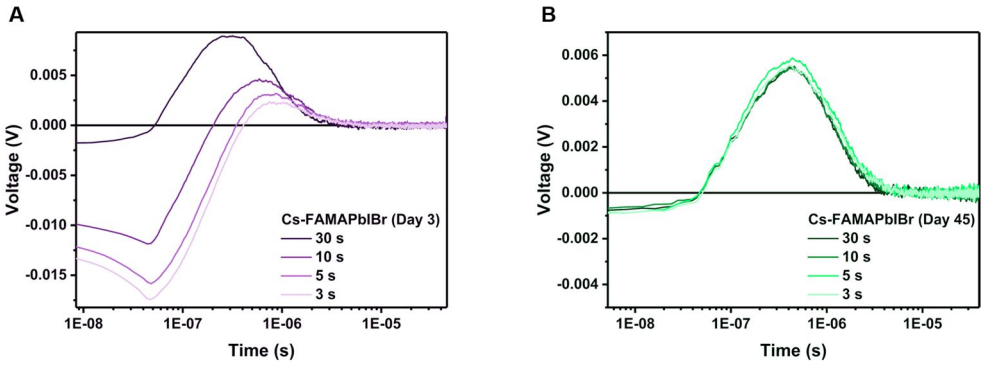

Figure 6.5. (**A**) TPV signals of the device measured on day 3 with different illumination times. (**B**) TPV signals of the device measured on day 45 with different illumination times.

Thus, lower voltages and negative transients are obtained due to enhanced recombination in this region. Once the electric field is compensated, by ion movement or with carriers flowing in that direction, the transient becomes positive.

To our surprise, the device measured on day 45, does not show any negative transient at any time during time stabilization (**Figure 6.5.b**). We also correlate the magnitude of the transient deflection with the V_{OC} stabilization (**Figure 6.3** and **Figure 6.6**). There is a good correlation between them, which confirms that when the recombination rate is at its maximum (maximum of the negative transient deflection), we obtain the lower values of V_{OC} [34].

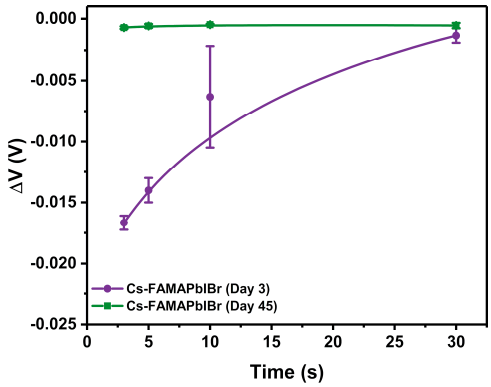

Figure 6.6. Amplitude of the negative transient deflection at different illumination times obtained from the TPV measurements.

As other groups have stated in previous publications, solar cells without hysteresis still present ionic motion[24,33], so, although ions remain at the interface, they seem to present an enhanced mobility that allow the fast electric field screening[33] or that carriers fill the band valleys immediately after illumination[24]. The reduced hysteresis and the absence of negative TPV seems to be an effect of oxygen storage under dark conditions. Meggiolaro *et al.*[35] suggested that O_2 could occupy some iodine defects in the interstitial perovskite framework that would lead to the reduction of deep traps in the perovskite, thus, an enhanced p-doping in the perovskite. Additionally, Senocrate *et al.*[36] suggested that perovskite under oxygen and dark conditions, presents a better electronic conductivity, although the ionic conductivity remains constant. Also, they claimed that mixed cation and anion perovskite present a better stability towards degradation under O_2 conditions compared to $MAPbI_3$, what would explain why solar cells kept in air conditions lasts for so long periods of time. Furthermore, there are some reports on Dye Sensitized Solar Cells (DSSC) were they studied the p-doping effect of O_2 in LiTFSI doped spiro-OMeTAD based DSSC, with an increase in conductivity, and also, in the final device efficiency[37,38]. Having all of this in mind, it seems that oxygen has an effect acting as a p-dopant in both perovskite and spiro-OMeTAD. This effect leads to greater carrier and ionic mobility that allows a faster compensation of the internal electric field created by the ions at the interface that led to the observation of hysteresis in JV curves and the negative deflections in the TPV experiments without air aging. Thus, the relation between ion migration and carrier recombination in PSC must be revisited and the age of the solar cell must be taken into account.

6.4.3. Aging effects on carrier recombination

Finally, we studied the influences of these findings on the complete carrier recombination scheme. For that, we measure TPV transients with a stable V_{OC} and with different light intensities (**Figure 6.7.a**). In addition,

charge extraction (CE) and transient photocurrent (TPC)[20] were measured. Here, we compare the small perturbation lifetimes at different photovoltages. Small perturbation lifetime follows an exponential decrease as a function of the voltage (**Equation 6.1**).

$$\tau_{\Delta n} = \tau_{\Delta n_0} \exp\left(-\frac{q\,V_{oc}}{\theta\,K_B\,T}\right) \qquad (6.1)$$

Being $\tau_{\Delta n0}$ the equilibrium small perturbation lifetime, and θ the slope deviations from the thermal voltage K_BT/q. Recently, Kiermasch *et al.*[22,23] underlined the influence over the small perturbation lifetime of a capacitive component due to the release of free carriers stored in the electrodes at low light illumination intensities. To assure that we are out of the capacitive lifetime (τ_{cap}) (**Equation 6.2**) that should be smaller than the measured small perturbation lifetime ($\tau_{\Delta n}$). If this statement is accomplished, the processes we are studying correspond to the processes in the bulk of the perovskite[22,23].

$$\tau_{cap} = \frac{n_{id}\,K_B\,T\,C_{geo}}{q\;J_{sc}(V_{oc})} \qquad (6.2)$$

In **Equation 6.2** n_{id} is the ideality factor, calculated with the relationship of the V_{OC} at different light intensities in reverse conditions (**Figure 6.8**), K_BT/q is the thermal voltage, C_{geo} is the geometric capacitance calculated from the linear part of the differential capacitance (DiffCap) analysis[2,20,21] (**Figure 6.9**), and $J_{SC}(V_{OC})$ is a relationship given by Tvingstedt *et al.*[39] In **Figure 6.7.b** it is shown the results for the capacitive component, being smaller than the measured small perturbation lifetime at voltages > 0.9 V approximately, being coincident with the observation of the exponential part in the differential capacitance analysis, related with charge in the bulk of the perovskite[2,21] (**Figure 6.9**).

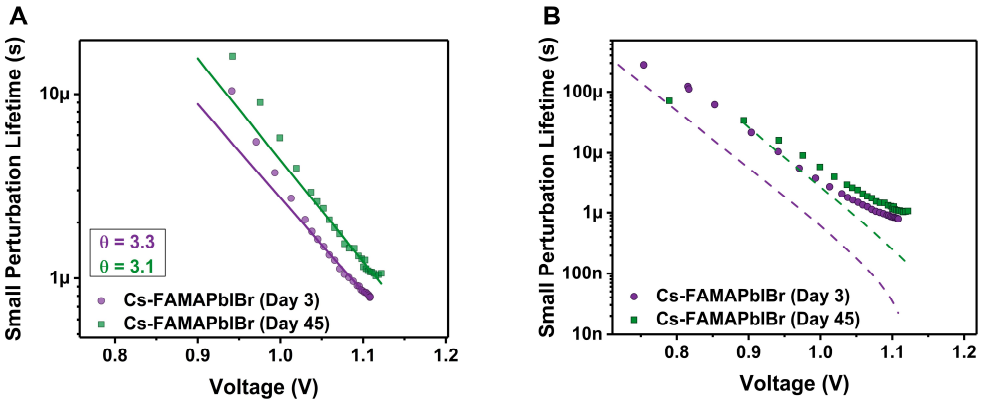

Figure 6.7. (**A**) Small perturbation lifetime as a function of the photovoltage generated in the devices with the exponential fitting (**A**) and the calculation of the capacitive discharge (dashed lines, **B**).

Figure 6.7.a is the zoom in the region close to 1 Sun conditions, where $\tau_{\Delta n} > \tau_{cap}$. We observe that carrier recombination decreases from day 3 to day 45, as we conclude from both faster carrier recombination in day 3 and also from the monoexponential fitting (**Equation 6.1**).

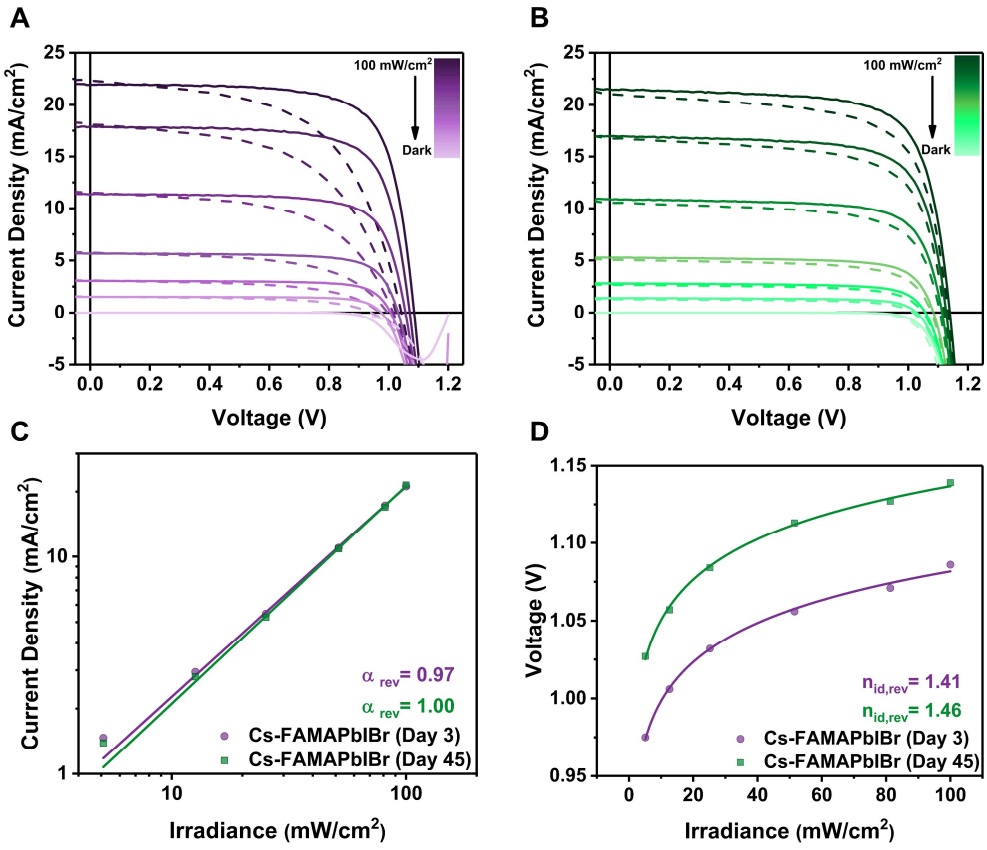

Figure 6.8. JV curves under different light intensities for the devices measured on day 3 (**A**) and day 45 (**B**). J_{SC} values at different light intensities and the fitting to a power law dependence in reverse conditions (**C**). V_{OC} dependence with the light intensity in reverse conditions (**D**) used to estimate the ideality factor.

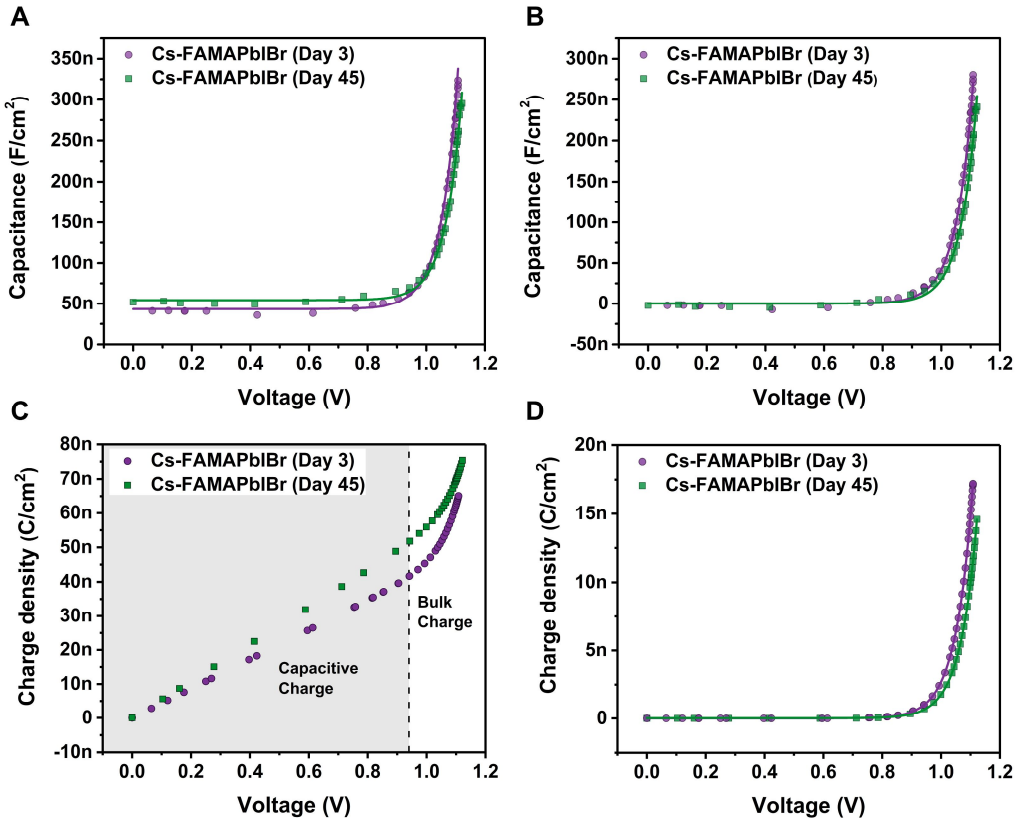

Figure 6.9. (**A**) Differential capacitance at different voltages (light bias). (**B**) Differential capacitance plot after the subtraction of the geometric capacitance (Charge at the contacts) (**C**) Charge density obtained upon integration of the capacitance in (**A**) at the same voltages., and (**D**) Charge density obtained upon the integration of the capacitance in (**B**) showing the charge stored in the bulk of the perovskite.

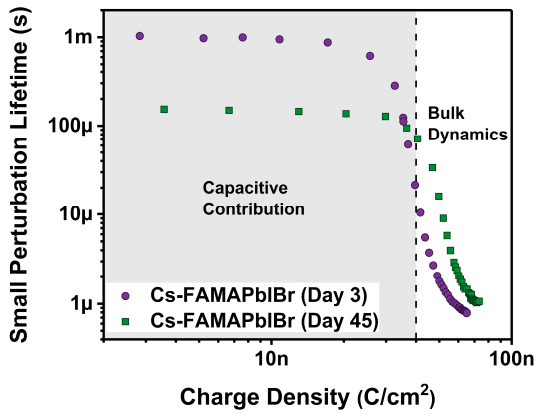

Figure 6.10. Small perturbation lifetime as a function of the charge density obtained from the integration of differential capacitance.

A better comparison is done comparing the small perturbation lifetimes with the charge density in the device (**Figure 6.10**). Two different regimes are observed. At low charge densities (predominance of the capacitive contribution) we observe longer lifetimes in the device measured on day 3. As the small perturbation lifetime is affected by the discharge of the capacitive component at low charge density[22,23] and the capacitance is affected by the ionic presence at the interfaces[40], we correlate this slower lifetime to a slower ionic movement. However, this is not the case at higher charge densities (bulk dynamics), where $\tau_{\Delta n}$(Day 45) is slower than $\tau_{\Delta n}$(Day 3). Additionally, we compare the small perturbation lifetime with the charge density subtracting the geometric capacitance (**Figure 6.11**). In this case, we observe no discernable differences in the bulk dynamics. All of this make us confirm that at higher charge densities, lifetimes are affected by the ionic accumulation at the interfaces[40], as we observe faster lifetimes on day 3 when ionic accumulation is greater, compared to a faster ionic redistribution (day 45). This behavior is also confirmed if we calculate the charge density using CE (**Figure 6.12**). Thus, ionic influence over TPV lifetime is reduced, and consequently, both V_{OC} and fill factor in these devices are enhanced.

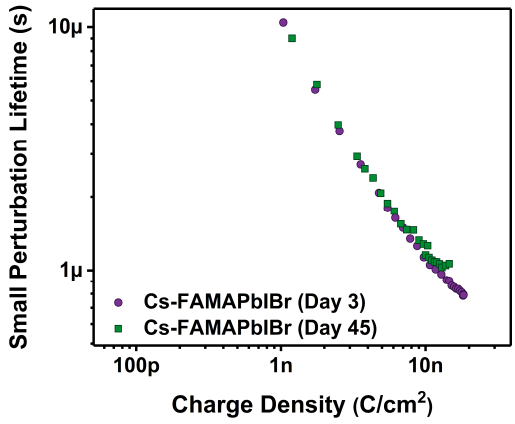

Figure 6.11. Small perturbation lifetime obtained from the TPV as a function of the charge density obtained from the integration of the differential capacitance after the subtraction of the geometric capacitance.

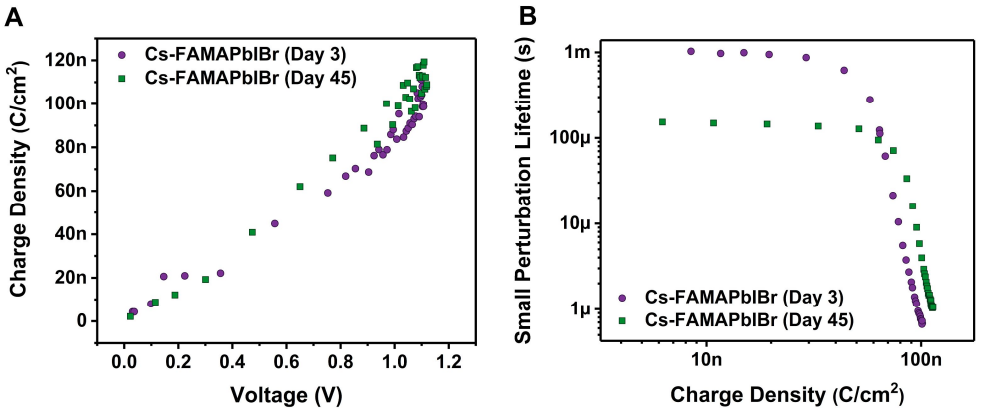

Figure 6.12. (**A**) Charge density obtained at different voltages using the CE technique. (**B**) Small perturbation lifetime as a function of the charge density obtained from CE.

Finally, we calculated the V_{OC} expected from the TPV and TPC measurements (**Equation 6.3**)[2,21].

$$V_{oc}(calc) = \frac{m\ K_B T}{q\ \delta} \ln\left(\frac{\tau_{\Delta n0}\ J_{sc}}{Q_0}\right) \qquad (6.3)$$

Where Q_0 is the equilibrium charge density and m is the deviation from the thermal voltage (K_BT/q) obtained from the exponential fitting of the charge density as a function of the voltage (**Figure 6.9.b** in the main text, **Equation 6.4**).

$$Q = Q_0 \exp\left(\frac{q\ V_{oc}}{m\ K_B\ T}\right) \qquad (6.4)$$

δ is the recombination order, $\delta = \left(\frac{m}{\theta}\right) + 1$, that is the slope of the small perturbation as a function of the charge density (**Figure 6.10**); q and $\tau_{\Delta n_0}$ are obtained from the exponential fitting of the lifetime as a function of the voltage (**Equation 6.1**).

In **Table 6.2**, we summarize the parameters obtained for the two devices and the final V_{OC} (calc). We obtain V_{OC} values that are in accordance with the V_{OC} obtained in the JV curves under 1 Sun conditions (**Figure 6.1**) and

that confirm the expected increase in the V_{OC} from day 3 to day 45, ΔV_{OC} (calc) = V_{OC} (calc, Day 45) - V_{OC} (calc, Day 3) = 30 mV.

Table 6.2. Summary of the fitting parameters to calculate the V_{OC} obtained from the TPV and TPC techniques.

	Day 3	**Day 45**
m	2.3	2.2
θ	3.3	3.1
δ	1.7	1.7
J_{SC} / A · cm^{-2}	0.0221	0.0216
$\tau_{\Delta n0}$ / s	0.337	1.41
n_0 / C · cm^{-2}	$1.0 \cdot 10^{-16}$	$4.8 \cdot 10^{-17}$
V_{OC}(calc) / V	**1.109**	**1.132**
V_{OC}(exp) / V	**1.087**	**1.139**

6.5. Conclusions

We have fabricated PSC that in a first approach showed a higher degree of hysteresis, decreasing over different measurement days when they were stored in air conditions. These devices were characterized using advanced transient techniques, such as TPV, CE, and TPC that give us information about carrier recombination in PSC. From the analysis, we conclude that the influence of ion migration over the carrier lifetime is reduced over different measurement days. As it seems, oxygen has an influence over both perovskite and spiro-OMeTAD as others have demonstrated before. As a result, both ionic and electronic conductivity increase, thus, the internal electric field associated with ionic accumulation at the interfaces is eliminated immediately after illumination. Therefore, an increased V_{OC} and fill factor in the devices are observed, associated with the decrease of carrier losses due to recombination.

6.6. References

(1) Tress, W. Perovskite Solar Cells on the Way to Their Radiative Efficiency Limit - Insights Into a Success Story of High Open-Circuit Voltage and Low Recombination. *Adv. Energy Mater.* **2017**, *7* (14), 1602358. https://doi.org/10.1002/aenm.201602358.

(2) Wheeler, S.; Bryant, D.; Troughton, J.; Kirchartz, T.; Watson, T.; Nelson, J.; Durrant, J. R. Transient Optoelectronic Analysis of the Impact of Material Energetics and Recombination Kinetics on the Open-Circuit Voltage of Hybrid Perovskite Solar Cells. *J. Phys. Chem. C* **2017**, *121* (25), 13496–13506. https://doi.org/10.1021/acs.jpcc.7b02411.

(3) Johnston, M. B.; Herz, L. M. Hybrid Perovskites for Photovoltaics: Charge-Carrier Recombination, Diffusion, and Radiative Efficiencies. *Acc. Chem. Res.* **2016**, *49* (1), 146–154. https://doi.org/10.1021/acs.accounts.5b00411.

(4) Correa-Baena, J. P.; Tress, W.; Domanski, K.; Anaraki, E. H.; Turren-Cruz, S. H.; Roose, B.; Boix, P. P.; Grätzel, M.; Saliba, M.; Abate, A.; et al. Identifying and Suppressing Interfacial Recombination to Achieve High Open-Circuit Voltage in Perovskite Solar Cells. *Energy Environ. Sci.* **2017**, *10* (5), 1207–1212. https://doi.org/10.1039/c7ee00421d.

(5) Yamada, Y.; Nakamura, T.; Endo, M.; Wakamiya, A.; Kanemitsu, Y. Photocarrier Recombination Dynamics in Perovskite $CH_3NH_3PbI_3$ for Solar Cell Applications. *J. Am. Chem. Soc.* **2014**, *136* (33), 11610–11613. https://doi.org/10.1021/ja506624n.

(6) Krogmeier, B.; Staub, F.; Grabowski, D.; Rau, U.; Kirchartz, T. Quantitative Analysis of the Transient Photoluminescence of $CH_3NH_3PbI_3/PC_{61}BM$ Heterojunctions by Numerical Simulations. *Sustain. Energy Fuels* **2018**, *2* (5), 1027–1034. https://doi.org/10.1039/C7SE00603A.

(7) Stranks, S. D.; Eperon, G. E.; Grancini, G.; Menelaou, C.; Alcocer, M. J. P.; Leijtens, T.; Herz, L. M.; Petrozza, A.; Snaith, H. J. Electron-Hole Diffusion Lengths Exceeding 1 Micrometer in an Organometal Trihalide Perovskite Absorber. *Science* **2013**, *342* (6156), 341–344. https://doi.org/10.1126/science.1243982.

(8) Zarazua, I.; Han, G.; Boix, P. P.; Mhaisalkar, S.; Fabregat-Santiago, F.; Mora-Seró, I.; Bisquert, J.; Garcia-Belmonte, G. Surface Recombination and Collection Efficiency in Perovskite Solar Cells from Impedance Analysis. *J. Phys. Chem. Lett.* **2016**, *7* (24), 5105–5113. https://doi.org/10.1021/acs.jpclett.6b02193.

(9) Jiménez-López, J.; Cambarau, W.; Cabau, L.; Palomares, E. Charge

Injection, Carriers Recombination and HOMO Energy Level Relationship in Perovskite Solar Cells. *Sci. Rep.* **2017**, *7* (1), 6101. https://doi.org/10.1038/s41598-017-06245-5.

(10) Pockett, A.; Eperon, G. E.; Peltola, T.; Snaith, H. J.; Walker, A.; Peter, L. M.; Cameron, P. J. Characterization of Planar Lead Halide Perovskite Solar Cells by Impedance Spectroscopy, Open-Circuit Photovoltage Decay, and Intensity-Modulated Photovoltage/Photocurrent Spectroscopy. *J. Phys. Chem. C* **2015**, *119* (7), 3456–3465. https://doi.org/10.1021/jp510837q.

(11) Marchioro, A.; Teuscher, J.; Friedrich, D.; Kunst, M.; van de Krol, R.; Moehl, T.; Grätzel, M.; Moser, J.-E. Unravelling the Mechanism of Photoinduced Charge Transfer Processes in Lead Iodide Perovskite Solar Cells. *Nat. Photonics* **2014**, *8* (3), 250–255. https://doi.org/10.1038/nphoton.2013.374.

(12) Tress, W.; Yavari, M.; Domanski, K.; Yadav, P.; Niesen, B.; Correa Baena, J. P.; Hagfeldt, A.; Graetzel, M. Interpretation and Evolution of Open-Circuit Voltage, Recombination, Ideality Factor and Subgap Defect States during Reversible Light-Soaking and Irreversible Degradation of Perovskite Solar Cells. *Energy Environ. Sci.* **2018**, *11* (1), 151–165. https://doi.org/10.1039/C7EE02415K.

(13) Stolterfoht, M.; Wolff, C. M.; Márquez, J. A.; Zhang, S.; Hages, C. J.; Rothhardt, D.; Albrecht, S.; Burn, P. L.; Meredith, P.; Unold, T.; et al. Visualization and Suppression of Interfacial Recombination for High-Efficiency Large-Area Pin Perovskite Solar Cells. *Nat. Energy* **2018**, *3* (10), 847–854. https://doi.org/10.1038/s41560-018-0219-8.

(14) Sarritzu, V.; Sestu, N.; Marongiu, D.; Chang, X.; Masi, S.; Rizzo, A.; Colella, S.; Quochi, F.; Saba, M.; Mura, A.; et al. Optical Determination of Shockley-Read-Hall and Interface Recombination Currents in Hybrid Perovskites. *Sci. Rep.* **2017**, *7* (March), 1–10. https://doi.org/10.1038/srep44629.

(15) Walker, A. B.; Peter, L. M.; Lobato, K.; Cameron, P. J. Analysis of Photovoltage Decay Transients in Dye-Sensitized Solar Cells. *J. Phys. Chem. B* **2006**, *110* (50), 25504–25507. https://doi.org/10.1021/jp064860z.

(16) Barnes, P. R. F.; Miettunen, K.; Li, X.; Anderson, A. Y.; Bessho, T.; Gratzel, M.; O'Regan, B. C. Interpretation of Optoelectronic Transient and Charge Extraction Measurements in Dye-Sensitized Solar Cells. *Adv. Mater.* **2013**, *25* (13), 1881–1922. https://doi.org/10.1002/adma.201201372.

(17) Maurano, A.; Shuttle, C. G.; Hamilton, R.; Ballantyne, A. M.; Nelson, J.; Zhang, W.; Heeney, M.; Durrant, J. R. Transient Optoelectronic Analysis of Charge Carrier Losses in a Selenophene/Fullerene Blend Solar Cell. *J. Phys. Chem. C* **2011**, *115* (13), 5947–5957. https://doi.org/10.1021/jp109697w.

(18) Maurano, A.; Hamilton, R.; Shuttle, C. G.; Ballantyne, A. M.; Nelson, J.; O'Regan, B.; Zhang, W.; McCulloch, I.; Azimi, H.; Morana, M.; et al. Recombination Dynamics as a Key Determinant of Open Circuit Voltage in Organic Bulk Heterojunction Solar Cells: A Comparison of Four Different Donor Polymers. *Adv. Mater.* **2010**, *22* (44), 4987–4992. https://doi.org/10.1002/adma.201002360.

(19) Montcada, N. F.; Marín-Beloqui, J. M.; Cambarau, W.; Jiménez-López, J.; Cabau, L.; Cho, K. T.; Nazeeruddin, M. K.; Palomares, E. Analysis of Photoinduced Carrier Recombination Kinetics in Flat and Mesoporous Lead Perovskite Solar Cells. *ACS Energy Lett.* **2017**, *2* (1), 182–187. https://doi.org/10.1021/acsenergylett.6b00600.

(20) O'Regan, B. C.; Barnes, P. R. F. F.; Li, X.; Law, C.; Palomares, E.; Marin-Beloqui, J. M. Optoelectronic Studies of Methylammonium Lead Iodide Perovskite Solar Cells with Mesoporous TiO_2: Separation of Electronic and Chemical Charge Storage, Understanding Two Recombination Lifetimes, and the Evolution of Band Offsets during J – V Hy. *J. Am. Chem. Soc.* **2015**, *137* (15), 5087–5099. https://doi.org/10.1021/jacs.5b00761.

(21) Du, T.; Kim, J.; Ngiam, J.; Xu, S.; Barnes, P. R. F.; Durrant, J. R.; McLachlan, M. A. Elucidating the Origins of Subgap Tail States and Open-Circuit Voltage in Methylammonium Lead Triiodide Perovskite Solar Cells. *Adv. Funct. Mater.* **2018**, *28* (32), 1801808. https://doi.org/10.1002/adfm.201801808.

(22) Kiermasch, D.; Gil-Escrig, L.; Baumann, A.; Bolink, H. J.; Dyakonov, V.; Tvingstedt, K. Unravelling Steady-State Bulk Recombination Dynamics in Thick Efficient Vacuum-Deposited Perovskite Solar Cells by Transient Methods. *J. Mater. Chem. A* **2019**, *7* (24), 14712–14722. https://doi.org/10.1039/c9ta04367e.

(23) Kiermasch, D.; Baumann, A.; Fischer, M.; Dyakonov, V.; Tvingstedt, K. Revisiting Lifetimes from Transient Electrical Characterization of Thin Film Solar Cells; a Capacitive Concern Evaluated for Silicon, Organic and Perovskite Devices. *Energy Environ. Sci.* **2018**, *11* (3), 629–640. https://doi.org/10.1039/C7EE03155F.

(24) Calado, P.; Telford, A. M.; Bryant, D.; Li, X.; Nelson, J.; O'Regan, B. C.; Barnes, P. R. F. Evidence for Ion Migration in Hybrid Perovskite Solar

Cells with Minimal Hysteresis. *Nat. Commun.* **2016**, *7* (1), 13831. https://doi.org/10.1038/ncomms13831.

(25) Pockett, A.; Carnie, M. J. Ionic Influences on Recombination in Perovskite Solar Cells. *ACS Energy Lett.* **2017**, *2* (7), 1683–1689. https://doi.org/10.1021/acsenergylett.7b00490.

(26) Pockett, A.; Eperon, G. E.; Sakai, N.; Snaith, H. J.; Peter, L. M.; Cameron, P. J. Microseconds, Milliseconds and Seconds: Deconvoluting the Dynamic Behaviour of Planar Perovskite Solar Cells. *Phys. Chem. Chem. Phys.* **2017**, *19* (8), 5959–5970. https://doi.org/10.1039/C6CP08424A.

(27) Belisle, R. A.; Nguyen, W. H.; Bowring, A. R.; Calado, P.; Li, X.; Irvine, S. J. C.; McGehee, M. D.; Barnes, P. R. F.; O'Regan, B. C. Interpretation of Inverted Photocurrent Transients in Organic Lead Halide Perovskite Solar Cells: Proof of the Field Screening by Mobile Ions and Determination of the Space Charge Layer Widths. *Energy Environ. Sci.* **2017**, *10* (1), 192–204. https://doi.org/10.1039/C6EE02914K.

(28) Tress, W.; Marinova, N.; Moehl, T.; Zakeeruddin, S. M.; Nazeeruddin, M. K.; Grätzel, M. Understanding the Rate-Dependent J–V Hysteresis, Slow Time Component, and Aging in $CH_3NH_3PbI_3$ Perovskite Solar Cells: The Role of a Compensated Electric Field. *Energy Environ. Sci.* **2015**, *8* (3), 995–1004. https://doi.org/10.1039/C4EE03664F.

(29) van Reenen, S.; Kemerink, M.; Snaith, H. J. Modeling Anomalous Hysteresis in Perovskite Solar Cells. *J. Phys. Chem. Lett.* **2015**, *6* (19), 3808–3814. https://doi.org/10.1021/acs.jpclett.5b01645.

(30) Eames, C.; Frost, J. M.; Barnes, P. R. F.; O'Regan, B. C.; Walsh, A.; Islam, M. S. Ionic Transport in Hybrid Lead Iodide Perovskite Solar Cells. *Nat. Commun.* **2015**, *6* (1), 7497. https://doi.org/10.1038/ncomms8497.

(31) Richardson, G.; O'Kane, S. E. J.; Niemann, R. G.; Peltola, T. A.; Foster, J. M.; Cameron, P. J.; Walker, A. B. Can Slow-Moving Ions Explain Hysteresis in the Current-Voltage Curves of Perovskite Solar Cells? *Energy Environ. Sci.* **2016**, *9* (4), 1476–1485. https://doi.org/10.1039/c5ee02740c.

(32) Senocrate, A.; Moudrakovski, I.; Kim, G. Y.; Yang, T.-Y.; Gregori, G.; Grätzel, M.; Maier, J. The Nature of Ion Conduction in Methylammonium Lead Iodide: A Multimethod Approach. *Angew. Chemie Int. Ed.* **2017**, *56* (27), 7755–7759. https://doi.org/10.1002/anie.201701724.

(33) Bertoluzzi, L.; Belisle, R. A.; Bush, K. A.; Cheacharoen, R.; McGehee, M. D.; O'Regan, B. C. In Situ Measurement of Electric-Field Screening in Hysteresis-Free PTAA/$FA_{0.83}Cs_{0.17}Pb(I_{0.83}Br_{0.17})_3$/$C_{60}$ Perovskite Solar

Cells Gives an Ion Mobility of ~3 × 10^{-7} cm^2 /(V s), 2 Orders of Magnitude Faster than Reported for Metal-Oxide-Contacted. *J. Am. Chem. Soc.* **2018**, *140* (40), 12775–12784. https://doi.org/10.1021/jacs.8b04405.

(34) Pockett, A.; Raptis, D.; Meroni, S. M. Pietro; Baker, J.; Watson, T.; Carnie, M. Origin of Exceptionally Slow Light Soaking Effect in Mesoporous Carbon Perovskite Solar Cells with AVA Additive. *J. Phys. Chem. C* **2019**, *123* (18), 11414–11421. https://doi.org/10.1021/acs.jpcc.9b01058.

(35) Meggiolaro, D.; Mosconi, E.; De Angelis, F. Mechanism of Reversible Trap Passivation by Molecular Oxygen in Lead-Halide Perovskites. *ACS Energy Lett.* **2017**, *2* (12), 2794–2798. https://doi.org/10.1021/acsenergylett.7b00955.

(36) Senocrate, A.; Acartürk, T.; Kim, G. Y.; Merkle, R.; Starke, U.; Grätzel, M.; Maier, J. Interaction of Oxygen with Halide Perovskites. *J. Mater. Chem. A* **2018**, *6* (23), 10847–10855. https://doi.org/10.1039/C8TA04537B.

(37) Abate, A.; Leijtens, T.; Pathak, S.; Teuscher, J.; Avolio, R.; Errico, M. E.; Kirkpatrik, J.; Ball, J. M.; Docampo, P.; McPherson, I.; et al. Lithium Salts as "Redox Active" p-Type Dopants for Organic Semiconductors and Their Impact in Solid-State Dye-Sensitized Solar Cells. *Phys. Chem. Chem. Phys.* **2013**, *15* (7), 2572. https://doi.org/10.1039/c2cp44397j.

(38) Cappel, U. B.; Daeneke, T.; Bach, U. Oxygen-Induced Doping of Spiro-MeOTAD in Solid-State Dye-Sensitized Solar Cells and Its Impact on Device Performance. *Nano Lett.* **2012**, *12* (9), 4925–4931. https://doi.org/10.1021/nl302509q.

(39) Tvingstedt, K.; Deibel, C. Temperature Dependence of Ideality Factors in Organic Solar Cells and the Relation to Radiative Efficiency. *Adv. Energy Mater.* **2016**, *6* (9), 1502230. https://doi.org/10.1002/aenm.201502230.

(40) Moia, D.; Gelmetti, I.; Calado, P.; Fisher, W.; Stringer, M.; Game, O.; Hu, Y.; Docampo, P.; Lidzey, D.; Palomares, E.; et al. Ionic-to-Electronic Current Amplification in Hybrid Perovskite Solar Cells: Ionically Gated Transistor-Interface Circuit Model Explains Hysteresis and Impedance of Mixed Conducting Devices. *Energy Environ. Sci.* **2019**, *12* (4), 1296–1308. https://doi.org/10.1039/C8EE02362J.

Chapter 7

General Conclusions

The charge carrier processes in perovskite solar cells have been a matter of discussion in the scientific community since the application of lead halide perovskites as light harvesters. Despite the intense research efforts, there is not a consensus yet about the processes taking place in perovskite solar cells.

In this thesis, it is shown that the use of transient optoelectronic techniques, such as TPV, TPC, and CE, that were widely applied in other emerging photovoltaic technologies, as Dye Sensitized Solar Cells or Organic Solar Cells, is very useful in perovskite solar cells. We have obtained precious information about the charge carrier recombination, and we have used variations of these techniques to study the ionic influences on recombination. Additionally, we have used femtosecond transient absorption spectroscopy to study the charge transfer processes at both interfaces, perovskite/ETM, and perovskite/HTM, getting information about the fate of hot carriers and also charge carrier loss pathways that may be detrimental to the final device performance.

We can get the following conclusions from every chapter.

In **Chapter 4**, we fabricated efficient solar cells with different low band gap semiconductor polymers that act as HTM and compare them with spiro-OMeTAD. The V_{OC} of such devices is not correlated with the HOMO levels of the HTM and that was corroborated with DiffCap measurements. With fsTA measurements, we found that the injection of hot carriers into semiconductor polymers with a LUMO level close to the conduction band minimum of the perovskite suppose a carrier loss pathway that may be detrimental to the final device performance. As a consequence, we suggested that a high LUMO level, certifying the electron blocking layer properties of the HTM, is desirable for the future design and synthesis of new materials for HTMs.

From **Chapter 5**, we determined that the modification of the interface $MAPbI_3/TiO_2$ with a thin layer of C_{60} effectively reduces the current-voltage

hysteresis in these devices. This is caused by defect passivation at the grain boundaries that reduces the ionic motion in the device. Additionally, using fsTA we have confirmed that the use of C_{60} avoids charge carrier accumulation at the interface, and that also is capable of hot carrier extraction.

Finally, in **Chapter 6**, we monitored the reduction of current-voltage hysteresis of perovskite solar cells with the aging of the devices under dry air conditions (< 10% H_2O). Using transient optoelectronic techniques, we have assigned this behavior to a reduction of the ionic influences over carrier recombination over time, which supposed an increased in both V_{OC} and fill factor.


UNIVERSITAT
ROVIRA i VIRGILI


ICIQ
Institute of Chemical
Research of Catalonia


FRIEDRICH-ALEXANDER
UNIVERSITÄT
ERLANGEN-NÜRNBERG